Doctoral theses at NTNU, 2021:337

Reidar André Skarbøvik

Multilayer Spooling of High-Performance Synthetic Fibre Ropes

Experimental Investigations of Rope Properties and Stresses in Winch Drums

Doctoral thesis

NTNU
Norwegian University of Science and Technology
Thesis for the Degree of Philosophiae Doctor
Faculty of Engineering
Department of Ocean Operations and Civil Engineering

NTNU
Norwegian University of Science and Technology

Reidar André Skarbøvik

Multilayer Spooling of High-Performance Synthetic Fibre Ropes

Experimental Investigations of Rope Properties and Stresses in Winch Drums

Thesis for the Degree of Philosophiae Doctor

Trondheim, November 2021

Norwegian University of Science and Technology
Faculty of Engineering
Department of Ocean Operations and Civil Engineering

NTNU
Norwegian University of
Science and Technology

NTNU
Norwegian University of Science and Technology

Thesis for the Degree of Philosophiae Doctor

Faculty of Engineering
Department of Ocean Operations and Civil Engineering

ISBN 978-82-326-6714-7 (printed ver.)
ISBN 978-82-326-6048-3 (electronic ver.)
ISSN 1503-8181 (printed ver.)
ISSN 2703-8084 (online ver.)

Doctoral theses at NTNU, 2021:337

Printed by NTNU Grafisk senter

To

Thea, Andrea

&

Ann-Kristin

Abstract

Winch drums can appear as relatively simple mechanical components. However, accurate quantification of loads in multilayer winch-rope systems depends on a complex interaction between rope and drum. As vital parts of lifting appliances and other handling systems, usually with no redundancy measures, proper load assessment is essential for structural integrity and optimized design.

This thesis addresses the loads induced in multilayer winch drums by high-performance synthetic fibre ropes (HPSFRs) and a comparable steel wire. Experiments with nine ropes are carried out on two winch drums equipped with strain measurements. The ropes are spooled in multiple layers with different rope tensions, and effects of rope properties as deformation under load, friction and stiffness are investigated. Further, the accuracy of classification rules and calculation methods considered as state-of-the-art are assessed against measurements.

Experiments prove that multilayer spooling of HPSFRs can induce considerably higher stresses in drum structures than steel wire rope. HPSFRs also require many more layers until stable tangential stress levels occur. The stresses are dependent on rope tension, spooling speed and rope properties such as deformation, friction, ratios between longitudinal and transverse stiffness and between drum and rope diameters.

Rope packages of HPSFRs appear as much stiffer than quantified from single ropes or multiple ropes in linearly stacked arrangements. The actual physics behind this stiffness-increasing effect is yet to be fully understood and requires further investigation. However, it is assumed that the higher loads induced by HPSFRs are related to the more significant rope deformations and contact conditions between ropes and between fibres. Possibly, this creates a more compact rope package with limited space for further deformations resulting in increased stiffness. A novel method measuring relative stiffness between rope layers directly on the drum indicates that a higher relative increase in rope package stiffness for the fibre rope than for the steel wire is possible.

Comparing results from this study with stress calculation methods show that the procedures specified by classification societies can considerably underestimate the actual stresses in multilayer winch drums with HPSFRs. A calculation method denoted as the "modified Dietz"-method takes both rope deformation and stiffness into account and is considered state-of-the-art. The radial pressure on drums with multiple layers of steel wire rope is predicted with reasonable accuracy by applying this method with the transverse stiffness determined from a single rope. It is shown that, unless empirically accounting for an increased rope package stiffness, this method fails to predict radial pressure for multilayer winch drums with HPSFR.

A calculation method for the maximum tangential stress level in multilayer winch drums with HPSFRs is proposed. This method is based on factors derived from the experiments and significantly improve calculations compared to classification rules.

Preface

This thesis is submitted to the Norwegian University of Science and Technology (NTNU) for partial fulfilment of the requirements for the degree of Philosophiae Doctor. The doctoral work has been performed as an Industrial-PhD project for Kongsberg Maritime AS (former Rolls-Royce Marine AS) at the Department of Ocean Operations & Civil Engineering, Aalesund, with Vilmar Æsøy as the primary supervisor and Henry Peter Piehl as co-supervisor. In addition, Sverre Torben and Mette Lokna Nedreberg were co-supervisors from Kongsberg Maritime AS.

The primary funding of this work was through Kongsberg Maritime's internal R&D funds, supported by the Research Council of Norway and the Industrial PhD-scheme - Doctoral projects in industry, project number 278450.

The author declares that this thesis results from original research that has not previously been submitted for a degree at any university or institution.

Reidar André Skarbøvik
Ålesund, November 2021

Acknowledgements

Research should not be carried out for the sake of research but be anchored in needs in society, e.g. industrial, medical or environmental issues. Through the Norwegian Research Council, industrial PhD projects are valuable as they ensure this by combining academic and commercial interests. In my opinion, such possibilities should be facilitated for and even more used by companies.

I want to thank the former senior management in Rolls-Royce Marine AS - Deck Machinery for the willingness to invest in knowledge and for giving me this opportunity. Thanks to Roy-Arne Stavik, Odd Arild Jakobsen and Karl Jørgen Hurlen for their strong support of my request.

The work has been challenging, fun and exhausting. Most of all, it has been exciting and rewarding. I have enjoyed the freedom and flexibility of planning my work and workdays over these years. The great responsibility of delivering a result both for myself and the company has been an important driver.

A special thanks go to my two supervisors at the Department of Ocean Operations & Civil Engineering at the Norwegian University of Science and Technology in Ålesund, Professor Vilmar Æsøy and Associate Professor Henry Piehl.

Vilmar, you are always supportive and committed. I remember and appreciate your immediate positive response to my request of being my supervisor. Your experience and guidance, keeping me on the right track, has been very valuable. I enjoyed our trip to the ICSOS 2019 conference, being your private chauffeur through Florida and enjoying Bahama Mamas (the drink) in the Caribbean.

Henry, I appreciate your knowledge, skills, quick responses, honest feedback, commitment and fantastic sense of humour.

I have enjoyed working with both of you.

Also, thanks to my supervisors in Kongsberg Maritime AS, Sverre Torben and Dr. Mette Lokna Nedreberg, for your positive support and contributions.

Thanks to my colleagues, Jan Chirkowsky, for reading through my publication manuscripts and Terje Kvangarsnes for solving control system issues in the laboratory.

Special thanks to Geir-Kåre Øvrelid for conducting all the experiments and carrying out work in the workshop at my request. During this work, the running distance of ropes spooled back and forth between winches is over 420 km! Your contribution is considerable, and your effort, skills, personality, sense of humour and incredible patience have been priceless. I enjoyed our co-operation, long days and laughs in the workshop.

Also, thanks to my colleagues in former Rolls-Royce Marine AS and Kongsberg Maritime Commercial Marine AS, especially those of you I have had the pleasure to work closely with over the years. Sadly, some of you had to leave the company or pursue other possibilities while I was busy with this work. You know who you are, and working with you has been an honour and a pleasure.

Thanks to Eirik Homlong and Offshore & Trawl Supply AS (OTS) for support and assistance with standard testing of the minimum breaking load of ropes and supplying longitudinal tension-extension curves.

Thanks to HBM Norge AS for advice and support regarding equipment and measurements, setting up the measurement system, and mounting the strain gauges according to my specifications.

Finally, thanks to my always supportive parents, family and friends. This work would not be possible without the support, patience, sacrifice, effort at home and love from my dear best friend and superhero Ann-Kristin and our lovely girls, Thea and Andrea.

Contents

Nomenclature

Abbreviations

CBOS	Cyclic bending over sheaves
CD	Clearance distance
FEA	Finite element analysis
FOV	Field of view
HBM	Hottinger Baldwin Messtechnik
HMHT	High modulus-High tenacity
HMPE	High modulue polyethylene
HPPE	High-performance polyethylene
HPSFR	High performance synthetic fibre rope
IWRC	Independent wire rope core
LCP	Liquid-crystal polymer
MBL	Minimum breaking load
MR	Measuring range
PET	Polyester
RO	Research objective
RQ	Research question

UHMWPE	Ultra-high molecular weight polyethylene
UV	Ultraviolet
x-Res.	Resoultion in x-direction
z-Lin.	Linearity in z-direction
z-Rep.	Repeatability in z-direction
z-Res.	Resoultion in z-direction

List of symbols

α	Angle during climbing of rope or wrap angle	[rad]
α_0	Rope package angle ("wedge" angle), or wrap angle	[rad]
α_L	Limit angle	[rad]
β	Misalignment angle	[rad]
χ	Geometric parameter for cylindrical shell	[mm^{-1}]
Δy_1	Compression of rope package	[mm]
$\Delta y_2, \Delta y_3$	Radial displacement of flanges	[mm]
δ_θ	Extension of rope due to unit pressure	[mm]
δ_D	Radial deformation of drum due to unit pressure	[mm]
δ_{iT}	Compression of the rope cross section due to unit pressure	[mm]
ϵ_θ	Strain in tangential direction	[mm/mm]
$\epsilon_{elastic}$	Elastic strain	[mm/mm]
ϵ_L	Longitudinal strain	[mm/mm]
$\epsilon_{plastic}$	Plastic strain	[mm/mm]
ϵ_r	Strain in radial direction	[mm/mm]
ϵ_T	Transverse strain	[mm/mm]
ϵ_z	Strain in axial direction	[mm/mm]
η	Multilayer exponent	[$-$]

γ	Water's "wedge" angle $(90^\circ - \alpha_0)$	[rad]
μ	Coefficient of friction between rope and flange/drum	$[-]$
μ_r	Coefficient of friction between ropes	$[-]$
μ_s	Coefficient of static friction	$[-]$
ν	Poisson's ratio	$[-]$
ν_r	"Poisson's ratio" of rope cross-section	$[-]$
$\overline{\sigma_\theta}(i)$	Average peak tangential stress in drum from i layers	[N/mm^2]
ψ	Tension reduction factor	$[-]$
ρ_{fibre1}	Density of fibre type one	[kg/m^3]
ρ_{fibre2}	Density of fibre type two	[kg/m^3]
σ_0	Tangential stress in thin-walled shell	[N/mm^2]
σ_1	Maximum principal stress in biaxial stress state	[N/mm^2]
σ_2	Minimum principal stress in biaxial stress state	[N/mm^2]
$\sigma_{\theta max}$	Maximum tangential stress	[N/mm^2]
σ_{θ_r}	Reduced tangential stress	[N/mm^2]
σ_θ	Tangential stress	[N/mm^2]
$\sigma_\theta(i)$	Tangential stress in drum from i layers	[N/mm^2]
σ_{b_r}	Reduced bending stress	[N/mm^2]
$\sigma_{b_{in}}$	Bending stress at inner side of drum core	[N/mm^2]
$\sigma_{b_{out}}$	Bending stress at outer side of drum core	[N/mm^2]
σ_b	Bending stress	[N/mm^2]
σ_K	Critical compressive stress	[N/mm^2]
σ_L	Longitudinal stress	[N/mm^2]
$\sigma_{plastic}$	Elasto-plastic stress	[N/mm^2]
σ_r	Radial stress	[N/mm^2]

$\sigma_{T_{lin}}$	Transverse stress of rope in linear stacked configuration	[N/mm^2]
$\sigma_{T_{pyr}}$	Transverse stress of rope in pyramidal configuration	[N/mm^2]
σ_T	Transverse stress	[N/mm^2]
σ_{VM}	von Mises stress	[N/mm^2]
σ_z	Axial stress	[N/mm^2]
τ_{in}	Shear stress at inner side of drum core	[N/mm^2]
τ_{out}	Shear stress at outer side of drum core	[N/mm^2]
θ	Rotational angle	[rad]
$\theta_1, \theta_2, \theta_3$	Parameters from non-linear regression analysis	$[-]$
φ	Angle of deformed shell element	[rad]
φ_c	Climbing sector	[rad]
φ_p	Parallel sector	[rad]
a	Distance between rope windings (rope pitch distance)	[mm]
d	Nominal rope diameter	[mm]
d_{nom}	Nominal diameter	[mm]
d_x	Major diameter of elliptical cross-section	[mm]
d_y	Minor diameter of elliptical cross-section	[mm]
f	Fill factor	$[-]$
f_i	Pressure reduction of winding i due to unit pressure	[N/mm^2]
f_m	Allowable yield stress capacity	$[-]$
h	Waters' equation for the coefficients of rope layers	$[-]$
i	Index	$[-]$
k	Ratio of force from recovered rope weight and rope tension	$[-]$
k_j	Neugebauer's factors	$[-]$
k_{PL}	Ratio between stresses in parallel and linear configurations	$[-]$

k_T	Ratio between transverse stress and longitudinal stress in rope	$[-]$
l_θ	Length of rope in winding on drum	[mm]
l_i	Gauge length	[mm]
n	Number of layers, number of repeated experiments	$[-]$
n_u	Number of unbalanced windings in the first layer	$[-]$
p_1	Pressure on drum from first winding or first layer	[N/mm^2]
p_{avg}	Average pressure	[N/mm^2]
p_D	Radial pressure on drum	[N/mm^2]
p_n	Pressure on drum from n layers	[N/mm^2]
p_r	Radial pressure on shell element	[N/mm^2]
p_x	Axial pressure on shell element	[N/mm^2]
p_z	Pressure on plate	[N/mm^2]
r	Radius	[mm]
r_1	Radius of first rope layer	[mm]
r_{avg}	Average rope layer radius	[mm]
r_D	Outer radius of drum	[mm]
$r_{i,c}$	Middle radius of rope in layer i in climbing sector	[mm]
$r_{i,p}$	Middle radius of rope in layer i in parallel sector	[mm]
r_i	Inner radius	[mm]
r_i	Middle radius of layer i	[mm]
r_m	Middle radius	[mm]
r_o	Outer radius	[mm]
s	Length of square substitution cross-section	[mm]
s_i	Middle radius of rope cross-section in layer i	[mm]
t	Thickness of drum core	[mm]

t_F	Thickness of flange	[mm]
u	Axial deformation	[mm]
$u(y)$	Linear elastic radial deformation of rope cross-section	[mm]
u_T	Standard uncertainty according to ASTM E 74-04	$[-]$
u_z	Axial deformation of flange	[mm]
w	Radial deformation	[mm]
w_{11}	Deformation of drum at winding one due to winding one	[mm]
w_{12}	Deformation of drum at winding one due to winding two	[mm]
w_h	Homogeneous solution	$[-]$
w_{max}	Maximum deflection of drum	[mm]
w_p	Particular solution	$[-]$
w_s	Extension of rope	[mm]
$x_{10\%}$	10% elongation	$[-]$
$x_{30\%}$	30% elongation	$[-]$
x_{fibre1}	Portion of fibre type one	$[-]$
x_{w_max}	Distance from flange to maximum deflection of drum	[mm]
y_{fibre2}	Portion of fibre type two	$[-]$
z	Distance through thickness	[mm]
Δl_θ	Change in length of rope in winding on drum	[mm]
$p_{f_{max}}$	Maximum flange pressure at drum surface	[N/mm^2]
A_0	Flexibility of drum	[mm/N]
A_1	Flexibility of first rope layer	[mm/N]
A_1	Flexibility of rope layer i	[mm/N]
A_r	Effective cross-sectional area of rope	[mm^2]
C	DNV GL's layer dependent factor for multilayer pressure	$[-]$

C_n	Coefficient of n rope layers	$[-]$
D	Diameter	[mm]
E	Modulus of elasticity	[N/mm^2]
E^*	Transverse rope stiffness measured direct on drum	[N/mm^2]
E_L	Longitudinal modulus of elasticity	[N/mm^2]
E_T	Transverse modulus of elasticity	[N/mm^2]
$F_L(r)$	Distributed line force on left flange as function of radius	[N/mm]
$F_R(r)$	Distributed line force on right flange as function of radius	[N/mm]
F_T	Compression force	[N]
K	Flexural rigidity	[Nmm]
K_L	ABS' layer dependent factor for multilayer pressure	$[-]$
L	Length	[mm]
$L_0(i)$	Initial height of rope package with i layers	[mm]
L_D	Distance between reaction forces	[mm]
L_{rope}	Length of rope	[m]
M_θ	Moment about θ-axis	[Nmm/mm]
M_{rope}	Mass of rope	[kg]
M_r	Moment about r-axis	[Nmm/mm]
M_x	Moment about x-axis	[Nmm/mm]
N_θ	Normal force in tangential direction	[N/mm]
N_i	Flange force in layer i	[N/mm]
N_{max}	Maximum number of rope layers	$[-]$
N_T	Total force on flange	$[N]$
N_x	Normal force in axial direction	[N/mm]
O_r	Relative ovality	$[-]$

Q_θ	Shear force in tangential direction	[N/mm]
Q_x	Shear force in axial direction	[N/mm]
R_σ	Ratio between max. and min. principal stress	$[-]$
$R_\theta(i)$	Tangential stress ratio for layer i	$[-]$
R_{ci}	Flange force in layer i according to Mupende	[N/mm]
R_c	Maximum flange force during climbing sector	[N/mm]
R_k	Total flange force in layer k	[N/mm]
R_L	Left reaction force	[N]
R_m	Tensile strength	[N/mm^2]
R_p	Flange force in parallel sector	[N/mm]
R_R	Right reaction force	[N]
$R_T(i)$	Ratio between transverse moduli for i layers and one layer	$[-]$
Rp_{02}	Yield limit defined at 0.2% plastic strain	[N/mm^2]
$S_F(i)$	Factor for tangential stress in drums with i layers of HPSFR	$[-]$
T	Rope tension force	[N]
T'	Tension reduction due to pressure from outer layers	[N]
$T_{10\%}$	Tension force at 10% elongation	[N]
$T_{30\%}$	Tension force at 30% elongation	[N]
T_i	Tension in rope layer i	[N]
T_k	Tension in layer k	[N]
U_{cal}	Uncertainty of calibration load cell	$[-]$
$U_{Modulus}$	Uncertainty of modulus of elasticity	$[-]$
U_{Pin}	Uncertainty of load cell in spooling sheave	$[-]$
U_{Strain}	Uncertainty of strain measurement	$[-]$
U_S	Expanded uncertainty of stress measurement	$[-]$

U_T	Expanded uncertainty of tension measurement system	$[-]$
U_x	Expanded uncertainty of laser measurement in x-direction	$[-]$
U_z	Expanded uncertainty of laser measurement in z-direction	$[-]$
V	Shear force	[N/mm]
V_{max}	Maximum shear force at end of drum	[N/mm]
W	Radial component of rope tension force	[N]
W'	Load factor dependent on D/d-ratio and number of layers	$[-]$
$X_{k,m}$	Partial pressure in layer k due to layer m	[N/mm^2]
X_p	Partial pressure	[N/mm^2]

Chapter 1

Introduction

1.1 Background

Since ancient times, winches have been used to handle ropes for various tasks. They are still essential tools for many operations and functions at both land and sea. Marine winches exist in numerous variants with various lifting capacities, sizes and configurations of different complexity. Winches for lifting appliances, towing and anchor handling, fishery, mooring or auxiliary equipment are examples. An overview of typical marine winch types is illustrated in Fig. 1.1, while a couple of these are shown in Fig. 1.2.

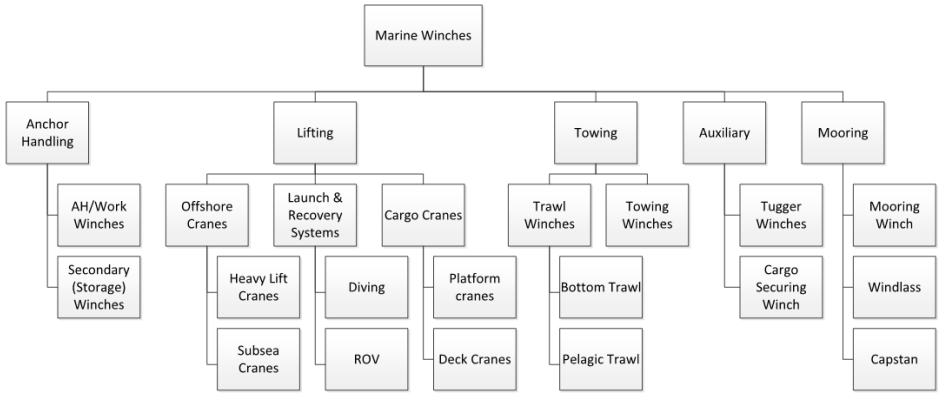

Figure 1.1: Example of marine winch taxonomy

(a) Multilayer winch on crane

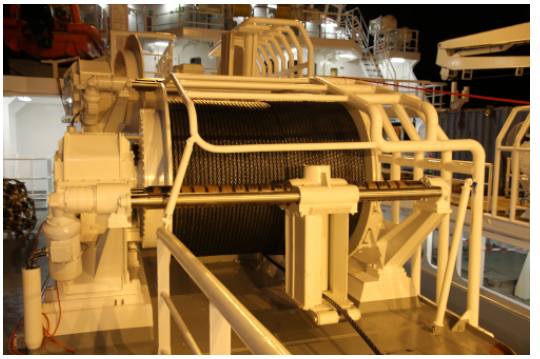

(b) Trawl winch with steel wire rope

Figure 1.2: Marine products with multi-layer winches

Compared to steel wire ropes, the use of HPSFR (high-performance synthetic fibre ropes) is limited. However, such ropes exhibit advantageous properties, such as low weight, practically floating in water, and strength comparable to steel wire ropes. Like deep-water subsea cranes, some applications are dependent on HPSFR to avoid the rope weight to consume a significant part of the lifting capacity. In addition, the absence of sticky lubricants, corrosion and dangerous steel cords are desirable properties concerning manual rope handling.

Despite the advantageous properties, the use of HPSFRs is yet not very widespread. A possible reason for this is scepticism to replace well-known technology based on steel wire ropes. Further reasons can be related to extensive certification and approval requirements or insecurity related to design rules. Sensitivity to mechanical damages and wear, fatigue and creep are often used as counterarguments for using such ropes. The relatively low melting temperature of many fibre materials is also a limiting factor. However, the risk of failures can be mitigated by proper handling equipment and good maintenance routines. A rope management system, counting bending cycles and controlling safety against fatigue along the rope length, is advantageous. In addition, the superb splice-ability of many HPSFRs allows for an economical partial replacement of critically worn segments instead of costly replacement of full rope length. On the other hand, with only a few manufacturers of raw fibre materials and low competition, fibre cost is possibly the most vital limiting driver for the extensive use of HPSFRs.

Familiar to the vast majority of winch configurations, independent of the domain and rope technology, is the horizontally oriented multilayer winch drum. Typically, the rope is wrapped in multiple layers around a cylindrical structure, with circular plates (flanges) constraining the rope axially on both ends. Such drums must be designed to handle "internal" loads arising when a rope is spooled in multiple layers and "external" bending and torsion from the payload, drives and brakes. However, stresses caused by the latter forces are usually minor compared to the loads and stresses induced by multilayer spooling. Consequently, accurate quantification of multilayer spooling loads is essential for economical and safe winch designs. However, due to complex rope-rope and rope-drum interactions, such load assessment is much more complicated than the apparent simplicity of the winch drum as a mechanical component. Figure 1.3 shows an example of magnitudes of forces on a multilayer winch drum.

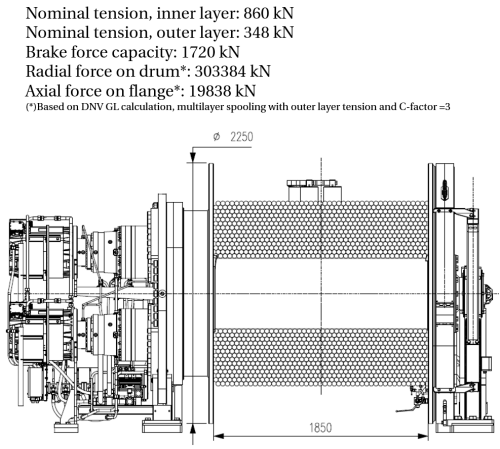

Figure 1.3: Example of loads magnitudes on a multilayer trawl winch

By acquiring Rolls-Royce Marine in 2019, the Norwegian company Kongsberg Maritime AS is now one of the world's leading companies within marine deck machinery. The research on the performance of HPSFRs and degradation in cyclic bending over sheaves (CBOS) by the former Odim AS company (acquired by Rolls-Royce in 2010) has provided essential knowledge. More than ten years of operational experience from pilot marine installation systems [1, 2] has resulted in significant differentiation and competitive edge over the recent decades.

In relation to the company's investments in equipment for subsea operations, utilization of HPSFRs, state-of-the-art knowledge of winch design, and component behaviours are important. Multilayer winch drums with HPSFRs have become of particular interest due to experiences with structural damages to such winch drums,

like the example shown in Fig. 1.4. This winch drum design had been successfully used for decades with steel wire ropes. Thus, there was reasonable cause for suspicion related to increased loads from the fibre rope.

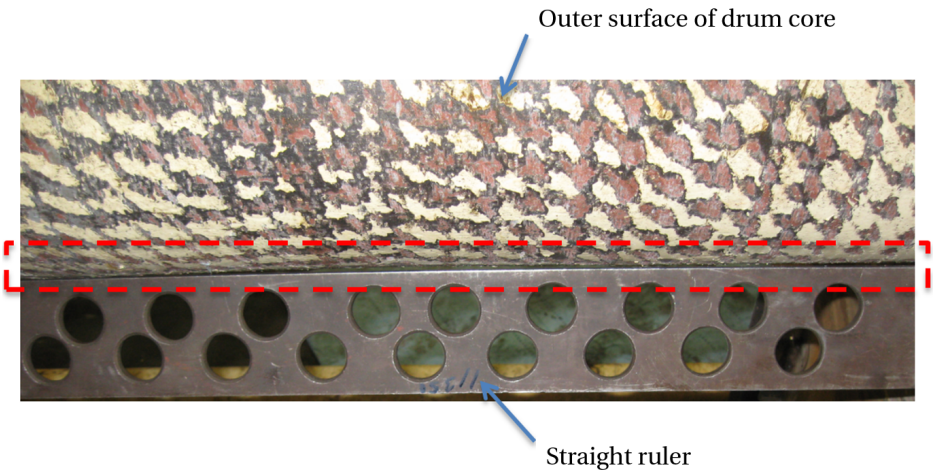

Figure 1.4: Damage to winch drum in service

A test with the relevant fibre rope and a comparable steel wire rope, typical for the relevant application, confirmed the suspicion. No damage was experienced with the steel wire rope. In contrast, the fibre rope caused accumulated stress overload and plastic deformation of the drum (Fig. 1.5a), similar to customers experiences. Further, strain measurements showed that the fibre rope induced larger tangential (hoop) stress in the winch drum compared to the steel wire, Fig. 1.5b. The measured stresses also exceeded guideline design values, and recommendations from DNV GL [3, 4]. With an increasing number of layers, the considerable difference in load from the two rope types was both interesting and disturbing.

The incidents and test revealed a knowledge gap related to multilayer winches with HPSFR, both within the company and industry. This thesis addresses this gap and presents results from extensive experimental investigations. Strain measurements during multilayer spooling with several 12-strand HPSFRs, of different designs and sizes are carried out on two different drums. In addition, a comparable steel wire rope is used as a reference. Further, calculation methods, identified as state-of-the-art and classification rules, are compared and evaluated with findings in this study. Based on this, an improved calculation is proposed for multilayer winch drums with high-performance synthetic fibre ropes.

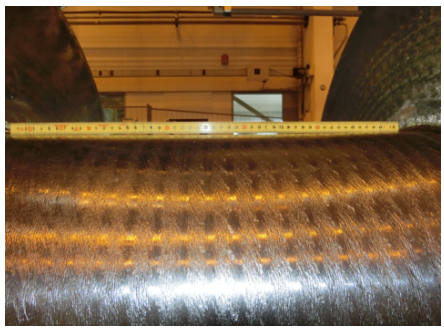

(a) Plastic deformation

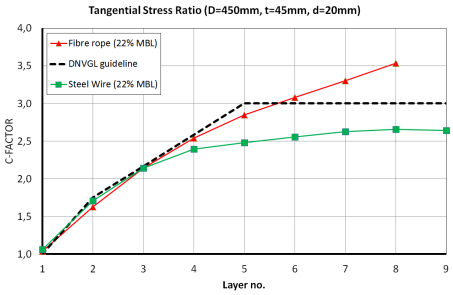

(b) Tangential stress ratios (C-factors)

Figure 1.5: Results from test by Kongsberg Maritime AS

1.2 Problem description

There are strong indications that multilayer spooling of high-performance synthetic fibre ropes can induce larger loads on winch drums than steel wire ropes. These load levels are both beyond current industry knowledge and classification rules. Consequently, uncertainties related to relevant design loads can lead to insufficient structural integrity or oversizing and unnecessary material costs.

The previous research and existing literature on multilayer spooling are mainly related to steel wire applications, while multilayer spooling with HPSFR is at the very front of related research. The number of experiments with HPSFRs evaluating and confirming theories and calculation methods is so far very few and limited to only five or six layers of rope on the drum.

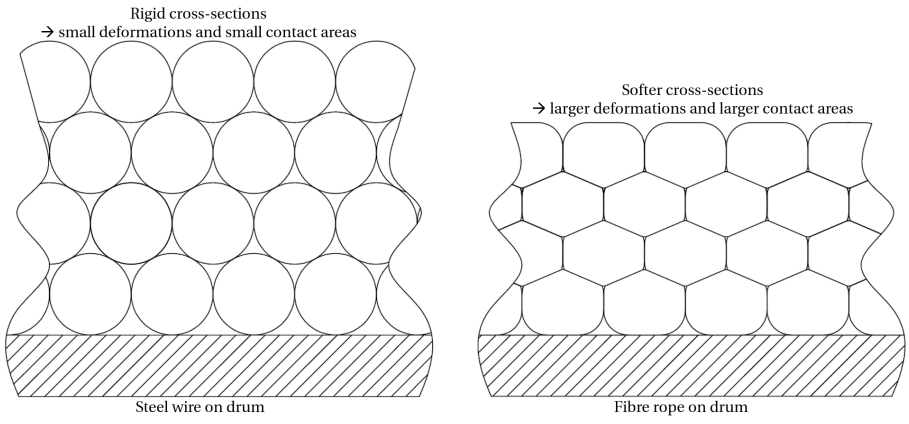

Figure 1.6: Radial deformations and contact conditions for steel wire and fibre ropes

In general, the mechanisms related to loads on multilayer spooling of steel wire rope are also assumed valid for HPSFR. These mechanisms, first described by Waters [5] and further developed by Egawa & Taneda [6] and Dietz [7], are related to transverse and longitudinal moduli of elasticity, compression of the rope cross-section and deformation of the drum. However, the pressure on the drum seems to be higher for multilayer spooling of HPSFRs compared to steel wire rope. Lohrengel et al. [8, 9] proposed an explanation for this related to the larger deformability of fibre ropes. Increased pressure can be caused by a more compact and stiffer rope package due to increased rope distortion and different contact conditions between ropes, Fig. 1.6.

Figure 1.7: Subcomponents of fibre rope compared to steel wire rope

There are also significant differences between the internal components and designs of fibre ropes compared to steel wire rope, Fig.1.7. The components of steel wire ropes are relatively few, stiff and large (macroscopic). The vast number of tiny (microscopic), flexible fibres in fibre ropes result in an extreme number of contact conditions within the rope structure. Thus, internal friction effects can also affect the behaviour and elasticity of such ropes and, consequently, stress and strain in winch drums during multilayer spooling.

1.3 Research questions

The main hypothesis of this work is that ***multilayer spooling with HPSFRs (12-strand high-performance synthetic fibre ropes) induces higher loads on winch drums than steel wire ropes of comparable size and strength.***

This introduces the following research questions:

- RQ1: *How is the stress in winch drums influenced by rope tension, number of layers, spooling speed and rope properties?*
- RQ2: *Which method for stress assessment of multilayer winch drums is state-of-the-art, and how does this method perform with HPSFR?*
- RQ3: *Are calculation methods specified in classification rules applicable to multilayer winches with HPSFRs?*
- RQ4: *How can stress calculation models be improved to include the effects of HPSFR?*

1.4 Research objectives

The main objective of this thesis is to ***improve understanding of structural loads and stresses in winch drums induced by multilayer spooling of HPSFRs, investigate rope properties effects and evaluate load assessment procedures for implementation in an improved design process for multilayer winch drums.***

Based on this and the given research questions, a set of objectives are formulated to structure the research. These objectives are related to the contributions resulting from this thesis.

The research objectives are:

- RO1: *Identify relevant rope properties and design test arrangement with suitable measurements. Carry out experiments to study their influence on multilayer spooling loads in addition to effects of rope tension and the number of layers.*
- RO2: *Identify state-of-the-art methods for assessment of loads and stresses in multilayer winches, and assess calculations against measurements.*
- RO3: *Evaluate measurements against suitable calculation methods specified by classification societies.*
- RO4: *Propose an improved design process for load assessment of multilayer winch drums.*

1.5 Scope of work

The research is quantitative, and the scope of work is illustrated in Fig. 1.8. It includes planning, design of experiments and equipment, execution of experiments and measurements with data analysis.

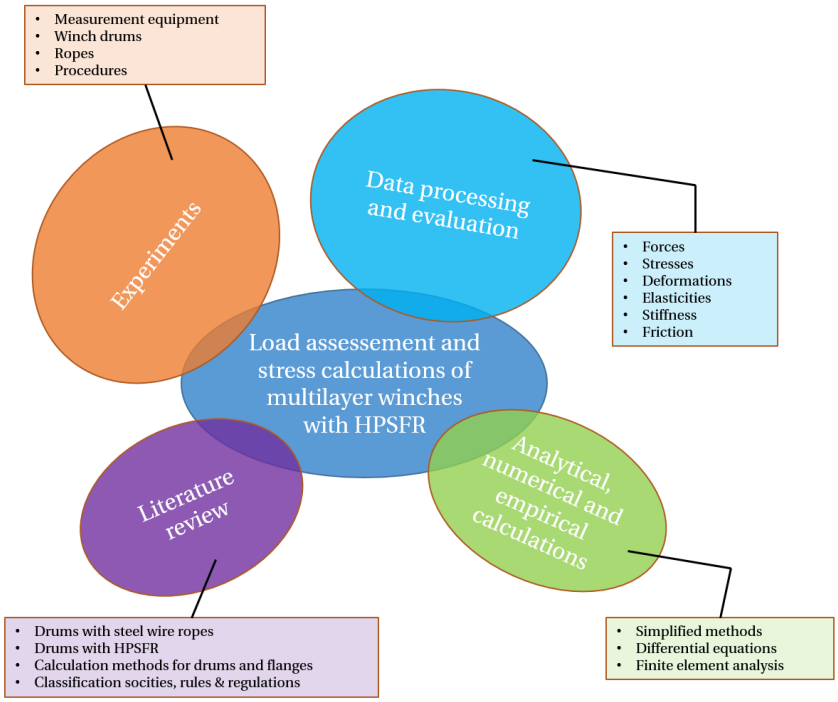

Figure 1.8: Scope of work

The experiments apply smooth drums (commonly used in many marine winch designs) to increase flexibility regarding rope sizes. Further, to reduce cost, Kongsberg Maritime's existing multi-purpose winch test rig is used. However, this limits the maximum nominal rope dimension to approximately 20 mm and the spooling tension to approximately 100 kN.

The following topics are included in the scope of work:

- Define details for measurements, instrumentation and procedures for experiments and validation of results.
- Experiments are applied on a typical Kongsberg Maritime winch design for subsea operations with a controllable spooling device and standard Kongsberg Maritime spooling pattern.
- Strain measurements on at least two drums, without grooves, of similar design with different dimensions.
- Measurements of rope properties as transverse elasticity, friction and cross-sectional deformation.

- Select rope types for testing.
- Design of experimental setup and prepare experiments.
- Analysis of experimental data.
- Analytical and numerical analysis for stress assessment of winch drums.

The following topics are not within the scope of this thesis.

- Investigation and analysis of potential damages and degradation of synthetic fibre ropes caused by multilayer spooling on winch drums.
- Winch drums with grooves.
- Spooling without spooling device.
- Different spooling patterns.

1.6 Publications

In addition to this thesis, the doctoral work has resulted in the following publications.

1. R.A.Skarbøvik, H.Piehl, S.Torben, M.L.Nedreberg and V.Æsøy. *Experimental Investigation of Stresses in Winch Drums Subjected to Multilayer Spooling Loads from Synthetic Fibre Ropes*. The 38^{th} International Conference on Ocean, Offshore and Arctic Engineering (OMAE), Glasgow, Scotland, June 9-14, 2019. [10]
2. R.A.Skarbøvik, H.Piehl and V.Æsøy. *Tangential Stress in Multilayer Winch Drums with High Performance Synthetic Ropes - Analytical Calculations versus Experimental Measurements*. Journal of Ships and Offshore Structures, Special Issue 2019. [11]

Reidar André Skarbøvik proposed the content and was the primary author for both of these publications. The co-authors assisted in improving the manuscripts.

The work presented in this thesis has developed further since the submitting and publication of these papers.

The publications are enclosed in Appendix A.

1.7 Summary of contributions

The main contributions from this thesis are related to the experimental results and verification of calculation methods. They are as follows:

- C1: Measurements prove that HPSFRs can induce considerably higher tangential stresses in winch drums compared to steel wire. The stress level's dependence on the number of layers, rope design, rope deformation, D/d-ratio, spooling tension and speed is confirmed.
- C2: For HPSFRs, the state-of-the-art method for assessing radial pressure on multilayer winch drums requires higher transverse rope stiffness than quantifiable from a single rope or several linearly stacked ropes.
- C3: The calculation method for tangential stress in multilayer winch drums specified by classification societies underestimate actual stresses considerably for multilayer winch drums with HPSFRs. It is recommended that class rules are revised and adapted to the latest findings.
- C4: A calculation method for multilayer winches with 12-strand braided high-performance fibre ropes is developed. This method improves the assessment of tangential stress in multilayer winch drums significantly compared to class rule calculations.

1.8 Structure of the thesis

This monograph consists of four main parts, each containing two chapters. The first part consists of Chapters 2 and 3. Chapter 2 gives the fundamental theoretical framework. Chapter 3 reviews the history of load and stress assessment of multilayer winch drums. This part addresses the first parts of research objectives RO1 and RO2.

The second part consists of Chapters 4 and 5. Chapter 4 presents applied methodology and methods with descriptions of the experiments, while experimental results are presented in Chapter 5. These chapters address research objective RO1.

In the third part, Chapters 6 and 7, identified calculation methods and classification rules are evaluated against experimental results. These chapters address research objective RO3 and the second part of research objective RO2.

The fourth part consists of Chapters 8 and 9. Research objective RO4 is addressed in Chapter 8 with a calculation method improving the assessment of tangential stress in multilayer winch drums with HPSFRs. At last, Chapter 9 gives a final

summary with answers to the research questions and states the contributions resulting from the work. The chapter is closed with suggestions for further research and bibliography.

In addition, supplementary material with the following content is enclosed:

- Appendix A - Publications related to the research.
- Appendix B - Fibre rope technology
- Appendix C - Supplementary results from transverse elasticity experiments
- Appendix D - Supplementary results from rope dimension experiments
- Appendix E - Supplementary results from stress measurements in drums
- Appendix F - Supplementary results from stress measurements in flanges
- Appendix G - Supplementary drum stress calculation results
- Appendix H - Supplementary evaluations of proposed calculations
- Appendix I - Procedure for design of multilayer winches

Part I

Theoretical framework and review of previous research

Chapter 2

Theoretical background

This chapter gives first a brief introduction to fibre rope structures and 12-strand braided ropes based on information from Hearle, McKenna and O'Hear [12] and Hearle [13]. This is followed by a general introduction of multilayer winch drums and fundamental calculation methods for stresses in drums and flanges.

2.1 Fibre rope structures

Rope properties differ with rope designs, fibre materials and constructions. However, the basic components of fibre ropes are the same for most such ropes. Compared to steel wire ropes, the subcomponents in fibre ropes consist of vast numbers of considerably smaller, softer and more flexible elements.

2.1.1 Basic rope components

Fibre rope structures are built of four main components. The lowest level consists of tiny individual fibres (monofilaments), with diameters typically in the range of 10-50 microns. The next level consists of yarns, made of several hundred twisted fibres (multifilaments). The thickness of such yarns is typically at a magnitude of up to 1 mm. Further, several yarns are twisted into larger rope yarn structures which, twisted together, create strands. Strands are the highest level of subcomponents. These are twisted, plaited or braided to rope structures. Dependent on design, fibre ropes can consist of additional structures, e.g. a core in the centre, an outer jacket (cover), or combinations. Figure 2.1 shows a rope where examples of a strand, yarn and a single fibre are indicated.

The fibres can be made of various natural or synthetic materials. For HPSFRs, high-modulus polyethylene (HMPE) is most common. Such fibres are manu-

factured by a gel-spinning process from ultra-high molecular weight polyethylene (UHMWPE) with long lengths of highly parallel and oriented molecules. This results in high strength and tensile stiffness in combination with low weight. Dyneema and Spectra are commercial brands of such fibres. Another fibre type relevant for HPSFRs is liquid-crystal polymer (LCP) fibres. Such fibres are manufactured by a melt-spinning process. Vectran is an example of a commercial brand of LCP fibres. A typical designation for these fibres, together with Aramid fibres, are high modulus-high tenacity fibres (HMHT).

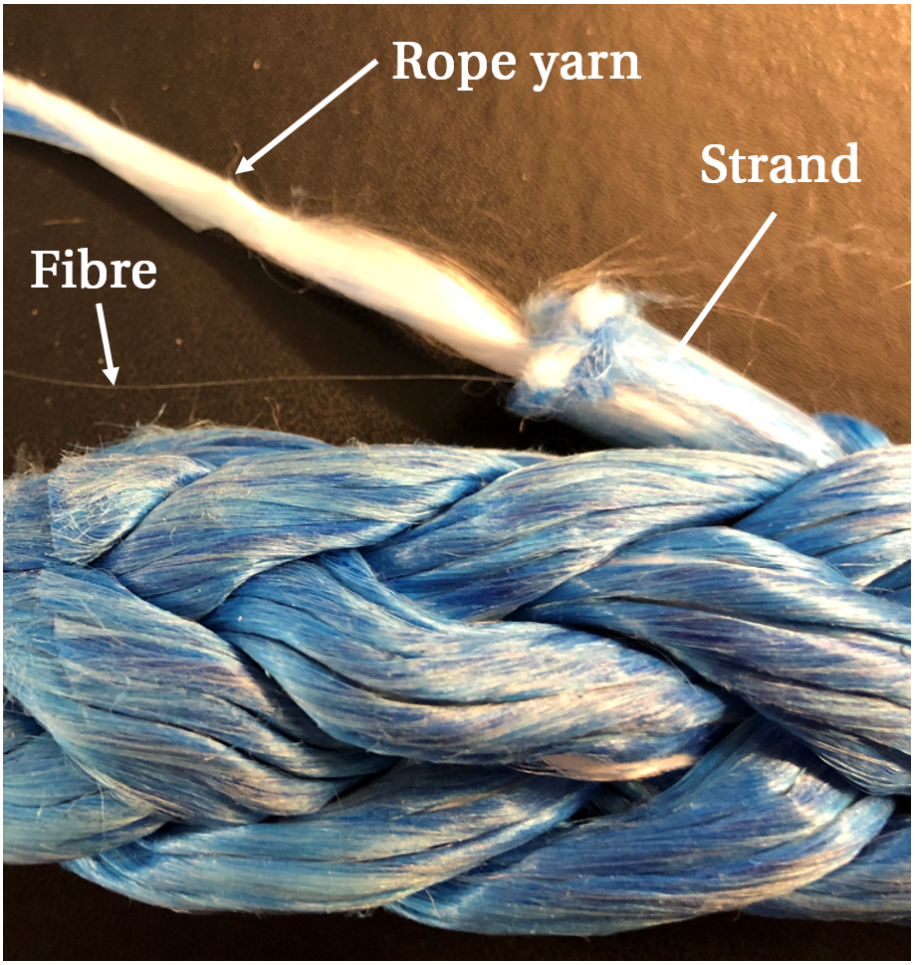

Figure 2.1: Rope components

The properties of different fibres vary, and ropes can be designed for particular purposes. Thus, ropes are commonly made of blends of various fibres to achieve

specific properties. As an example, polyester (PET) is commonly utilized in fibre blends to increase external friction.

In addition, individual fibres or finished ropes are impregnated by different types of coatings and additives. Typically, such coatings protect against UV radiation and wear, reduce internal friction and improve fatigue properties. Colour is also added to ropes through coatings.

The hydrophobic property common to PET, LCP and HMPE fibres is advantageous. Such fibres practically do not absorb water (less than 1%).

2.1.2 12-strand braided ropes

The 12-strand braided rope design is most common for advanced marine applications. Such ropes are also designated "hollow single-braid ropes" and can utilize all types of fibre materials. They are recognized by 12-strands braided in a pattern where each strand goes under and over two strands in the opposite direction. The ropes are round in shape, torque-balanced, and are typically easy to splice. The rope structure has a hole in the centre which closes to a gap no more prominent than the gap between the strands when the rope is tensioned.

Figure 2.2: Pure 12-strand braided rope

Figure 2.2 shows an example of a 12-strand braided rope. The rope is gently compressed in the upper pictures, making the strands go apart, and the rope cross-section expands. In the lower pictures, the rope is firm, and the gap is closed.

Typically, 12-strand braided ropes become flattened when running over sheaves or are spooled onto drums. Strands can be braided around a central core to improve the dimensional stability of ropes. Depending on desired properties, such cores can be metallic, made of fibres or other materials. In addition, the rope can be protected by an outer jacket. Typically, such shape controlling- and protective measures do not carry tensile load. Examples are shown in Fig. 2.3.

Figure 2.3: 12-strand braided ropes with shape stabilizing measures

Under tension, the rope structure creates significant transverse pressure and forces are effectively transferred between fibres due to friction. This effect is why very long ropes and partial repair of ropes are possible through splicing. However, with variable loading, internal friction heat can also cause damage to fibres and consequently reduce rope strength.

2.1.3 Friction in fibre ropes

Friction is very much related to the condition and state of the fibre surfaces, coatings and additives. Low friction is advantageous to reduce abrasion while holding force, splice- and traction capacity benefit from higher friction coefficients. For some fibre materials, e.g. nylon, polyester and aramid, friction coefficients are higher in wet than in dry conditions [12]. They are also reduced with increasing surface pressure. HMPE fibres typically exhibit very low coefficients of friction.

Deformation of fibre ropes causes relative motion between structural components

and fibres. As mentioned, the geometry of the rope structure forces fibres together under tension. This compression creates increased contact pressures, which limit slippage. The resulting friction force can be considerable due to the enormous amount of contacts.

Friction modes

Leech [14] categorized friction in fibre structures into *inter* and *intra* modes. *Inter* mode friction is related to relative motion between components, while deformation, dilation and distortion of the component are *intra* modes.

The different friction modes as defined by Leech [15] are:

- **Mode 1** - Axial slip
  "Slip between contiguous yarns and strands in the same layer due to rope stretch and rope twist. This acts axially along the components, but in opposite directions on opposite contact faces. On the component it will produce a shear or couple, whereas on the structure it will oppose the extensional mode."

- **Mode 2** - Component twist
  "Slip in rotation of a strand/yarn in a rope/strand; the torsion developed within the strand is resisted by the friction torque at the end of the strand. This action opposes the unwinding of a twisted strand from its end. The degree of slip is length-dependent since the friction (torque) developed is proportional to the strand length."

- **Mode 3** - Scissoring
  "Scissoring, where the relative angle between crossing strands changes due to rope stretch. This is most applicable in braided/plaited ropes, rope flexure and splices."

- **Mode 4** - Sawing
  "Sawing due to the action of one yarn over another as they slide due to rope stretch. This is not significant in geometry-preserving deformations, but since it results from flexure at the component level, it is present."

- **Mode 5** - Dilation and **Mode 6** - Distortion
  "Dilation and distortion, occurring as a result of change in strand cross-section as it is stretched in the helix, presses against contiguous strands and is squashed towards the final wedge geometry."

2.2 Multilayer winch drums - force and stress analysis

The typical multilayer winch has rope spooled in multiple layers around a horizontal drum with circular plate structures, or flanges, in both ends, preventing the rope from sliding off axially. The winch structure must be designed to handle the bending moment, shear forces and torsion from the rope tension. Stresses and deflections related to these forces can be assessed through classical mechanics and beam theory. However, these stresses are usually small compared to the stresses that can arise when spooling the rope in multiple layers with tension.

Different winch types and applications can require different design criteria, e.g. crane winches, trawl winches, auxiliary winches or mooring winches. In the case of a drive system with constant torque, the available lifting capacity of the winch decreases with each layer due to increasing layer radius. Hence, the relevant multilayer spooling load is related to the tension force capacity of outer rather than inner layers. For systems with constant tension force capacity for all layers, the situation is different. In such cases, the multilayer spooling loads are determined by the maximum available rope tension.

2.2.1 Stresses due to bending and torsion

Figure 2.4 shows a typical winch drum configuration with a drive mechanism to the left, brake band and free-floating bearing support to the right. D is the outer diameter of the drum, t is the drum core thickness, L_D is the distance between reaction forces R_L and R_R. The rope pitch distance is a, and the radius of the first rope layer is r_1.

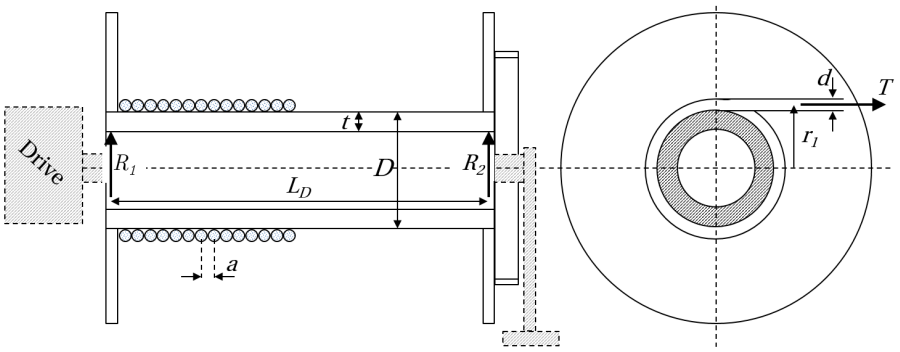

Figure 2.4: Typical winch drum configuration

The rope exit at the centre of the drum, in the middle between the reaction forces, cause maximum bending moment from which bending stresses, σ_{b_out} and σ_{b_in}, acting on the outer and inner side of the drum core are calculated by Eqs. 2.1 and

2.2. Correspondingly, Eqs. 2.3 and 2.4 give the shear stresses, τ_{out} and τ_{in}, at the outer and inner side of the drum, caused by torsion from rope tension, drive mechanism or brake.

$$\sigma_{b\_out} = \frac{8TL_D}{\pi D^3 \left[1 - \left(1 - 2\frac{t}{D}\right)^4\right]} \quad (2.1) \qquad \sigma_{b\_in} = \sigma_{b\_out}\left(1 - \frac{2t}{D}\right) \quad (2.2)$$

$$\tau_{out} = \frac{16Tr_1}{\pi D^3 \left[1 - \left(1 - 2\frac{t}{D}\right)^4\right]} \quad (2.3) \qquad \tau_{in} = \tau_{out}\left(1 - \frac{2t}{D}\right) \quad (2.4)$$

2.2.2 Stresses due to multilayer spooling

Winding rope onto a drum in multiple layers induces radial pressure on the drum and axial forces on the flanges. Quantification of these forces is complex. It depends on rope properties, and when assuming stresses below the materials yield limits, the elastic interaction between rope and drum and rope and flanges. Further, the forces can be affected by geometry and components, like, e.g. internal stiffeners.

The radial pressure causes deformation of the drum, bending moments and radial contraction on the inner radii of the flanges. The ropes in each layer press against the flanges and create shear forces, axial tension force in the drum and bending moments to ends of the drum, Fig. 2.5. Consequently, the transitions between drums and flanges are usually highly stressed areas. From a fatigue perspective, these are possible weak points in the structure.

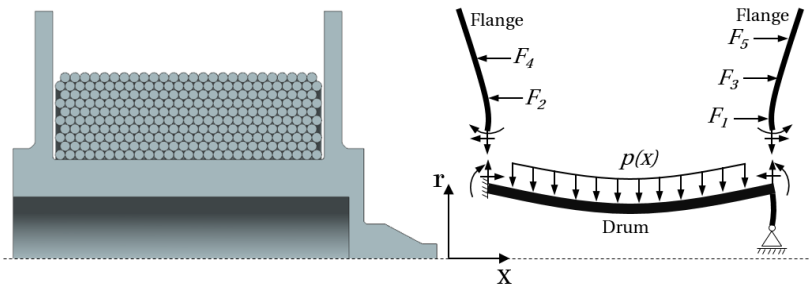

Figure 2.5: Forces on multilayer winch drum (figure inspired by Mupende [16])

During spooling, for each revolution, there is at least one sector where the rope runs parallel with the previous winding and one sector where it is axially displaced. Consequently, windings in each layer, except for the first, have different

radii. Due to the axial displacement, the contact between rope and flanges is not continuous around the circumference. Further, there is contact with the rope in either odd- or even-numbered layers on each flange. These contact patterns make multilayer spooling loads asymmetric. However, for calculations, the loads are often simplified as axisymmetric.

The parallel- and climbing sectors can be controlled by spooling devices, grooved drums, or combinations. The much applied LeBus groove system (LeBus International, Inc.) has two climbing (or cross-over) sectors and two parallel sectors for each revolution. Free spooling on smooth drums results in a helical spooling pattern.

The drum as a cylinder exposed to external pressure

Figure 2.6 illustrates a section of a long drum with a rope, with tensile force T, wrapped around it along the entire length L. When neglecting friction, equilibrium of rope forces gives the radial pressure p_D acting on the outer drum radius (r_D) from one single layer of rope, Eq. 2.5. The length L is given as n times the distance a between each winding.

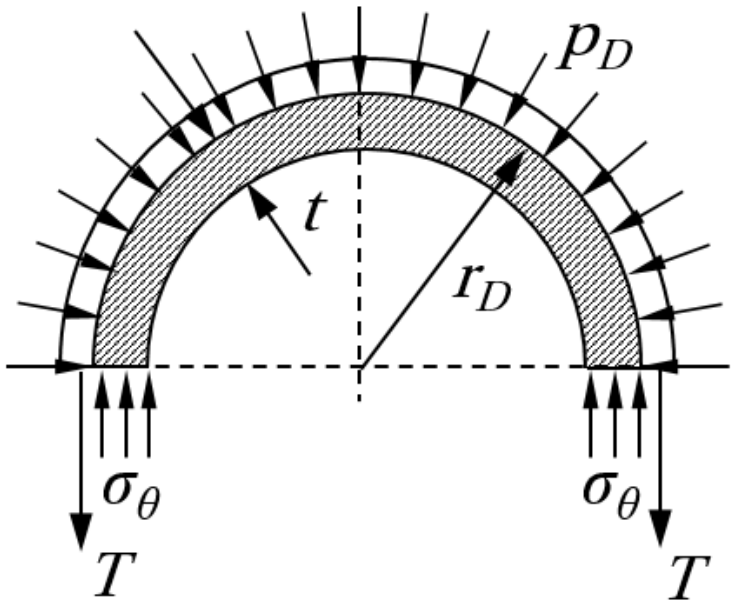

Figure 2.6: Rope wrapped around a long drum

$$2r_D n a p_D = 2Tn \Leftrightarrow p_D = \frac{T}{r_D a} \tag{2.5}$$

By considering the drum as a straight, thin-walled cylinder ($t << r_D$) with middle radius r_m exposed to a uniform external pressure, the compressive tangential stress σ_θ, acting at a sufficient distance from the drum ends, and any internal stiffeners, is calculated by Eq. 2.6. This stress is assumed constant through the thickness.

When the drum becomes thicker than about 10-20% of the drum radius, the stress variation through the thickness should be taken into account. For such thick-walled drums, the peak tangential stress acts on the inner side of the drum and is given by Eq. 2.7.

$$\sigma_\theta = -\frac{r_m}{t} p_D \approx -\frac{T}{ta} \tag{2.6}$$

$$\sigma_\theta = -\frac{2p_D}{1 - \left[\frac{(r_D - t)^2}{r_D^2}\right]} = -\frac{2T}{\left[r_D - \frac{(r_D - t)^2}{r_D}\right] a} = -\frac{DT}{ta(D - t)} \tag{2.7}$$

The drum as axisymmetric circular cylindrical shell

Deformations and stresses along the full drum length can be assessed by applying the bending theory for an axisymmetrically loaded circular cylindrical shell [17].

The following assumptions apply:

- The material is homogeneous, isotropic and linear-elastic.
- Deflections are small relative to the shell thickness.
- Plane sections through the shell thickness are normal to the mid surface and remain plane and normal to the mid surface when the shell is subjected to bending.
- The stress through the shell thickness is negligible.
- The shell thickness is small relative to the mid surface radius, $\frac{t}{r_m} \leq 0.2$.
- Friction between rope and drum is ignored, and the pressure from each winding is constant around the circumference.

With reference to Fig. 2.7, equilibrium of axial normal forces N and radial shear forces Q are given by Eqs. 2.8 and 2.9 for an undeformed shell element. Equilibrium of moments M about the θ-axis is given by Eq. 2.10.

As force and moment, N_θ and M_θ, are constant with respect to rotational angle θ, the circumferential deformation v is zero. Thus, only displacements in x- and z-directions, u and w, are considered.

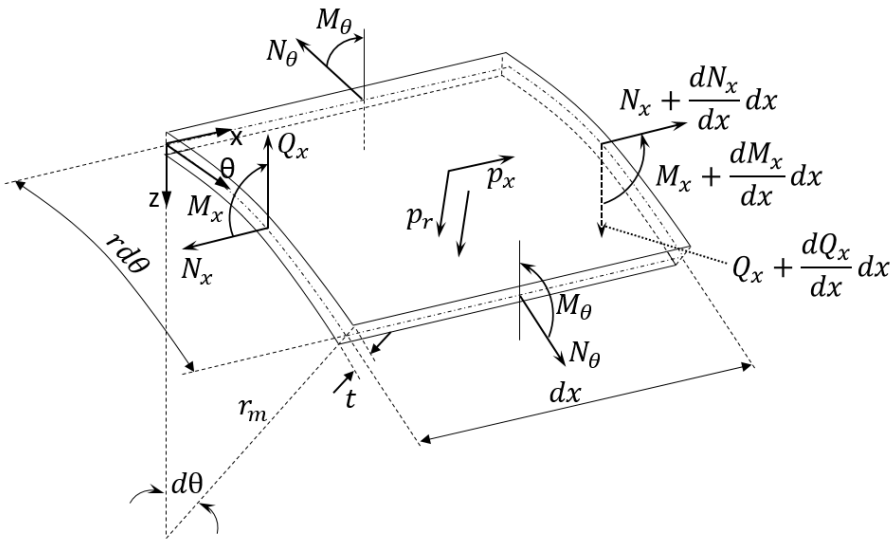

Figure 2.7: Forces and moments on undeformed circular cylindrical shell element

$$\frac{dN_x}{dx}dxr_m d\theta + p_x r_m d\theta dx = 0 \Rightarrow \frac{dN_x}{dx} + p_x = 0 \tag{2.8}$$

$$\frac{dQ_x}{dx}dxr_m d\theta + N_\theta dx d\theta + p_{r_m} dx r_m d\theta = 0 \Rightarrow \frac{dQ_x}{dx} + \frac{N_\theta}{r_m} + p_{r_m} = 0 \tag{2.9}$$

$$\frac{dM_x}{dx}dxr_m d\theta - Q_x r_m d\theta dx = 0 \Rightarrow \frac{dM_x}{dx} - Q_x = 0 \tag{2.10}$$

$$\epsilon_x = \frac{du}{dx} \tag{2.11}$$

$$\epsilon_\theta = \frac{(r_m - w)d\theta - r_m d\theta}{r_m d\theta} = -\frac{w}{r_m} \tag{2.12}$$

$$\begin{aligned} N_x = \frac{Et}{1-\nu^2}(\epsilon_x + \nu\epsilon_\theta) = \frac{Et}{1-\nu^2}\left(\frac{du}{dx} - \nu\frac{w}{r_m}\right) \\ \Downarrow \\ \frac{du}{dx} = \frac{1-\nu^2}{Et}\left(N_x + \nu\frac{w}{r_m}\right) \end{aligned} \tag{2.13}$$

$$N_\theta = \frac{Et}{1-\nu^2}(\epsilon_\theta + \nu\epsilon_x) = -\frac{Et}{1-\nu^2}\left(\frac{w}{r_m} - \nu\frac{du}{dx}\right) \tag{2.14}$$

$$M_x = -K\frac{d^2w}{dx^2} \quad (2.15) \qquad M_\theta = \nu M_x \quad (2.16) \qquad K = \frac{Et^3}{12(1-\nu^2)} \quad (2.17)$$

The axial and tangential strains, ϵ_x and ϵ_θ, are given by Eqs. 2.11 and 2.12. Applying Hooke's law, with the shell material's elastic modulus E and Poisson' ratio ν, gives axial force N_x, tangential force N_θ and bending moments M_x and M_θ from Eqs. 2.13 through 2.17.

Combining Eqs. 2.9 and 2.10 gives

$$\frac{d^2M_x}{dx^2} + \frac{N_\theta}{r_m} + p_{r_m} = 0 \quad (2.18)$$

which further develops into the differential equation for an undeformed shell of constant thickness, Eq. 2.19, by employing Eqs. 2.13, 2.14 and 2.15. The shell bending stiffness K and geometric parameter χ are given by Eqs. 2.17 and 2.20, respectively.

$$\frac{d^4w}{dx^4} + 4\chi^4 w = \frac{1}{K}\left(p_r + \frac{\nu}{r_m}N_x\right) \quad (2.19) \qquad \chi = \sqrt[4]{\frac{3(1-\nu^2)}{(r_m t)^2}} \quad (2.20)$$

Equation 2.21 gives the general solution of Eq. 2.19, where w_p is the particular solution, Eq. 2.22, and C_1, C_2, C_3 and C_4 are constants of integration dependent on boundary conditions.

$$w = e^{-\chi x}\left(C_1 cos\chi x + C_2 sin\chi x\right) + e^{\chi x}\left(C_3 cos\chi x + C_4 sin\chi x\right) + w_p \quad (2.21)$$

$$w_p = \frac{1}{4\chi^4 K}\left(p(x) - \frac{\nu}{r_m}n_x\right) \quad (2.22)$$

The following boundary conditions can apply:

- Free edge: $w \neq 0$, $\frac{dw}{dx} \neq 0$, $M_x = 0$, $Q_x = 0$ & $u \neq 0$
- Simply supported edge: $w = 0$, $\frac{dw}{dx} \neq 0$, $M_x = 0$, $Q_x \neq 0$ & $u = 0$
- Fixed edge: $w = 0$, $\frac{dw}{dx} = 0$, $M_x \neq 0$, $Q_x \neq 0$ & $u = 0$
- Elastic supported edge: $w \neq 0$, $\frac{dw}{dx} \neq 0$, $M_x \neq 0$, $Q_x \neq 0$ & $u = 0$

Equations 2.23 and 2.24 give the axial and tangential stresses in the shell at a distance z through the thickness t. The first and second terms are membrane and bending stresses, respectively.

$$\sigma_x = \frac{N_x}{t} + \frac{12M_x z}{t^3} \qquad (2.23) \qquad \sigma_\theta = \frac{N_\theta}{t} + \frac{12M_\theta z}{t^3} \qquad (2.24)$$

The flange as axisymmetric annular plate

The flanges can be simplified and considered as axisymmetrical annular plates exposed to axial circumferential line loads [17], as shown in Fig. 2.8.

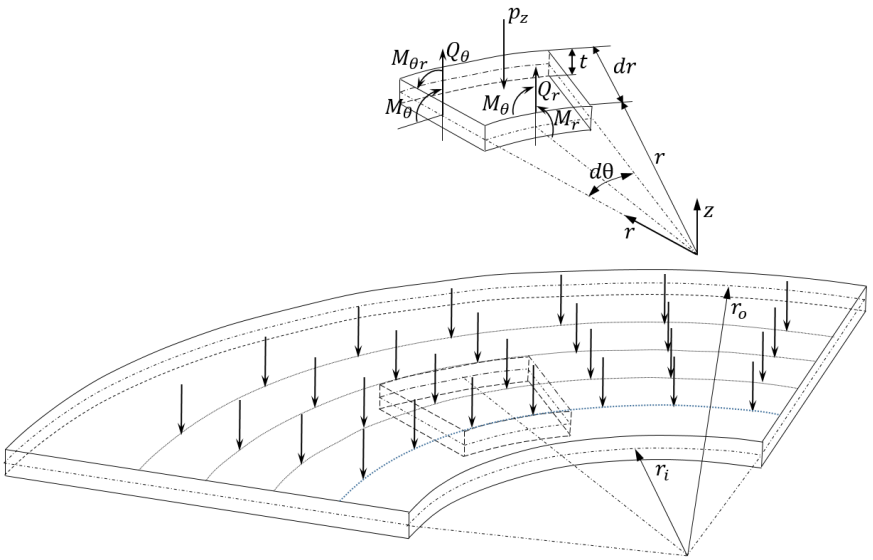

Figure 2.8: Flange as axisymmetric annular plate

The assumptions given for the drum shell in Section 2.2.2 apply in addition to the following:

- The plate is continuous in the region $0 \leq \theta \leq 2\pi$.
- The loading is not a function of θ.
- The boundary conditions are constant around the circumference.

Due to symmetry, $M_{\theta r} = Q_\theta = 0$ and moments M_r, M_θ and shear force Q_r are given by Eqs. 2.25, 2.26 and 2.27.

Equation 2.28 is the differential equation for deflection of an axisymmetrically loaded plate of constant thickness and material properties.

The solution of this equation is given by Eq. 2.29 where w_h and w_p is the homogeneous and particular solutions, respectively. Solutions for different boundary conditions are omitted but can be found in literature, e.g. Roark's formulas for stress and strain [18].

Further, related radial and tangential stresses, σ_r and σ_θ, are given by Eqs. 2.30 and 2.31.

$$M_r = -K\left(\frac{d^2w}{dr^2} + \frac{\nu}{r}\frac{dw}{dr}\right) \quad (2.25) \qquad M_\theta = -K\left(\frac{1}{r}\frac{dw}{dr} + \nu\frac{d^2w}{dr^2}\right) \quad (2.26)$$

$$Q_r = -K\frac{d}{dr}\left(\frac{d^2w}{dr^2} + \frac{1}{r}\frac{dw}{dr}\right) = -K\frac{d}{dr}\left[\frac{1}{r}\frac{d}{dr}\left(r\frac{dw}{dr}\right)\right] \quad (2.27)$$

$$\frac{1}{r}\frac{d}{dr}\left\{r\frac{d}{dr}\left[\frac{1}{r}\frac{d}{dr}\left(r\frac{dw}{dr}\right)\right]\right\} = \frac{p_z(r)}{K} \quad (2.28)$$

$$w = w_h + w_p = C_1 lnr + C_2 r^2 lnr + C_3 r^2 + C_4 + w_p \quad (2.29)$$

$$\sigma_r = -\frac{Ez}{1-\nu^2}\left(\frac{d^2w}{dr^2} + \frac{\nu}{r}\frac{dw}{dr}\right) = \frac{12M_r z}{t^3} \quad (2.30)$$

$$\sigma_\theta = -\frac{Ez}{1-\nu^2}\left(\frac{1}{r}\frac{dw}{dr} + \nu\frac{d^2w}{dr^2}\right) = \frac{12M_\theta z}{t^3} \quad (2.31)$$

2.2.3 Finite element analysis

The described analytical methods applying shell and plate theories are limited to axisymmetric loads and geometry. In addition, the interaction between drum and flanges are ignored by treating drum and flanges separately.

More realistic, efficient and practical calculations can be achieved employing linear elastic, or if required, nonlinear elasto-plastic FEA.

2D axisymmetric analysis

Like the presented analytic methods, 2D-axisymmetric FEA requires axisymmetric geometry and loads. However, the stiffness between drum and flanges are more realistically taken into account. This method is very efficient as the number of equations and degree's of freedom is considerably reduced by only considering one single radian of revolution.

If the required simplifications are acceptable, this method is usually preferred in non-linear analysis due to its efficiency.

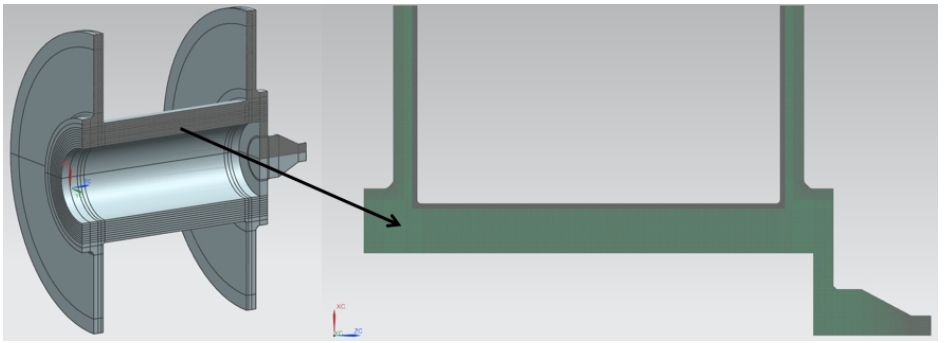

Figure 2.9: Axisymmetric FEM

3D axisymmetric analysis

In some cases, symmetry can be cyclic, preventing 2D simplification. A 3D solid axisymmetric analysis of one of the cyclic sectors can then be efficient.

3D solid finite element analysis

A complete 3D solid analysis removes the limitations of loads, boundary conditions and geometry related to axisymmetric analysis. Hence, loads varying with rotational angle can also be applied.

2.3 Summary - theoretical background

High-performance synthetic fibre ropes are complex structures with many elements, internal contact and friction effects. The many possibilities for unique engineered solutions make it difficult to generalize properties and effects.

Stresses induced by spooling loads are dominating for multilayer winch drums. In some cases, calculation models can be simplified and stresses assessed analytically by considering winch drums as rotational-symmetric shells and flanges as annular plates. However, finite element analysis is preferred. Such analysis effectively include the interaction between drum and flanges and allow for non-symmetric loads.

Chapter 3

Previous research

This chapter holds a chronological presentation of previous research. It is followed by discussing the impact and relevance of the different contributions and identifying state-of-the-art calculation methods for multilayer winch drums.

3.1 Methods for load assessment of multilayer winches

Quantification of relevant radial pressure and flange forces on multilayer winch drums has been subject to research for more than a century and is fundamental to stress calculations.

The simplest estimate for the resulting radial pressure on the drum, p_D, from multiple layers of rope is to summarize the radial pressures from each layer without further considerations. This is calculated by Eq. 3.1 where T is rope tension force, d is nominal rope diameter, D is outer drum diameter and n is the maximum number of layers. However, this method assumes rigid rope cross-sections. It results in too high radial pressure even with only a few layers on the drum. Consequently, this results in oversized and unnecessary expensive winch drums.

$$p_D = \frac{2T}{d} \sum_{i=1}^{n} \frac{1}{D + 2\,(i-1)\,d} \tag{3.1}$$

Improvement of load assessment has been and still is the main issue in research on multilayer winches. A chronological review of the relevant contributions on the topic of multilayer load assessment is presented in the following. The timeline of the treated contributions is illustrated in Fig. 3.1.

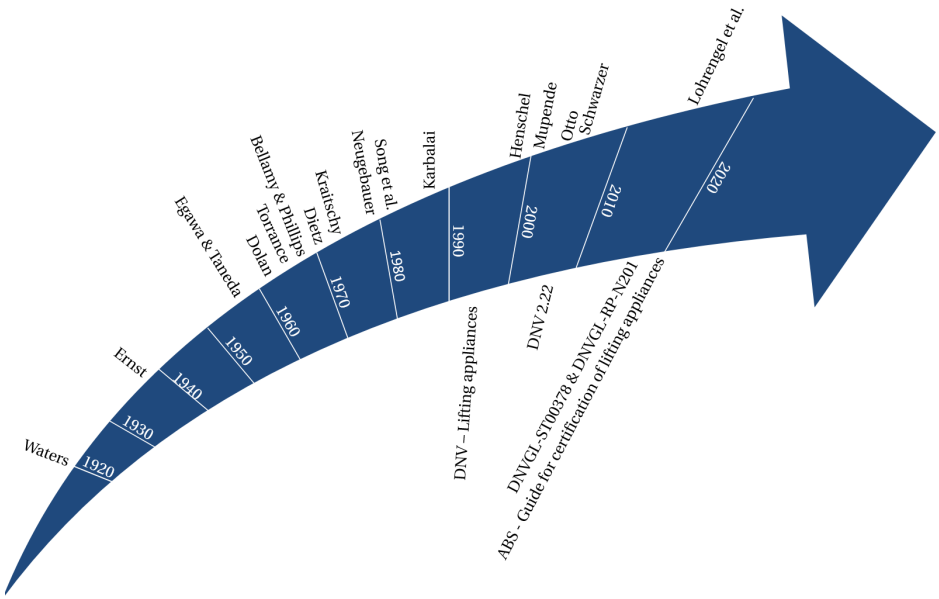

Figure 3.1: Chronological overview of previous contributions

3.1.1 Methods by Waters (1920)

In the first publication on multilayer winch drum loads, Waters [5] presented two different methods for calculating forces acting on the flanges. He also introduced the layer dependent reduction of rope tension on multilayer drums with steel wire rope.

Multilayer rope tension reduction effect

Waters introduced the ratio of the rope's longitudinal and transverse moduli of elasticity, E_L and E_T, and the coefficient of lateral deformation ("cross-sectional Poisson's ratio") ν_r, Eq. 3.2 in calculations. A_r is the effective cross-sectional area of the rope and r_{avg} the average radius of the ropes layers. The angle between the drum surface and the centre of ropes in different layers (rope package angle) is α_0.

Figure 3.2 shows the coefficients of rope layers, the ratio between radial load on the drum caused by a given number of layers relative to the radial load caused by a single layer (C-factors), as presented by Waters for five different values of h, Eq. 3.2. The reduced pressure on the drum was related to compression of ropes reducing tension in underlying layers. Unfortunately, Waters' did not give any other equations or information about detailed calculations.

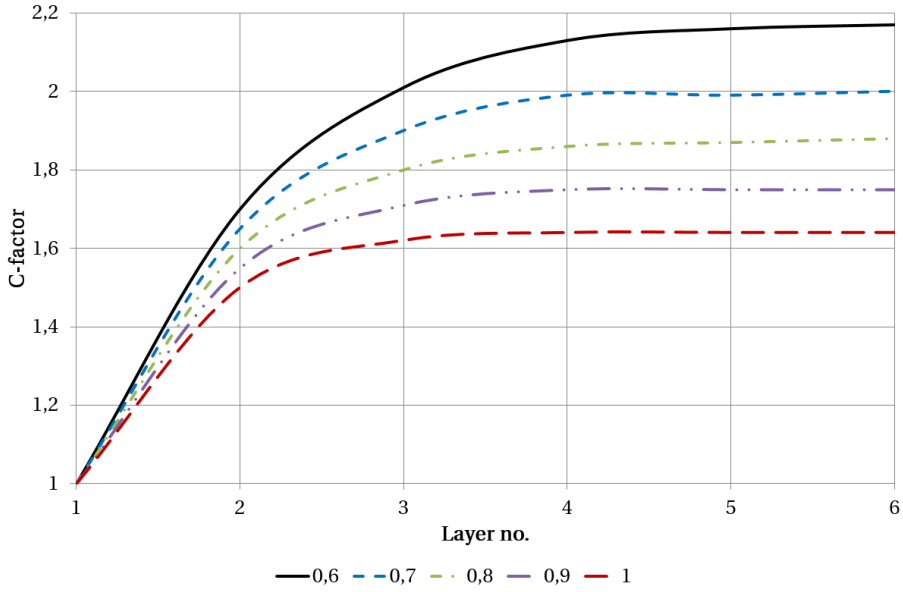

Figure 3.2: Waters' coefficients of rope layers for different values of h [5]

$$h = \frac{A_r E_L}{E_T r_{avg}^2} \left(\frac{\alpha_0}{45°} - \frac{90° - \alpha_0}{45°} \nu_r \right) \tag{3.2}$$

Flange forces

Waters' first method for calculating flange forces ignores friction between ropes and rope and drum. It is based on an axisymmetric model of stacked rigid cylinders supported by the grooves between underlying windings, Fig. 3.3.

With grooved drums, the rope windings in the middle of the drum (shaded area) are self-supported. The flanges support the windings enclosed by the two wedge-shaped areas in each end.

Compared with experiments, Waters found that calculations based on this method resulted in excessive forces. He explained this by the effects of omitting friction, sectors with rope cross-over and multilayer tension reduction. For an odd number of layers $(2m-1)$ the forces are calculated by Eqs. 3.3 and 3.4, while Eqs. 3.5 and 3.6 apply for even number of layers $(2m)$. The variable $b = 2m - i$ is the number of rope windings contributing to flange force in each layer i.

The total force acting on the flange from n layers is estimated by Eq. 3.7.

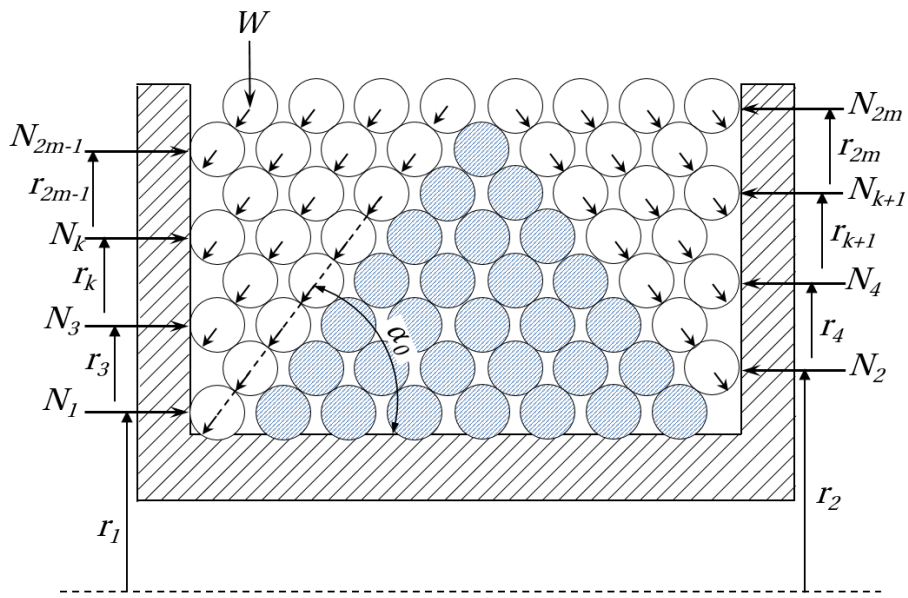

Figure 3.3: Flange forces from stacked solid cylinders

$$N_{2m-b} = bWcot\alpha_0 = 2\pi bTcot\alpha_0 \tag{3.3}$$

$$N_1 = (m-1)Wcot\alpha_0 = 2(m-1)\pi Tcot\alpha_0 \tag{3.4}$$

$$N_{2m-b} = (b+1)Wcot\alpha_0 = 2(b+1)\pi Tcot\alpha_0 \tag{3.5}$$

$$N_1 = \left(m - \frac{1}{2}\right) Wcot\alpha_0 = (2m-1)\pi Tcot\alpha_0 \tag{3.6}$$

$$N_1 + N_3 + N_5 + ... + N_n \approx N_2 + N_4 + N_6 + ... + N_n \approx \frac{n^2 - 1.5}{2}\pi Tcot\alpha_0 \tag{3.7}$$

Waters' second method accounts for both friction and multilayer tension reduction effects. The total force acting on the flange is determined by considering the rope windings enclosed by an imaginary wedge pressing against the flange, Fig. 3.4.

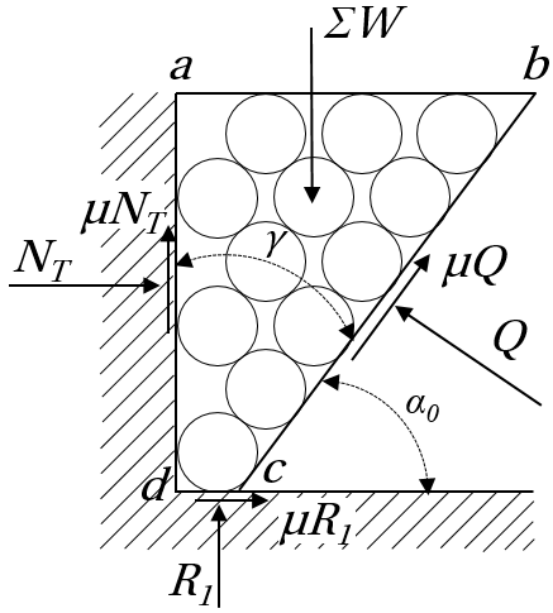

Figure 3.4: "Wedge" flange force by Waters [5]

Waters estimated the indeterminate radial force R_1 for n layers by Eq. 3.8. R_1 is eliminated together with Q through equilibrium conditions, and Eq. 3.9 gives the total axial load on the flange N_T. The multilayer load reduction effect is included by applying Eq. 3.10, where T is the tension during spooling of each layer. Correspondingly, T' is the tension reduction in each layer.

$$R_1 = \frac{2}{n+1}\left[R_1 + Q\left(sin\gamma + \mu cos\gamma\right)\right] \tag{3.8}$$

$$N_T = \frac{\left[\left(\left(\frac{2}{n+1}\right) - \mu^2 - 1\right) cos\gamma - \mu\left(\frac{2}{n+1}\right) sin\gamma\right] \sum W}{\left(1-\mu^2\right)\left(\frac{2}{n+1}\right) sin\gamma + \mu\left(\left(\frac{4}{n+1}\right) - \mu^2 - 1\right) cos\gamma} \tag{3.9}$$

$$\sum W = 2\pi \sum \left(T - T'\right) \tag{3.10}$$

Considering Waters' first method, disregarding friction and tension reduction effects, the distribution of flange force is assumed as indicated by the lines ABC in Fig. 3.5. Including the effect of friction is assumed to reduce the axial force by a constant amount, visualised by lines DEF. Further, including tension reduction effect and considering rope compression to be most prominent in windings close

to the drum surface result in a more uniform distribution as indicated by lines GHI. Experiments supported the latter, and Waters proposed a "uniform" force distribution along the flange radius, meaning that the product of load per unit area and radius from the drum axis is constant.

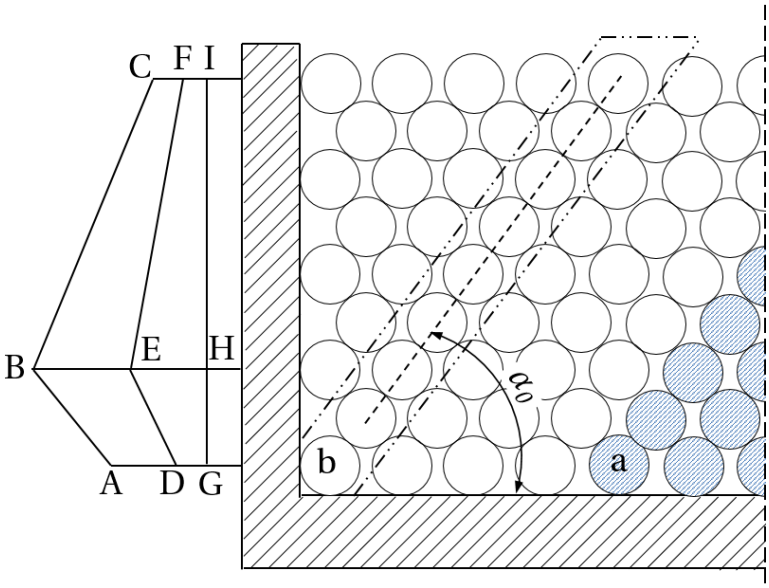

Figure 3.5: Distribution of flange force

On smooth drums, the number of windings balanced by opposite forces is limited, e.g. the windings to the right of winding a in Fig. 3.5. Consequently, an additional shear force acts on the drum flange. This shear force is reduced by friction preventing the bottom unbalanced windings from slipping sideways. Equation 3.11 estimates this additional shear force for n layers caused by n_u number of unbalanced windings in the first layer.

$$\sum (N_1) = \frac{\pi n_u}{2} \left[(n-1)T - \sum (T') \right] \frac{cot\alpha_0 - \mu}{1 - \mu^2} \tag{3.11}$$

Waters did not differentiate between friction coefficients in his calculations. This decision was based on experiments resulting in minor differences between measured friction coefficients between rope-rope and rope-drum ($\mu_r = 0.201$ and $\mu = 0.181$).

3.1.2 Method by Ernst (1938)

Through experiments with several drums of steel and cast iron, Ernst [19] discovered that the critical compressive stress, σ_K, for a pipe exposed to external pressure, Eq. 3.12, and the tangential stress, Eq. 3.13, resulted in deviations from actual stresses in winch drums with one single layer of steel wire rope.

Based on the elastic deformation of a strip segment of the winch drum Fig. 3.6 Ernst derived equations for the tangential and bending stresses in the winch structure induced by a single rope winding, Eqs. 3.14, 3.15 and 3.16.

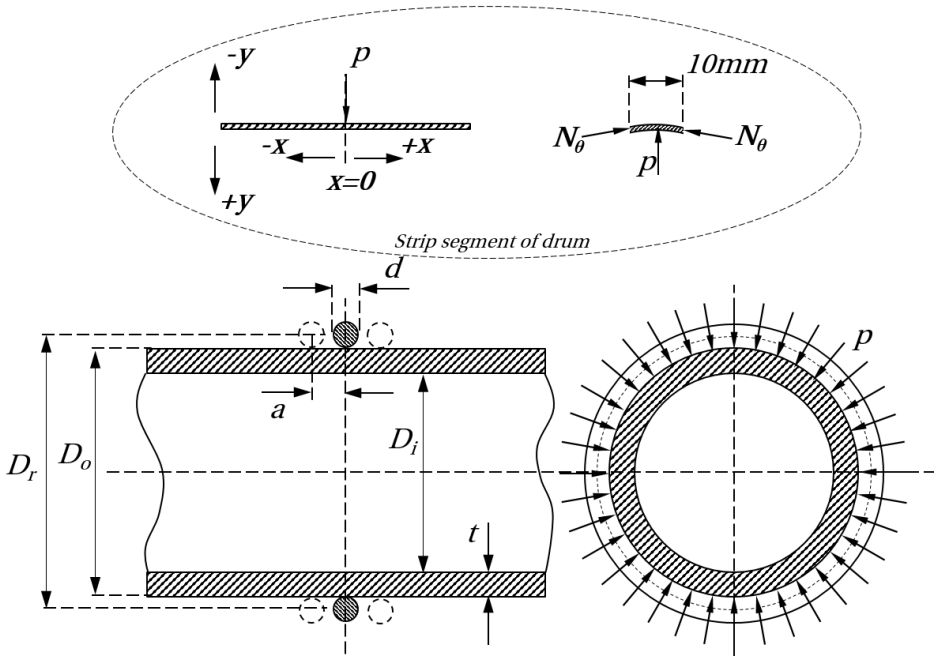

Figure 3.6: Ernst's model of drum with one single rope winding

$$\sigma_K = -\frac{Et^2}{4r_m^2} \qquad (3.12) \qquad \sigma_0 = -\frac{T}{ta} \qquad (3.13) \qquad \alpha = \sqrt[4]{\frac{12}{D^2t^2}} \qquad (3.14)$$

$$\sigma_\theta = \frac{\sigma_0}{2}\sqrt[4]{12\left(\frac{a}{t}\right)^2\left(\frac{a}{D}\right)^2}e^{-\alpha x}(cos(\alpha x) + sin(\alpha x)) \qquad (3.15)$$

$$\sigma_b = \frac{\sigma_0}{4}\sqrt[4]{12\left(\frac{a}{t}\right)^2\left(\frac{a}{D}\right)^2}e^{-\alpha x}(cos(\alpha x) - sin(\alpha x)) \qquad (3.16)$$

These equations showed that the distribution of tangential stress spreads relatively wide into the structure to both sides of the loaded winding, Fig. 3.7(a). In contrast, the bending stress occurs more locally, Fig. 3.7(b). Consequently, the peak tangential stress is lower than the stress calculated by Eq. 3.13. However, the peak tangential stress approaches this value with decreasing drum thickness or increasing distance between windings.

During spooling of several windings in one layer, the radial deformation of the drum causes a reduction in the rope tension in previously spooled windings. Consequently, the pressures from these windings and the effective tangential stress in the drum structure are reduced. Ernst derived equations, giving good correspondence with experiments, for the tangential and bending stresses taking this effect into account, Eqs. 3.17 and 3.18.

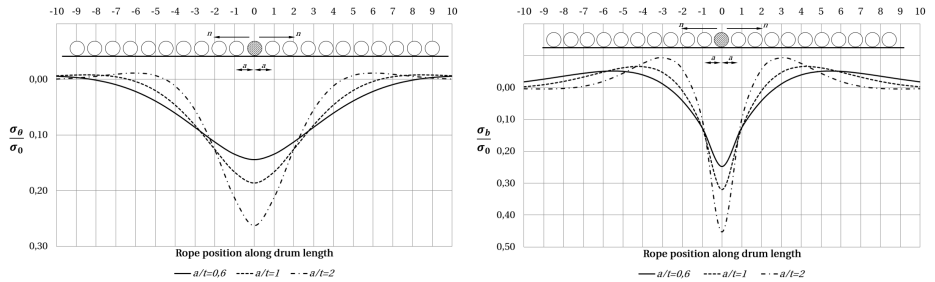

(a) Tangential stress **(b)** Bending stress

Figure 3.7: Stress distribution in drum due to pressure from one winding

$$\sigma_{\theta\_r} = \frac{\frac{4atE_D}{\pi d^2 f E_L}}{\frac{1}{2} + \frac{4atE_D}{\pi d^2 f E_L}} \sigma_\theta \qquad (3.17) \qquad \sigma_{b\_r} = \sigma_b - \frac{\frac{2atE_D}{\pi d^2 f E_L}}{\frac{1}{2} + \frac{4atE_D}{\pi d^2 f E_L}} \sigma_b \qquad (3.18)$$

(E_D and E_L are the elastic modulus of the drum material and the longitudinal modulus of the rope, respectively.)

The first layer stress reduction effect can be significant for tangential stresses in thin-walled winch drums but practically negligible for thicker drums, Fig. 3.8(a). The stress reduction is also dependent on the drum material's modulus of elasticity. Materials with a lower modulus of elasticity result in more considerable stress reduction than materials with a higher modulus. When it comes to bending stress, the effect is reversed. Thus, bending stresses increase with decreasing drum thickness or modulus of elasticity, Fig. 3.8(b).

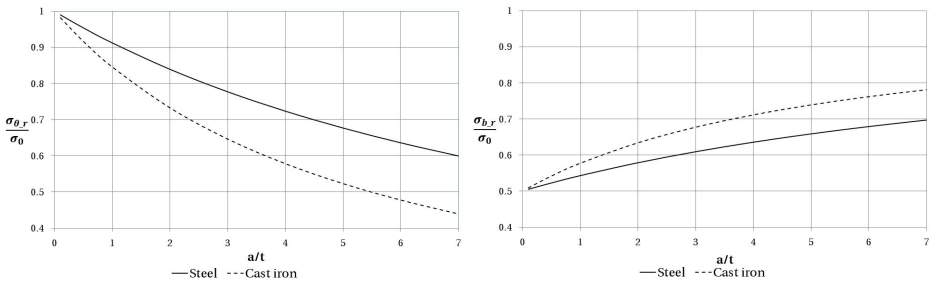

(a) Tangential stress **(b)** Bending stress

Figure 3.8: Example of stress reduction effect due to drum deformation

3.1.3 Egawa & Taneda (1958)

Egawa and Taneda [6] carried out a theoretical and experimental investigation of multilayer spooling loads. They presented an iterative calculation method for the resulting radial pressure on the drum, considering both drum and steel wire rope stiffness.

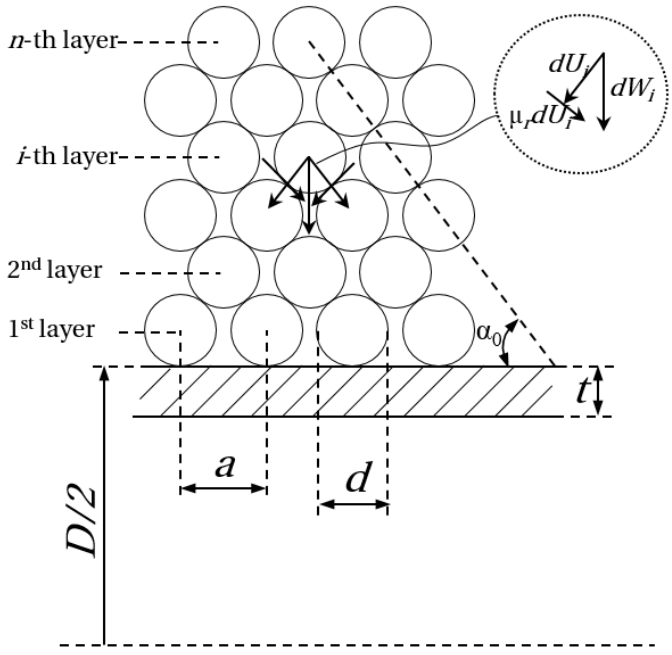

Figure 3.9: Rope forces in multilayer arrangement according to Egawa & Taneda [6]

Figure 3.9 shows the forces acting between ropes in layers, stacked with an angle α_0, from which Egawa and Taneda derived their formulas. The tensions T in each layer n are calculated employing Eqs. 3.19 through 3.26. The maximum number of layers is N_{max}, E_T and E_L are the transverse and longitudinal moduli of the rope, and D is the outer drum diameter. The drum core thickness is t, the nominal rope diameter is d, and the centre distance between ropes is a. Further, the ratio between lateral expansion and radial compression of the rope cross-section (analogous to the Poisson's ratio) is denoted ν_r.

The multilayer tension reduction effect was explained by the radial deformation of the drum and the flattening of rope windings in lower layers due to the pressure from preceding layers.

The calculation method takes both the rope's longitudinal and transverse moduli of elasticity and the rope's lateral expansion under radial compression into account. The method also allows for gradually reduced tension, T_w, due to recovered rope weight during spooling. Constant tensions for all layers are achieved by setting Eq. 3.25 equal to one.

The drum deformation is simplified and can be either included or ignored. Deformation at sufficient distance to "disturbances", e.g. flanges, stiffeners, and boundary conditions at drum ends, are included by applying Eq. 3.22. Stresses in the vicinity of such "disturbances" or very thick-walled drums are approximated by ignoring Eq. 3.22.

Equation 3.27 gives Egawa and Taneda's coefficients of rope layers. Their calculated values gave relatively good correspondence with the experiments and were somewhat higher compared to the values presented by Waters [5].

$$T_{t,n} = \left(\frac{\frac{1}{2} E_L f \pi d^2}{D + (1 + 2(i-1) sin\alpha_0) d} \right) M, i = 1, 2, ..., n-1 \tag{3.19}$$

$$M = \left\{ \begin{array}{l} A_0(\Omega T - T_{1,n} - T_{2,n} .... - T_{(n-1),n} \\ +A_1(\Omega T - T_{2,n} - T_{3,n} .... - T_{(n-1),n}) \\ +A_2(\Omega T - T_{3,n} - T_{4,n} .... - T_{(n-1),n}) \\ +..... \\ +A_{t-1}(\Omega T - T_{t,n} - T_{(t+1),n} .... - T_{(n-1),n}) \\ +\frac{1}{2} A_t(\Omega T - T_{(t+1),n} - T_{(t+2),n} .... - T_{(n-1),n}) \end{array} \right\} \tag{3.20}$$

$$\delta = arctan(\mu_r) \tag{3.21}$$

$$A_0 = \frac{D}{2E_D ta} \tag{3.22}$$

$$A_1 = \frac{(1 + sin\alpha_0)(2 - \nu_r cot(\alpha_0 + \delta))}{2E_T(D + d)} \tag{3.23}$$

$$A_i = \frac{(2sin\alpha_0(1 - \nu_r cot(\alpha_0 + \delta))}{E_T(D + (1 + 2(i-1)sin\alpha_0)d)}, i \neq 1 \tag{3.24}$$

$$k = \frac{T_w}{T} \tag{3.25}$$

$$\Omega = \left(1 - \frac{(n-1)k}{N_{max}}\right) \tag{3.26}$$

$$C_n = C_{n-1} + \left(\Omega - \left(\frac{T_{1,n}}{T} + \frac{T_{2,n}}{T} + ... + \frac{T_{(n-1),n}}{T}\right)\right), C_1 = 1 \tag{3.27}$$

3.1.4 Dolan (1963) & Torrance (1965)

Both Dolan [20], who carried out an extensive investigation of failures to winch drums in the mining industry, and Torrance [21] referenced Patrick Hendry (1913) and his unpublished empirical calculation method for pressure on multilayer winch drums. Hendry's calculations were based on the spooling tensions T_i in each layer, the drum's modulus of elasticity E_D and thickness t, the rope's longitudinal modulus of elasticity E_L, middle drum radius r_m and rope diameter d with a fill factor f of approximately 61%. Equations 3.28 and 3.29 give the pressure p_D acting on the drum.

$$p_D = \frac{[T_1 + (1 - J)(T_2 + T_3 + ... + T_n)]}{r_m d} \tag{3.28}$$

$$J = \frac{1}{1 + \left(\frac{2.08tE_D}{dE_L}\right)} \tag{3.29}$$

Torrance derived other equations, Eqs. 3.30 and 3.31, based on rope layers idealized as thin-walled cylinders with diameters d, shrunk onto the drum. Compared

to Eqs. 3.28 and 3.29, this approach results in a progressive decrease in the radial pressure with an increasing number of layers.

$$p_D = \frac{\left[T_1 + G\left(T_2 + ... + \frac{T_n}{((n-1)-(n-2)G)}\right)\right]}{r_m d} \tag{3.30}$$

$$G = \frac{1}{\left(1 + \left(\frac{E_L d}{t E_D}\right)\right)} \tag{3.31}$$

Further, Torrance corrected errors in Hendry's equations regarding the deflection of the drum, maximum tangential stress and shear force at drum ends. Equations 3.32 and 3.33 give drum deflection w along length x of an unstiffened drum, while Eq. 3.34 gives the maximum deflection w_{max} at the distance x_{w_max} from the flange calcualted by Eq. 3.35. The shear force at drum ends, V_{max}, and maximum tangential stress, $\sigma_{\theta max}$, are given by Eqs. 3.36 and 3.37, respectively. (ν is the Poisson's ratio of the drum material).

$$w(x) = \frac{p_D r_m^2 (1-\nu^2)\left[1 - e^{-bx}(cosbx + sinbx)\right]}{E_D t} \tag{3.32}$$

$$b = \frac{1.32}{\sqrt{r_m t}} \tag{3.33}$$

$$w_{max} = \frac{p_D r_m^2 (1-\nu^2)}{E_D t} \tag{3.34}$$

$$x_{w\_max} = 2.39\sqrt{r_m t} \tag{3.35}$$

$$V_{max} = 0.76 p_D \sqrt{r_m t} \tag{3.36}$$

$$\sigma_{\theta max} = \frac{p_D r_m}{t}(1 + 0.075\nu) \tag{3.37}$$

Figure 3.10 shows the values given in Torrance's publication [21]. The coefficients of rope layers from Torrance's and Hendry's (unpublished) equations are compared with results from Egawa and Taneda [6] and Waters [5].

3.1.5 Bellamy & Phillips (1968)

Bellamy and Phillips [22] carried out an experimental analysis of flange forces from four different steel wire ropes. With nominal sizes of about 9.5 mm, the ropes were spooled in up to 16 layers. Both smooth and grooved drums were used with load cells in one of the flanges and strain gauges inside the drum and at the transition between drum and flange.

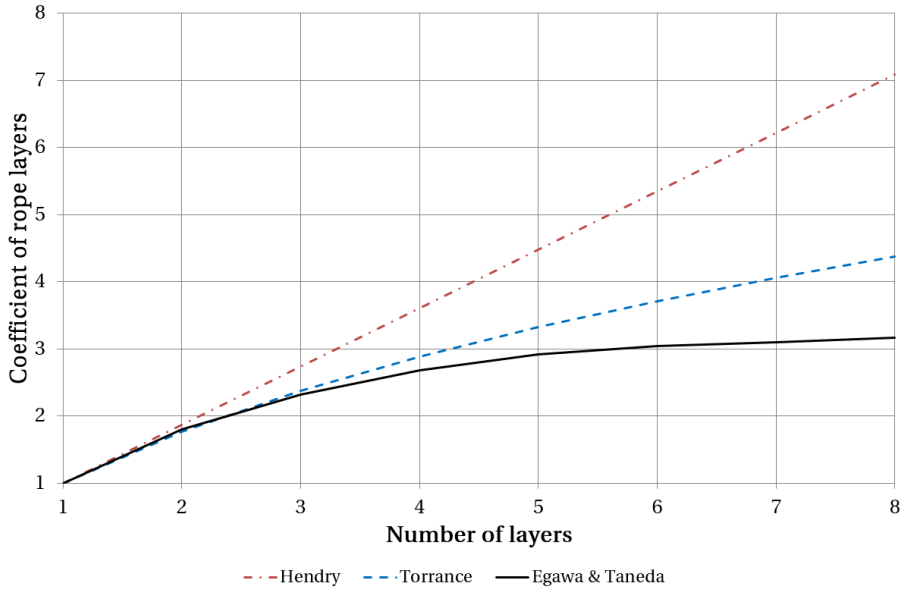

Figure 3.10: Comparison of calculations from Torrance [21]

The results indicated a general shape of flange force curves but with considerable deviations between different ropes. The tangential stress in the drum was also found to be dependent on the type of rope. One of the ropes was more distorted and induced noticeably larger tangential stress in the drum than the others. The authors assumed that the high flexibility of this rope resulted in a more compact shape during winding. Consequently, the tension reduction effect with this rope was mitigated.

In general, regular spooling was challenging to achieve on the smooth drum. On the other hand, the grooved drum resulted in higher tangential stresses. The authors related this to the grooves causing limited rope deformation and less tension reduction in the first layer.

After a few layers, the average pressure on the flange was constant with a reasonably uniform distribution. This observation was important. Consequently, the stresses could be calculated by considering the flange as a flat circular plate supported at the centre and exposed to uniform pressure. Further, the flange pressure was not directly proportional to the rope tension. This was assumed related to a more compact rope at high tension resulting in increased flange pressure.

3.1.6 Dietz (1972)

Based on the work by Ernst [19], Dietz [7] carried out experiments and developed calculations for the pressure on both single layer and multilayer winch drums. In addition, he developed an experimental method to determine the rope's transverse and longitudinal modulus of elasticity as well as theories for flange forces.

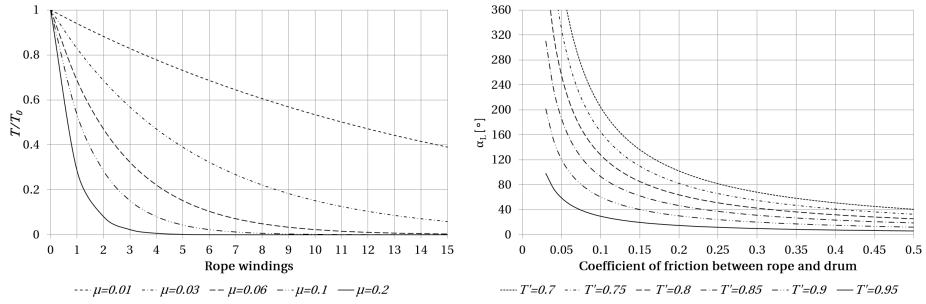

(a) Ratios of rope tension due to friction **(b)** Limit angle for various tension reductions

Figure 3.11: Effects of friction between rope and drum

Dietz found the assumptions and calculation method for tension reduction in the first layer proposed by Ernst reasonable.

Figure 3.11(a) shows ratios between rope tensions T and T_0 calculated by Eq. 3.38 for different coefficients of friction. With friction coefficients between wire ropes and drums in the range of 0.1-0.2, full torsion from the rope tension is transmitted to the drum by friction within the first few windings.

Dietz found that drum deformation will not induce rope slippage and cause influence between windings when the friction force between rope and drum is larger than the tension reduction. Figure 3.11(b) shows limiting angles, α_L for rope slippage, calculated by Eq. 3.39, plotted relative to coefficients of friction for tension reductions, T', between 70-95%. A friction coefficient between rope and drum as low as 0.03 can transmit a tension reduction of 80% nearly within one winding (about 310° wrap angle).

$$T = T_0 e^{\mu\alpha} \qquad (3.38) \qquad\qquad \alpha_L = \frac{1}{\mu} ln\left(\frac{1}{T}\right) \qquad (3.39)$$

The basis for Dietz's stress calculations is the differential equation for the elastic radial deformation of a rotational symmetric cylindrical shell with no axial force ($N_x = 0$), Eq. 2.19.

The drum was split longitudinally into elements for which deformations, rotations, forces and moments were calculated at the boundaries and added by the principle of super-positioning, Fig. 3.12. By this method, Dietz could allow for different geometric properties as internal stiffeners, change in diameter, and separate calculation of each rope winding in the first layer.

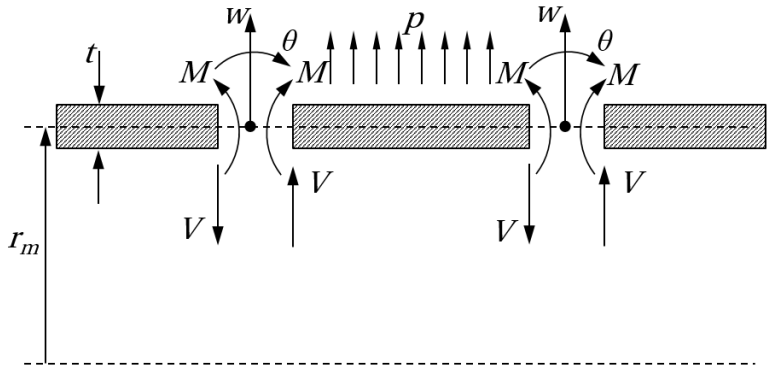

Figure 3.12: Forces on element of drum as defined by Dietz

Radial pressure on drum from a single layer of rope

Dietz replaced the rope windings with concentric closed rings with square cross-sections equivalent to the metallic cross-section, A_r, of the rope, Fig. 3.13 and Eq. 3.40. This results in a longitudinal (tangential) stress in the rope σ_θ, Eq. 3.41, and a constant pressure p on the drum along a length s from each rope winding, Eq. 3.42. (a is the center distance between rope windings, r_m is the middle drum radius, d is nominal rope diameter and f is the rope's fill factor.)

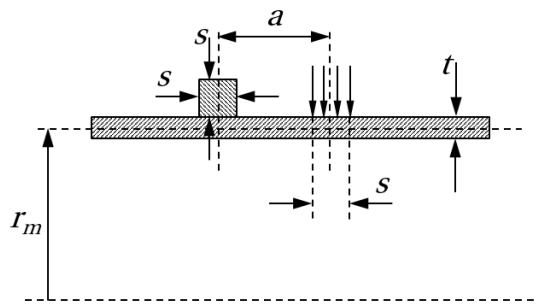

Figure 3.13: Rope winding with idealized square cross-section on drum

$$s = \sqrt{A_r} = \sqrt{f\frac{\pi d^2}{4}} = \frac{d}{2}\sqrt{f\pi} \qquad (3.40) \qquad \sigma_\theta = \frac{T}{s^2} \qquad (3.41)$$

$$p = \sigma_\theta \frac{s}{r_m + \frac{t}{2} + \frac{s}{2}} = \frac{T}{s\left(r_m + \frac{t}{2} + \frac{s}{2}\right)} \qquad (3.42)$$

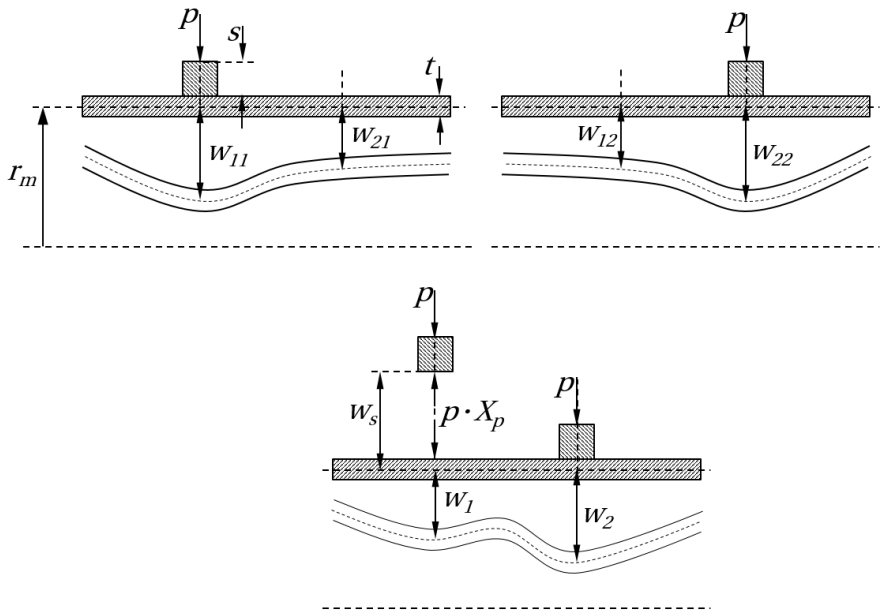

Figure 3.14: Drum deformation due to pressure from rope

With reference to Fig. 3.14, the tension reduction effect related to drum deformation is described as follows using two windings in the first layer:

The pressure p from the first winding causes radial deformations to the drum. The deformation directly underneath the first winding is w_{11}, and the deformation at the location of the next is w_{21}. The pressure from the second winding causes additional deformations at the same locations (w_{12} and w_{22}). Thus, as the circumference of the drum decreases, the first winding is relieved. Consequently, the radial pressure on the drum at this location is reduced. This process continues along the drum length until all windings in the first layer are completed.

The radial deformation and pressure are calculated by introducing the partial pressure X_p. Equation 3.43 calculates the total deformation of the drum at the location of the first winding. Based on the equation for tangential stress in a thin-walled

cylinder and Hooke's law, the resulting extension of the rope is calculated by Eq. 3.44. Assuming no gap and continuous contact between the winding and the drum gives Eq. 3.45.

$$w_1 = (1 + X_p)w_{1,1} + w_{1,2} \tag{3.43}$$

$$\begin{aligned} \sigma_\theta &= \frac{r_m}{s} X_p p \\ \Rightarrow E_L \frac{\Delta r}{r_1} &= \frac{r_m}{s} X_p p \\ \Rightarrow w_s &= \frac{\left(r_m + \frac{t+s}{2}\right)\left(r_m + \frac{t}{2}\right)}{E_L s} X_p p \end{aligned} \tag{3.44}$$

$$w_{12} + X_p w_{1,1} + w_s = 0 \tag{3.45}$$

Further calculations are carried out by applying the unit load method. This gives Eqs. 3.46, 3.47 and 3.48.

$$\delta_1 = (1 + X_p)\delta_{1,1} + \delta_{1,2} \tag{3.46}$$

$$\delta_\theta = \frac{\left(r_m + \frac{t+s}{2}\right)\left(r_m + \frac{t}{2}\right)}{s E_L} \tag{3.47}$$

$$X_p = -\frac{\delta_{1,2}}{\delta_{1,1} + \delta_s} \tag{3.48}$$

The reduced radial pressure and deformation acting at the location of the first winding can now be determined by Eqs. 3.49 and 3.50.

$$p_1 = p(1 + X_p) \tag{3.49}$$

$$w_1 = p\left[(1 + X_p)\delta_{1,1} + \delta_{1,2}\right] \tag{3.50}$$

Equation 3.51 shows the calculation in matrix format. The partial pressures are calculated when the radial deformations due to a unit pressure load are known.

$$\begin{bmatrix} (\delta_{1,1}+\delta_s) & \delta_{1,2} & \delta_{1,3} & . & \delta_{1,n-1} \\ \delta_{2,1} & (\delta_{2,2}+\delta_s) & \delta_{2,3} & . & \delta_{2,n-1} \\ \delta_{3,1} & \delta_{3,2} & (\delta_{3,3}+\delta_s) & . & \delta_{3_n-1} \\ . & . & . & . & . \\ \delta_{n-1,1} & \delta_{n-1,2} & \delta_{n-1,3} & . & (\delta_{n-1,n-1}+\delta_s) \end{bmatrix} \begin{bmatrix} X_{p_{1,i}} \\ X_{p_{2,i}} \\ X_{p_{3,i}} \\ . \\ X_{p_{n-1,i}} \end{bmatrix} = \begin{bmatrix} -\delta_{1,i} \\ -\delta_{2,i} \\ -\delta_{3,i} \\ . \\ -\delta_{n-1,i} \end{bmatrix} \tag{3.51}$$

The total deformation of the drum is calculated by super-positioning the calculation results for each winding in the first layer. As no further deformation is caused after the last winding, the pressure from the last winding is not reduced.

Radial pressure on drum from multiple layers of rope

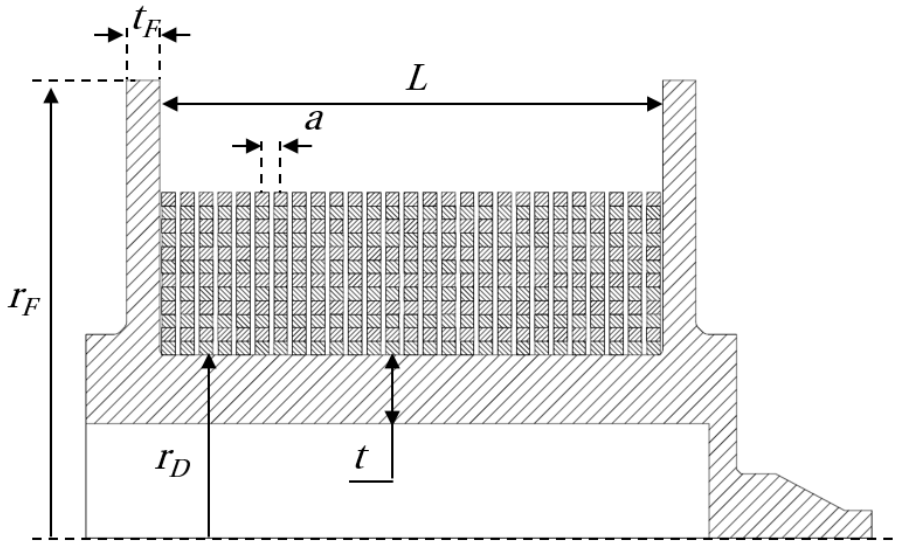

Figure 3.15: Multilayer drum with rope in stacks

With more than one rope layer on the drum, the radial deformations of ropes in each layer are considered. Due to pressure from subsequent layers, the radii of the drum and each rope layer are reduced. These deformations cause reduced rope tensions in all layers except for the outer. Consequently, the resulting radial pressure on the drum is also reduced.

Dietz modelled multiple rope layers as stacked concentric closed rings with square cross-sections and orthotropic material properties, Fig. 3.15. As illustrated in Fig. 3.16, linear elastic radial deformation of the rope cross-section, $u(y)$, is assumed and calculated by Eq. 3.52.

The radial compression causes a change in rope length, l_θ, at middle cross-section height $\left(y = \frac{s}{2}\right)$ given by Eq. 3.53. By applying Hooke's law, the resulting change in longitudinal (tangential) rope stress, $\Delta\sigma_\theta$, is calculated by Eq. 3.54. Further, Eq. 3.55 gives the change in pressure, Δp, due to rope compression. (E_L and E_T are the rope's longitudinal and transverse moduli of elasticity, r_i and r_m are the inner and middle radii of the rope cross-section.)

$$u(y) = \frac{p}{E_T} y \tag{3.52}$$

$$l_\theta - \Delta l_\theta = 2\pi \left(r_m - \frac{ps}{2E_T} \right) \Rightarrow \Delta l_\theta = \frac{\pi ps}{E_T} \tag{3.53}$$

$$\Delta\sigma_\theta = \frac{E_L \Delta l_\theta}{l_\theta} = \frac{\pi E_L ps}{2\pi r_m E_T} = p \frac{s}{2r_m} \frac{E_L}{E_T} \tag{3.54}$$

$$p \frac{s}{2r_m} \frac{E_L}{E_T} = \Delta\sigma_\theta = \frac{\Delta T}{s^2} = \frac{\Delta p r_i s}{s^2} \Rightarrow \Delta p = p \frac{s^2}{2r_m r_i} \frac{E_L}{E_T} \tag{3.55}$$

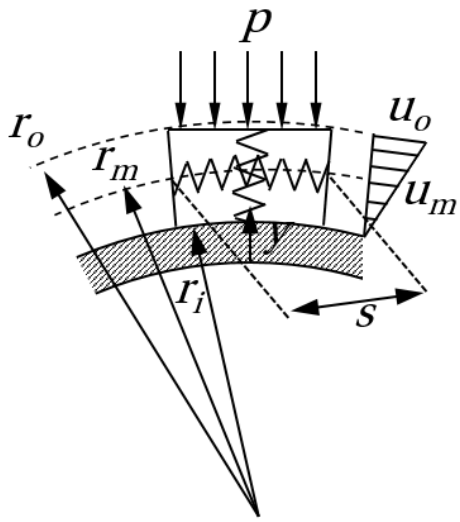

Figure 3.16: Compressed rope segment on drum

Further calculations are based on a unit pressure load and the following equations:

$$\delta_i = -\frac{r_i^2}{E_L s} \quad (3.56) \qquad \delta_{iT} = \frac{s}{E_T} \quad (3.57) \qquad f_i = \frac{s^2}{2r_i^2} \left(\frac{E_L}{E_T} \right)_i \quad (3.58)$$

Equation 3.56 calculates the reduction of the middle layer radius r_i of winding i, Eq. 3.57 the compression of the rope cross-section and Eq. 3.58 the resulting reduction of the radial pressure from winding i.

Partial and resulting pressures are calculated for one stack at a time. The different stacks are assumed to be connected through the elastic deformation of the drum

only, and the influence between rope stacks is ignored. As the drum is considered much stiffer than the rope, this is considered a valid simplification.

Considering a single stack with two layers of rope, Fig. 3.17 (left), the drum deformation, $\delta_{D,2}$, due to the partial pressure from layer two on layer one, X_{12}, is calculated by Eq. 3.59. Correspondingly, Eq. 3.60 gives the deformation of layer one from the partial pressure $X_{1,2}$ and the pressure from the outer layer $X_{2,2}$ which always equals the full pressure p. As contact between the drum and rope is required, w_{D2}=$w_{1,2}$, the partial pressure $X_{1,2}$ can be determined by Eq. 3.61. Further, the change in longitudinal rope stress in the first layer due to the second is given by Eq. 3.62. Equations 3.63 and 3.64 calculate the resulting stress in the second and first layers, respectively. Equation 3.65 determines the resulting pressure on the drum from two layers of rope.

The process is identical for each rope layer added to the drum. With an increasing number of equations, the equations are most efficiently solved in matrix form, Eqs. 3.66 through 3.70. Finally, Eq. 3.71 gives the resulting pressure from all layers in each stack.

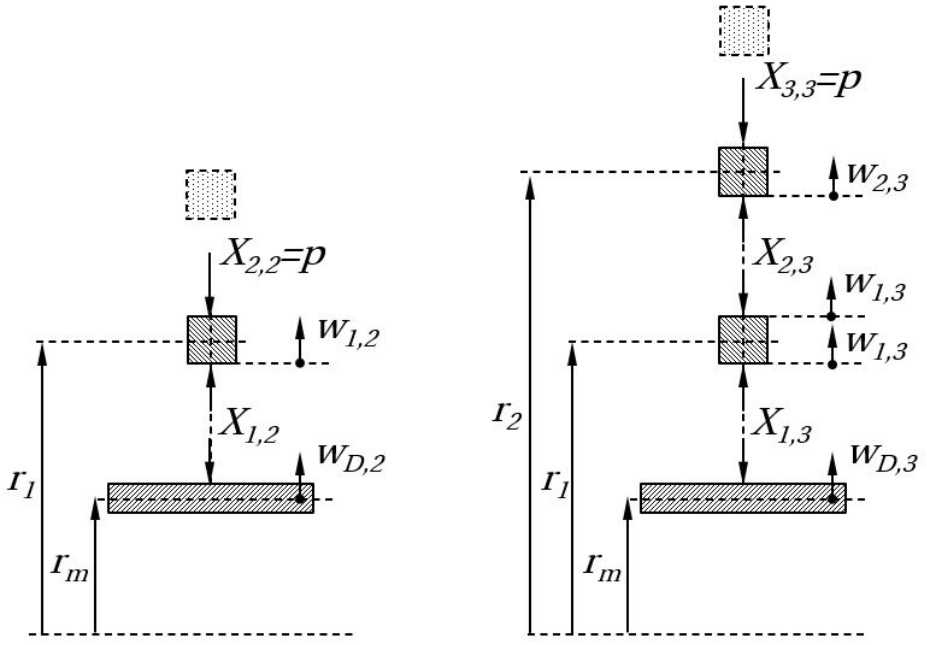

Figure 3.17: Radial pressure - two layers (left) and three layers (right)

$$\delta_{D,2} = X_{1,2}\delta_D \tag{3.59}$$

$$\delta_{1,2} = X_{1,2}\delta_1 - X_{2,2}\delta_1 + X_{1,2}\frac{\delta_{1T}}{2} \tag{3.60}$$

$$X_{1,2} = -X_{2,2}\frac{\delta_1}{\delta_D - \frac{\delta_{1T}}{2} - \delta_1} = -p\frac{\delta_1}{\delta_D - (1+f_1)\delta_1} \tag{3.61}$$

$$\Delta\sigma_{\theta_{1,2}} = (X_{1,2} - X_{2,2})\frac{r_1}{s} \tag{3.62}$$

$$\sigma_{\theta_{2,2}} = \frac{T}{s^2} \tag{3.63}$$

$$\sigma_{\theta_{1,2}} = \frac{T}{s^2} + (X_{1,2} - X_{2,2})\frac{r_1}{s} \tag{3.64}$$

$$p_{T2} = X_{1,1} + X_{1,2} = p - p\frac{\delta_1}{\delta_D - (1+f_1)\delta_1} \tag{3.65}$$

$$\alpha_1 = \delta_D - (1+f_1)\delta_1 \tag{3.66}$$

$$\alpha_i = -[(1+f_{i-1})\delta_{i-1} + (1+f_i)\delta i] \tag{3.67}$$

$$r_i = r_D + \left(i - \frac{1}{2}\right)s \tag{3.68}$$

$$X_{n,n} = \frac{T_n}{r_n s} \tag{3.69}$$

$$\begin{bmatrix} \alpha_1 & \delta_1 & 0 & 0 & 0 & 0 & 0 \\ \delta_1 & \alpha_2 & \delta_2 & 0 & 0 & 0 & 0 \\ 0 & \delta_2 & \alpha_3 & \delta_3 & 0 & 0 & 0 \\ \dot{0} & \dot{0} & \dot{0} & \dot{\delta_k} & \dot{\alpha_{k+1}} & \dot{\delta_{k+1}} & \dot{0} \\ \dot{0} & \dot{0} & \dot{0} & \dot{0} & \dot{0} & \dot{\delta_{n-2}} & \dot{\alpha_{n-1}} \end{bmatrix} \begin{bmatrix} X_{1,n} \\ X_{2,n} \\ X_{3,n} \\ \dot{X_{k,n}} \\ \dot{X_{n-1,n}} \end{bmatrix} = \begin{bmatrix} 0 \\ 0 \\ 0 \\ \dot{0} \\ \dot{-\delta_{n-1}X_{n,n}} \end{bmatrix} \tag{3.70}$$

$$p_D = \sum_{i=1}^{n} X_{1,i} \tag{3.71}$$

Rope elasticity

The ratio between the rope's longitudinal and transverse moduli of elasticity is essential for calculating the radial pressure on multilayer winch drums.

The transverse modulus is determined from the principle shown in Figs. 3.18 and 3.19. With the rope under longitudinal tension T, a piston of length l compresses the rope with a force F_T and the transverse travel of the piston (d-d_1) is measured.

Analogously, the longitudinal rope modulus is determined by measuring longitudinal tension and elongation.

According to Dietz, the transverse and longitudinal modulus are calculated by Eqs. 3.72 and 3.73 (n is the number of compressed ropes).

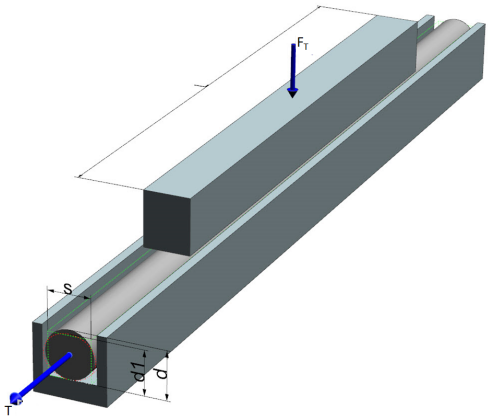

$$E_T = \frac{\sigma_T}{\varepsilon_T} = \frac{\frac{F_T}{sl}}{\frac{(d-d_1)}{sn}} \tag{3.72}$$

$$E_L = \frac{\sigma_L}{\varepsilon_L} = \frac{\frac{T}{s^2}}{\frac{\Delta l}{l}} \tag{3.73}$$

Figure 3.18: Testing of transverse modulus

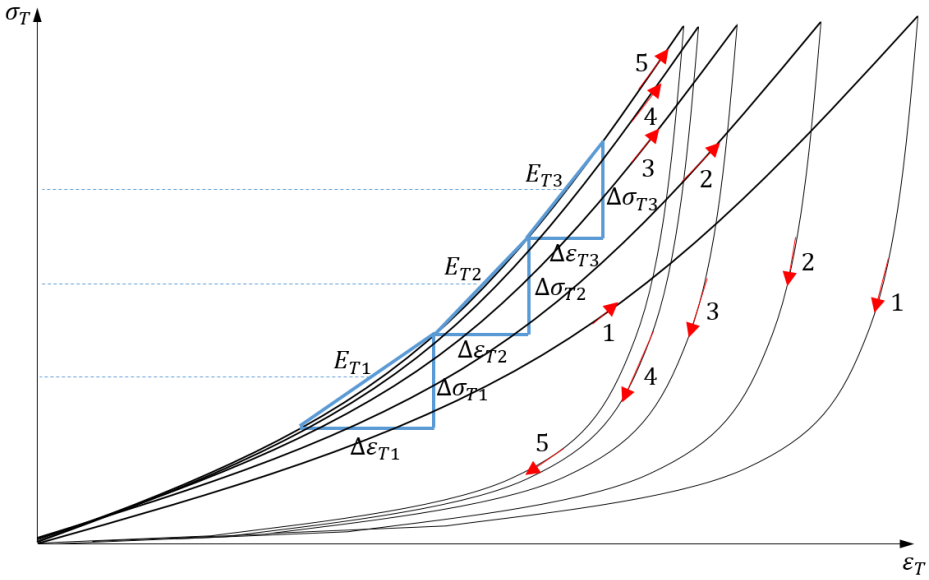

Figure 3.19: Example of stress-strain curves with hysteresis and transverse moduli

From his experiments with steel wire ropes, Dietz identified the following:

- The transverse modulus is nonlinear and dependent on rope tension force.
- The internal friction and plastic deformation result in considerable hysteresis effects, Fig. 3.19.
- Depending on rope type, between five to eight load repetitions are required to stabilize the load-deflection curve and determine the transverse modulus.
- The transverse modulus is dependent on the number of layers and decreases asymptotically with an increasing number of layers.
- Drum grooves constrain the rope and increase the transverse modulus.
- The transverse modulus increase with usage and age of the rope.

Dietz also modified the flange force theories proposed by Waters [5], described in section 3.1.1.

Flange forces - stacked cylinders

Equation 3.74 includes the tension reduction effect and gives the axial force N_k from each layer in contact with the flange. The angle α_0 between the centre of ropes in different layers and the drum axis is given by Eq. 3.75 while the layer radii r_k are estimated by Eq. 3.76. (μ_r is the coefficient of friction between ropes, t is drum thickness, d is nominal rope diameter, and s is the side length of the simplified square rope cross-section.)

$$N_i = s(cot\alpha_0 - \mu_r) \sum_{m=1}^{n} (X_{i,m} + X_{i-1,m}) \tag{3.74}$$
$$i = 1, 3, 5, ...n - 1 \text{ or } n$$

$$cos\alpha_0 = \frac{a}{2d} \tag{3.75}$$

$$r_i = r_m + \frac{t}{2} + \sum_{m=1}^{i-1} \left[\frac{1}{2}(d_m + s_m)\right] + \frac{1}{4}(d_i + s_i) \tag{3.76}$$

Flange forces - rope wedge

The wedge-theory was modified to differentiate friction coefficients between rope-rope, μ_r, and rope-drum, μ, Eqs. 3.77 and 3.78.

$$N_T = \frac{\mu + \left(\frac{n+1}{2} - 1\right)\phi}{1 - \mu^2 + \left(\frac{n+1}{2} - 1\right)} \left[\sum_{m=1}^{n} \left(\sum_{k=1}^{\leq m} X_{k,m} + \sum_{i=2}^{\leq m} \frac{m}{2} X_{m,m}\right) s\right] \tag{3.77}$$

$$k = 1, 3, 5, ...m - 1 \text{ or } m$$
$$i = 2, 4, 6, ...m - 1 \text{ or } m$$
$$m = 1, 2, 3, ...n$$

$$\phi = \frac{(\mu_r - \mu)cos\alpha_0 - (\mu_r\mu - 1)sin\alpha_0}{\mu_r sin\alpha_0 + cos\alpha_0} \tag{3.78}$$

Flange forces - climbing of "the last" winding

In addition to the above modifications, Dietz also introduced a new theory for flange forces. This model is related to the forces induced by the last winding in a layer. During spooling, this winding is squeezed into the gap between the flange and the second last winding and forced to climb to the next layer, Fig. 3.20.

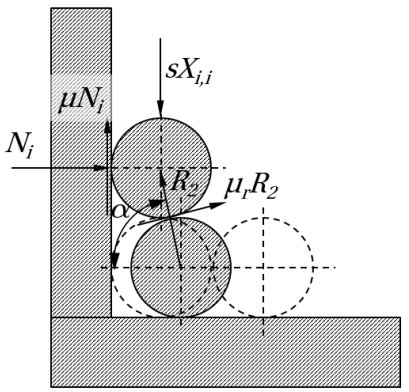

Figure 3.20: Forces during rope climbing

Equation 3.79 gives the ratio between axial and radial load, while Eq. 3.80 is an equivalent averaged rotational symmetric load, based on the average integral with a climbing angle of 360°, μ=0.18 and μ_r=0.2. This value is considered valid for helical spooling and many layers of rope on the drum. Corresponding values for 60° and 120° climbing angles are 0.15 and 0.3.

Dietz calculated the resulting moments, shear forces and stresses in the flange applying a “Kirchoff-plate” fixed at the inner side with the flange forces as line loads.

$$\frac{N_i}{sX_{i,i}} = \frac{cos\alpha - \mu_r sin\alpha}{(1 - \mu\mu_r)sin\alpha(\mu + \mu_r)cos\alpha} \tag{3.79}$$

$$\frac{N_i}{sX_{i,i}} = 0.6 \tag{3.80}$$

3.1.7 Kraitschy (1974)

Like Bellamy and Phillips [22], Kraitschy [23] also carried out experiments and investigated flange force calculations.

Kraitschy defined the axial loads from the rope layers and the loads from the forces at the boundary between flange and drum as decisive for designing and calculating multilayer drum flanges. He stated that the flange load is dependent on rope tension, the number of layers and the type of rope. Further, assuming small deformations, the flange stresses could be calculated by Kirchoff's plate theory. However, defining realistic boundary conditions for the transition between flange and drum was challenging. Calculations were improved by correcting the bending moment at the boundary between drum and flange. The influence on this boundary increases with flange thickness, and the flanges should preferably not be thicker than required to handle the loads.

3.1.8 Neugebauer (1980)

Neugebauer [24, 25] investigated the influence of drum grooves and flange stiffness on multilayer winch drums.

He modelled the rope as thin-walled hollow rings with cross-sections equal to the effective metallic area of the wire rope. The maximum von Mises stress in the drum was calculated by eight factors taking different properties of drum grooving and rope into account, Eq. 3.81.

The flange forces were calculated using the radial force in each rope layer, $W[n, z]$, Eq. 3.82. $W'[n, z]$ is a load factor dependent on D/d-ratio and the number of layers.

$$\sigma_{VM} = \sqrt{\sigma_x^2 + \sigma_\theta^2 - \sigma_x\sigma_\theta} = \frac{T}{td}\prod_{j=1}^{8} k(j) \tag{3.81}$$

$$W[n, z] = W'[n, z]\frac{T[z]}{d}10^{-2}\prod_{j=1}^{8} k(j) \tag{3.82}$$

Neugebauer's factors k_j are as follows:

- k_1 - the effect of drum and rope dimensions.
- k_2 - the effect of rope fill factor.
- k_3 - the effect of transverse rope stiffness.
- k_4 - the effect of longitudinal modulus of rope.
- k_5 - the effect of the rope crossing-sector.
- k_6 - the effect of ratio between groove pitch and rope diameter.
- k_7 - the effect of groove opening angle.
- k_8 - the effect of ratio between groove height and drum thickness.

With grooved drums, all eight factors apply, while smooth drums only require the first six.

Based on drums with helical grooving and symmetrical loading Neugebauer's investigations gave the following conclusions regarding stresses due to multilayer spooling:

- Drum stress increases with the use of wire ropes with a high fill factor.
- The influence of the rope's longitudinal modulus of elasticity is essential.
- The influence from the rope crossing is small.
- Drum grooves restrict the deformation of ropes in the first layer. This influences the overall deformation of the rope package and limits the tension reduction effect. The increased thickness of the drum partly compensates for the effect on stresses. Hence, considering multilayer loads, the overall difference between grooved and smooth drums is limited.
- With identical drum dimensions and rope tension, a rope with a smaller diameter induce higher stresses in the drum than a larger rope.

Neugebauer's calculations were in relatively good correspondence with the experimental results from both Kraitschy [23] and Dietz [7].

3.1.9 Song et al. (1980)

Song et al. [26] related failures of mooring winches with large wire ropes (Ø76-89 mm), where the flanges had been separated from the drum to deficiencies in the existing calculation methods. Empirical modifications and extrapolation from

experiments with small wire rope sizes and few layers were blamed. Dietz's two-point measurement method for transverse elasticity of ropes was criticised and assumed to give too low transverse stiffness in relation to the actual conditions between ropes on the drum.

As an attempt to improve calculations for large wire ropes, a modification of Dietz's original theory [7] was proposed. This method applies transverse rope modulus determined from 4-point testing and both inner (r_i) and outer radii (r_e) of the rope's cross-section in each layer, Fig. 3.21.

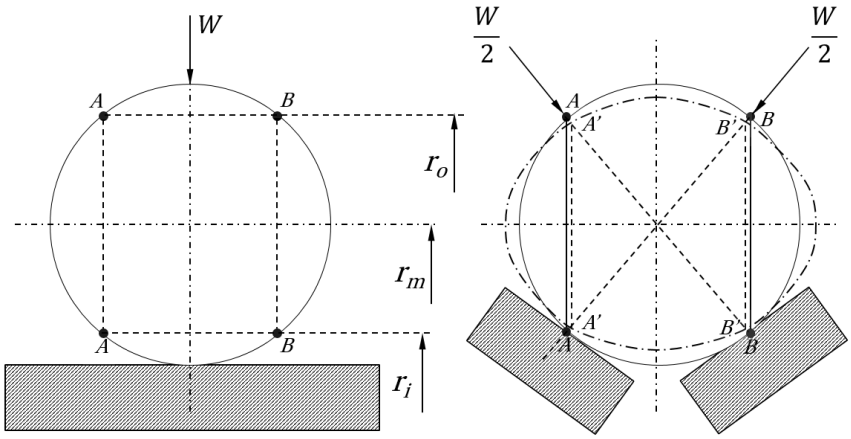

Figure 3.21: 2-point vs. 4-point compression of rope

3.1.10 Karbalai (1988)

Karbalai [27] picked up on the work by Egawa & Taneda [6] and modified the equations to handle thick-walled drums. Further, Karbalai carried out experiments and measured transverse rope stiffness and lateral expansion of a few steel wire ropes of different sizes.

With low transverse force, measurements of transverse expansion ratios ("Poisson ratio's") of steel wire ropes resulted in values of about 0.25. With increasing transverse force, the values converged towards 0.4. However, the ropes were tested without axial tension force.

A novel finite element analysis for drum stress calculations was also presented and applied. This method included the radial pressure on the drum and the multilayer tension reduction effect. The rope was modelled as axisymmetric concentric rings with rectangular cross-sections and orthotropic material properties. Radial pressure was applied by an iterative procedure reducing the temperature of rope elements in the tangential direction until the tensile load in the rings were within

acceptable limits. Further, the second layer was modelled on top of the distorted shape of the first. This process continued until all layers were included. However, the calculations did not account for flange forces.

3.1.11 Henschel (1999)

Henschel [28] continued the work by Dietz [7] and designed a machine for testing transverse elasticity of ropes at the University of Clausthal in Germany.

Transverse moduli of several modern wire ropes were tested at different tension levels and in different configurations as illustrated in Fig. 3.22. Up to six layers of rope were tested in linearly stacked configurations as well as pyramidal configurations with five and six ropes (two and three layers).

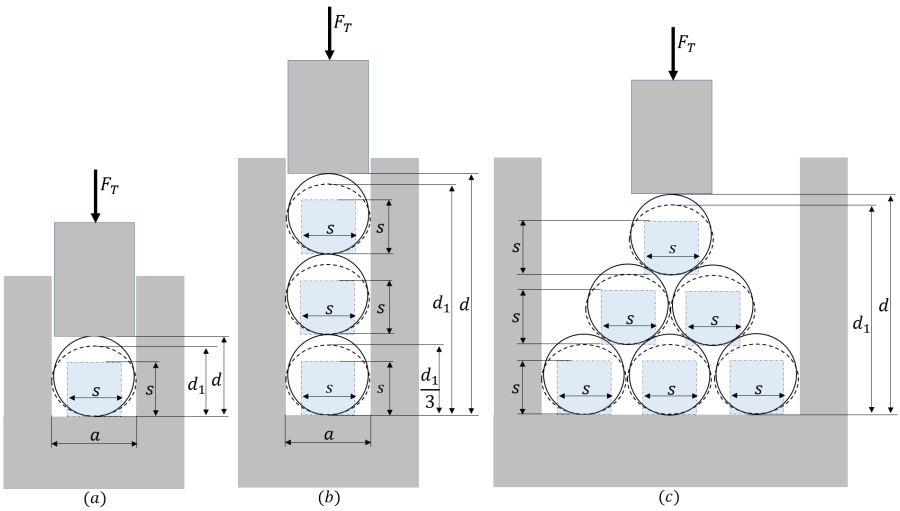

Figure 3.22: Single rope (a), linear configuration (b) and pyramidal configuration (c)

Compared to the steel wires tested by Dietz, modern and more compact steel wires were considerably stiffer, resulting in higher loads on multilayer winch drums. The tendency of asymptotic decrease of transverse rope modulus, as identified by Dietz, was confirmed for linearly stacked rope configurations. However, there was little change in moduli with more than four rope layers. With a corresponding number of layers, ropes in pyramid configurations resulted in lower transverse modulus than linearly stacked configurations. Based on the experiments, Henschel included transverse rope moduli varying with the number of layers in calculations. The moduli were modelled as either linear- or square functions.

Lateral expansions of transversely compressed steel wires and a fibre rope were also investigated. The measurements resulted in asymptotic tendencies for the steel

wire ropes with limits in the range of 0.2-0.5. The behaviour of the synthetic fibre rope was different. It did not give the same asymptotic growth but continued to expand with increased transverse pressure. Henschel assumed that the expansion could continue until the rope was damaged and thus result in considerably more significant transverse expansion than steel wire ropes. Consequently, higher flange forces could be expected with multilayer spooling of synthetic fibre ropes.

3.1.12 Mupende (2001)

Mupende [16] evaluated shell theories of both 1^{st} and 2^{nd} order and developed the "coupled method" for practical and efficient analytical parameter studies of winch drums. He also further developed Dietz's "climbing of the last winding" theory for flange forces and investigated differences between transverse rope stiffness in linear- and pyramidal rope configurations. In addition, he investigated possibilities for exploiting the elastic-plastic regime of the drum material to allow for increased utilization of multilayer winch drums.

Shell theories

The 1^{st} order theory is based on an undeformed shell (Eq. 2.19), while the 2^{nd} order theory, Eq. 3.83, takes shell deformation into account, Fig. 3.23.

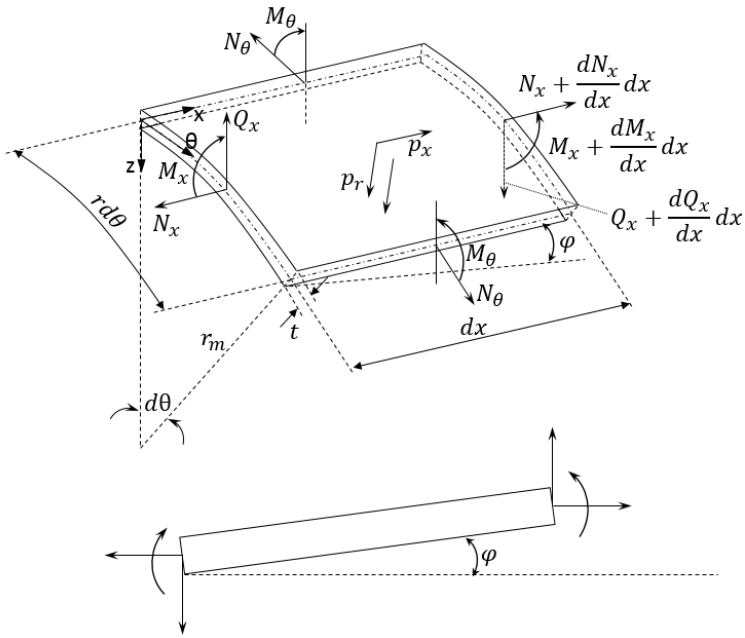

Figure 3.23: Principle of second order shell theory

$$\frac{d^4w}{dx^4} + \frac{N_x}{K}\frac{d^2w}{dx^2} + 4\chi^4 w = \frac{1}{K}\left(p + \frac{\nu}{r}N_x\right) \tag{3.83}$$

Mupende evaluated these theories using two winch drums with different lengths. The ratio between drum thickness and radius was 0.11 for both cases. When axial force was ignored, the two theories gave identical results and only minor differences (less than 1%) when axial force was considered. Therefore, Mupende recommended the 1^{st} order theory as generally applicable for winch drum calculations, except for drums with a small ratio between shell thickness and drum radius (very thin-walled drums).

The "coupled method"

Until the "coupled method" was developed, winch drums and flanges were typically treated separately as shell and plate structures with fixed boundary conditions.

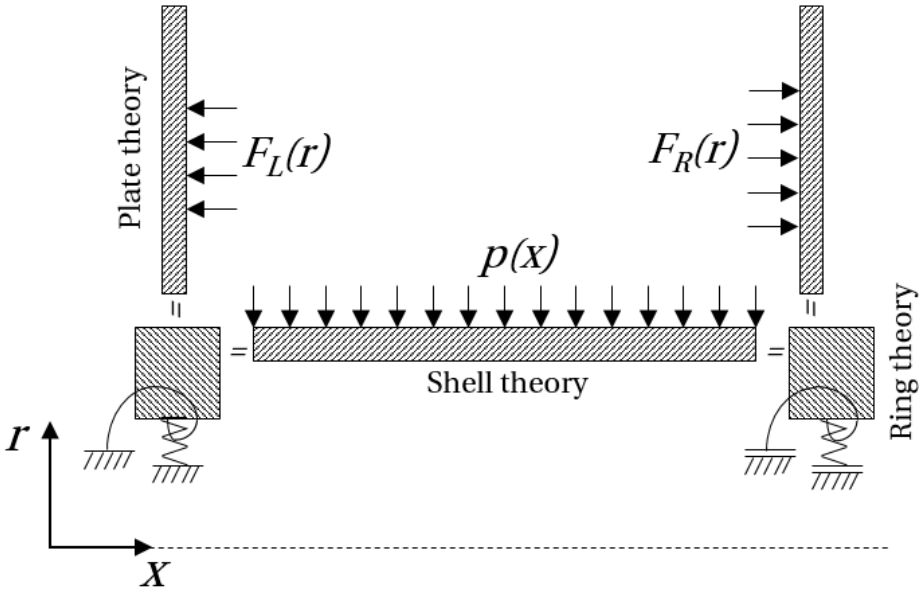

Figure 3.24: Principle of the "coupled method" by Mupende [16]

The "coupled method" is based on an analytical axisymmetric model with transition couplings transmitting forces and moments between drum and flanges. This results in an integrated analytical model which takes reciprocal effects between flanges and drums into account, Fig. 3.24.

The basic principles of the "coupled method" are:

- Drum modelled using shell theory with radial and axial forces.
- Flanges are modelled using the Kirchoff plate theory, including bending and radial forces.
- Transition coupling between drum and flanges modelled using ring theory.

The method allows for efficient analytical studies of drum parameters to minimize bending stresses in the transition between drum and flanges. As a result, Mupende proposed an optimal ratio between flange thickness and drum thickness in the range between 1 and 2.

Short or long drums

According to Mupende, the definition of a long drum is given by a "reduced length" larger than six, Eq. 3.84. (χ is the geometric parameter for a cylindrical shell, Eq. 2.20, and L the length of the drum).

$$\text{long drum: } \chi L > 6 \tag{3.84}$$

For short drums, stress disturbances from geometry as flanges and boundary conditions are not dampened out and affect stresses along the length of the drum. Long drums ensure sufficient distance from such disturbances. At distances greater than this, stress calculations are possible with reasonable accuracy without detailed boundary conditions.

Flange forces

Mupende further developed Dietz's theory of the "climbing of the last winding" and derived equations for the contact between rope and flange in both the rope's climbing- and parallel sectors.

The rope climbing is illustrated in Fig. 3.25. Equation 3.85 gives the flange force, while Eqs. 3.86 and 3.87 result in the radial force during climbing. The maximum flange force during the rope's climbing to the next layer is calculated by Eq. 3.88.

$$R_{ci} = \frac{(cot\alpha - \mu_r)}{(1 - \mu_r\mu + (\mu_r + \mu)cot\alpha)} P_{rc} \tag{3.85}$$

$$P_{rc} = \frac{dF_r}{ds_c} = \frac{T_k d\varphi}{ds_c} \tag{3.86}$$

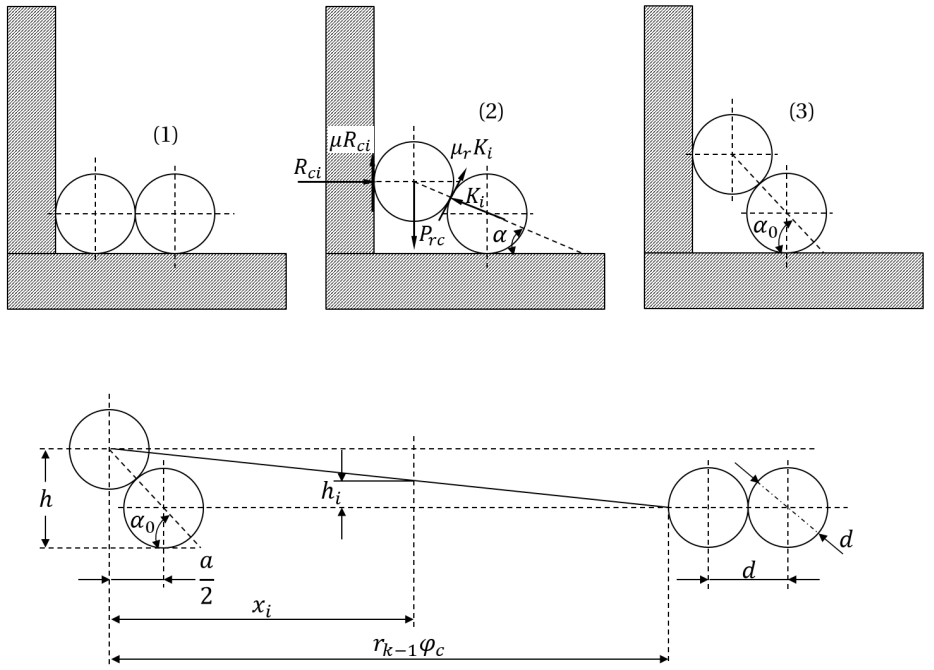

Figure 3.25: Forces during climbing of rope as derived by Mupende

$$ds_c = \sqrt{r_{k-1}\left(r_{k-1} + \frac{\varphi}{\varphi_c} tan\alpha_0 a\right) + (1+\varphi^2)\left(\frac{tan\alpha_0 a}{2\varphi_c}\right)^2} d\varphi \tag{3.87}$$

$$R_c = \frac{(cot\alpha - \mu_r)}{(1 - \mu_r\mu + (\mu_r + \mu)cot\alpha)} \frac{T_k d\varphi}{ds_c} \tag{3.88}$$

In the parallel sector, the radial force is given by Eq. 3.89 and the flange force by Eq. 3.90.

The total force on the flange in a layer is the sum of the axial forces integrated over the climbing- and parallel sectors, Eq. 3.91.

$$P_{rp} = \frac{T_k}{r_k} = \frac{T_k}{r_{k-1} + \frac{tan\alpha_0 a}{2}} \tag{3.89}$$

$$R_p = \frac{(cot\alpha_0 - \mu_r)}{(1 - \mu_r\mu + (\mu_r + \mu)cot\alpha_0)\left(r_{k-1} + \frac{tan\alpha_0 a}{2}\right)} T_k \tag{3.90}$$

$$R_k = \frac{1}{2\pi r_k}\left[\int_0^{s_c} R_c ds_c + \int_0^{s_p} R_p ds_p\right] \tag{3.91}$$

Equation 3.94 include additional forces from overlying rope layers in the parallel sector. The equation can be solved by applying Eqs. 3.92 and 3.93.

$$cot\alpha = \frac{2\varphi_c d - (2d-a)\varphi}{\varphi tan\alpha_0 a} \tag{3.92}$$

$$tan\alpha_0 = \sqrt{4\left(\frac{d}{a}\right)^2 - 1} \tag{3.93}$$

$$R_k = \frac{T_k}{2\pi r_k}\int_0^{\varphi_c} \frac{(cot\alpha - \mu_r)}{(1-\mu_r\mu + (\mu_r+\mu)cot\alpha)} d\varphi + \tag{3.94}$$
$$+\frac{\varphi_p}{2\pi}\frac{cot\alpha_0 - \mu_r}{(1-\mu_r\mu + (\mu_r+\mu)cot\alpha_0)}\sum_{i=k}^{n}\frac{T_i}{r_i}$$

Transverse rope elasticity

In calculations of multilayer radial pressure using Dietz's theory, a transverse modulus of elasticity relevant for the actual rope tension and drum geometry is required.

The ratio of transverse and longitudinal stress in the rope, Eq. 3.95, was presented by Henschel [28],

$$k_T = \frac{\sigma_T}{\sigma_L} = \frac{2\sqrt{A_r}}{D} \tag{3.95}$$

while Mupende introduced the stress ratio taking friction between rope and drum, μ, and wrap angle, α, into account, Eq. 3.96.

$$k_T = \frac{\sigma_T}{\sigma_L} = \frac{2\sqrt{A_r}}{\mu\alpha D}(e^{-\alpha\mu} - 1) \tag{3.96}$$

These equations calculate the limit stress ratios for the drum and rope under consideration. For calculations, a transverse modulus is defined from measurements with a stress ratio within these limits. Ignoring friction gives a higher modulus.

Mupende also compared measurements of transverse elasticity for steel wire ropes in linear- and pyramidal configurations. He also found that the transverse modulus

for pyramidal configurations resulted in lower values than linearly stacked configurations. Figure 3.26 shows average values from Mupende's measurements with nine different steel wire ropes.

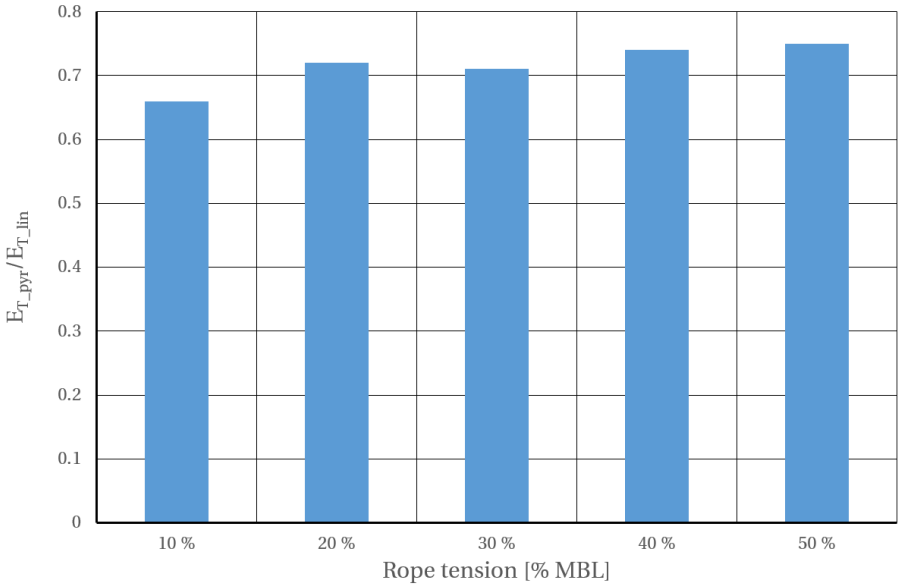

Figure 3.26: Ratios of transverse moduli in pyramidal- and linear configurations [16]

According to Mupende, Eq. 3.97 gives the ideal theoretical relationship between stresses from ropes in pyramidal- and linearly stacked configurations. For ropes in pyramidal configurations, the stress and transverse modulus increase with decreasing angle between the centre of ropes in different layers, α_0.

$$k_{PL} = \frac{\sigma_{T_{pyr}}}{\sigma_{T_{lin}}} = \frac{1}{2sin\alpha_0} \tag{3.97}$$

Mupende also measured the transverse expansion coefficients ("Poisson ratios") of nine steel wire ropes. He found that the values increased non-linearly with increasing transverse strain and significant variations between the different ropes. Figure 3.27 shows the average values for the nine ropes.

Based on his investigations, Mupende concluded that ropes with low transverse moduli would induce lower pressure on the drum and higher axial force on the flanges and vice versa.

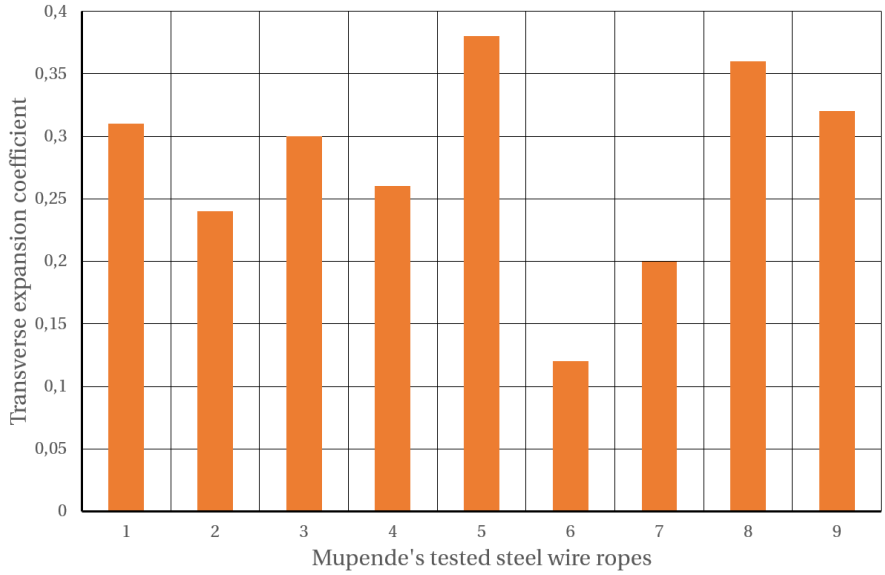

Figure 3.27: Average "Poisson's ratio" for nine steel wires exposed to compression [16]

3.1.13 Otto (2004)

Otto [29] related observed asymmetric pressure on Lebus-grooved winch drums to the change in radius when the rope is axially and radially displaced within each layer during winding, Fig. 3.28.

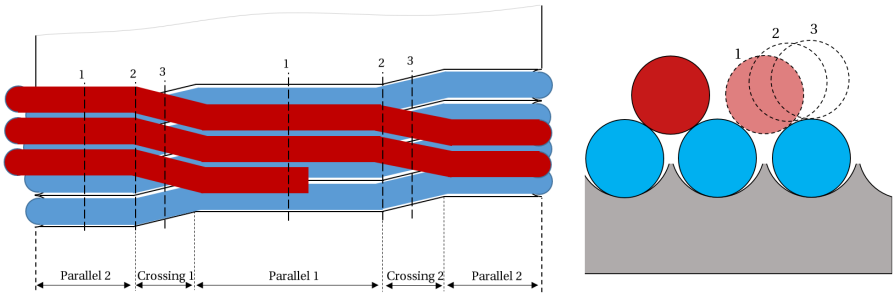

Figure 3.28: Principle of Lebus spooling pattern

As the radial pressure is inversely proportional to the layer radius, the pressure is lower in the crossing- than in the parallel sectors. On the other hand, transverse moduli were found lower in the parallel- than in the crossing sectors. Altogether, the controlled and regular spooling pattern on grooved drums causes an increase in stress due to additional bending stresses along the circumference of the drum.

3.1.14 Schwarzer (2012)

Schwarzer [30] carried out experimental measurements and calculations of multilayer winches with hybrid ropes, a combination of steel wire rope and fibre ropes. Two different hybrid ropes, one with "high modulus" and one with "standard modulus", and two steel wire ropes were used in the experiments.

The measured transverse moduli of the hybrid ropes were lower than the steel wire ropes. Further, the transverse modulus of the "high modulus" hybrid rope was slightly higher in pyramidal than in linear configuration. This finding is contrary to former measurements on steel wires by Henschel [28] and Mupende [16]. No data for the pyramidal configuration of the "standard modulus" rope was presented.

The Dietz/Mupende calculation methods were also compared with measurements for one of the steel wire ropes and the hybrid ropes. The calculations corresponded well with experiments for the steel wire and the "high modulus" hybrid rope. On the other hand, the stress calculations considerably underestimated the actual stresses (about 30%) for the "standard modulus" hybrid rope.

Compared to the steel wire rope, more uniform stress distribution around the circumference was also noticed for the hybrid ropes. However, no significant differences in the peak tangential stress were identified in measurements.

Schwarzer concluded that further research was required to update the present calculation methods and tools to incorporate the effects of hybrid and fibre ropes. Investigations of friction between fibre ropes and the drum and internal friction between fibres were particularly mentioned.

3.1.15 Lohrengel et al. (2009-2017)

Effects related to multilayer spooling with synthetic fibre ropes have been investigated by Lohrengel et al. and published through a series of papers on the topic at OIPEEC (the International Organisation for the Study of Ropes) conferences.

The work by Schwarzer [30] was mainly presented in [31] and [32] along with results from testing of transverse moduli of small-diameter fibre ropes (Ø6 and Ø12 mm) made of Dyneema, Vectran and Technora fibres. The experiments resulted in a slightly higher transverse modulus for the Dyneema rope than the other fibre ropes. Relative to values typical for steel wire ropes, all fibre ropes exhibited low transverse moduli. Further, experiments with multilayer spooling of ropes with low transverse stiffness caused problems as the rope forced itself down in between underlying windings (rope "knifing" or "diving"). A spooling tension giving sufficient transverse stiffness of at least 400 N/mm^2 was proposed as a rule of thumb to avoid this. Due to the low transverse moduli, theoretical calculations of the fibre

ropes resulted in considerably lower stresses in the winch drum compared to a steel wire rope.

Effects on calculations of multilayer winch drums from rope's deformation, transverse modulus of elasticity and friction were presented in [33]. Measurements of transverse moduli of different fibre ropes revealed that polyester ropes with parallel cores and non-load-bearing jackets gave the lowest moduli. Eight-strand plaited polyester ropes followed these. Ultra-high molecular weight polyethylene (UHMWPE) ropes exhibited higher transverse moduli.

A novel method using lasers to measure rope cross-sectional deformation and rope profiles on the drum was also presented. The rope deformation was expressed by the relative ovality, calculated by Eq. 3.98.

$$O_r = \frac{|d_x - d_y|}{max(d_x; d_y)} \tag{3.98}$$

Examples of measured ovalities for a steel wire rope and a fibre rope on a grooved drum were in the range of 0.004-0.011 and 0.22-0.27, respectively. With values in the range of 0.23-0.31, more significant deformations were measured for the fibre rope on a smooth drum. The experiments also indicated that a linear decrease in rope distortion could be expected with an increasing number of layers on a grooved drum. On the other hand, with fibre rope on a smooth drum, a non-linear decrease should be expected with more extensive deformation in lower layers.

Comparisons of stress measurements on a drum with five rope layers and finite element calculations, applying Dietz's theory for multilayer loads [7] were also carried out. The calculations for the steel wire rope corresponded well with experiments, while the fibre rope calculations underestimated the actual stresses. These results were explained by the more significant cross-sectional deformation of the fibre rope and reduced layer radii on the drum. An additional effect of smaller layer radii is reduced bending moment on the flanges. For the typically highly stressed transition between drum and flange, this is favourable. However, flange forces are strongly related to friction, and the expected lower friction of fibre ropes would counteract this effect.

To take the larger deformations related to fibre ropes into account, modifications of Dietz's calculation method by using elliptical rope shapes, Fig. 3.29, was proposed in [8]. Equation 3.99 gives the multilayer tension reduction in each layer considering the major and minor diameters of an ellipse d_x and d_y. Equations 3.100 and 3.101 give the layer radii related to the rope's parallel- and crossing sectors on the drum, respectively.

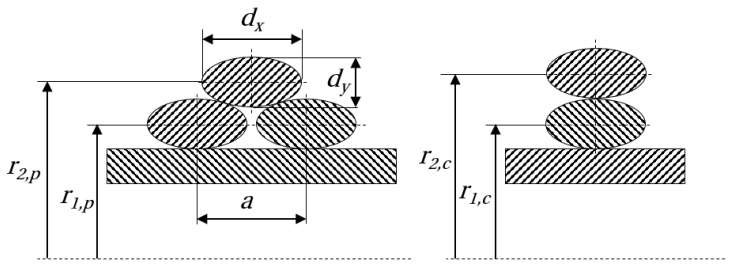

Figure 3.29: Elliptic rope cross-sections [8]

$$\Delta T_i = p_i \frac{\sqrt{f\frac{\pi}{4}d_x d_y}}{2r_i}\frac{E_L}{E_T}A_r \tag{3.99}$$

$$r_{i,p} = r_D + \frac{d_y}{2} + \frac{n-1}{2}\sqrt{d_y^2\left(4 - \frac{a^2}{d_x^2}\right)} \tag{3.100}$$

$$r_{i,c} = r_D + \frac{d_y}{2} + (n - \frac{1}{2})d_y \tag{3.101}$$

Examples of friction coefficients of a braided Dyneema SK75 rope in contact with itself and a steel wire rope were also presented. The results showed that the friction coefficient decreases with increasing rope tension and transverse force. The fibre rope against steel wire gave friction coefficients roughly between 0.053 and 0.115. For fibre rope against fibre rope, the values were lower and in the range of 0.042-0.097.

In [9] further measurements on rope deformation, transverse modulus of elasticity and multilayer stresses in a winch drum with different ropes were presented. The fibre ropes were of various designs from the Icelandic company Hampidjan and made of Dyneema fibres. The transverse moduli were tested in up to three layers in both linearly stacked- and pyramidal configurations. For the fibre ropes, all measurements resulted in higher transverse moduli in pyramidal configuration than in linear. Differences in contact conditions between the ropes and more significant deformations relative to steel wire ropes giving a more compact rope configuration on the drum were mentioned as possible causes for this.

Figure 3.30 shows both longitudinal and transverse moduli for the different ropes. The transverse moduli of the fibre ropes are in the range of 173-640 N/mm^2. A comparable steel wire rope (SWR) is considerably stiffer with 1577 N/mm^2. Fibre rope 1 (FR1) was dimensionally stable with relative ovality between 0.05-0.09.

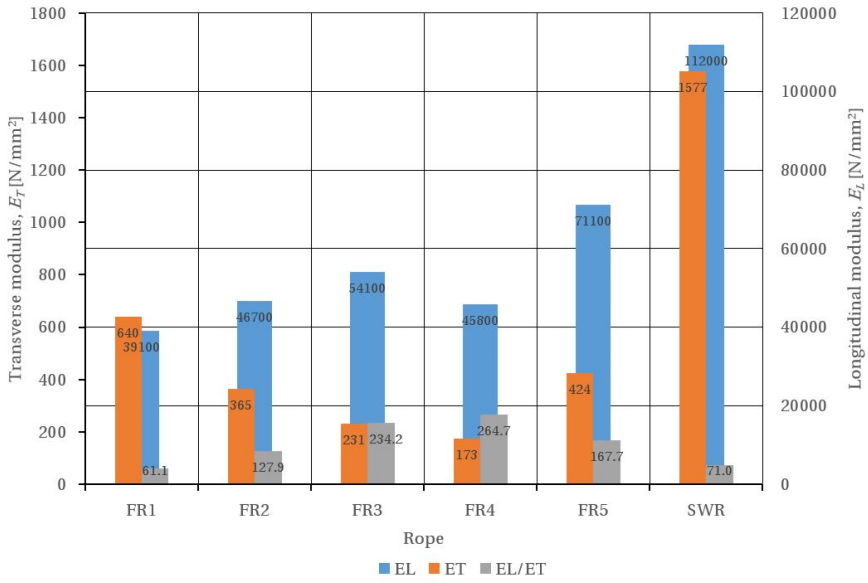

Figure 3.30: Longitudinal and transverse rope moduli from Lohrengel et al. [9]

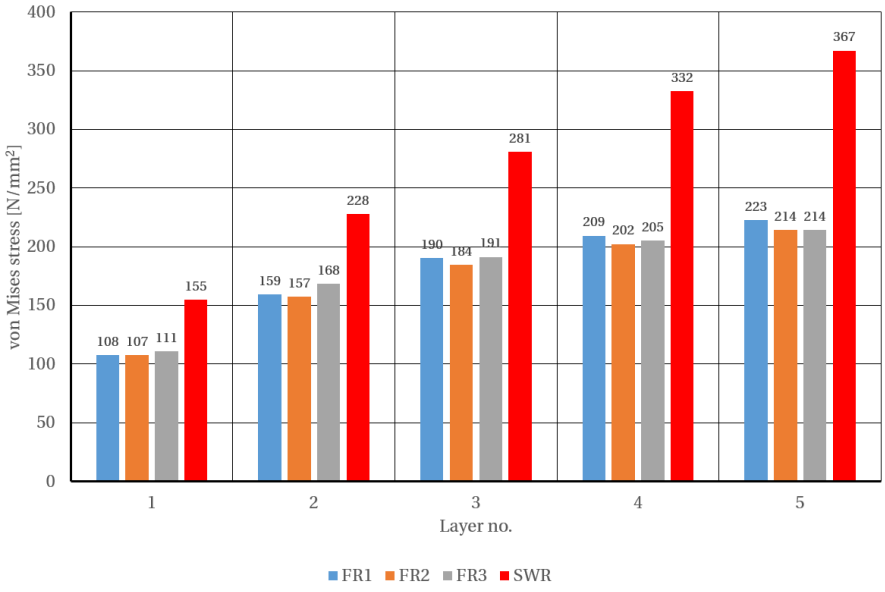

Figure 3.31: von Mises stress in drum from Lohrengel et al. [9]

The respective ranges for the more deformable fibre ropes 2 (FR2) and 3 (FR3) were 0.19-0.25 and 0.14-0.23.

Measured stresses in a winch drum subjected to multilayer spooling with three fibre ropes and the steel wire were also compared. The results are illustrated in Fig. 3.31. The steel wire rope induced the highest stress, while the fibre ropes induced approximately similar stresses for all layers. FR1 was expected to induce higher stresses due to the ratio between longitudinal and transverse modulus being similar to the wire rope. The authors mentioned varying transverse stiffness with an increasing number of layers and variable influence of friction effects as possible causes for this.

An essential detail with these experiments is the rope tension of 50 kN, which is approximately 10%, or less, of the rope's minimum breaking strength.

3.1.16 Class rules

Both DNV GL [3] and ABS [34] have design rules, or guides, for winch drums.

Former DNV released their first *"Rules for certification of lifting appliances"* in 1989. This version is no longer available, and it is therefore unknown if this version treated winch drums. However, winch drums were included in the 1994 release of the rules, which more or less are unchanged until today. The exception is the C-factor values which were increased in 2010.

ABS had no specific winch drum calculation requirement until the 2018 version of their *"Guide for certification of lifting appliances"*.

DNV GL

DNV GL assumes the flange pressure to be continuous and linearly decreasing from a maximum value $p_{f_{max}}$ at the drum surface to the outer layer. There is also a requirement for the distance between the outer edge of the flange to the outer layer on the winch, Fig. 3.32. The maximum flange pressure, maximum radial pressure p_d on the drum and the tangential stress (hoop stress) σ_θ in the drum are given by Eqs. 3.102 through 3.104. Values for the layer dependent C-factor are given in Table 3.1. The calculated tangential stress in the drum σ_h shall not exceed 85% of the material yield stress.

$$p_{f_{max}} = \frac{CT}{3r_D a} \quad (3.102) \qquad p_d = \frac{CT}{r_D a} \quad (3.103) \qquad \sigma_\theta = \frac{CT}{ta} \quad (3.104)$$

For drums with steel wire rope, the required minimum ratio between drum and rope diameters (D/d-ratio) is 18. For active heave compensated applications, the

minimum D/d ratio is 20. However, for drums with fibre ropes, special agreements considering rope and drum sizes are required.

A maximum number of three layers of steel wire rope are recommended. However, more layers can be accepted in the case of steel wire ropes with independent wire rope cores (IWRC) combined with one of the following conditions:

- A spooling device is provided.
- The drum is grooved.
- The fleet angle is restricted to 2°.
- A split drum is arranged.
- A separate traction drum is fitted.

Special considerations and approval are required in all cases if the number of rope layers is more than seven.

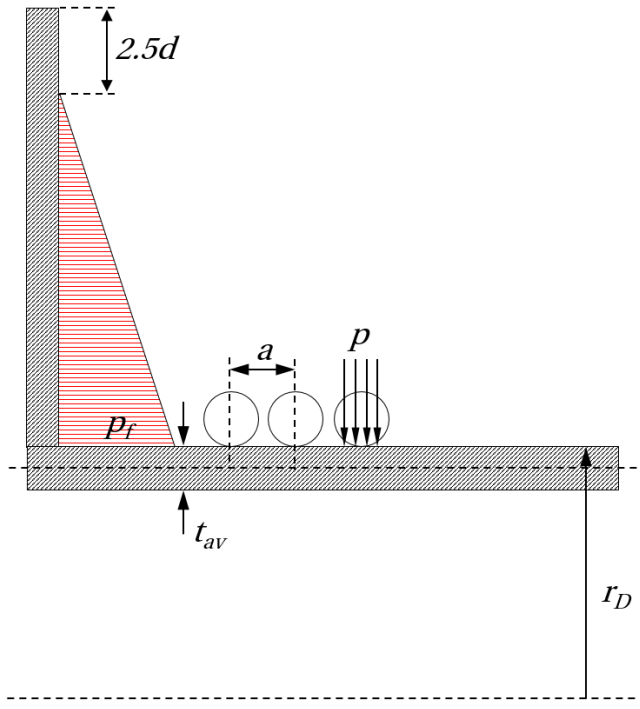

Figure 3.32: Pressure on drum and flange according to DNV GL [3]

DNV GL points out that the C-factors depend on several variables: drum design, rope stiffness and characteristics, operation, and spooling. However, a C-factor of three will usually be accepted for subsea retrieval operation with winch drums with five or more rope layers with "stiff" steel wire ropes. Further, in recommended practice N201 [4], DNV GL states that a C-factor of three is usually also considered acceptable for subsea handling with fibre ropes. As an alternative to the rules, calculation methods by Dietz [7] and Mupende [16] can be applied.

It is also mentioned that the drum can be protected, and the tangential stress in the drum reduced by a protective first rope layer spooled with a lower tension. This rope layer cannot be utilized to maintain protection. Consequently, the rope capacity of the winch becomes somewhat reduced.

Table 3.1: Layer dependent factors by class societies

Multilayer factors, C (DNV GL) or K_L (ABS)					
Layer no.	1	2	3	4	5
DNV GL	1	1.75	2.17	2.58	3
ABS	1	1.8	2.3	2.7	3

American Bureau of Shipping

ABS specifies a tangential stress calculation which in principle is equivalent to DNV GL, Eq. 3.104. However, ABS denote the layer dependent load factor K_L instead of C. The values are very similar and given in Table 3.1.

Unless special approval based on detailed stress analysis is given, ABS requires a minimum of five full rope windings to always remain on the drum. The requirement for D/d-ratio is equivalent to DNV GL.

With more than five layers of wire rope on the drum, ABS also requires special considerations and approval. However, lower K_L-factors can also be admitted when justified by detailed analysis and testing.

When it comes to flange forces, ABS requires the flanges and connections to the drum to withstand the horizontal components of the radial forces of the wire ropes calculated with the maximum number of layers. However, no equations for flange forces calculations are specified.

The allowable tangential stress in the winch drum is, as with DNV GL, limited to 85% of the material yield stress. In addition, fatigue is also to be considered if the expected number of hoisting cycles is above 10^5.

3.2 Summary of previous research

The review of existing literature shows that the main contributions regarding load assessment and stress calculation of multilayer winch drums are old. They also origin from land-based industries as mining and hoisting, while contributions from the marine industry are modest and limited to rules from classification societies. Figure 3.33 gives a brief overview of the different contributions and relations between them. Further, the primary type of approach, components, types of ropes and properties are mapped.

Authors	Relations	Approach		Structure		Rope type			Considered properties				
		Theoretical	Experimental	Drum	Flange	Steel	Hybrid	Fibre	E_D	E_L	E_T	d_x, d_y	μ
Waters (1920)	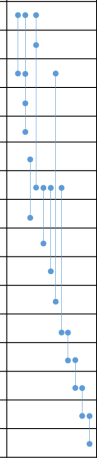	✓	✓	✓	✓	✓			✓	✓	✓		✓
Ernst (1938)		✓	✓	✓		✓			✓	✓			
Egawa & Taneda (1958)		✓	✓	✓		✓			✓	✓	✓		✓
Dolan (1963)				✓		✓							
Torrance (1965)		✓				✓			✓	✓			
Bellamy & Phillips (1968)			✓		✓	✓							
Dietz (1972)		✓	✓	✓	✓	✓			✓	✓	✓		✓
Kraitschy (1974)		✓	✓		✓	✓							
Neugebauer (1980)		✓	✓	✓	✓	✓			✓	✓	✓		
Song et al. (1980)		✓		✓	✓	✓			✓	✓	✓		✓
Karbalai (1988)		✓	✓	✓		✓			✓	✓	✓		✓
Henschel (1999)		✓	✓	✓	✓	✓			✓	✓	✓		✓
Mupende (2001)		✓	✓	✓	✓	✓			✓	✓	✓		✓
Otto (2004)		✓	✓	✓		✓			✓	✓	✓		
Schwarzer (2012)		✓	✓	✓	✓	✓	✓		✓	✓	✓		✓
Lohrengel et al. (2009-2017)		✓	✓	✓	✓	✓		✓	✓	✓	✓	✓	✓

Figure 3.33: Properties of and couplings between historical contributions

With his theories for flange forces, the introduction of the transverse rope modulus and the multilayer tension reduction effect, Waters [5] can be considered as the pioneer in load assessment of multilayer winch drums. Detailed information about Waters' calculations for radial pressure on drums will probably be an eternal mystery. However, the stress ratios are also considered too low and obsolete concerning modern steel wire ropes and HPSFRs. His theories for flange forces are also considered too conservative, and further developments by other actors are considered more relevant.

Ernst's [19] work is only relevant for winches with single layers, and the further developed methods by Dietz [7] are far more interesting. An example of the challenges related to the age of much of the research on multilayer winch drums is Ernst's warning against radial stiffeners causing bending stresses inside drums. This was probably a valid concern for its time, with extensive use of brittle cast iron but less relevant for modern ductile materials and manufacturing methods.

The work by Dolan and Torrance [20] did not take the rope's anisotropic properties into account. Their contributions are also considered too conservative, even for rough estimates of radial pressure on multilayer winch drums. Egawa & Taneda's [6] theory for radial pressure is more attractive as it takes rope stiffness, transverse expansion and the climbing angle between rope layers into account.

The observations by Bellamy & Phillips [22] regarding increased tangential stress with increasing rope distortion are interesting. At the same time, Kraitschy's [23] and Neugebauer's [24, 25] contributions are considered as reference information only.

Possibly, one might claim that the work by Dietz [7] formed the basis for modern load assessment for multilayer winch drums. His theories seem to be the only further developed in recent times, by Henschel [28], Otto [29] and Mupende [16].

Motivated by reported damages on winches, Song et al. [26] modified Dietz's method to better deal with larger rope sizes. The 2-point method for testing transverse elasticity and the use of data extrapolated from smaller ropes were criticised. The justification of their claims does not seem to be supported by experiments. Developments in steel wire rope technology with increased radial stiffness should possibly have been taken into account as potential causes of the damages.

Figure 3.34 shows ratios of radial pressure on the drum for multiple layers relative to a single layer of rope. The values are calculated by the methods by Dietz [7], Eqawa & Taneda [6] and Song et al. [26]. For direct comparisons, drum deformations, rope deformation and friction are ignored. This shows that there are only minor differences between the equations by Song et al. and Dietz. The results based on Egawa & Taneda's method give a very similar curve as the two other methods but with somewhat higher values.

When it comes to flange forces, the most promising theory is Dietz's "climbing of the last winding" [7] with further developments by Mupende [16]. With the latter method, the challenges are to define proper coefficients of friction and accurate sizes of sectors with contact between rope and flange.

Most of the previous contributions are limited to five or six layers of rope. This is also the case for the work related to multilayer load assessment of fibre ropes by Schwarzer [30], Dietz et al. [31] and Lohrengel et al. [32, 33, 8, 9]. Winches applied in marine applications often utilize many more rope layers, and the validity of the theories need to be confirmed for such winches. The latest developments in calculation theories for multilayer spooling of fibre ropes are related to incorporating such ropes' more significant cross-sectional deformations. However, the effect of the modified calculations needs to be proved by experiments.

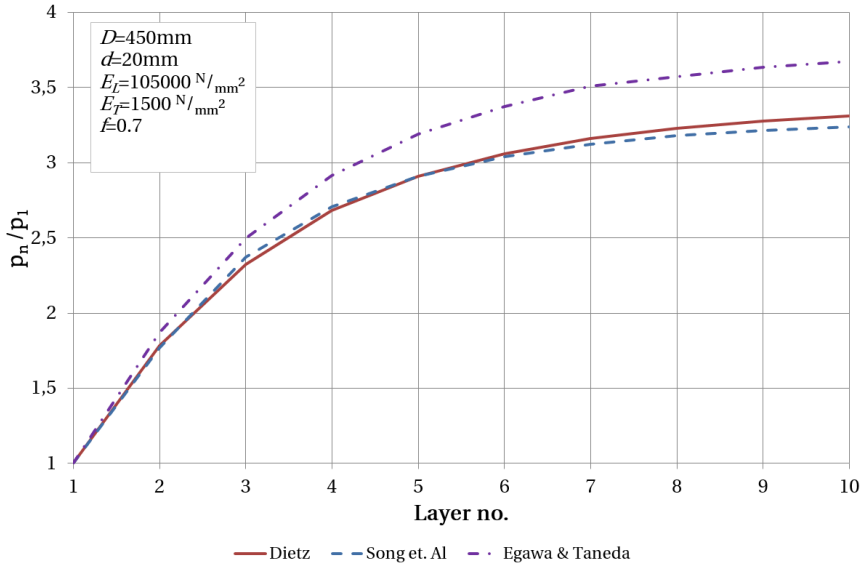

Figure 3.34: Comparison of calculated multilayer pressure

The transverse modulus of single fibre ropes is proven to be much lower than single steel wire ropes. Thus, lower pressure on the drum and higher stresses in the flanges were first expected with multilayer spooling of fibre ropes compared to steel wire ropes. Further investigations and developments now indicate that the radial pressure on the drum can be higher with multilayer spooling of fibre ropes than with steel wires. However, existing experimental results are not unambiguous. The number of experiments is limited considering scope, number of layers and rope tension level.

There is consensus regarding the reasons behind multilayer tension reduction effects and the importance of the anisotropic elasticity of rope cross-sections in the literature. However, the challenge is to determine relevant moduli for calculations.

There are indications that fibre ropes can cause more considerable stiffness in pyramidal configuration than steel wires. It is feasible that this is related to the more extensive deformation and different contact conditions between the ropes. There are apparent differences between testing of transverse stiffness on straight ropes and ropes wound around a winch drum. Consequently, it can be questioned if a linearly stacked and even a pyramidal configuration of ropes reflects the actual conditions of rope on a drum sufficiently. However, some compromises are inevitable and arranging a more relevant and practical test system for transverse rope stiffness is considered very complicated.

The applicability of rules and recommendations from DNV GL [3, 4] and ABS [34] for multilayer winches are easy to use. However, they are also questionable and too general as they ignore both drum and rope stiffness. The applicability of these rules for winches with HPSFRs are unknown, and verification against measurements are required.

When it comes to stress calculations, 3D FEM is preferred due to possibilities for detailed geometry, loads and boundary conditions. Simplified analysis using axisymmetric elements, Mupende's analytic "coupled method", or even the simple equations for tangential stress in drums, are also helpful for parameter studies and iterations in early design phases. The accuracy of these simplifications needs to be evaluated, particularly for thicker winch drums.

The application of FEM for direct stress calculations, e.g. like Karbalai's method [27], is fascinating. Such methods might be applicable for steel wire ropes with relatively stable cross-sections. However, for fibre ropes with more significant and unknown deformations, this is considered very challenging. Regardless of rope type, one should be careful by modelling a rope cross-section or similar structures as a continuum. With the vast number of fibres and contacts in a fibre rope, uniquely designed and very efficient simulations techniques are required.

3.3 State-of-the-art and important rope properties

Based on this review, Dietz's method for calculation of radial pressure on drum [7], modified for fibre rope deformations by Lohrengel et al. [8] is considered as the state-of-the-art calculation method for radial pressure on multilayer winch drums. For simplicity, this is denoted as the "modified Dietz" method in the following.

Further, Mupende's equations [16] are considered the best method for determining forces acting on winch drum flanges. Regarding class rules, ABS [34] and DNV GL [3] requirements are practically considered as equivalent.

Rope properties as transverse and longitudinal moduli, friction, deformation and layer radius are identified as necessary for proper load assessment of multilayer winches with HPSFR.

This review partially fulfils research objective RO2 and answers the first part of research question RQ2. It also partly fulfils research objective RO1.

Part II

Methodology, methods and experimental test results

Chapter 4

Methodology and methods

This chapter describes details of and rationale for the research methodology and methods applied to answer the research questions (RQ1-RQ4) and research objectives (RO1-RO4) defined in Sections 1.3 and 1.4. Figure 4.1 gives a general overview of the research.

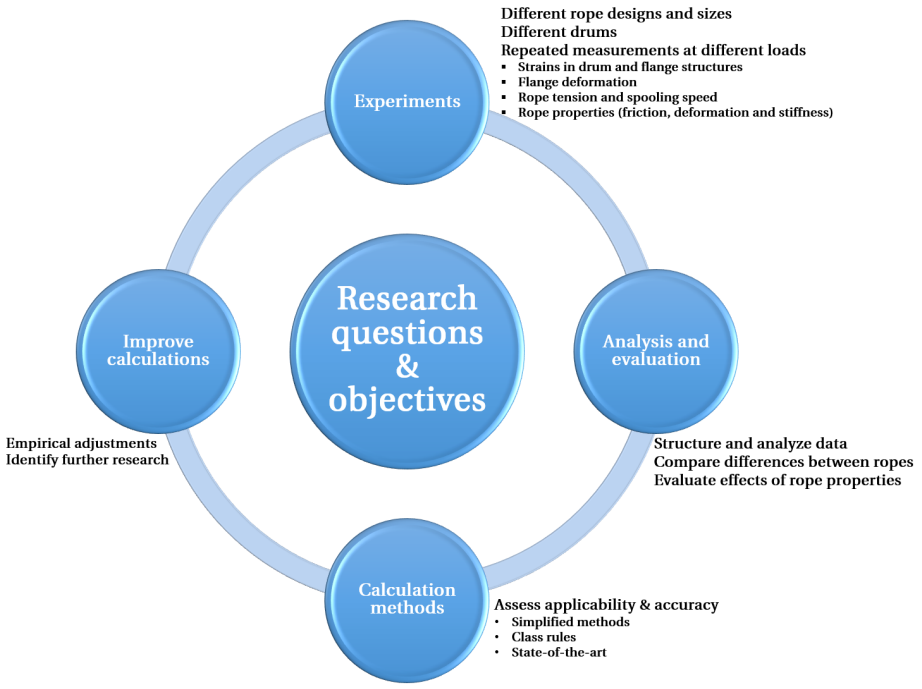

Figure 4.1: Research approach

4.1 Research approach

The research was based on quantitative methodology using different measurement methods. Data from experiments were analyzed to compare and assess the relative effects on multilayer spooling from different ropes and their characteristic properties. Accuracy of both simplified and more complex load and stress calculations were assessed against measurements through analytical and numerical methods (FEM). Further, an empirical methodology was applied to improve calculations. Figure 4.2 gives an overview of the research process and relations to the specific research objectives and research questions.

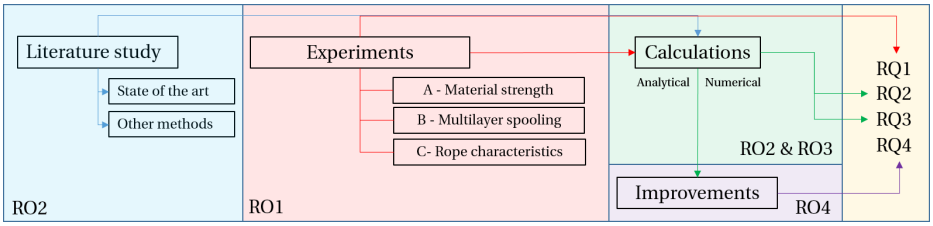

Figure 4.2: Process overview

The main experimental work was carried out from May 2018 to December 2019 in Kongsberg Maritime's workshop in Hjørungavåg, Norway. The majority of the experiments were carried out in a multilayer spooling test rig. In addition, some measurements were also carried out using a cylinder arrangement in Kongsberg's Maritime's large CBOS (Cyclic Bending Over Sheaves) test rig. Rope strength tests were carried out with assistance from Offshore, Trawl & Supply (OTS) at their facilities on Valderøy, Norway.

4.1.1 Choice of measurements and methods

The choice of measurements and methods was based on a thorough literature review of previous work combined with engineering knowledge and experience. Specific expertise was consulted about measurement details and equipment.

The experiments were adapted to existing measurement equipment and the multilayer spooling test rig. This introduced some limitations related to drum and rope sizes as well as maximum spooling tension. However, it was considered suitable for the research questions and very efficient considering both time and cost.

Measurements of the following rope properties were required in order to evaluate state-of-the-art calculation methods:

- Transverse stiffness
- Rope deformation
- Layer radius
- Friction

Measurement methods described in the literature were applied. A specially designed compression device was used to measure transverse rope stiffness, while laser technology was applied to measure rope dimensions, deformation and layer radii.

The multilayer spooling test rig had a measurement of rope tension and spooling speed in place. Rope friction measurements were also possible in the test rig using a vertical capstan winch.

As proven technology and the most common way to measure mechanical loads in structures, conventional electrical resistance strain gauge measurements were chosen to measure strains in the winch drum and flange structures. Other methods, e.g. optical strain measurements, were not considered as better or more applicable methods.

Displacement transducers measured the axial deformations of the flanges. These deformations were considered as additional helpful information for the evaluation of calculations (FEM) against measurements.

The applied measurements and methods are summarized below, and further details are given in the following sections.

- Rope tension measurements using load cells (available in test rig).
- Rope spooling speed using rotary encoders (available in test rig).
- Strains in drum structures using electrical resistance strain gauges.
- Deflection of flanges using displacement transducers.
- Rope cross-sectional dimensions and deformation using lasers.
- Rope radii on the drum using laser.
- Transverse rope stiffness using specially designed compression device.
- Rope friction using a capstan winch and special drum (available in test rig).

Figure 4.3 gives details of the experiments, equipment, tools and technologies.

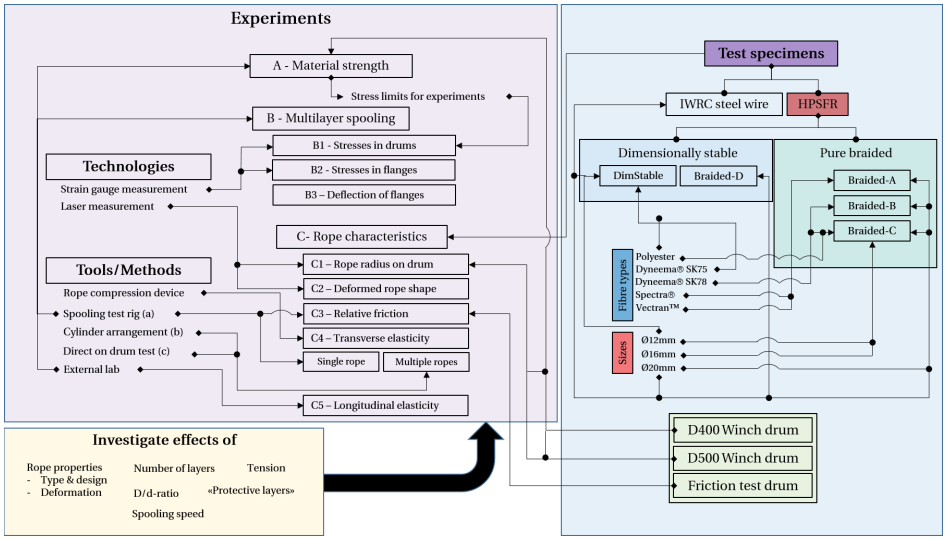

Figure 4.3: Details of the experiments

4.2 Test program

The test program was divided into three main phases, as illustrated in Fig. 4.4.

In the first phase, multilayer spooling experiments were conducted on the D400 drum. In addition, initial testing of transverse stiffness (single ropes) was carried out in the spooling test rig.

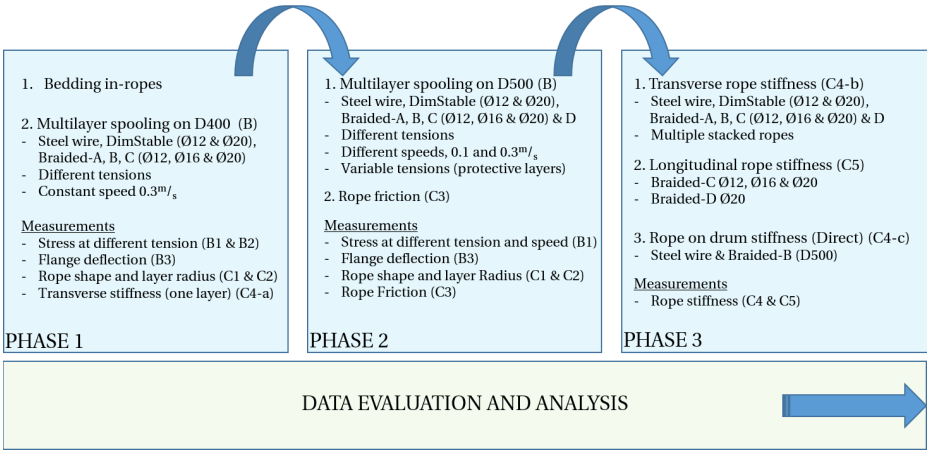

Figure 4.4: Overview of experimental test program

The ropes were bedded in by several test runs. Rope tension was increased in steps until approximately 50% of the MBL or the maximum capacity of the spooling test rig. The ropes were considered bedded-in when the differences between peak tangential stresses in the drum of two equivalent trailing test runs were within 5-10%.

The rope tension during spooling was targeted at 10%, 15%, 20% and 25% of MBL. For some ropes, the maximum capacity of the spooling test rig prevented 25% of MBL. On the other hand, the smaller rope sizes allowed experiments with higher utilization of rope strength.

Experiments were repeated to capture statistical variations, but the number of repetitions was limited. The experiments on D400 were conducted with 0.3 m/s spooling speed. They were in general repeated three ($n = 3$), or in a few cases four ($n = 4$) times. Experiments carried out in phase 2 on D500 were generally conducted at 0.3 m/s spooling speed but with additional experiments at two different tension levels with 0.1 m/s spooling speed. The number of repeated experiments on D500 was in general limited to two ($n = 2$).

The experimental test program was planned in detail, with some adjustments and improvisations along the way. One rope was identified and acquired during phase 2 of the program. The possibilities for transverse testing of multiple ropes and the direct on drum experiment evolved during phase 3.

The experimental work was carried out by a Lab-engineer experienced in rope testing together with the PhD candidate.

4.3 Calculations

Theory and methods for stress assessment of multilayer winch drums were compared with experimental results using analytical calculations and finite element analysis results.

Both 2D axisymmetric and 3D linear elastic FEA applying NX Nastran SOL101 solver was applied.

Fixed constraints were applied at the drive interface of the drum. The axle on the opposite side was only constrained radially. The pressure on the drum was applied as an evenly distributed radial pressure along the length of the drum. Flange forces were applied according to the different methods. Either as line-loads distributed over the middle radius of each rope layer or as distributed pressure decreasing from a maximum at the drum surface to zero at the outer layer.

Structured meshes were used for both axisymmetric and 3D-solid analysis. An elastic modulus of 200 GPa and a Poisson's ratio of 0.3 was applied for the steel materials for analytical and numerical simulations and stress calculations from experimental strain measurements. The element sizes were verified to give converged stresses in the areas of interest.

Figure 4.5 shows an overview of locations for measured strains and derived stresses that are compared with calculations.

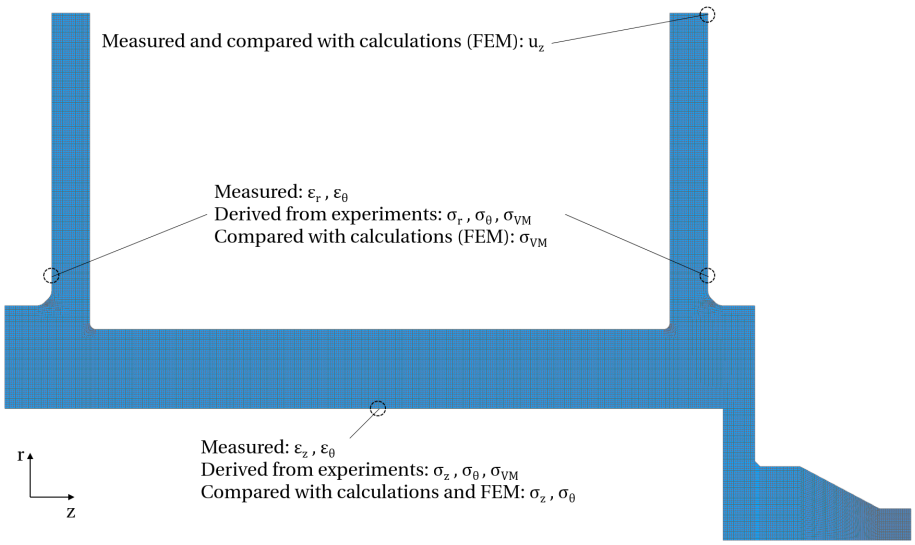

Figure 4.5: Axisymmetric FEM with loads according to DNV GL

4.4 Test ropes

The selection of ropes was based on ropes most common for marine applications and relevant to Kongsberg Maritime's products and experience. Due to torque-free design, high strength and splice-ability, different 12-strand braided ropes (hollow single-braid) were chosen. Nine ropes were subjected to testing, eight fibre ropes and one steel wire. The primary nominal diameter was Ø20 mm, while two of the ropes were Ø12 mm and one was Ø16 mm. Examples of the test specimens with representative cross-sections are shown in Fig. 4.6.

The DimStable ropes (Ø12 and Ø20 mm) have 12-strand Dyneema fibres braided around a stiff plastic core with metal in the centre. The ropes are heat set, stretched and enclosed by tight braided Dyneema SK62 jackets. The design gives high cross-sectional stability and steel wire-like behaviour.

Figure 4.6: Test ropes

Braided-A, B and C are pure 12-strand braided ropes. Braided-A (∼20 mm) consists of a blend of Spectra and Vectran fibres optimised for bending and with good creep resistance. Braided-B (Ø20 mm) is a pure Dyneema rope, and Braided-C (Ø12, Ø16 and Ø20 mm) are very similar to Braided-B with a blend of Dyneema and polyester fibres.

Braided-D (∼Ø20 mm) is also a mixed blend 12-strand braided design with a polyester core in the centre. Details of the fibre blend are subjected to manufacturers intellectual properties and therefore unknown. This rope was identified and incorporated in the test program during testing, but after testing on D400 in phase 1 (Ref. Fig. 4.4) was completed. Due to available resources and the progress of the test program, multilayer spooling measurements with this rope was limited to the D500 drum.

In order to compare properties and effects of the HPFRs relative to steel wire

ropes, an independent wire rope core (IWRC) steel wire (Ø20 mm) of comparable strength to the Ø20 mm HPSFRs, was selected.

Some ropes were already available in stock as Kongsberg Maritime's property. The other ropes were acquired especially for the project. The ropes were of different lengths resulting in varying maximum number of layers on the test drums. The main rope properties are summarized in Table 4.1.

Table 4.1: Main rope properties

Rope	**Size** [mm]	**MBL**[1] [kN]	**Weight**[2] [kg/m]	**Design**	**Fibres**
Steel wire	20	∼299	-	IWRC	Steel
DIMSTABLE	12	∼118(106)	0.11	12-strand braided w/jacket & core	Dyneema SK75 + SK62(jacket)
	20	∼345(383)	0.295		
BRAIDED-A	∼20	∼330(367)	-	12-strand braided	Spectra + Vectran
BRAIDED-B	20	∼371(412)	0.22	12-strand braided	Dyneema SK78
BRAIDED-C	12	∼144(160)	0.111	12-strand braided	Dyneema SK78 +polyester
	16	∼213(237)	0.153		
	20	∼323(359)	0.295		
BRAIDED-D	∼20	∼288(320)	0.27	12-strand braided w/polyester core	Mixed blend

[1] Spliced Strength(Unspliced strength) [2] Weight in air

4.5 Multilayer spooling test rig

The test rig, Figs. 4.7 and 4.8, uses two high-pressure hydraulically driven winches (pos. 1 and 14). Hydraulic cylinders (pos. 6 and 12) control the spooling devices for each winch, while a control system regulates the operation. The control system receives information from load cells (pos. 4 and 10) in the spooling device sheaves (pos. 5 and 11), Fig. 4.9, and rotary encoders (pos. 3 and 9) on the hydraulic motors (pos. 2 and 13) and continuously regulates load and speed against preset values. In addition, position and pressure sensors give information about spooling device position and hydraulic pressures.

When the rope runs from the left (tension side) to the right (speed control side), the left load cell controls the load while the encoder on the right side controls the speed. Due to symmetrical design, the system is bidirectional, and the procedure reversed when running from right to left.

The test rig is designed for Ø20 mm nominal rope dimensions and maximum dynamic rope tension in the range of 90-100 kN. The control of the spooling devices is programmable, allowing for different spooling patterns on the drum, e.g. number of axial displacements of the rope for each revolution. The experiments used a basic spooling pattern, with the rope being displaced axially once per revolution.

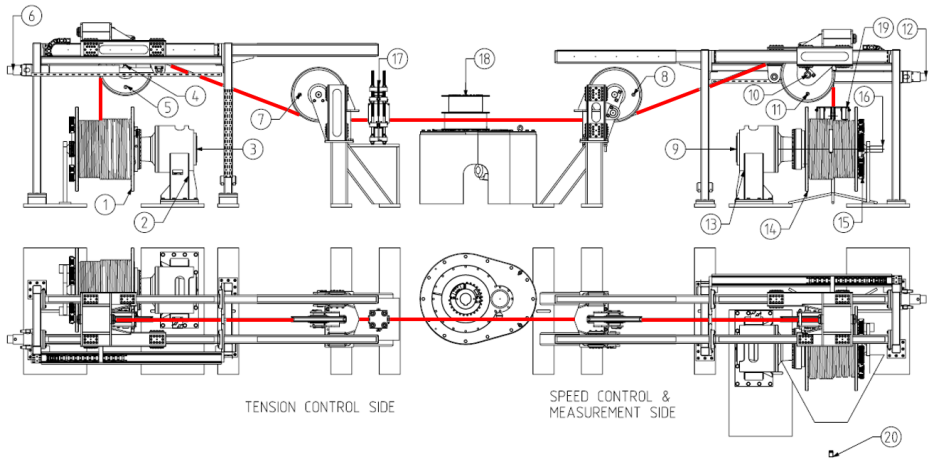

Figure 4.7: Overview of multilayer spooling test rig

Rope friction was measured using the vertical capstan winch with a unique designed drum (pos. 18) combined with the guide sheaves (pos. 7 and 8).

Pos. 17, 19 and 20 illustrate the compression device for testing transverse stiffness of ropes, laser measurement equipment measuring rope cross-sections and laser for rope radii measurements.

Due to limited measurement devices and prioritization of resources, all spooling measurements were carried out on the test rig's right side. Thus, the test drums were interchanged, and measurement equipment, fastened on the outer side of the drum flange, was moved between the drums. Power (24 V) was supplied to the measurement equipment through a slip-ring on the free-end axle (pos. 16).

The ropes were spooled from left to right at a constant speed, while strains in the right drum were measured and recorded. Before each run, the winch was rotated to a defined initial position, with a few load-free wraps of rope on the drum and all strain gauges were zero balanced. All ropes were tested several times at different tensile loads with repetitions.

The drive end of the drum was defined as the "fixed end" and the opposite as the "free end".

Figure 4.8: Multilayer spooling test rig

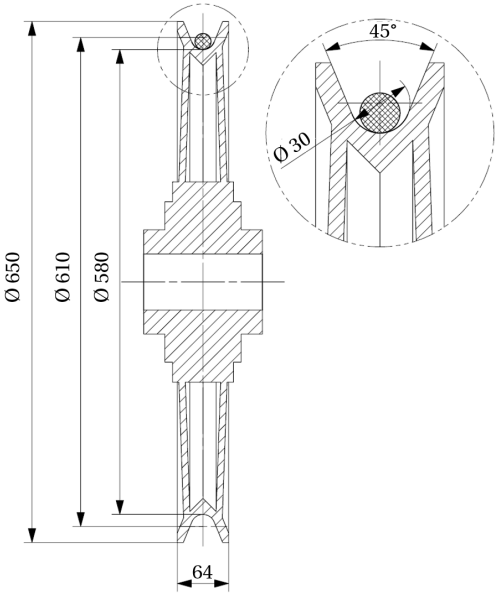

Figure 4.9: Size and profile of test rig sheaves

4.5.1 Winch test data - rope tension and spooling speed

An example of measured rope tension and rope spooling speed is shown in Fig. 4.10.

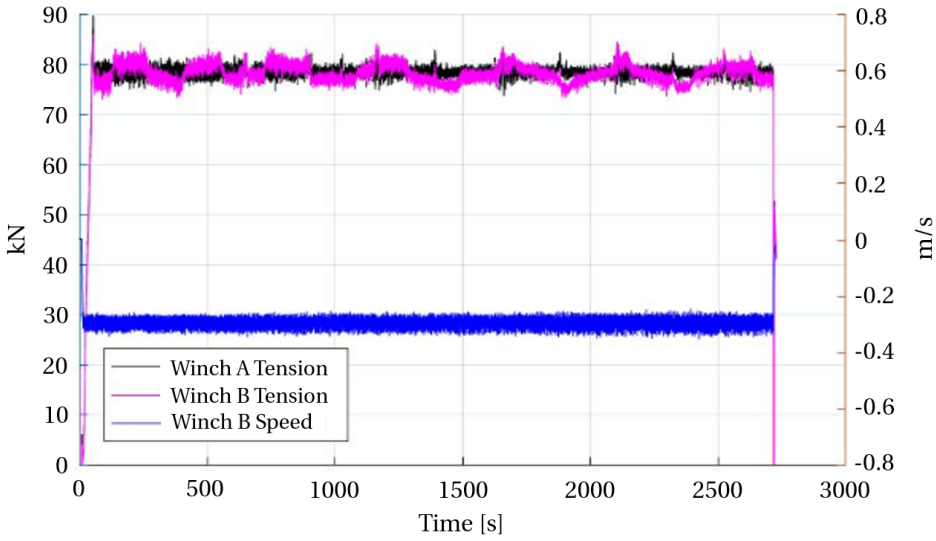

Figure 4.10: Example of winch test data - rope tension and speed

The rope tension on the speed control and measurement side (Winch B) varies more than on the tension control side of the test rig (Winch A). This is because the test rig's tension control side behaves as a stiffer and more responsive subsystem than the complete test rig due to the short distance from the drum to the load cell. The rope tension is also slightly influenced by the motion of the spooling device. When moving in one direction, the spooling device sheave pulls the rope while being pulled by the rope in the other direction.

The test-rig load cells are ScanSense LS-3010-SP shear bolts holding the spooling device sheaves. The capacity is 25 metric tons with $\pm 1\%$ of full-scale accuracy at 20°C ambient temperature. The load measurement system was tuned against a calibrated load cell spliced into the rope between the winches. The values from the load cell closest to the strain gauge measurements (measurement side) were defined as the relevant rope tension. Tension levels for each experiment were determined from the averaged rope tension during spooling of ropes onto the measurement drum.

4.6 Test drums

Two drums with different diameters were applied in the experiments to evaluate the effects of different D/d-ratios of the ropes.

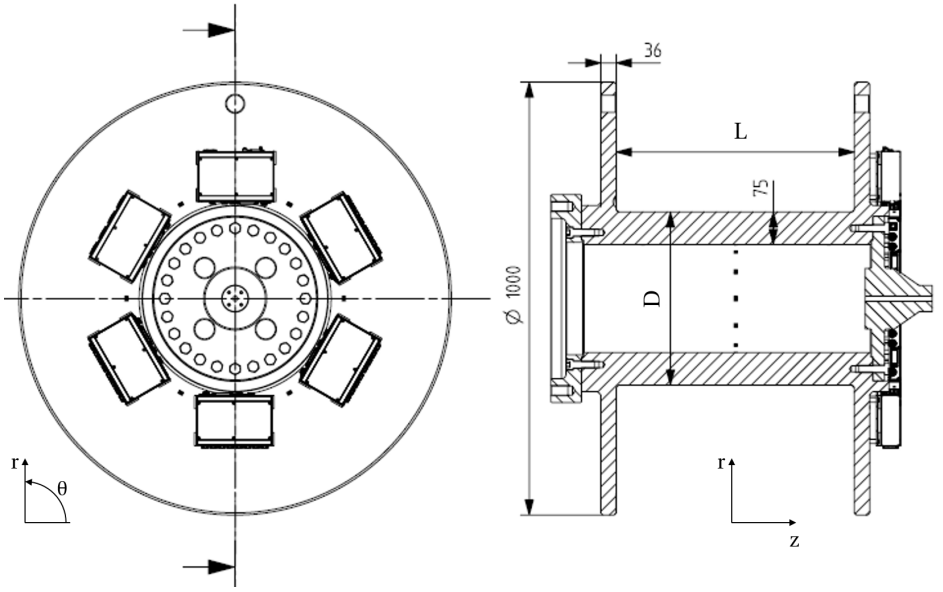

Figure 4.11: Test drum

The two winch drums, Fig. 4.11, were designed to handle expected high loads and stresses during testing. D400 was designed with 400 mm outer diameter (D) and 550 mm (L) distance between flanges, while the length and diameter of D500 were 625 mm and 500 mm, respectively. To compensate for a shorter length and fit the test rig foundations, D400 was equipped with a spacer adapter on the drive end. Both drums were smooth, without grooves, and with 75 mm thick drum cores. The flanges, 36 mm thick plates, were welded to the drum core.

The drums were machined to tolerances ($\pm$0.2 mm and Ra 6.3 μm) inside and outside of both flanges and drum cores. This removed uncertainties related to dimensions and prepared for mounting of strain gauges. Machining of the flanges was carried out after welding and post-weld heat treatment of the complete drums. (The thickness tolerances of the flanges were $\pm$0.3 mm.) The drums were also painted with one layer of Intergard 269 primer for corrosion protection. Unpainted areas specified for strain gauges were temporarily protected by solid plastic tape.

The base material of the drum cores was forged round bars of AISI4130 normalized, quenched and tempered steel. The drum cores were vital to the experiments

considering costs and limited possibilities for repair after instrumentation. Therefore, in order to confidently determine the maximum load and prevent excessive plastic deformation during testing, additional tensile tests of the base material were conducted (Ref. Experiment A, Fig. 4.3). Test specimens were taken from extra pieces of material from both drum cores in axial and circumferential directions. These were taken from three different positions through the thickness in both directions, Fig. 4.12.

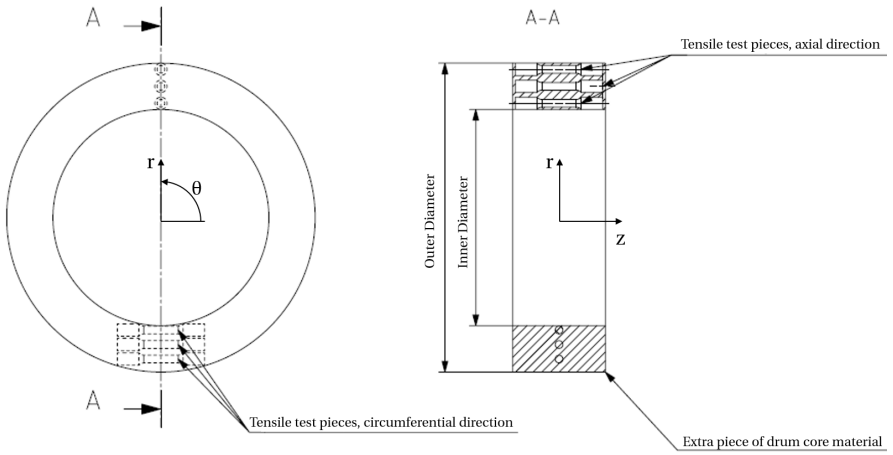

Figure 4.12: Tensile test specimens from test drum materials

The results confirmed AISI4130 strength to vary through the thickness, increasing from the inside to the outside. The largest drum was slightly stronger than the smallest, Fig. 4.13. The measured strength on the inner side of the drums was lower than the values specified by the material certificates for both drum cores.

The flanges were made of 40 mm quenched and tempered JFE-HITEN780S steel plates. The welded interface to the drum core was considered the most critical part of the flanges. With higher yield stress than required by the standard, the delivered material certificate was accepted with no further verification.

The minimum measured mechanical properties of the drum core and flange materials are summarized in Table 4.2. Acceptance values according to standards are indicated in brackets. The minimum measured yield stress with an additional margin of 10% gave 420 N/mm^2 as the maximum allowable stress in the drum core during experiments. The extra margin compensated for unknown effects like measurement accuracy.

The dimensions of the two drums were chosen to fit the test rig, be as similar as possible, and handle at least ten layers of Ø20 mm rope. Further, an important

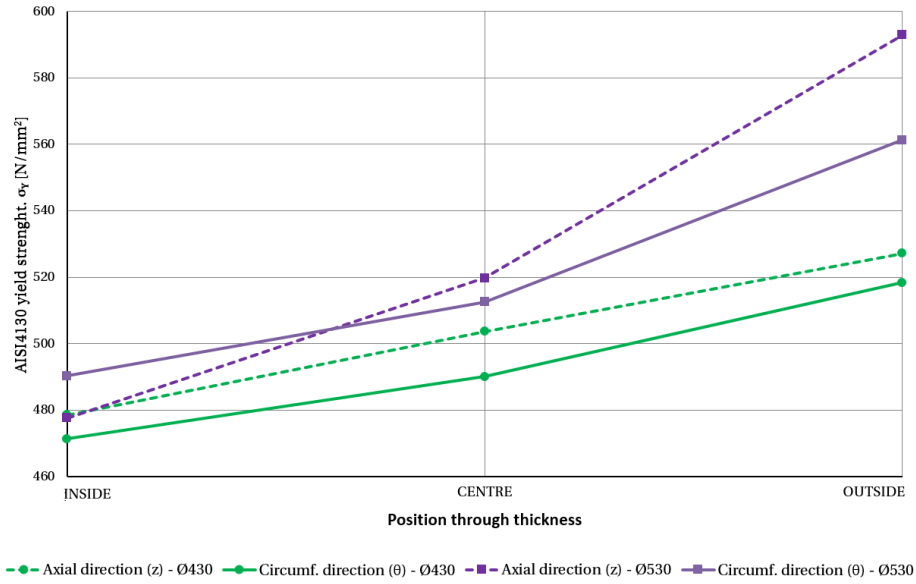

Figure 4.13: Yield stress through thickness of drum core material (AISI4130)

Table 4.2: Test drums - material properties

Material	Yield Strength, $Rp_{0.2}$ [N/mm^2]	Tensile Strength, R_m [N/mm^2]	Elongation, A_5 [%]
Drum Core Ø430	471 ($\geq$517)	651 ($\geq$655)	26.2 ($\geq$18)
Drum Core Ø530	478 ($\geq$517)	663 ($\geq$655)	24.3 ($\geq$18)
Flanges 40mm	840 ($\geq$685)	893 (780-930)	21 ($\geq$16)

aspect was to minimize geometric effects (from flanges and ends) on stresses at the centre of the drums where strain measurements were planned. This was achieved as both drums fulfilled the requirement for long drums, see Section 3.1.12. The "reduced length" for D400 and D500 were 6.4 and 6.36, respectively.

The assumption that geometric effects and disturbances did not influence measurements was verified by comparing stress distributions from linear elastic axisymmetric FE-analysis. In the FE-analysis, unit loads were applied to the drum and flange and distributed according to DNV GL [3]. Figures 4.14 and 4.15 show simulation results comparing pure radial pressure and radial pressure in combination with flange forces. The geometry and change in stiffness induce axial stresses in the vicinity of the flanges, even for the hypothetical condition of multilayer spooling with no flange forces. However, the differences are minimal for tangential stress at the drum centre and less than 0.81% and 0.49% for D400 and D500,

respectively. This justifies that effects from geometry and flange forces can be ignored for strain measurements inside the drum in the centre between the flanges.

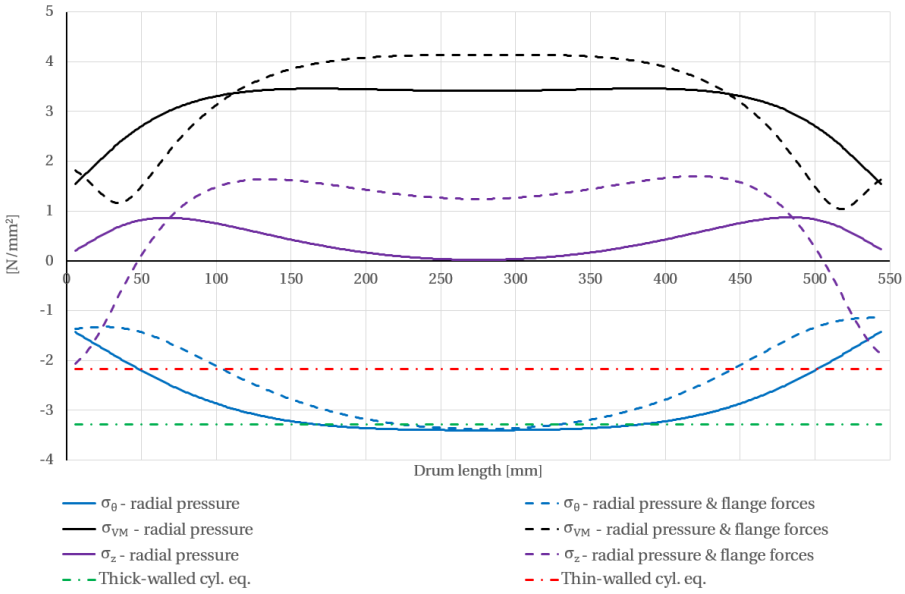

Figure 4.14: Stress distribution D400 drum - FEA calculations

Stresses calculated by the simple closed-form equations for infinitely long thin- and thick-walled cylinders, Eqs. 2.6 and 2.7 are also plotted and show a noticeable difference. Relative to the FE simulation with pure radial pressure, the thick-walled cylinder equation calculates tangential stress within 4%. In contrast, the thin-walled cylinder equation underestimates the stress by more than 30%.

The relative error between the two equations is strongly dependent on the ratio of drum thickness and radius, as shown in Fig. 4.16. With a thickness/radius ratio of 0.1, the difference is approximately 10%, while it requires a ratio of 0.05 to reach less than 5% difference. Winches for marine applications often have t/r-ratios higher than 0.1, and by applying Eq. 2.6, without considering this difference, there is a risk for underestimating the tangential stresses.

Bending and shear stress also acts on the drum. Considering the drum as a simply supported beam, the maximum bending stress on the inner side of the drum is approximately ± 1 N/mm^2 for D500 (Eq. 2.2). The shear stress due to torsion (Eq. 2.4) is of the same order of magnitude. Therefore, the effects of these stresses were ignored. The directions of principal stresses on the surface of the drums' inner side were considered tangential (circumferential) and axial.

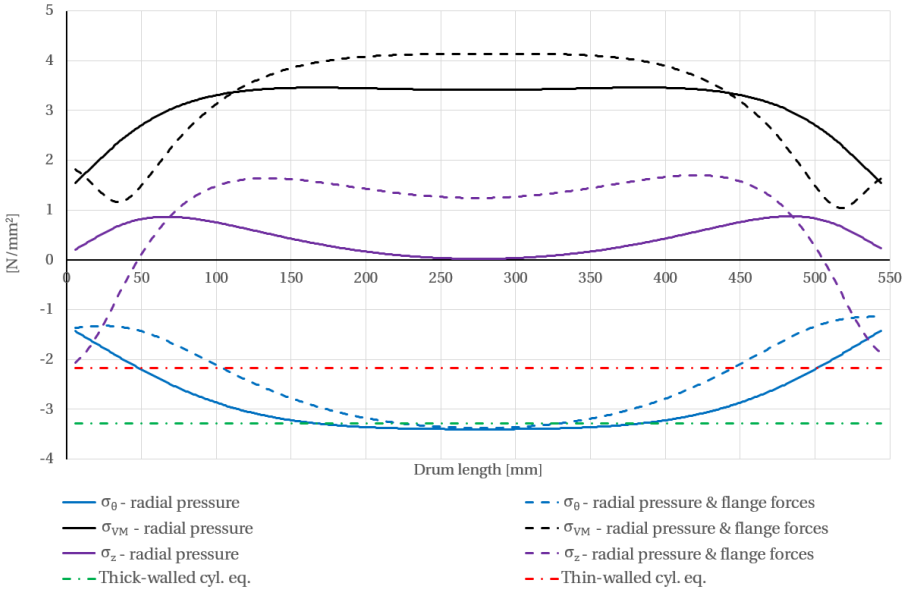

Figure 4.15: Stress distribution D500 drum - FEA calculations

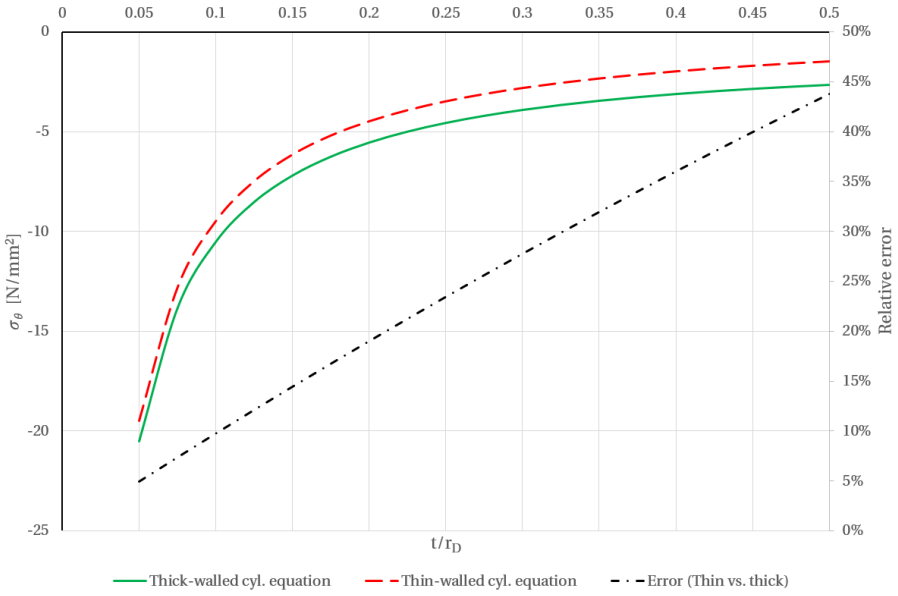

Figure 4.16: Tangential stress - thin versus thick cylinder theory

4.7 Strain measurement

Proper strain measurements were critical to the experiments. Therefore, Hottinger Baldwin Messtechnik (HBM) consultants were hired to mount strain gauges and set up the strain gauge measurement system.

4.7.1 Measurement principle

The principle of strain gauge measurement is based on surface strains being transferred from the object to the gauge through an adhesive, changing the gauge's electrical resistance. It is assumed that strains are transferred without loss, which requires a very close bond and a high grade of cleanliness during mounting. The change in resistance is minimal, and a measurement system must amplify the signals to measure the strains precisely. When strain changes the resistance of the gauges, the symmetry of the Wheatstone bridge is disturbed, resulting in an output voltage that is proportional to the unbalance. Electrical power is supplied to the gauge and an amplifier making the output voltage manageable for a display and a data recorder.

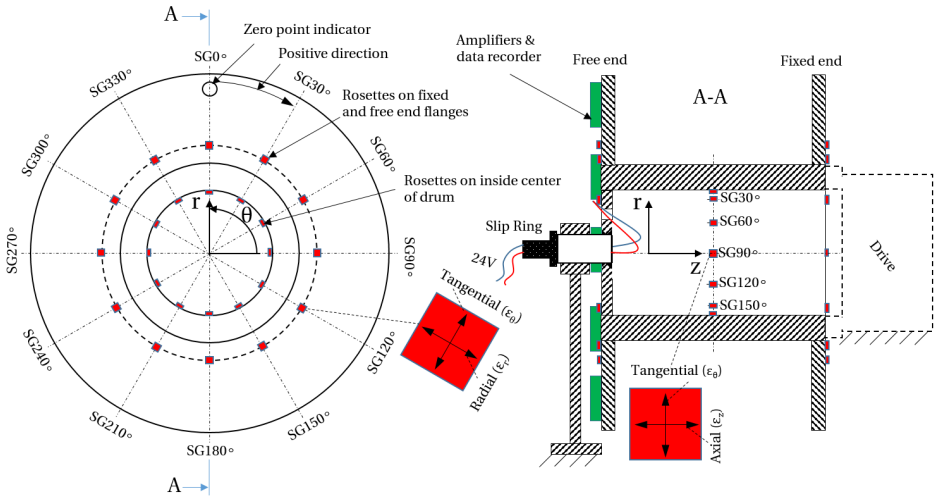

Figure 4.17: Overview of strain gauge measurement

Figures 4.17 and 4.18 show a basic overview of the measurement setup. T-rosettes of type HBM K-CXY3-0030-1-350-4-030-N with two 3 mm and 350 Ω measuring grids positioned 90° to each other were used. The gauges were delivered with three meters flat band cables pre-soldered to each grid. HBM's patented 4-wire technology (Kreuzer circuit), ensuring high temperature stability and compensation of cable lead resistance, was used. Each grid was coupled as one-quarter of

the Wheatstone bridge resulting in half-bridges (Poisson half-bridges). All rosettes were glued with HBM Z70 and covered with SG250 silicone for protection. Shunt calibration with a 100 kΩ resistor was used to verify the setup. The calculated tolerance for a correct setup was -1761.5 μm/m $\pm$ 20 μm/m and the measured value was -1764 μm/m. The excitation voltage was 2.5 V.

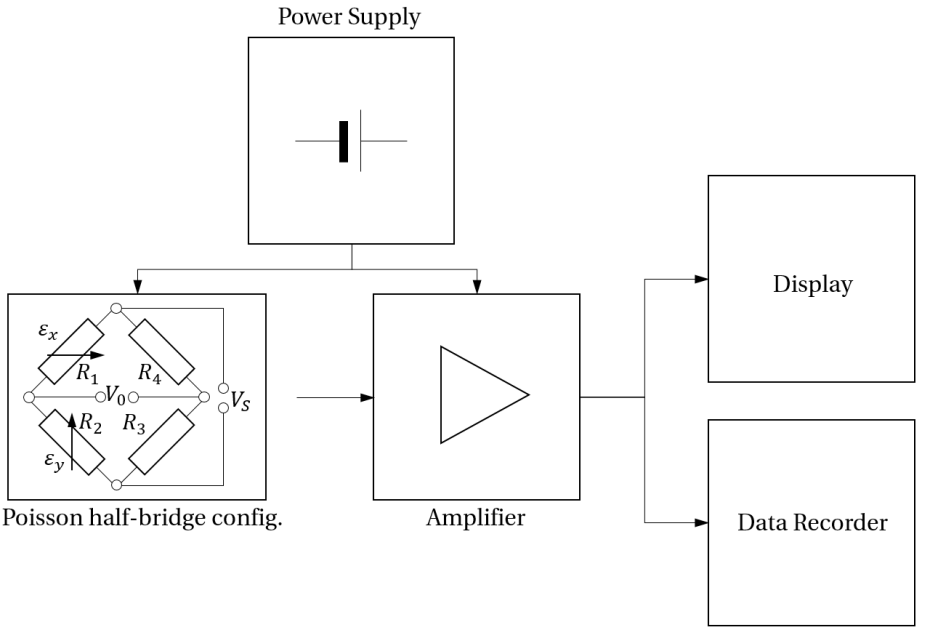

Figure 4.18: Strain measurement principle

Compensating for temperature effects is very important concerning strain gauge measurements. The gauges were temperature compensated for ferritic steel, with a thermal expansion coefficient of 10.8×10^{-6}/°C. However, the actual coefficient for the used materials was unknown. Due to the half-bridge configuration and T-rosettes, measuring in two perpendicular directions, temperature expansion was effectively compensated for. Strictly, to be 100% effective, this compensation requires isotropic thermal properties. Admittedly, anisotropic strength was identified to some extent for the AISI4130 material and could also be expected for the flanges being made of rolled steel plates. Nevertheless, isotropic thermal properties were assumed. In combination with experiments carried out indoor, in a controlled environment with stable ambient temperature, the thermal compensation and stability of the measurements were considered good.

No high-voltage equipment, electric rotating machinery or magnetic sources were present in the vicinity of the measurement equipment.

4.7.2 Measurements on drum cores (B1)

Each drum was equipped with twelve T-rosettes to measure the tangential and axial strains. The rosettes were equally distributed around the circumference, inside the drum in the centre between the flanges. In addition, two optional rosettes were mounted on each side of the centre. The wires were routed to the outside of the free-end flange through holes in the plate holding the free-end axle. Figure 4.19 shows the type of rosette used, locations of these on an "unfolded" view of drum and as mounted.

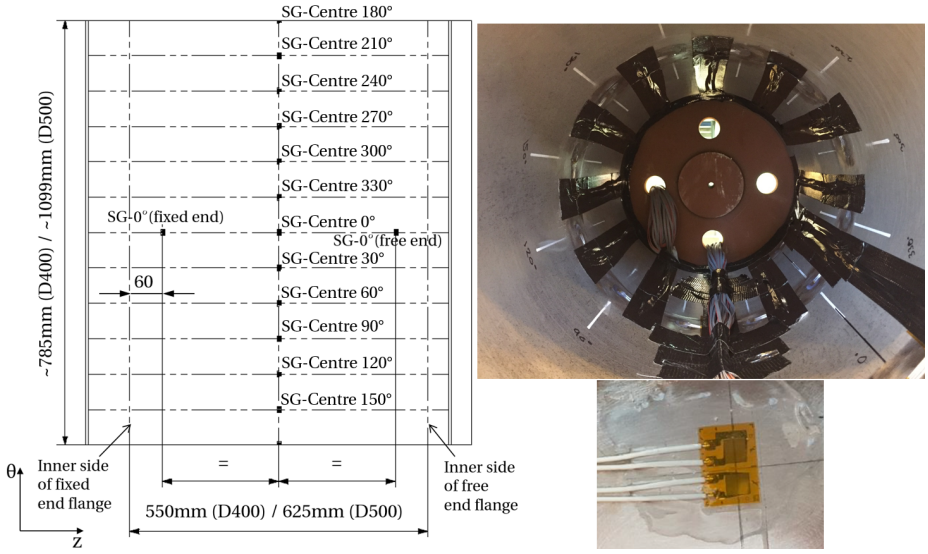

Figure 4.19: Strain gauges inside drum

4.7.3 Measurements on flanges (B2)

Each flange on the two drums was also equipped with twelve T-rosettes to measure radial and tangential strains.

Figure 4.20 shows an example of rosette locations on the outer side of the fixed-end flange. Measuring on the outside was considered the best option due to the high risk of damage to gauges on the inside or at least influence on results due to mechanical pressure from rope contact. The rosettes on the flanges were aligned with the rosettes inside the drum.

Wires from the fixed-end flange were routed through the drum to the free-end flange, where the measurement electronics were fastened.

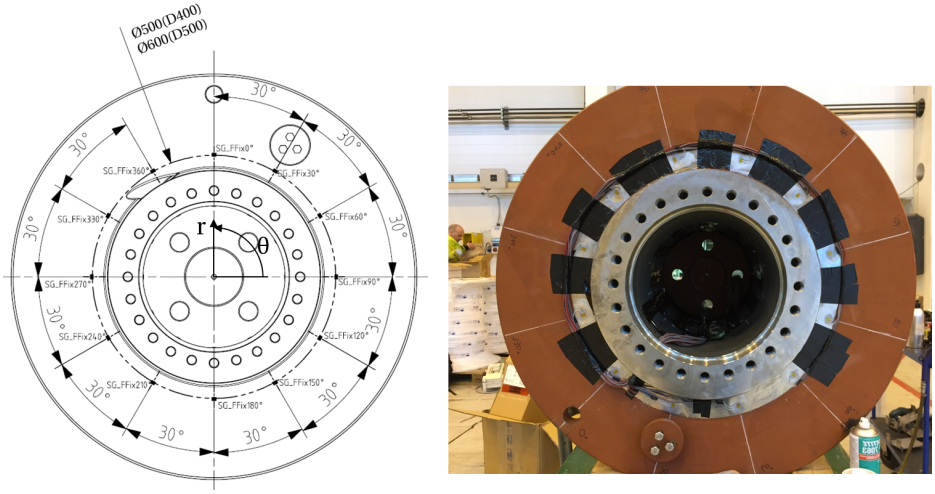

Figure 4.20: Strain gauges locations on D400 drum

4.7.4 Measurement electronics

Strain data acquisition was handled by five synchronized amplifiers (four HBM Quantum MX1615B and one HBM MX840A) combined with a data recorder (HBM CX22B-W), all mounted on the free-end flange, Figs. 4.21 and 4.22. The measurement frequency for all strain gauge measurements was set to 10 Hz.

The equipment was verified and calibrated by the supplier before any experiments.

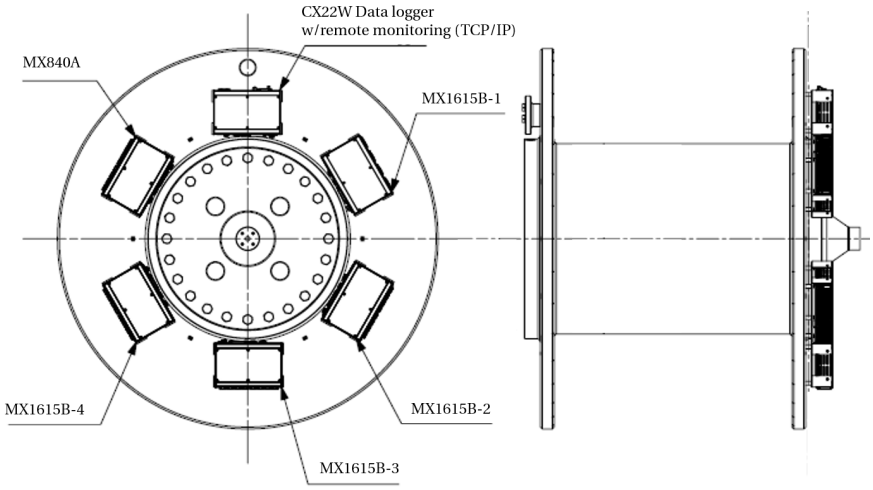

Figure 4.21: Overview of amplifiers and data logger

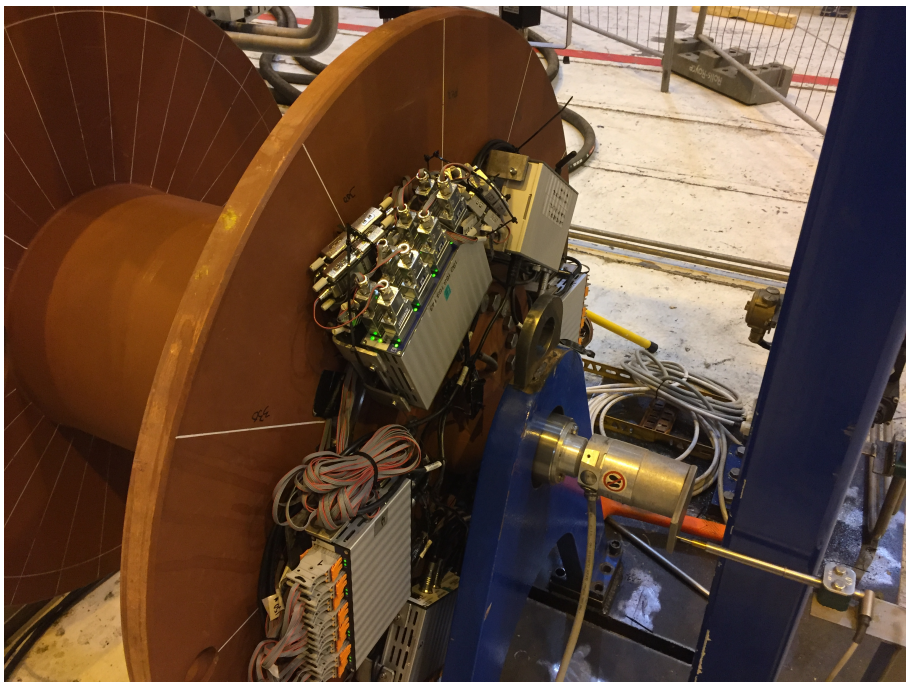

Figure 4.22: Strain gauge electronics on drum

4.7.5 Stress data

Stresses were calculated from the measured biaxial strains in combination with the material's elastic modulus and Poisson's ratio. Equation 4.1 gave the tangential stress from the tangential strain in combination with axial or radial strain for the drum and flange, respectively. Correspondingly, axial stress in drum or radial stress in the flanges were calculated by Eq. 4.2. Equivalent stresses (von Mises) were calculated by Eq. 4.3.

$$\sigma_\theta = \frac{E}{(1-\nu^2)}\left(\varepsilon_\theta + \nu\varepsilon_z\right),\ \sigma_\theta = \frac{E}{(1-\nu^2)}\left(\varepsilon_\theta + \nu\varepsilon_r\right) \tag{4.1}$$

$$\sigma_z = \frac{E}{(1-\nu^2)}\left(\varepsilon_z + \nu\varepsilon_\theta\right),\ \sigma_r = \frac{E}{(1-\nu^2)}\left(\varepsilon_r + \nu\varepsilon_\theta\right) \tag{4.2}$$

$$\sigma_{VM_{(Drum)}} = \sqrt{\sigma_\theta^2 + \sigma_z^2 - \sigma_\theta\sigma_z},\ \sigma_{VM_{(Flange)}} = \sqrt{\sigma_\theta^2 + \sigma_r^2 - \sigma_\theta\sigma_r} \tag{4.3}$$

An example of measured stresses around the circumference of the drum core is shown in Fig. 4.23. Each layer is visible with distinct steps in stress levels. Locations from where the peak axial, tangential and von Mises stresses were extracted are also indicated. It can be noticed that the peaks of the different stress components are not coincident. Peak axial stresses occur when the rope is straight over the gauges, while the peak tangential stresses occur slightly later. Consequently, the maximum von Mises stresses are somewhere in between.

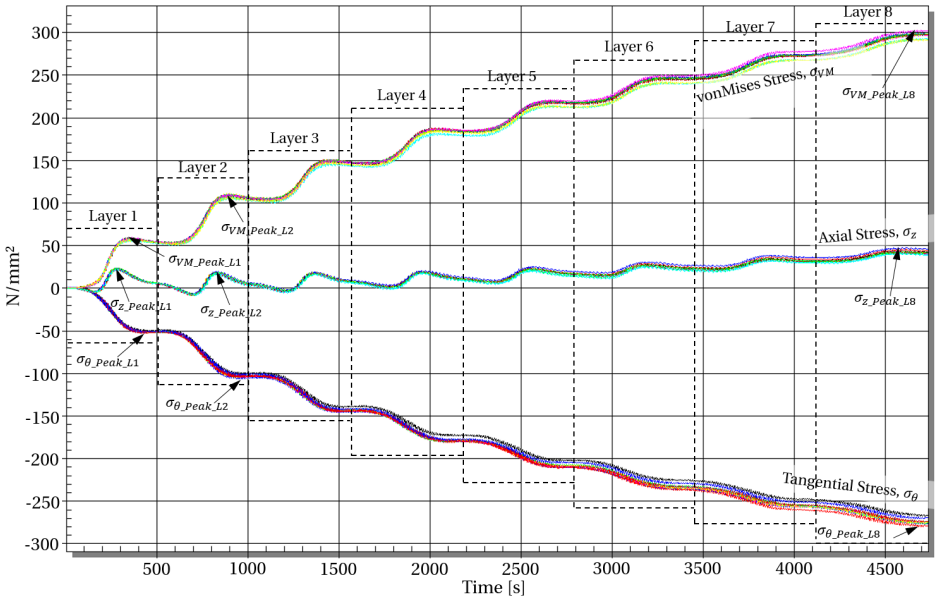

Figure 4.23: Example of stress in drum (12 gauges) - one test cycle during on-spooling

Figure 4.24 shows an example of von Mises stress in the drum flanges. The red and black curves are measurements from twelve gauges on each free- and fixed-end flange.

When the rope comes in contact with the flange and climbs to the next layer, the stress level increases distinctly. As the spooling started from the fixed-end flange, stresses increase for every odd-numbered layer in the free-end flange and every even-numbered layer in the fixed end.

Due to controlled spooling, climbing to the next layer occurs approximately at the same sectors for each layer. An increasing number of layers results in increased stress variation around the circumference.

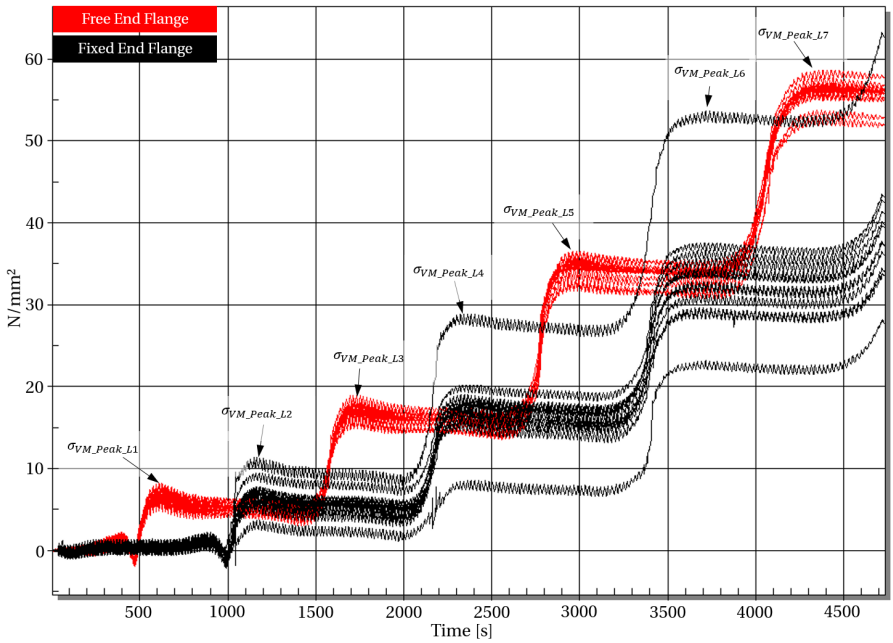

Figure 4.24: Example of von Mises stress in flanges - one test cycle during on-spooling

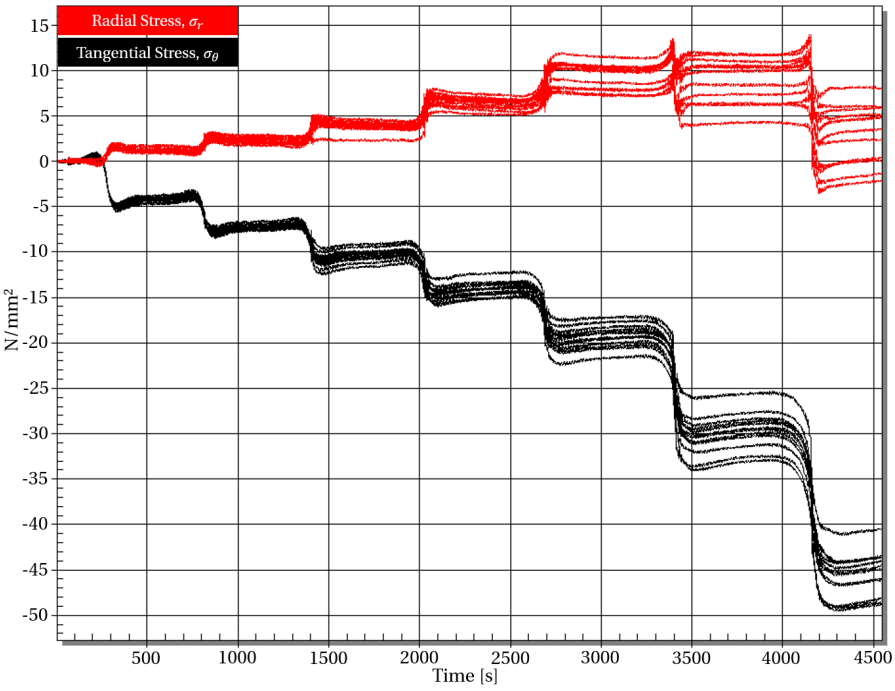

Figure 4.25: Example of stresses in free-end flange - one test cycle, during on-spooling

The tangential and radial stresses develop differently with an increasing number of layers. While the compressive tangential stress growth is continuous, the radial stress typically starts in tension and change to compression with an increasing number of layers. This change is because the axial forces and bending moment are small with few layers on the drum. Actually, for the first layers, the outer flange edges move inwards due to the radial compression of the drum. When the number of layers increases, the bending moment increases, causing the flanges to be bent outwards. Figure 4.25 shows this effect, where the red curves are radial stresses and the black tangential stresses from the twelve strain gauges on the free-end flange.

4.8 Flange deformation (B3)

Three displacement transducers (HBM K-WA with 50 mm range) were applied to measure flange deflections. The sensors were mounted on vertical angle bars, welded to the ground. They measured the axial displacements at the outer end of each flange and the centre of the free-end axle, Fig. 4.26. Measurement data was processed by an available Spider 8 amplifier and a separate computer. Consequently, these measurements had an individual timer and were not perfectly synchronized with the strain gauge measurements.

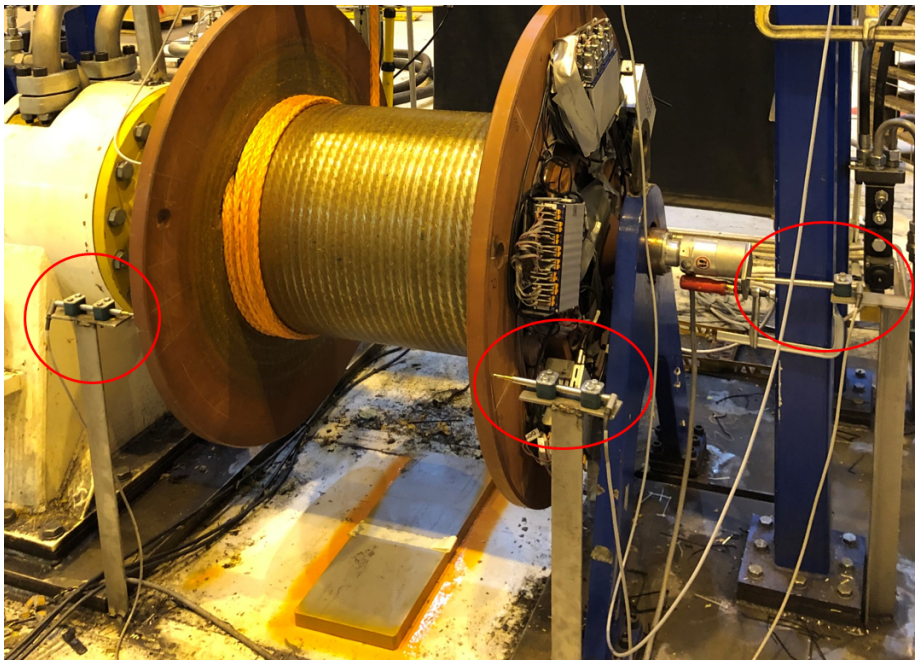

Figure 4.26: Displacement transducers on flanges

Figure 4.27 shows examples of measured lateral displacement for each flange and the free-end centre. The positive and negative values are outward and inward deflections of the flanges. With a measurement frequency of 10 Hz, the sensors were quite sensitive. They picked up a lot of variations around the circumferences for each revolution. Mean values were calculated for every revolution of the drum and are indicated as dark solid lines.

The displacement transducer on the fixed-end side lost the rounded tip on the probe during the measurements. This resulted in considerable variations, and due to unknown trustworthiness, results from this sensor were disregarded.

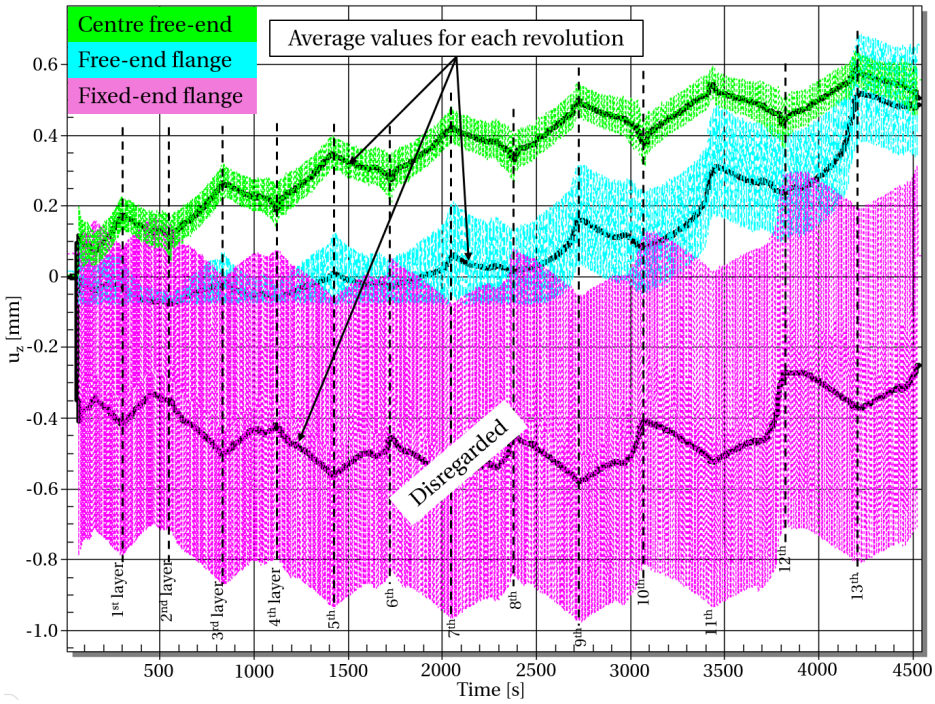

Figure 4.27: Example of flange deflection data

4.9 Rope deformation, shape and dimensions (C1 and C2)

Laser measurements of ropes related to multilayer spooling were introduced by Lohrengel et al. [9] and applied to measure rope dimensions and rope when spooled onto drums. Figure 4.28 shows the equipment from LMI Technologies that was used, mounted on tripods.

Figure 4.28: Laser measurement equipment

4.9.1 Laser measurement principle and setup

The laser measurement system projects a laser line from an emitter onto the target, and a camera captures the reflection from an angle, Fig. 4.29. Profile heights are determined by laser triangulation using the triangle formed by the three main components (emitter, camera and target), the distance between the camera and emitter and two angles.

The setup and results are dependent on clearance distance (CD), the field of view (FOV) and measurement range (MR). The clearance distance is the minimum distance between the target and sensor. The measurement area is the area where targets can be scanned and measured. It is defined by the MR and the width of near and far FOV's.

The sensor has a defined number of measurement points. The x-resolution is the distance between each point along the laser line (x-axis). The resolution is higher (smaller distance between points) at close range than at the far range. The z-resolution defines the smallest detectable distance difference at each point along the z-axis. As with the x-resolution, the z-resolution is higher closer to the sensor.

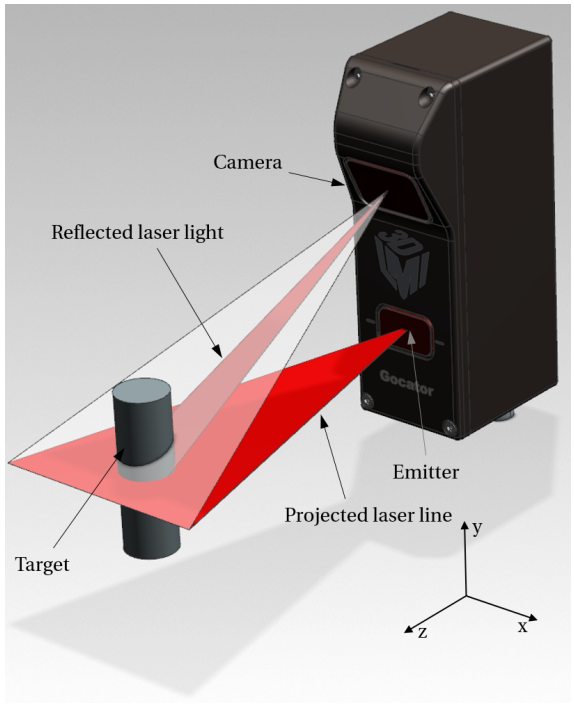

Figure 4.29: Laser measurement principle

The z-linearity indicates how accurate the sensor can measure absolute distance. It is the difference between actual distance and measured distance for the whole measurement range.

One Gocator 2380 3D smart profile sensor with 1280 data points was used to measure rope layers on the drum (C1). Figures 4.30 and 4.31 show the measuring principle and a test scan during setup. Due to the large range of the sensor, the complete width of the drum was captured. Through a signal from the winch drive encoder, the system was set up to scan the drum every 10° of rotation (36 scans per revolution). The drum was scanned during both on- and off-spooling of rope. This made it possible to compare the rope layer radii before and after compression from subsequent layers.

Table 4.3: Gocator specifications

Sensor	z-Rep. [μm]	z-Lin. [$\pm$% of MR]	z-Res. [mm]	x-Res. [mm]	CD [mm]	MR [mm]	FOV [mm]
2130	0.8	0.01	0.006-0.014	0.088-0.150	90	80	47-85
2380	0.12	0.04	0.092-0.488	0.375-1.100	350	800	390-1260

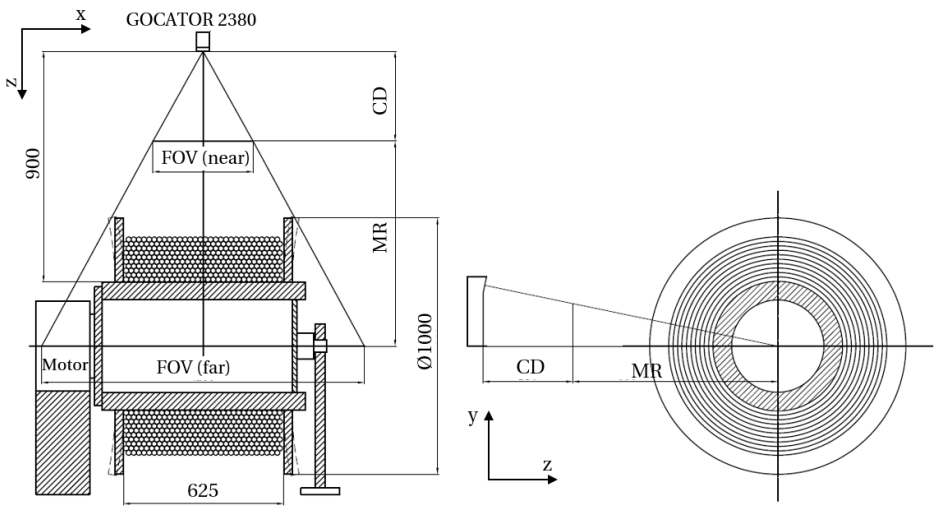

Figure 4.30: Principle and range of drum scanning with Gocator 2380

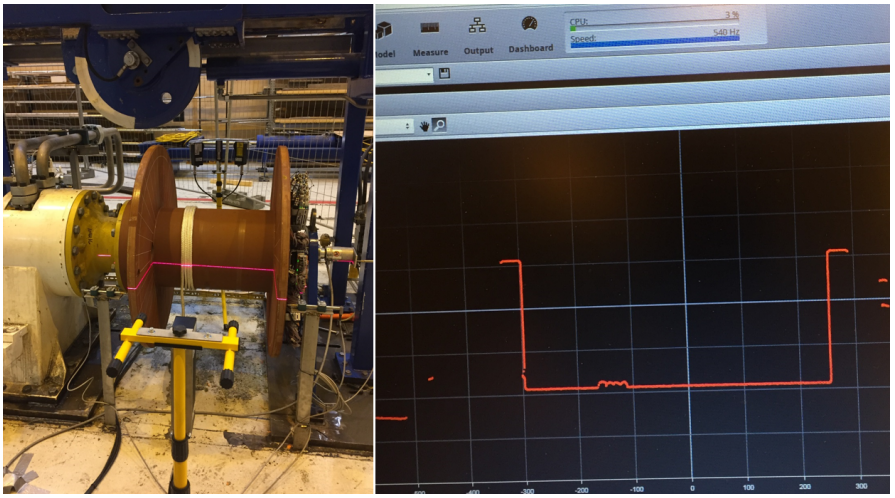

Figure 4.31: Test of drum scanning using Gocator 2380 (C1)

Three Gocator 2130 3D smart profile sensors (640 data points), synchronized by a Gocator Master 810 network controller, were applied to scan the rope shape (C2). The three sensors were attached to an aluminium plate and oriented to measure sectors of 120° each. The sensors were aligned and calibrated by standard Gocator software in combination with a specially made calibration piece. Figure 4.32 shows the measurement principle and range. Specifications for the laser sensors are given in Table 4.3.

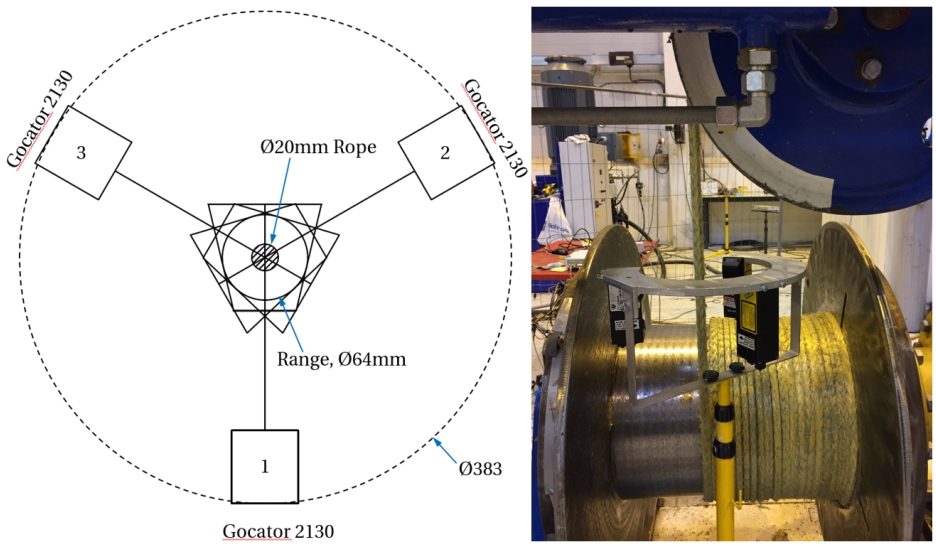

Figure 4.32: Principle and range of rope shape scanning (C2)

It was desirable to measure rope shapes as close to the drum as possible. Due to the test rig, with moving spooling sheave and potentially disturbing vibrations, the efforts of continuous and automatic rope shape measurements were considered too high, complicated and risky. Instead, snapshots were taken once for each layer. The rope was then approximately in the centre between the flanges and the scanning plane between the centres of drum and sheave, Fig. 4.33. These snapshots were taken when the ropes were spooled off the drum only.

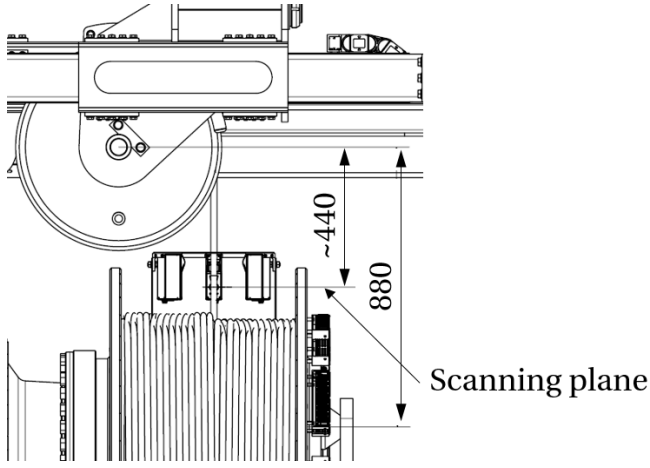

Figure 4.33: Scanning plane for rope profile measurements

4.9.2 Laser measurement data

The rope layer radii were determined using a .csv file of the measurements from the Gocator Emulator (standard software) and a MATLAB code. The code determined the peak points of each rope winding for each 10° measurement within ±150 mm of the centre between the flanges, Fig. 4.34. From this, the average radii and standard deviations were calculated for each layer both during on- and off-spooling.

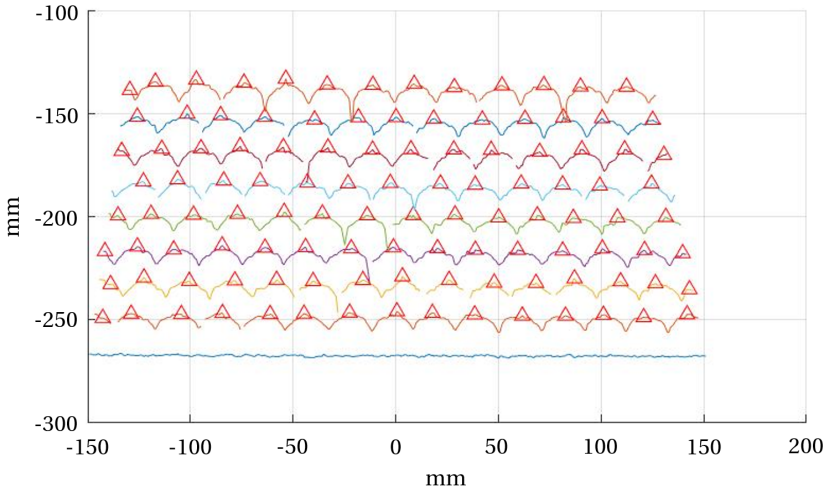

Figure 4.34: Peak points of rope windings on drum

Measurements of rope cross-sections, dimensions and enclosed area were carried out on selected tests with different rope tensions using Gocator software, Fig. 4.35.

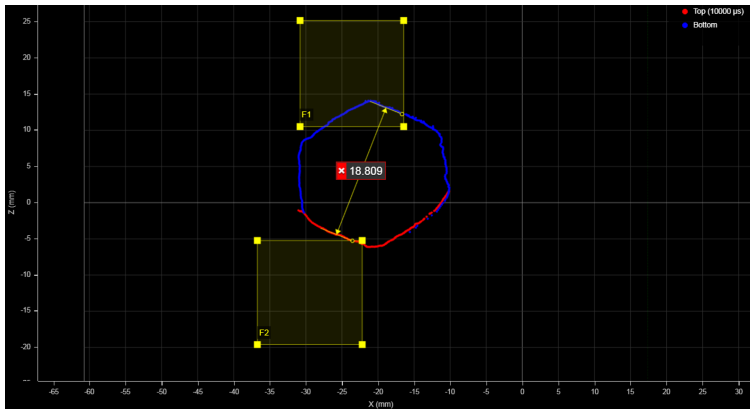

Figure 4.35: Measurement of rope cross-section

4.10 Rope friction (C3)

Rope friction tests were conducted in the spooling rig using a special drum ("friction drum") on a capstan winch equipped with a rotary encoder, Fig. 4.36.

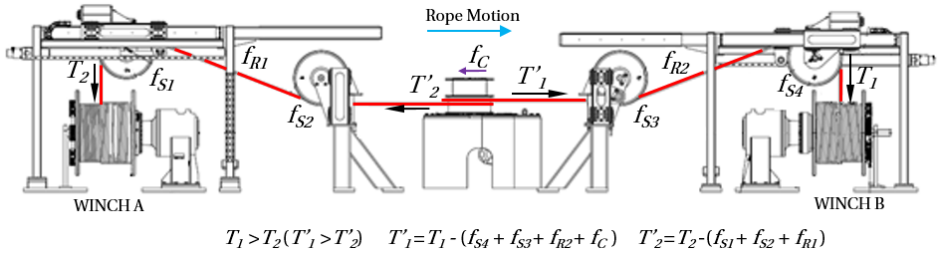

Figure 4.36: Principle of rope friction measurement

The rope was spooled from winch A to winch B with the rope wrapped around the friction drum. With sufficient friction force, the friction drum was rotating at the same speed as the winches. The rope tension force (T_1) from winch B was then increased while it (T_2) was kept constant on winch A. When the driving force became too high, slippage occurred between the rope and friction drum, and the friction drum lost speed rapidly. Figure 4.37 shows an example of the logged forces and speeds. Several tests were carried out with increasing tension levels after each slippage was detected.

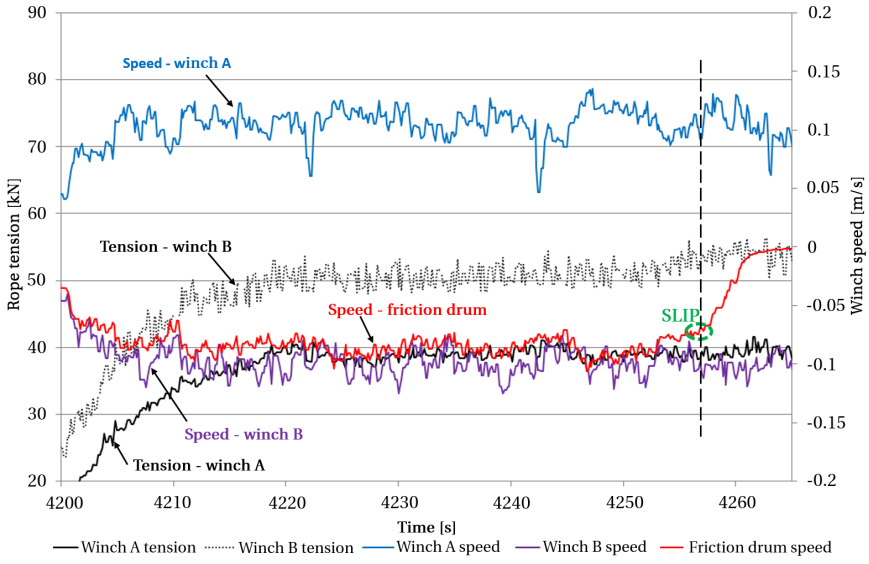

Figure 4.37: Example of friction data

The coefficient of static friction was calculated by Eq. 4.4, derived from the rope friction equation Eq. 3.38. T_1 and T_2 are rope tension forces at the point of slippage, and α is the wrap angle in radians. The related average contact pressure was calculated by Eq. 4.5 using the friction drum diameter D and nominal rope diameter d, Fig. 4.38.

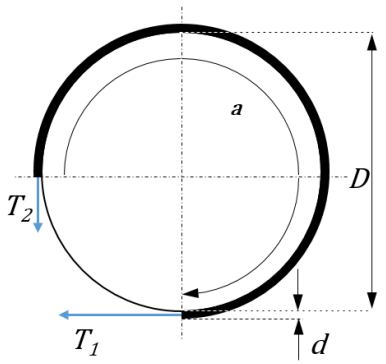

Figure 4.38: Rope friction

$$\mu_s = \frac{1}{\alpha} ln \left(\frac{T_1}{T_2} \right) \qquad (4.4)$$

$$p_{avg} = \frac{T_1 + T_2}{Dd} \qquad (4.5)$$

With reference to Fig. 4.36. Due to friction forces in the rope sheaves ($f_{\text{S1-S4}}$), hydraulic resistance and friction in the capstan winch (f_{C}) and rope weight ($f_{\text{R1-R2}}$), the rope tension forces T_1 and T_2 are higher than the actual driving forces T_1' and T_2' in the immediate vicinity of the friction drum. The rope weight can be ignored with fibre ropes, and friction in the rope sheaves is also considered low. The torque required to initiate rotation of the capstan winch was estimated to be in the range of 1.5-2 kNm. These forces were ignored as the testing was conducted to investigate the relative difference between the ropes.

The friction drum, Fig. 4.39, was arranged so a layer of rope could be spooled onto the drum to simulate rope-rope friction. An encoder, mounted on the top centre, measured rotational speed.

The material of the friction drum was S355 steel. Due to the significant difference in hardness between steel and fibre ropes, any potential effects due to the harder AISI4130 used in the test drums were considered negligible. The surface texture and surface treatment were identical to the test drums.

The testing was carried out with one and two wraps on Ø400 mm diameter. The spooling speeds were 0.1 and 0.3 m/s. The rope-on-rope tests were problematic. It was not possible to wrap the rope layers tight enough to avoid the rope forcing itself down in between underlying windings, Fig. 4.40. Therefore, these tests were stopped without any valuable results.

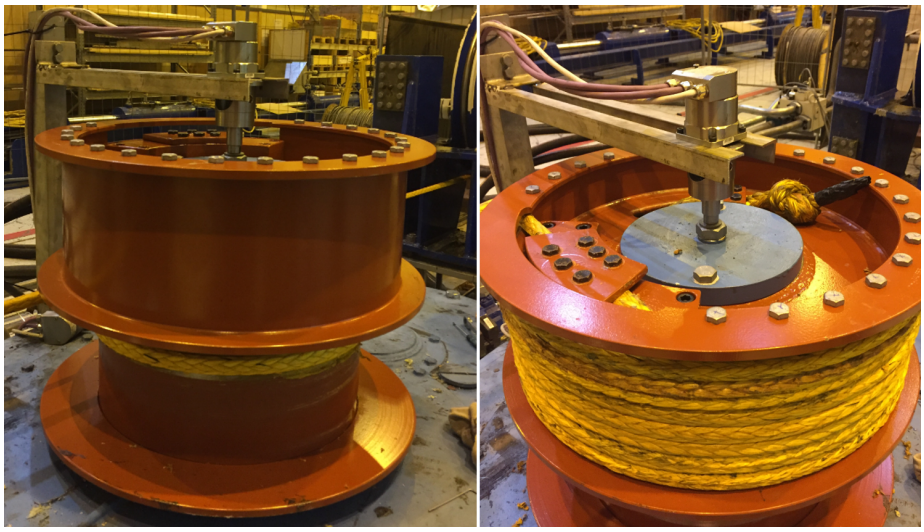

Figure 4.39: Rope friction drum on capstan winch

Figure 4.40: Rope stuck in the underlying layer during rope on rope friction test

4.11 Transverse rope stiffness (C4)

The method for testing of transverse rope modulus from Dietz [7] was applied, Fig. 4.41. Based on the principle from Henschel [28], a special test device was designed, Fig. 4.42.

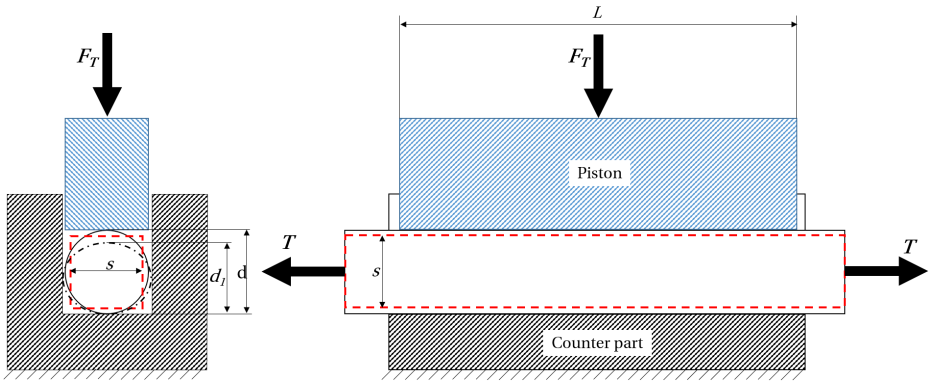

Figure 4.41: Test principle for transverse rope stiffness

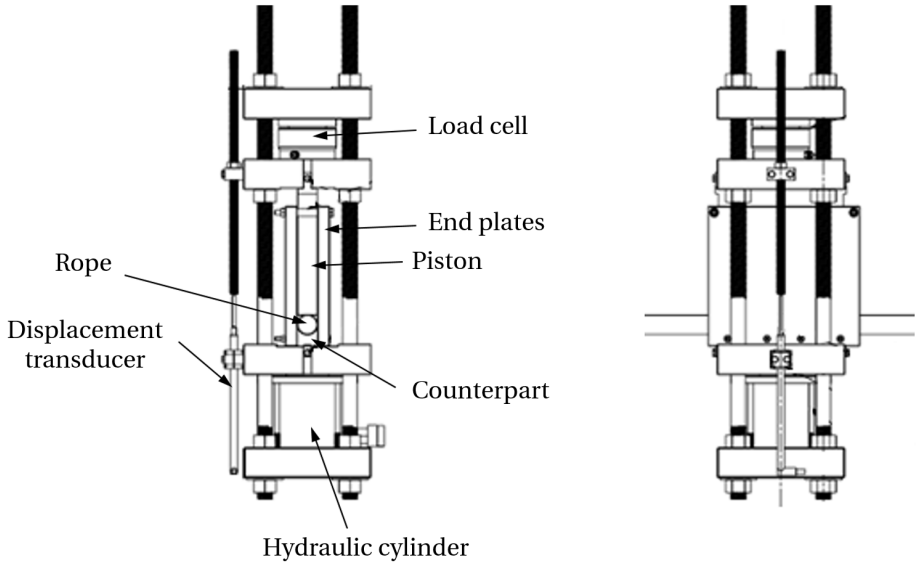

Figure 4.42: Test device for transverse rope stiffness

The test device used an Enerpac RCS502 Hydraulic Jack with 45 metric ton lifting capacity and 60 mm stroke. The device was designed to use both HBM U3 and C6A compression load cells with various capacities. A C6A load cell with a 200 kN capacity was suitable for the rope sizes.

An HBM K-WA displacement transducer with a 50 mm range was used to measure the piston travel. Pistons, counterparts and endplates were made in different sizes adapted to the relevant ropes. Plastic bearings ensured low frictional resistance between moving parts. The test device was made of high strength stainless steel (17-4 PH and S165M).

The counterparts were made in two designs to evaluate the effects of lateral constraint on transverse rope stiffness, Fig. 4.43. The curved counterpart partly constrained lateral expansion of the rope, while the flat design allowed free lateral expansion.

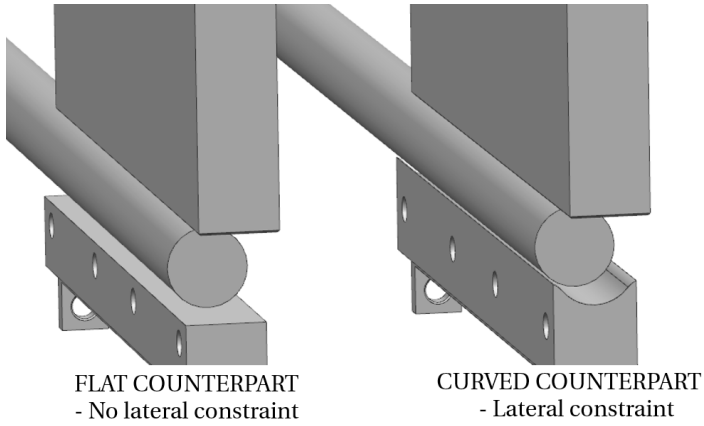

Figure 4.43: Counterparts with different degree of constraint

Rope tension was measured by an HBM Z16 special tension load cell (weight cell, accuracy class C3) with 15 metric ton capacity. An automatic pneumatic pedal pump controlled hydraulic power. The measurements were handled by an HBM Quantum MX840A connected directly to a laptop, and the measurement frequency was 100 Hz.

Initially, tests were carried out in the spooling test rig (C4-a), Fig. 4.44, and later in a linear cylinder arrangement (C4-b), Fig. 4.45. The latter improved load control as rope tension was controlled by hydraulic cylinders instead of hydraulic motors.

The cylinder arrangement also allowed for the testing of up to eight ropes in a linearly stacked arrangement. The test rope was then wrapped several times around two bolts, one fixed and one on a wagon pulled by a cylinder. The two rope ends were spliced to each end of the HBM Z16 tension load cell.

The required number of ropes for each test were placed between the counterpart and piston, while the other ropes bypassed the compression unit.

Figure 4.44: Test in spooling test rig (C4-a)

Figure 4.45: Test in linear cylinder arrangement (C4-b)

4.11.1 Test procedure and calculations

Before testing, all sensors were zero-balanced with 10 kN rope tension. Then the rope tension was increased to the required level, and the rope was compressed repeatedly. The number of compression cycles continued until the hysteresis curve was considered stable (typically 8-10 cycles), Fig. 4.46. The procedure was repeated for each specified rope tension level. Tests with both curved and flat counterparts were carried out.

The transverse moduli were determined for different ratios of transverse and longitudinal stress (k_T, Eq. 4.6) using the rising part of the stabilized stress-strain curve.

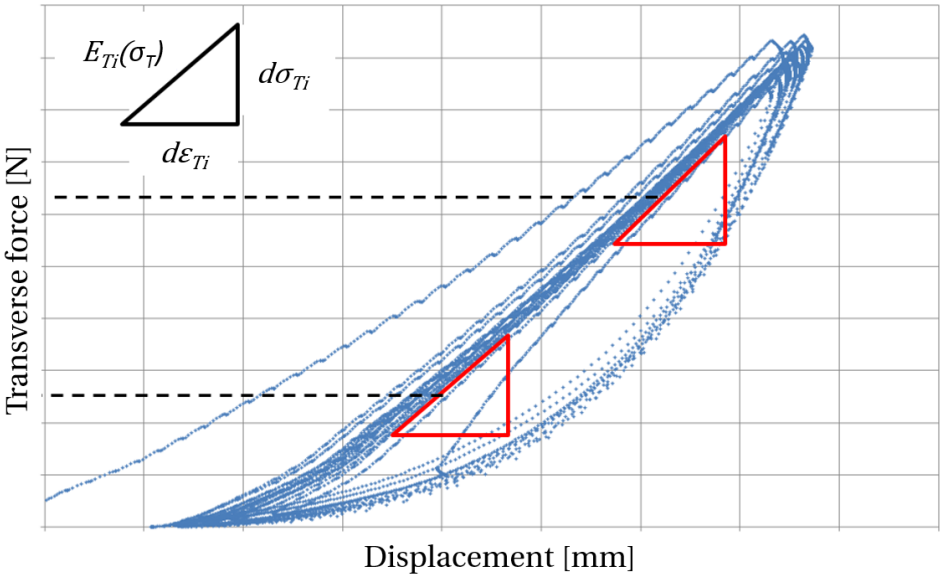

Figure 4.46: Example of force/displacement curve and rope modulus

The measured forces and displacements were transferred to transverse stress, σ_T, and strain, ε_T, by Eqs. 4.8 and 4.7. With reference to Fig. 4.41, the piston length is L, rope tension is T and the compressive force is F_T. The rope width is defined by the length s of the square replacement cross-section (Eq. 3.40) and the measured piston stroke during compression $\Delta d = d - d_1$.

$$k_T = \frac{\sigma_T}{\sigma_L} = \frac{2\sqrt{A_r}}{D} \quad (4.6) \qquad \varepsilon_T = \frac{(d - d_1)}{s} \quad (4.7) \qquad \sigma_T = \frac{F_T}{sL} \quad (4.8)$$

The effective rope cross-section of the steel wire was calculated by using the fill-factor f (ratio of actual effective cross-sectional area, A_r, relative to the nominal area) specified by the manufacturer, Eq. 4.9. For the fibre ropes, fill factors f_{HPSFR} were calculated by using the rope mass, M_{rope}, rope length, L_{rope}, and fibre densities, ρ_{fibre1} and ρ_{fibre2}, in combination with proportions of fibre types, x_{fibre} and y_{fibre}, Eq. 4.10.

$$A_r = f\frac{\pi d^2}{4} \quad (4.9)$$

$$f_{(\text{HPSFR})} = \frac{M_{\text{rope}}}{L_{\text{rope}}}\left(\frac{x_{\text{fibre1}}}{\rho_{\text{fibre1}}} + \frac{y_{\text{fibre2}}}{\rho_{\text{fibre2}}}\right), x_{\text{fibre1}} + y_{\text{fibre2}} = 1 \quad (4.10)$$

The effects of additional compaction and diameter reduction of the ropes due to tension forces were ignored, and the calculated effective cross-sectional areas are given in Table 4.4.

Table 4.4: Effective rope cross-sectional area

Rope type	Size [mm]	A_r [mm^2]	f	Note
Steel wire	Ø20	204	0.65	
DimStable	Ø12	70	0.62	Excl. jacket & core
DimStable	Ø20	195	0.62	Excl. jacket & core
Braided-A	Ø20	251*	0.75*	
Braided-B	Ø20	224	0.72	
Braided-C	Ø12	103	0.91	
Braided-C	Ø16	149	0.74	
Braided-C	Ø20	215	0.69	
Braided-D	Ø20	176*	0.53*	Excluding core

*Estimated due to unknown fibre composition and ratios

By means of regression analysis, each stress-strain curve was described by polynomial equations. The lowest possible grade of polynomials was preferred to avoid overfitting. Therefore, due to the non-linear characteristics, the stress-strain curves were split into sections according to ranges of k_T relevant for the two test drums. This resulted in a good fit with 2^{nd} order polynomials, Eq. 4.11. The different moduli were calculated by deriving the polynomial stress-strain equations, Eq. 4.12.

$$\sigma_T\left(\varepsilon_T\right) = A\varepsilon_T^2 + B\varepsilon_T + C \tag{4.11}$$

$$E_T = \frac{d\sigma_T}{d\varepsilon_T} = 2A\varepsilon_T + B \tag{4.12}$$

Result tables were generated for each rope and for each test with a different number of ropes in stacks. Transverse moduli were computed for every combination of rope tension and compression force.

Examples of transverse elastic moduli for D400 and D500 (Ø20 mm Braided-C rope) are shown in Fig. 4.47.

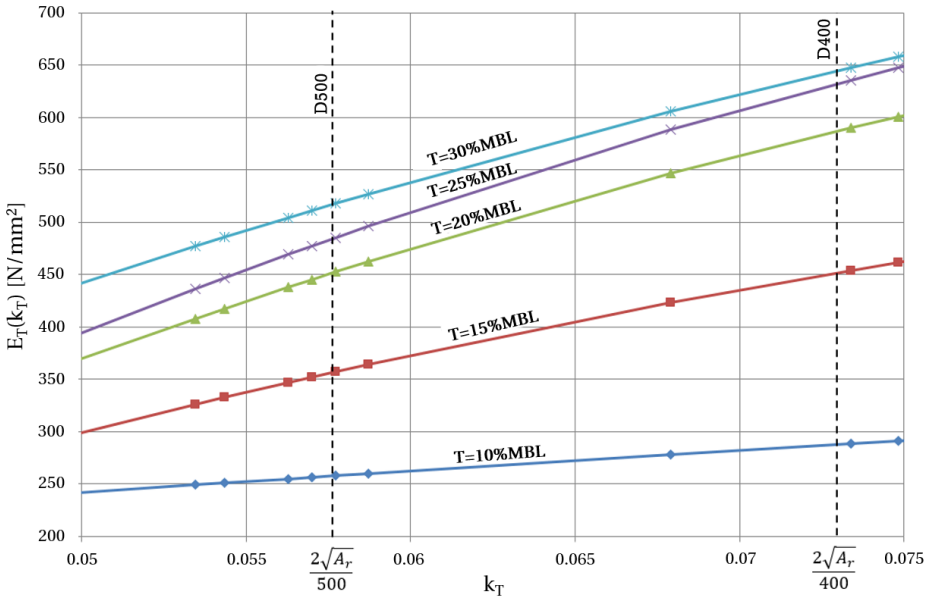

Figure 4.47: Example of transverse moduli for Ø20 mm Braided-C

Multilayer exponents

The moduli from tests with HPSFRs in linear stacked configurations were used to calculate multilayer exponents for the different ropes. The linear stacked configuration can be considered as a series of stacked springs, or more precisely, springs and dampers for HPSFRs. Such an arrangement reflects the rope condition during climbing- and crossing-sectors on the drum, Fig. 4.48.

A linear relationship between the compression of the stacked ropes was assumed, and an average modulus was calculated by dividing the modulus from multiple ropes by the number of stacked ropes. The multilayer exponent, η, was determined for each rope by fitting a power function to the ratios between multi-rope and single rope modulus, Eq. 4.13.

In theory, a stack of ideal linear springs should give an exponent of $\eta = -1$. In contrast, $\eta > -1$ indicates a stiffening rope package, and $\eta < -1$ indicates a softening rope package. In reality, the ideal conditions are disturbed by effects like, e.g. friction.

$$R_T(i) = \frac{E_T(i)}{iE_T(1)} \approx i^{\eta} \tag{4.13}$$

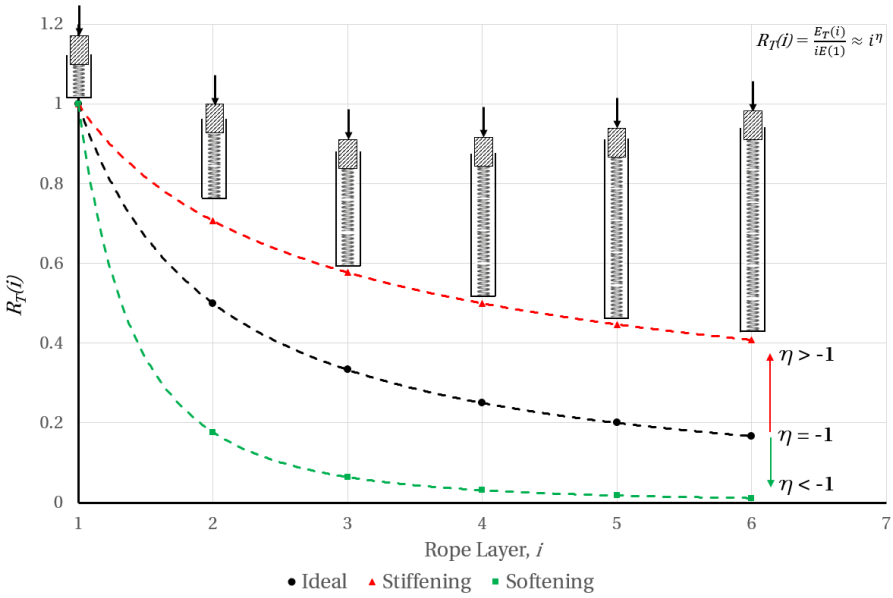

Figure 4.48: Example of multilayer exponents

Direct stiffness test (C4-c)

There are compromises and simplifications related to the transverse stiffness test with ropes in a linearly stacked configuration. Lohrengel et al. [9] found an indication of significant differences of stiffness with three layers of HPSFRs in pyramid configuration relative to linear configuration. However, there were no practical possibilities for testing ropes in pyramid configuration in the test facility. Therefore, a few experiments were carried out by compressing the rope directly onto the drum.

With a few additional components, the compression test device was converted to a hydraulic jack, equipped with force and displacement measurements. The jack was placed below the drum with the piston perpendicular to the drum axis.

The rope was spooled onto the drum at a specified tension, one layer at a time. Several cycles of compression were applied to the rope for each layer while force F_T and compression of rope Δy_1 were measured. Two displacement transducers (HBM WA50), measuring at the upper point of each flange, were used to compensate for the vertical displacement (Δy_2 and Δy_3) of the drum itself.

Figures 4.49 and 4.50 show the experimental setup of the direct transverse stiffness testing.

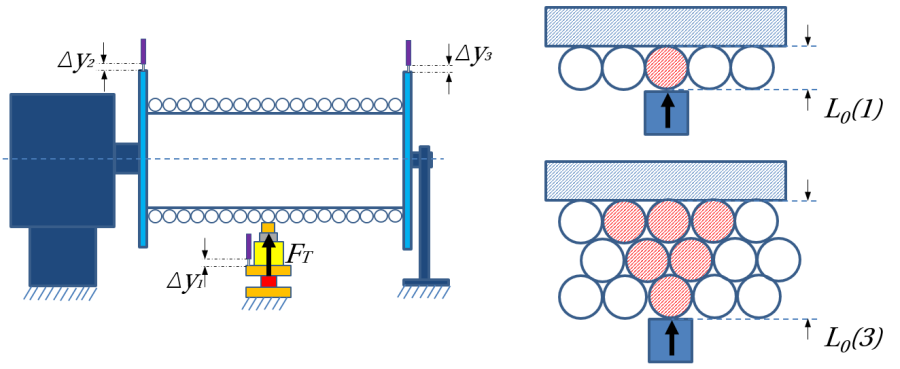

Figure 4.49: Principle of direct transverse stiffness test

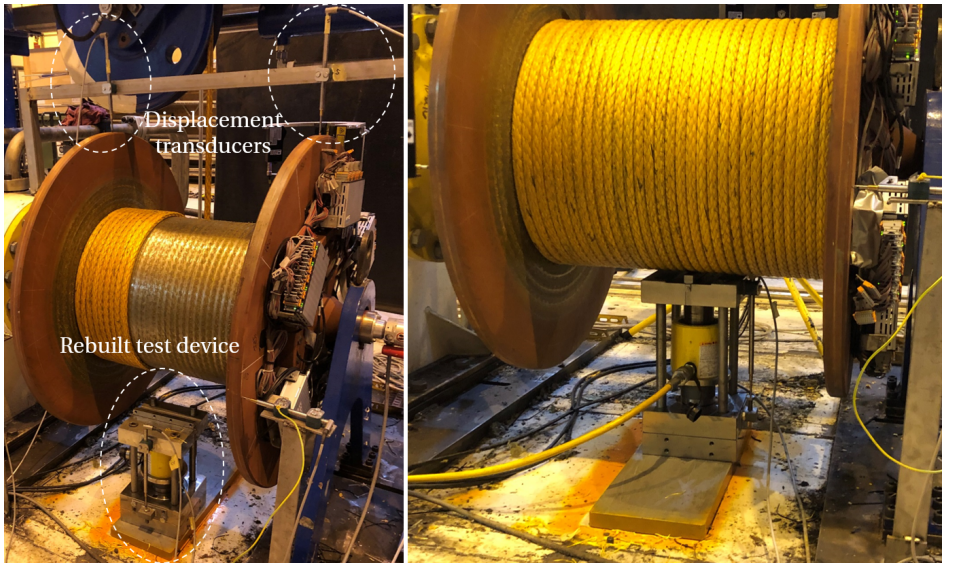

Figure 4.50: Example of direct test (C4-c)

As the contact area between the piston and rope was unknown, stresses were not calculated. The stiffness was determined by force-elongation curves instead, Fig. 4.51, and calculated for each layer by Eq. 4.14 for two ranges of compressive force (20-40 kN and 60-80 kN).

Due to the unknown stress and the layer dependent volume of rope subjected to compression (caused by the curvature of the drum and rope layers), the calculated values are only valid for relative comparison between tests with the same method. They cannot be compared with the values determined by linearly stacked ropes.

$$E^*_{a-b}(n) = \frac{F_T L_0(n)}{\Delta y_1 - \left(\frac{\Delta y_2 + \Delta y_3}{2}\right)} \tag{4.14}$$

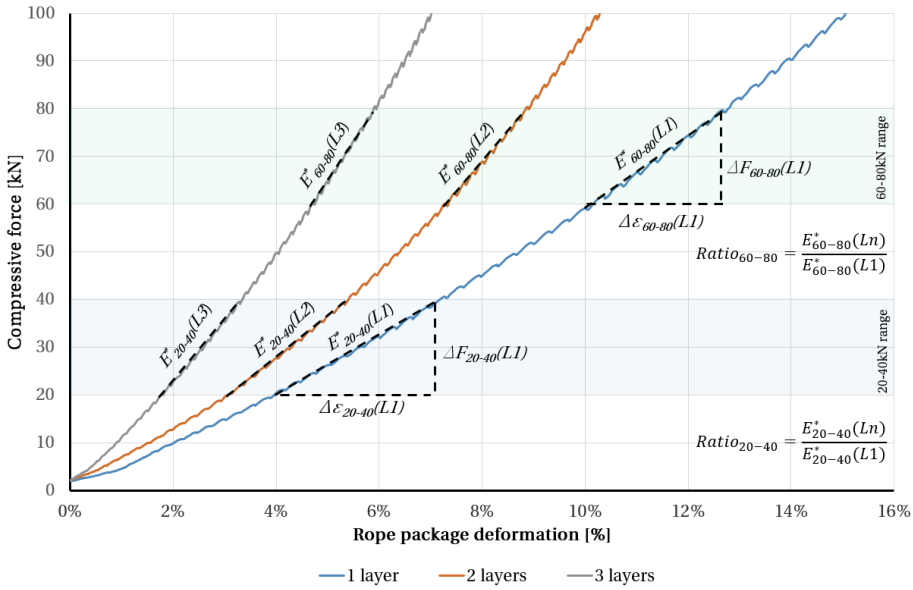

Figure 4.51: Calculation principle for rope package stiffness - direct on drum test

Longitudinal (axial) modulus of elasticity (C5)

The longitudinal moduli were determined through estimates from available data using the method specified in ISO 12076 [35]. For a few ropes, specific tests were carried out in cooperation with the rope manufacturer.

ISO 12076 determines the rope modulus using elongations at forces equivalent to 10% and 30% of minimum breaking force. If specified, other force ranges are allowed. The rope condition must also be stated and are initial (E_{i}), partly bedded ($E_{\mathrm{p\text{-}b}}$) or fully bedded (E_{f}).

Equation 4.15 calculates the longitudinal modulus from tensions $T_{30\%}$ and $T_{10\%}$, corresponding elongations $x_{30\%}$ and $x_{10\%}$, gauge length l_i and the calculated effective cross-sectional area of the rope A_r.

The standard also allows for using the rope's nominal cross-sectional area. However, this results in a significantly lower modulus, and it is essential to specify how the modulus is calculated.

$$E_{10-30} = \frac{\Delta T}{\Delta L} L_0 = l_i \frac{T_{30\%} - T_{10\%}}{A_r(x_{30\%} - x_{10\%})} \tag{4.15}$$

The longitudinal moduli are strictly not constant but vary non-linearly with rope tension. This non-linearity could be considered, but the differences are relatively small. When taking measurement uncertainties and statistically variations into account, constant values were considered sufficient.

The longitudinal moduli applied in this thesis were based on the effective cross-sectional area of ropes (A_r) and determined from ropes in fully bedded condition (E_f) with rope tension range 10-30% of MBL.

4.12 Uncertainties related to the experiments

The uncertainties of the presented experiments are estimated for the force measurement system in the multilayer spooling test rig, stress and laser measurements.

The applied uncertainty of stresses derived from measurements was calculated employing tests on the D400 drum. The number of repetitive experiments on this drum (repeated experiments under identical conditions with the same instrumentation) was three or, in a few cases, four. Concerning statistics, this is in the very low end of a required population. On the other hand, the number of repetitive experiments for D500 was only two, resulting in higher calculated uncertainties. However, when comparing calculated uncertainties for both drums with equal repetitive test runs (n=2), the uncertainties were comparable. Based on this, the calculated uncertainties for stresses derived from measurements calculated for D400, with higher populations, were also considered valid for D500.

Concerning relative comparison of experimental results, the significance of statistics and uncertainties were considered less important as all measurements were carried out in the same test rig and environment.

Testing of transverse moduli was conducted in two different ways. However, the number of repetitions was not sufficient for valid statistical calculations. As an approximation, the uncertainty was not considered to be less than the multilayer stress measurements.

Table 4.5 presents possible causes influencing the measurement uncertainties.

The behaviour of HPSFRs during multilayer spooling is influenced by their relatively large deformability. This can cause variations in repeated tests and consequently influence measurement accuracy of stress and rope dimensions to a rel-

Table 4.5: Possible causes of uncertainty

Influence by...	Type	Effect on...	Grade
Behaviour of rope during test	A	Stress and rope dimensions	High
Imperfections in test drums	B	Stress	Minor
Elastic material parameters	B	Stress	High
Wear of ropes and loss of lubricant	A	Strain	Medium
Order of tension level	A	Strain	Medium
Accuracy of instruments	B	Force and strain	Minor
Calibration of equipment	A/B	Force/Stress	Medium
Resolution of data	B	Strain	Minor
Environment	A	Force and stress	Minor
Characteristics of the observer	B	Force and stress	Minor
Number of repeated experiments	A	Stress	Medium
++			

atively high grade. Due to the spooling sheave being parallel to the drum, the ropes were forced to twist ninety degrees during travel from the sheave to the drum during spooling. In some cases, windings with the rope in an "upright" position were observed on the drums.

Due to machining and controlled dimensions, the influence on stresses due to imperfections in the test drums was considered minor.

The influence of elastic modulus can be relatively high on stresses derived from strain gauge measurements. The moduli of the materials should have been determined by high-precision measurements applying eigenfrequency or ultrasonic methodology to reduce uncertainty. However, as such experiments were not conducted, the specific elastic moduli were unknown, and a 4.5% variation, as stated by HBM [36] was applied. With a 95% confidence interval, the moduli were considered to be in the range of 191-209 GPa. This makes the applied modulus of 200 GPa reasonable.

During testing, ropes were subjected to wear, and coatings were in some cases liquefied and squeezed out of the ropes. The related influence from this on measurements was considered medium.

The order of tension level was considered to influence the statistical variation of the strain measurements to some degree. In repetitive tests with the same rope tension, the peak stresses tended to increase between test runs before stabilizing. Tests with high rope tensions, followed by tests with lower rope tensions, resulted in higher stresses than test runs with reversed order of loading. This was due to the rope's load-dependent compaction and "memory effect" retaining the deformation caused by the highest load.

The instruments applied in the experiments were of high quality, calibrated and verified by the manufacturer before the start of the experiments. Therefore, the influence on force and strain measurements were considered minor.

Calibration of strain gauges is impossible, but the quality and measurement accuracy depends on the installation and equipment. The measurements were not dependent on the zero-point, but the change in measured strain during each test run. The zero-point drift was verified low and not considered to influence the measurements to any level of significance.

The uncertainty of the measured strains was considered to be within $\pm 3\%$ by the HBM experts who mounted and verified the strain gauges and setup of related equipment. This is a conservative estimate for non-zero point related measurement, considering the following:

- Curvature of measurement surface
- Elastic after-effects (delay in strain increase due to mechanical loading)
- Installation effects as misalignment of strain gauges
- Creep and hysteresis of the strain gauges
- Uncertainty of the gauge factor
- Measuring grid length
- Linearity deviations

The spooling rig force measurement was subjected to specific calibration before the start of the test program. In addition, the calibration was verified during the program. This is elaborated in Section 4.12.1.

The 10 Hz strain measurement frequency was considered sufficient, and the effect of data resolution on accuracy minor. Some uncertainty was related to the laser measurements as the resolution depended on the distance between sensor and target.

The experiments were carried out indoor, in a controlled environment with stable temperature. In addition, the strain measurements were temperature compensated and the overall influence from the environment considered to be minor.

The characteristics of the observer were also considered minor. This was based on the experience of the test personnel and well-known test procedures. Data treatment and analysis followed specific and consistent procedures.

4.12.1 Uncertainty of the tension measurement system

The force measurement system in the spooling rig was based on a shear-pin load cell in the centre of the spooling sheave. It was calibrated against a high accuracy load cell to ensure accuracy. The load cell was spliced to a rope and located between the test rig's tension control side and speed and measurement side. Average values from several measurements were used to adjust the test rig control system and measurements.

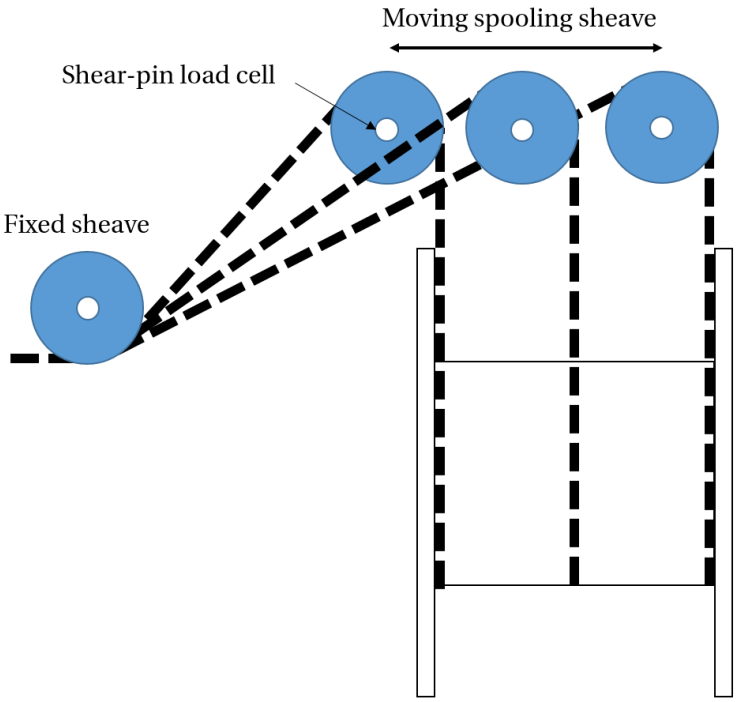

Figure 4.52: Moving spooling sheave with shear-pin load cell

The force measurements were influenced by the spooling sheave motion altering the engagement angle of the measured force, Fig. 4.52. Related uncertainties were estimated from repeated calibration experiments (type A) and the accuracy of the shear-pin load cells (type B). The statistics were based on an adapted principle from ASTM E 74-04 [37] where the standard uncertainty u_{T} was determined by the differences d_{j} between the multilayer winch load cell and the linear equation of the calibration load cell (m=1), Eq. 4.16. Totally 508 individual measurement values n from five repeated measurements for each of three spooling sheave positions (inner, outer and middle) were used.

$$u_T = \sqrt{\frac{\sum d_j^2}{n-m-1}} \tag{4.16}$$

$$U_T = K\sqrt{u_T^2 + \left(\frac{U_{Cal}}{2}\right)^2 + \left(\frac{U_{Pin}}{2}\right)^2} \tag{4.17}$$

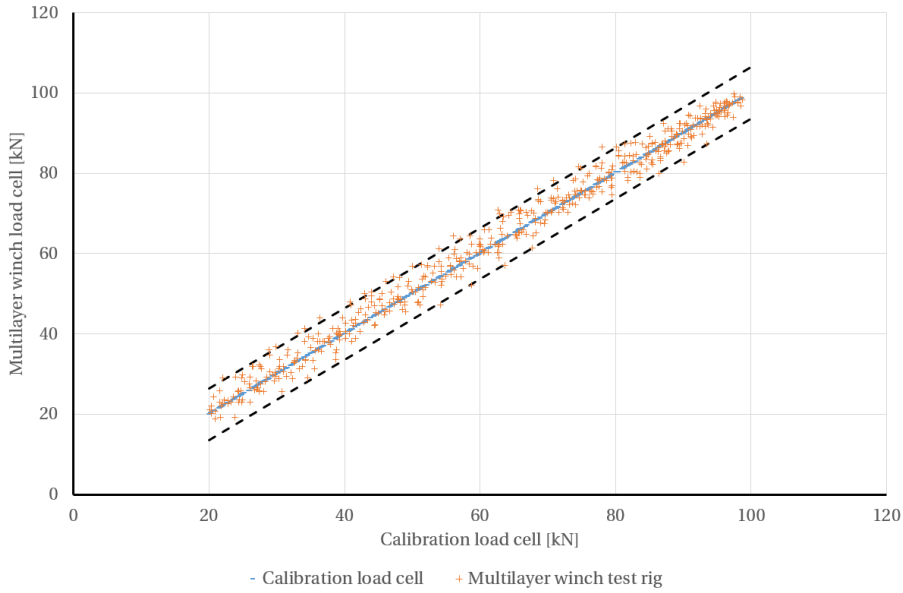

Figure 4.53: Winch test rig force values vs. calibration load cell

The type B uncertainties of the calibration U_{Cal} and multilayer winch U_{Pin} load cells were $\pm 0.02\%$ and $\pm 1\%$ of their respective full scales (147 kN and 245 kN). The expanded uncertainty of the tension measurement system U_{T} with K=2 (95% confidence interval) was estimated to 6.4 kN by Eq. 4.17 (2.6% of the full load cell range). Figure 4.53 shows the measured values with the expanded uncertainty limits. This uncertainty was relatively high for lower rope tensions but reasonable for tensions above 50-60 kN.

4.12.2 Uncertainty of the stress measurements

The stress measurement uncertainty U_{S} was estimated by statistical variations of tangential stress in the drum with different ropes and tensions (type A). Uncertainties of 3% (U_{Strain}) and 4.5% (U_{Modulus}) related to the strain measurement and elastic modulus (type B), respectively, were applied. The standard uncertainties

of the mean values for each experiment (68.3% confidence level) were calculated employing the t-distribution. The expanded uncertainties for each layer, with 95% confidence level ($K = 2$), were calculated by Eq. 4.18.

$$U_S = K\sqrt{u^2_{\text{Statistics}} + \left(\frac{U_{\text{Strain}}}{2}\right)^2 + \left(\frac{U_{\text{Modulus}}}{2}\right)^2} \tag{4.18}$$

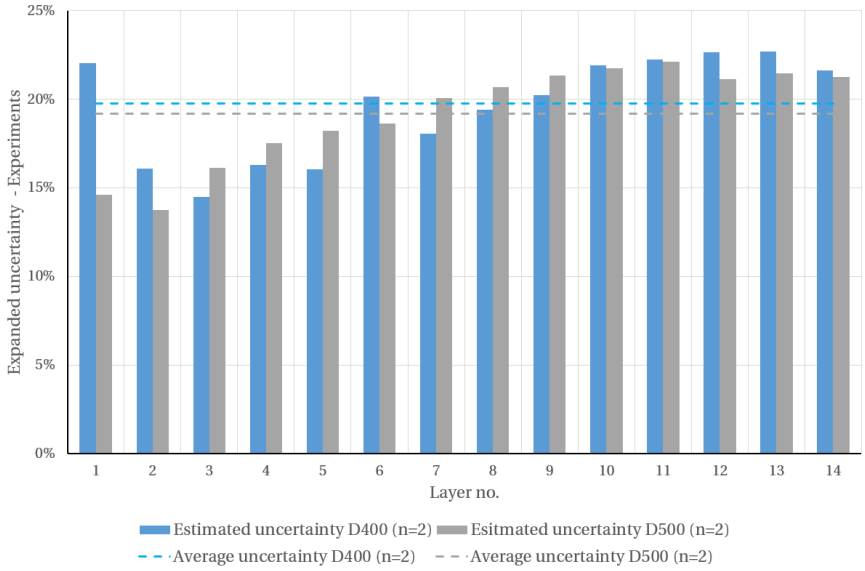

Figure 4.54: Comparison of expanded uncertainties on D400 and D500 (n=2)

Figure 4.54 shows uncertainties for each layer calculated for D400 and D500 with two repetitive test runs, while Fig. 4.55 shows values for D400 with three repetitive test runs. The higher uncertainty of the first layer was related to dead wraps and ramping of rope tension. This is most significant for D400 due to the shorter drum and smaller diameter.

The number of layers for experiments with Ø20 mm ropes was fewer than for the smaller ropes. Consequently, more data was available for less than 10-11 layers. This is reflected in uncertainties and indicate decreasing uncertainty with an increasing number of experiments.

The overall expanded uncertainty of the derived stresses was estimated to 10.2% from the average uncertainty of all layers. The corresponding uncertainty of the strain measurements was estimated to be 7.1%. With more precise measurements of the actual elastic moduli for the steel materials, e.g. by applying ultrasonic

testing, the uncertainty of derived stresses could be reduced to a value close to this.

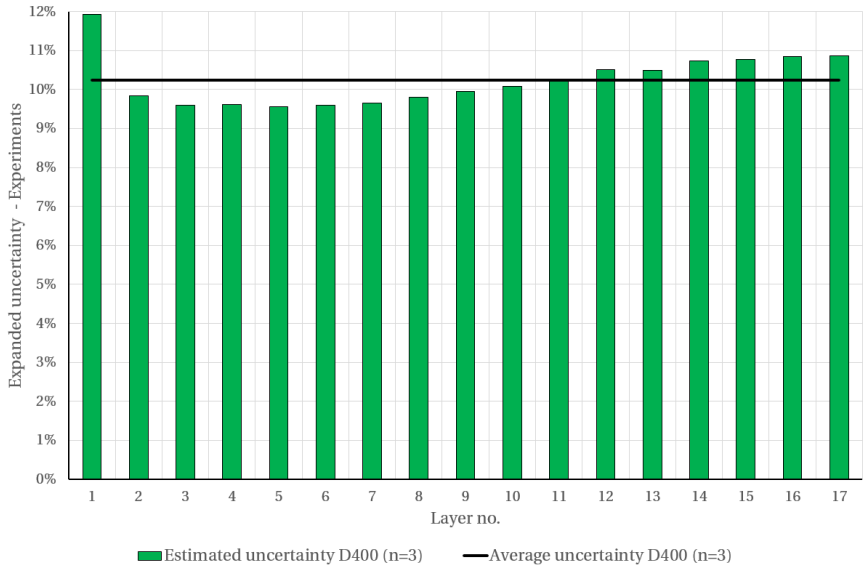

Figure 4.55: Estimated expanded uncertainty for stress measurements on D400

4.12.3 Uncertainty of the lasers

The uncertainties related to the rope dimensions and layer radii measurements were estimated based on the manufacturer data for the sensors (type B). As the laser resolution varies within the measuring range, the uncertainty is dependent on the distance from the sensor and the target. Thus, both extremes were estimated.

Table 4.6: Estimated expanded ($K = 2$) laser uncertainties

Sensor	x-Direction, U_x min/max [mm]	z-Direction, U_z min/max [mm]
2130	0.05/0.09	0.016/0.018
2380	0.22/0.64	0.64/0.7

Table 4.6 gives the estimated uncertainties for the Gocator 2130 and 2380 sensors in x- and z-directions. The values in z-direction were based on the combined uncertainty of linearity, repeatability and resolution. Values for the x-direction was based on resolution only. It was assumed that the true value had an equal probability of being located between two resolution points. Uniform probability distribution with limits equal to half the resolution was applied.

Chapter 5

Experimental test results

This chapter holds experimental test results. First, properties characterizing the different ropes (elasticity, friction and deformability) are presented. These are followed by rope deformation and stresses in drums and flanges due to multilayer spooling. Further, the stresses in drums due to low tension in initial layers ("protective layers") and the development of stresses in the rope package over time are investigated.

5.1 Rope characteristics (C)

5.1.1 Longitudinal rope modulus (C5)

The longitudinal moduli for the different rope types are listed in table 5.1. The values are determined according to ISO 10276 [35], based on ropes in fully bedded condition, rope tension range 10-30% of MBL and effective cross-sectional area.

Table 5.1: Longitudinal rope modulus

Rope type	$E_{L(10-30)}$ [N/mm^2]	Method (ISO 12076)
Steel wire	107000	Estimated from manufacturer data
DimStable	63000	Estimated from manufacturer data
Braided-A	47000	Estimated from manufacturer data
Braided-B	64000	Tested and calculated
Braided-C	55000	Tested and calculated
Braided-D	36000	Estimated from manufacturer data

5.1.2 Transverse modulus of elasticity (C4)

Figures 5.1 and 5.2 show transverse moduli for the different Ø20 mm ropes. The values are based on measurements with curved counterparts and determined for the D400 and D500 drums without considering friction (Eq. 3.95). The measurements were carried out in the cylinder test arrangement (CylRig, C4-b), except for the steel wire, which was only tested in the spooling test rig (SpolRig, C4-a). This was related to challenges with the fastening of the steel wire and safety issues. However, the two different test arrangements give rather similar results with a noticeable increase in transverse stiffness with increasing rope tension.

The steel wire is significantly stiffer than the HPSFRs. For the two drums, D400 and D500, the transverse moduli are in the range of 743-1727 N/mm^2 for rope tensions between 10-30% of MBL. The corresponding transverse moduli of the braided ropes are in the range of 177-691 N/mm^2. Despite the shape-controlling core, the stiffness of Braided-D is noticeably lower than the pure braided ropes, whose differences are relatively small. The DimStable moduli are in the range of 507-966 N/mm^2 and are between the steel wire and the other HPSFRs.

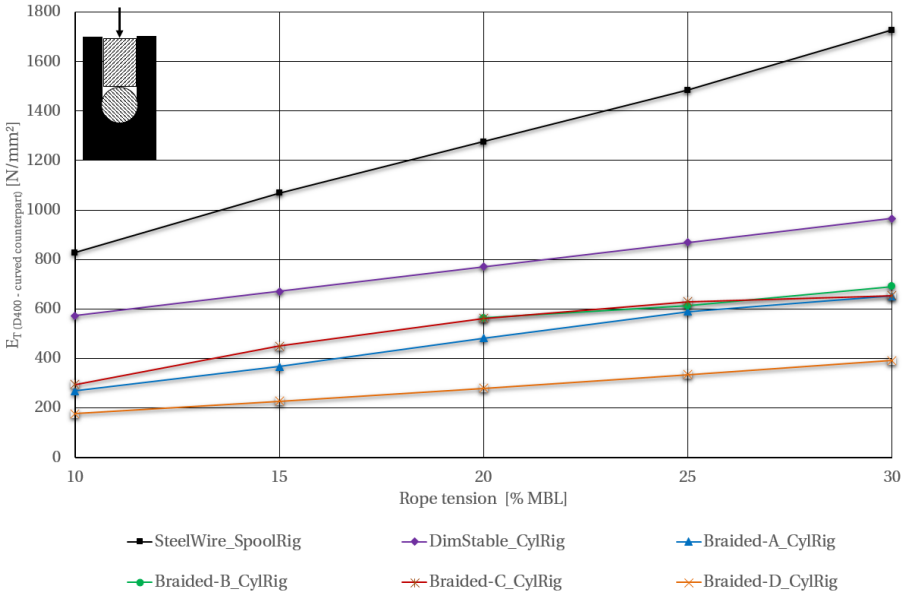

Figure 5.1: Transverse modulus, curved counterpart, Ø20 mm ropes, D400

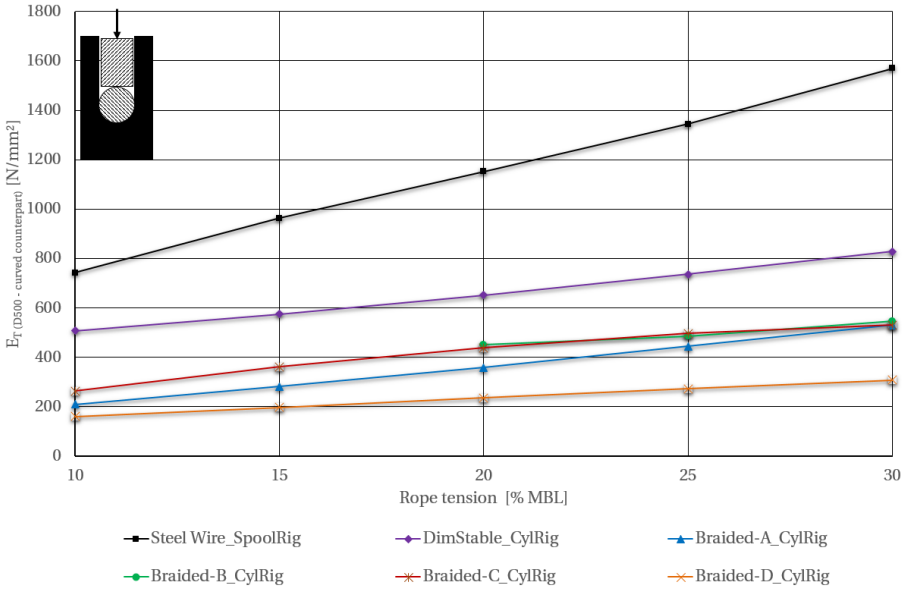

Figure 5.2: Transverse modulus, curved counterpart, Ø20 mm ropes, D500

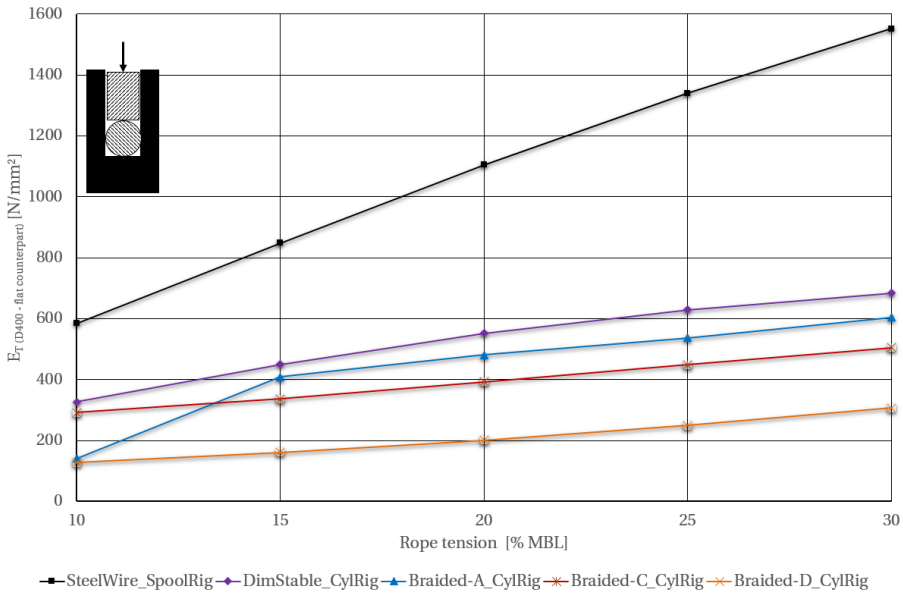

Figure 5.3: Transverse modulus, flat counterpart, Ø20 mm ropes, D400

Testing with a flat counterpart results in lower moduli, as shown in Fig. 5.3 for the D400 drum. This corresponds with findings by Dietz related to steel wire ropes [7] and is caused by less constraint of the ropes and thus more freedom to deform during compression. With reduced constraint (flat counterpart), the respective moduli for DimStable and the steel wire reduce to ranges between 256-684 N/mm^2 and 558-1551 N/mm^2, while ranges for Braided-A, -C and -D reduce to 112-605 N/mm^2, 247-505 N/mm^2 and 121-307 N/mm^2. The differences in rope stiffness related to the two drums can be approximated as a vertical shift of the curves. Due to lower D/d-ratio, the values for D400 are higher.

Transverse moduli for different sizes of the same rope are shown in Figs. 5.4 and 5.5. The stiffness of the Ø12 mm DimStable rope is lower than the Ø20 mm, in the range of 257-639 N/mm^2, with rope tension between 10-40% of MBL. The Ø16 mm and Ø20 mm Braided-C ropes yield very similar transverse moduli. For the Ø12 mm rope, the modulus is lower. The relative differences in transverse stiffness for Ø20 mm and Ø12 mm rope sizes are smaller for Braided-C than for DimStable.

Additional result plots, including results from the spooling rig experiments, are enclosed in Appendix C.

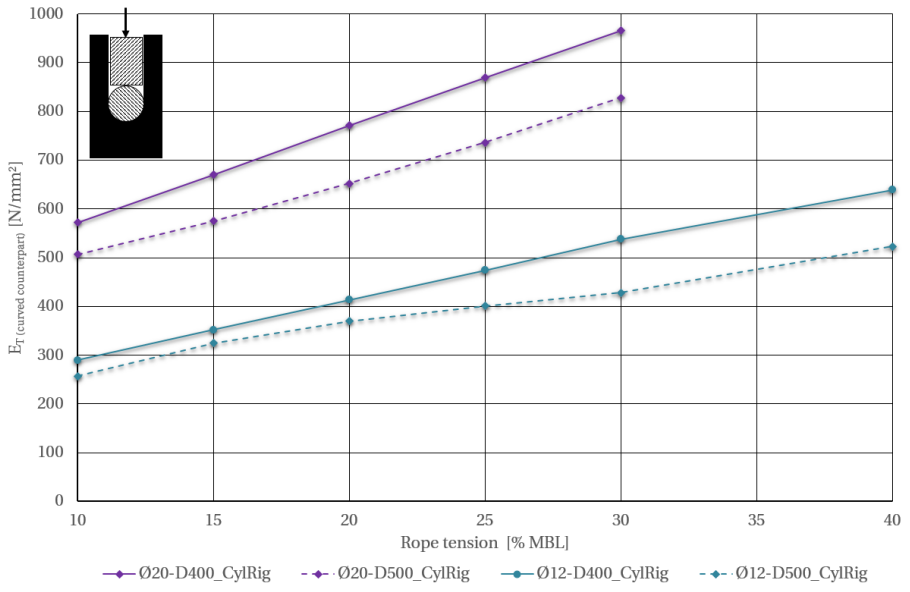

Figure 5.4: Transverse modulus, curved counterpart, Ø12 and Ø20 mm DimStable

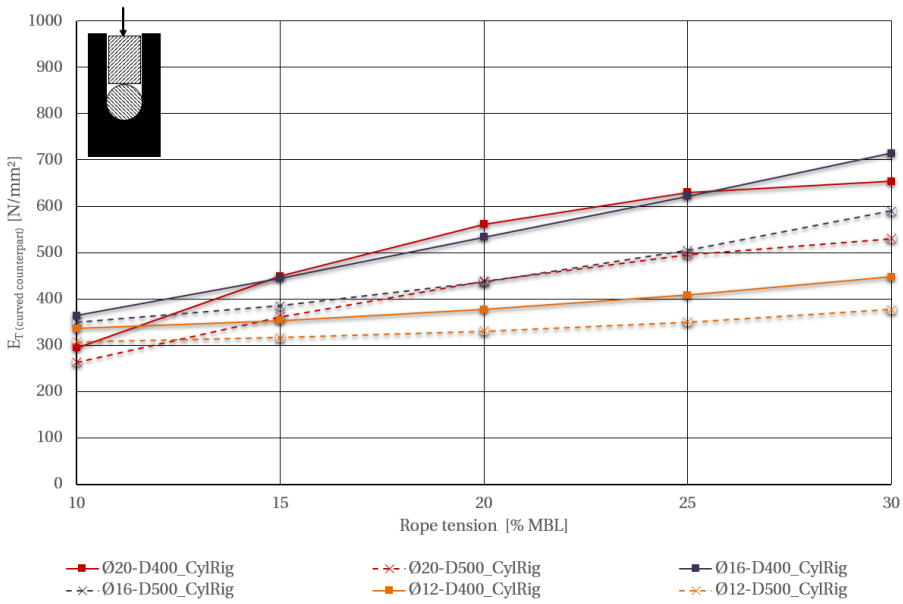

Figure 5.5: Transverse modulus, curved counterpart, Ø12, Ø16 and Ø20 mm Braided-C

Multilayer exponents (C4-b)

Concerning multilayer spooling, the accumulated transverse stiffness of multiple rope layers (rope package) is of significant interest. Figure 5.6 shows examples of ratios between the transverse moduli of up to six and eight ropes relative to a single rope. The values are based on measurements of ropes in a linearly stacked configuration (C4-b) and different rope tension levels.

The exponents from power-law curves fitted to the data for both flat and curved counterparts are listed in Table 5.2. These values generally represent the ropes as the differences in multilayer exponents for different tension levels were very small.

For the Ø20 mm DimStable rope, the values for curved counterparts and D400 indicate a softening rope package with an increasing number of layers. In general, the values for Ø20 mm Braided-A, -B and -D are not far from -1. This is the value for compression of ideal linear springs in series resulting in a constant rope package stiffness with an increasing number of layers. The Ø20 mm Braided-C indicates the most aggressive increase in accumulated stiffness among the ropes of the same size.

The values for the smaller Ø12 mm DimStable ropes are different from the Ø20 mm and indicate an increasing rope package stiffness with decreasing rope size.

For Braided-C, there is no clear trend related to the different rope sizes. The values from testing with flat counterparts are not significantly different. However, they indicate a slightly more aggressive increase in rope package stiffness compared to curved counterparts. The values for D500 show a similar trend as the values for D400, with indications of slightly higher accumulated stiffness for most of the ropes.

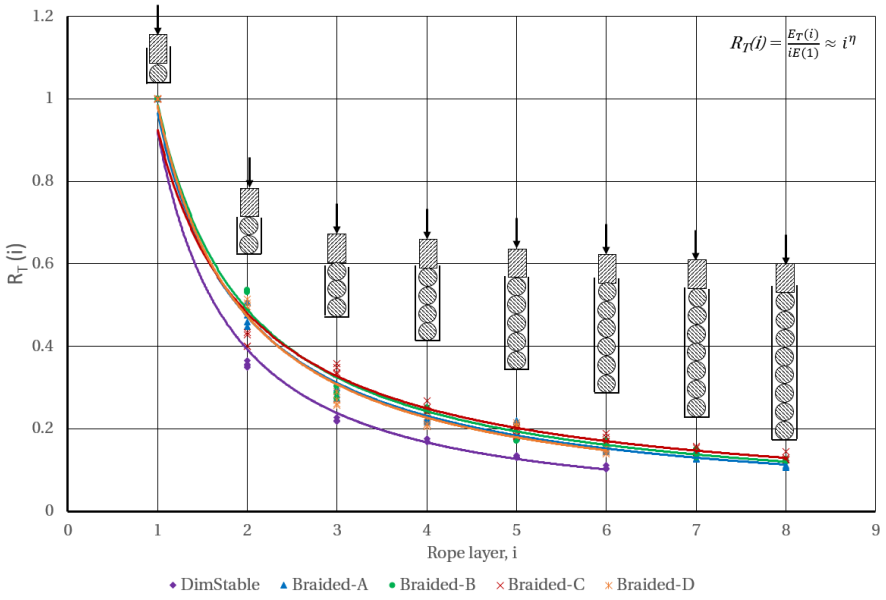

Figure 5.6: Transverse elasticity ratios - Ø20 mm ropes - D400 - curved counterpart

Table 5.2: Multilayer exponents for the HPSFRs

Rope type	D400		D500		Tension range
	Curved	Flat	Curved	Flat	% MBL
DimStable Ø20	-1.232	-1.184	-1.073	-1.008	15-30%
DimStable Ø12	-0.938	-0.880	-0.931	-0.835	15-45%
Braided-A Ø20	-1.063	-1.026	-1.033	-0.979	15-30%
Braided-B Ø20	-1.020	-0.972	-1.104	-1.070	15-30%
Braided-C Ø20	-0.945	-0.896	-0.893	-0.843	15-30%
Braided-C Ø16	-1.139	-1.081	-0.832	-0.792	15-35%
Braided-C Ø12	-0.920	-0.924	-0.967	-0.938	15-50%
Braided-D Ø20	-1.066	-0.981	-0.966	-0.873	15-30%

Rope package stiffness - direct on drum test (C4-c)

It is questionable that the test method using linearly stacked ropes reflects the actual stiffness condition of rope packages on drums. Therefore, an attempt to measure differences in stiffness directly on the drum was carried out. These experiments were carried out with D500 and applied a maximum of six layers for the steel wire and eight for Braided-B.

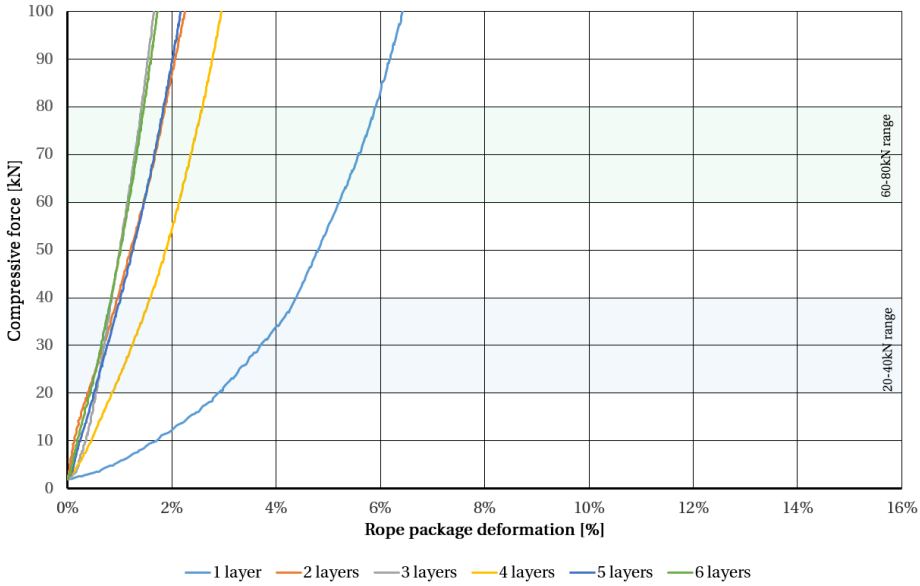

Figure 5.7: Force-deformation curves - Steel wire - direct test on D500 - 23% MBL

Figures 5.7 and 5.8 show force-compression curves for each layer. Multilayer exponents were approximated for two different ranges of compressive force, 20-40 kN and 60-80 kN, Fig. 5.9.

For the lowest force range, the measurements indicate a stiffer rope package for the steel wire than the Braided-B rope with respective exponents of -0.39 and -0.29. However, significant variations can be noticed for the steel wire measurements. With the higher force range, the situation is the opposite, and the exponents for Braided-B and the steel wire rope are -0.19 and -0.61. These numbers indicate a significantly higher degree of stiffening for Braided-B compared to the steel wire. The rope tension is the same for both ropes, but the rope strength utilization is only 20% for Braided-B while 23% for the steel wire. The differences related to the number of layers does not alter the results as the exponents for Braided-B, when limited to six layers, become -0.26 for both force ranges.

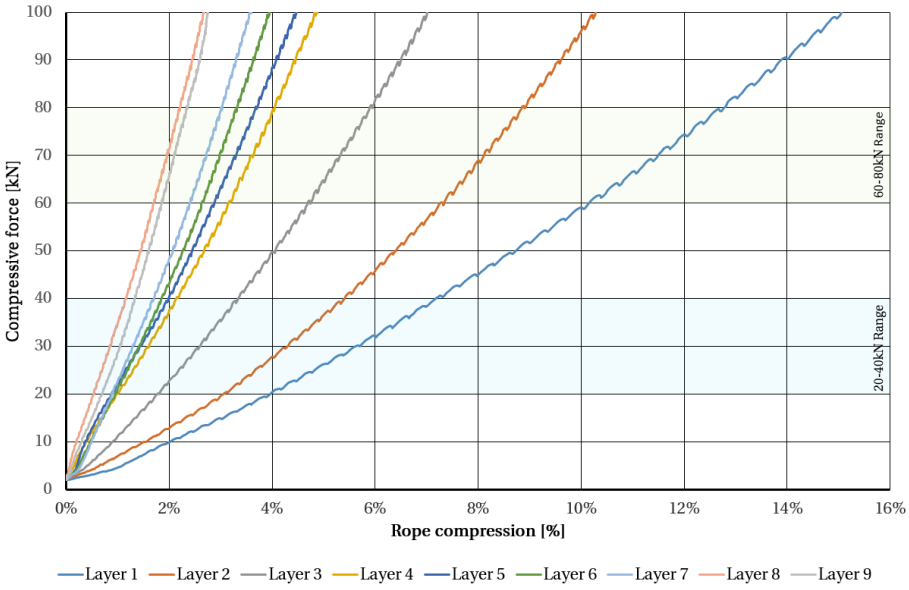

Figure 5.8: Force-deformation curves - Braided-B - direct test on D500 - 20% MBL

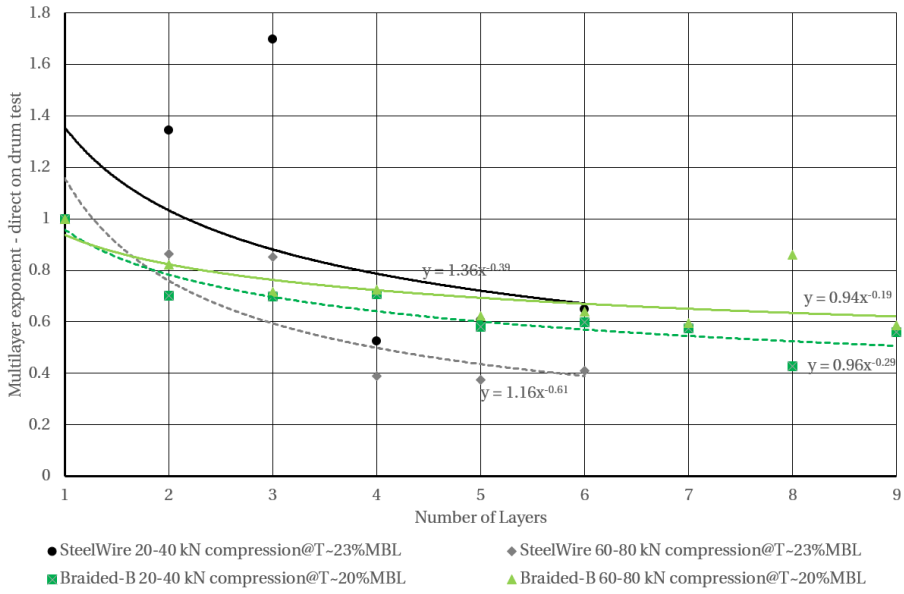

Figure 5.9: Multilayer exponents for the steel wire and Braided-B - direct on drum test

5.1.3 Rope friction (C3)

Figure 5.10 shows dry coefficients of static friction between the various ropes and a steel drum. As friction cannot be negative, curve fitting using power-law functions was applied.

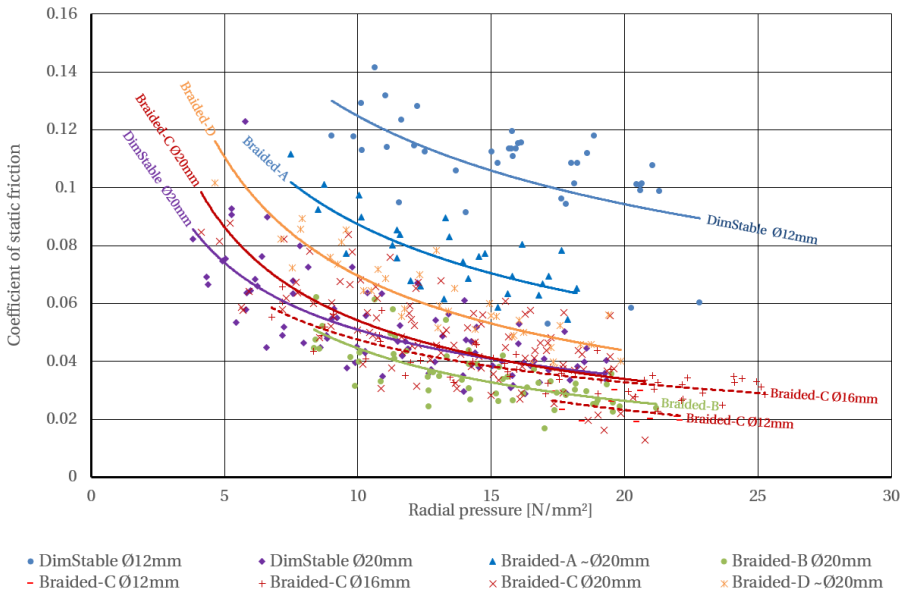

Figure 5.10: Relative comparison of dry static friction for HPSFRs

There is a clear relation between friction and contact pressure, and the coefficients decrease with increasing pressure. In contrast to the pressure independent Coulomb friction valid for the contact between metals, this is typical for friction with polymer materials.

Except for Ø12 mm DimStable, the coefficients of friction are, in general, very low for all the ropes. With contact pressures between 5-20 N/mm^2, the values are roughly in the range of 0.12-0.02. Braided-A and Braided-C are designed with a blend of fibres to increase external friction and thus improve performance on traction winch systems. This is also reflected in the measurements. Braided-A has the highest friction of all the pure braided ropes, while the friction of Braided-C is higher than the very similar Braided-B rope with pure Dyneema fibres. Braided-D also has a blend of fibres, but the manufacturer does not disclose the details. However, the measurements indicate that this rope also might have measures to increase friction. The manufacturer indicates a coefficient of friction for this rope in the range of 0.04-0.08. This corresponds well with the measurements.

While the three different sizes of Braided-C give similar values, there is a significant difference between the Ø20 mm and Ø12 mm DimStable ropes. The values for the Ø20 mm rope are very close to Braided-C and Braided-D and approximately in the range of 0.035-0.085. The coefficients measured for the Ø12 mm rope are higher with coefficients in the range of 0.09-0.13, with a somewhat higher contact pressure range. This is somewhat surprising as the Ø20 mm rope was in used condition and the smaller rope was new at the start of the test program. One could expect that wear would increase friction. On the other hand, fibre coating had been squeezed out of the Ø20 mm rope during previous tests, which could have influenced the properties. Further investigations are required on this matter.

5.1.4 Cross-sectional profiles (C2)

Compared to steel wire ropes, the layer radii and compactness of the rope package are much more influenced by the fibre ropes' lower stiffness and higher deformability. Figure 5.11 shows typical measured cross-sectional profiles for the different rope designs. The steel wire has a circular shape, and a hexagonal profile characterizes DimStable. Braided ropes A, B and C are similar with a nearly rectangular profile. Braided-D, with a shape-controlling fibre core, takes a rounded hexafoil shape.

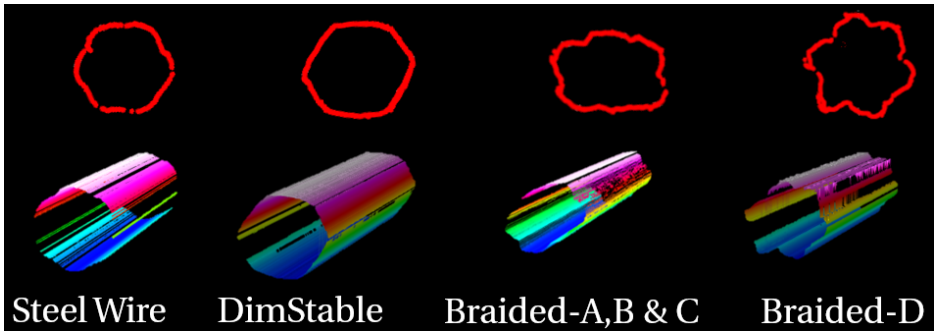

Figure 5.11: Cross-sectional profiles for different rope types

Figure 5.12 shows measurements of dimensions, d_x plotted against d_y, for the different ropes. The measurements were taken when the ropes were spooled off the drums with three different rope tension levels. The average of the plotted values and empirical standard deviations are given in Table 5.3. Transverse compression (reduced d_y) causes a natural axial expansion (increased d_x) of the rope cross-sections. There are significant dimensional differences between different rope constructions. Both sizes of the DimStable rope design exhibit limited deformations and retain dimensions relatively close to their respective nominal sizes. On the other hand, the pure braided ropes exhibit a significant compression and

reduced height compared to the nominal sizes. For the similar Ø20 mm ropes, Braided-A gives the lowest grade of deformation and Braided-C the highest. The shape-controlled Braided-D rope shows much less deformation.

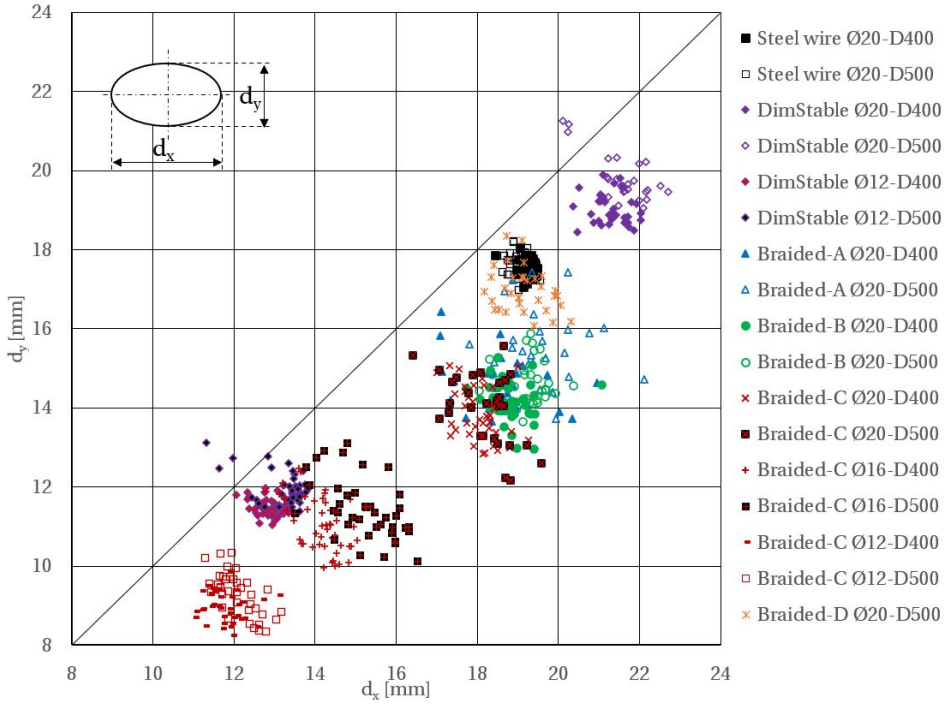

Figure 5.12: Dimensions of deformed ropes

Table 5.3: Average rope dimensions with standard deviations

Rope type	D400		D500	
	d_x [mm]	d_y [mm]	d_x [mm]	d_y [mm]
Steel wire Ø20	19.3(0.22)	17.5(0.24)	19.0(0.23)	17.7(0.320)
DimStable Ø20	21.3(0.43)	19.0(0.39)	21.6(0.65)	19.8(0.589)
DimStable Ø12	12.9(0.31)	11.5(0.21)	13.3(0.56)	12.0(0.394)
Braided-A Ø20	18.6(0.90)	14.7(0.81)	19.7(0.90)	15.6(0.89)
Braided-B Ø20	18.8(0.54)	14.2(0.51)	19.2(0.50)	14.6(0.57)
Braided-C Ø20	18.1(0.49)	13.9(0.65)	18.2(0.72)	14.0(0.89)
Braided-C Ø16	14.1(0.52)	11.0(0.67)	15.2(0.77)	11.4(0.76)
Braided-C Ø12	11.8(0.46)	9.0(0.37)	12.1(0.48)	9.3(0.54)
Braided-D Ø20	-	-	19.2(0.56)	17.0(0.55)

For the fibre ropes, there is a slight indication of reduced transverse compression and increased axial expansion with increasing D/d-ratio. In contrast, the tendency is the opposite for the steel wire. The twisted strands of the steel wire give an impression of a compressed cross-section. However, the deformability is low, and the values for d_x are most relevant for the steel wire diameter.

There is a relatively large spread in the measurements for the HPSFRs. Some of this variation is related to the flexible nature of such ropes. At the same time, other factors might also have some influence, like the smooth drums allowing relatively free expansion of the ropes in the first layer. A forced 90° twist due to the spooling sheave being parallel to the drum axis probably also cause distortions. This twist caused some rope windings to be spooled onto the drums in an "upright" position in a few cases. Further, rope tension, grade of rope wear, the presence of a splice (Braided-A) and the manual measurement evaluations carried out in the laser post-processing software might influence the results. However, the measurements are considered to reflect the general trends and relative differences between the ropes.

5.1.5 Rope deformation on drum (C1)

The rope characteristics and deformability influence layer radii during multilayer spooling.

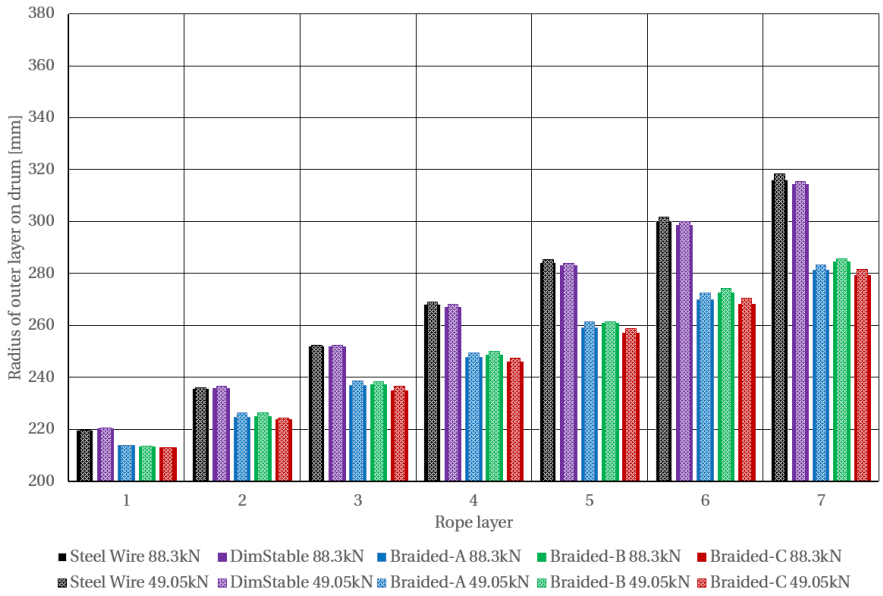

Figure 5.13: Outer layer radius, Ø20 mm ropes - D400, on-spooling

Figures 5.13 and 5.14 show comparisons of outer radii from the first to the seventh layer for the Ø20 mm ropes on both test drums. The values are averages of outer layer radii calculated from the windings located within +/-150 mm to each side of the midpoint between the flanges. The measurements were taken when ropes were spooled onto the drums and for every 10° around the circumference. The measurements are based on at least two repetitions with 49.05 kN and 88.3 kN rope tension, with a few exceptions. Tables of the plotted values with empirical standard deviations are enclosed in Appendix D, tables D.1 and D.2.

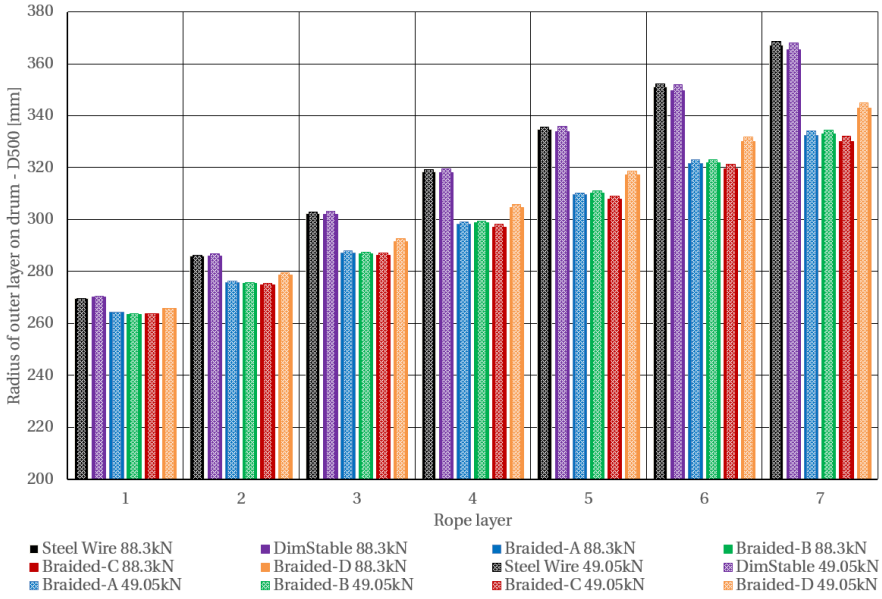

Figure 5.14: Outer layer radius, Ø20 mm ropes - D500, on-spooling

The measurements show an increase in radial compression with increasing rope tension. In general, the characteristics of the various ropes from the cross-section measurements can be recognized. The layer radii of the steel wire and DimStable are relatively similar and considerably larger than Braided-A, -B and -C ropes. The differences between these pure braided ropes are small. The radii for Braided-D are somewhat larger but considerably smaller than for the steel wire and DimStable.

Figures 5.15 and 5.16 show the average rope heights in the first layer. The measurements were taken both when the ropes were spooled onto and off the drums. The values indicate a further load-dependent compression while the ropes are on the drum for all HPSFRs and even marginally for the steel wire.

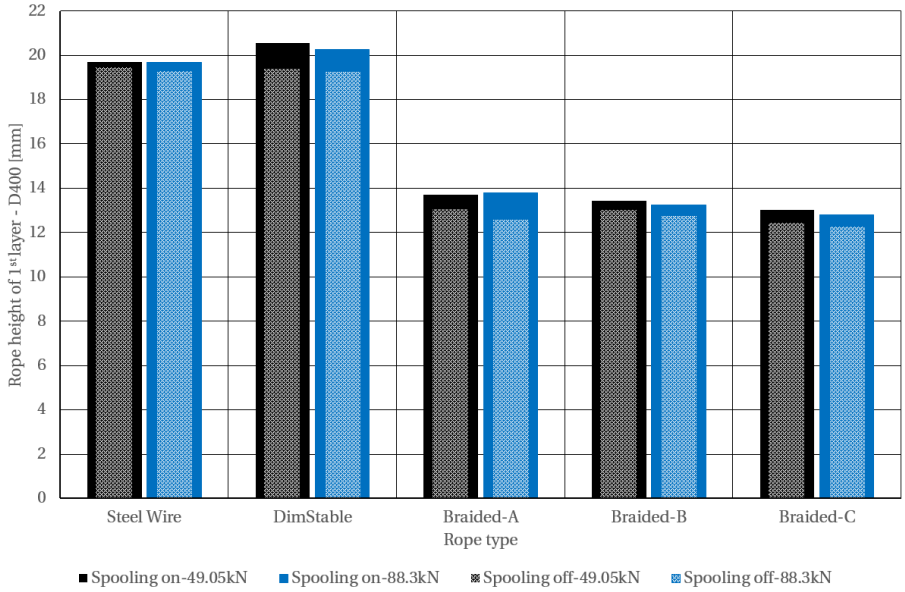

Figure 5.15: Rope height in 1st layer, Ø20 mm ropes - D400

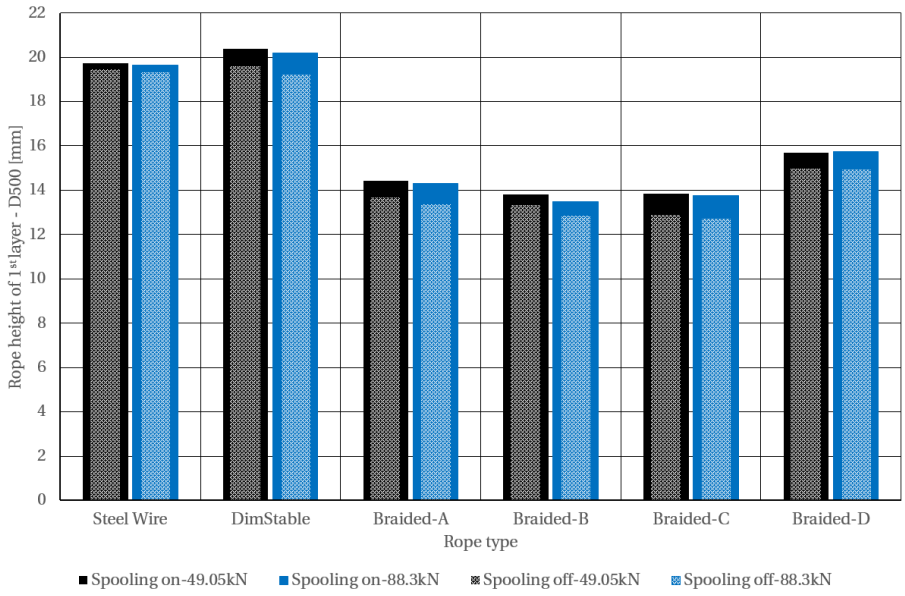

Figure 5.16: Ø20 mm rope height in 1st layer, Ø20 mm ropes - D500

As the maximum number of layers was different for the ropes, only values from the on-spooling are considered relevant for comparisons between the ropes.

Comparisons between different sizes of fibre ropes are shown in Fig. 5.17. Relative to the nominal dimensions, Ø12, Ø16 and Ø20 mm, the radial deformations in the first layer for Braided-C rope designs are 73.3%, 62.9% and 64.6% on D400 and 72.9%, 63.6% and 68.2% on D500. The lower relative radial deformation of the Ø12 mm rope compared to the larger can be related to higher fibre content.

For DimStable, the differences are small between the two sizes (Ø12 and Ø20 mm). The relative radial deformations are 99.8% and 102% on D400 and 101.9% and 101.4% on D500. Some of these values indicate that the DimStable ropes are slightly larger than the nominal diameter, but this is probably related to the measurements of the hexagonal profile.

For the Ø20 mm ropes, the effect of increased D/d-ratio is noticeable for Braided-C but insignificant for DimStable. With increased D/d-ratios (Ø12 and Ø16 mm ropes), the effect is also minor for the Braided-C rope design.

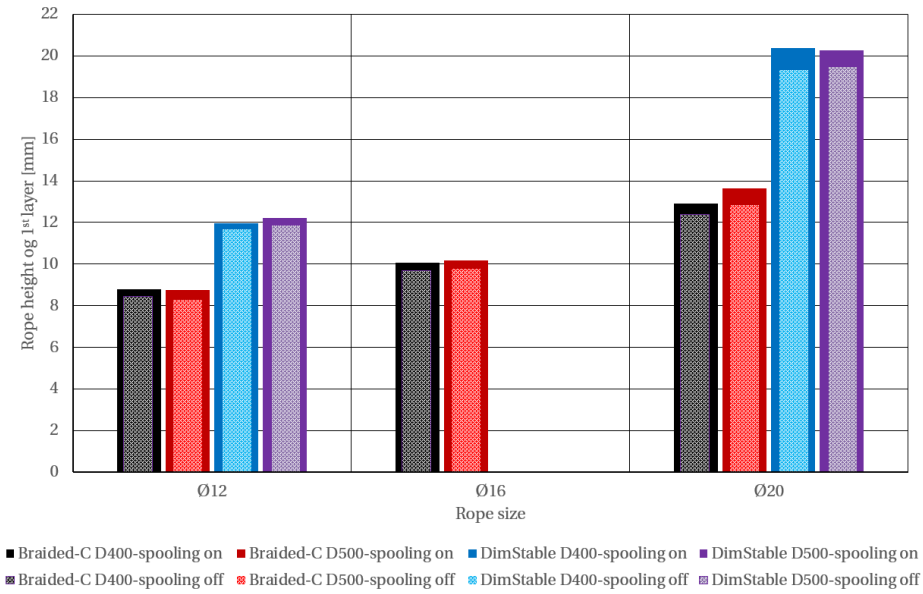

Figure 5.17: Rope height in 1st layer, size effects

5.2 Stress measurements (B)

Measurements of stresses induced by the different ropes and related effects are presented in the following. This includes stresses and circumferential stress distribution in drums, stresses in flanges and the effect of spooling speed.

5.2.1 Tangential stress in drum structures (B1)

Figures 5.18 through 5.21 show examples of measured peak tangential stresses induced by the different Ø20 mm ropes when spooled with 49.05 kN and 88.3 kN rope tensions.

In Fig. 5.18, the tangential stresses induced in D400 (D/d=20) are plotted relative to the peak tangential stress induced by the steel wire. All ropes are spooled with 49.05 kN rope tension.

The DimStable rope induces stresses very similar to the steel wire. In contrast, the pure braided ropes give higher values from 2-3 rope layers. Braided-C induces more than 1.5 times higher stress from ten layers than the steel wire, and the stress continues to increase beyond this. Braided-A and B show similar trends but with somewhat lower stresses.

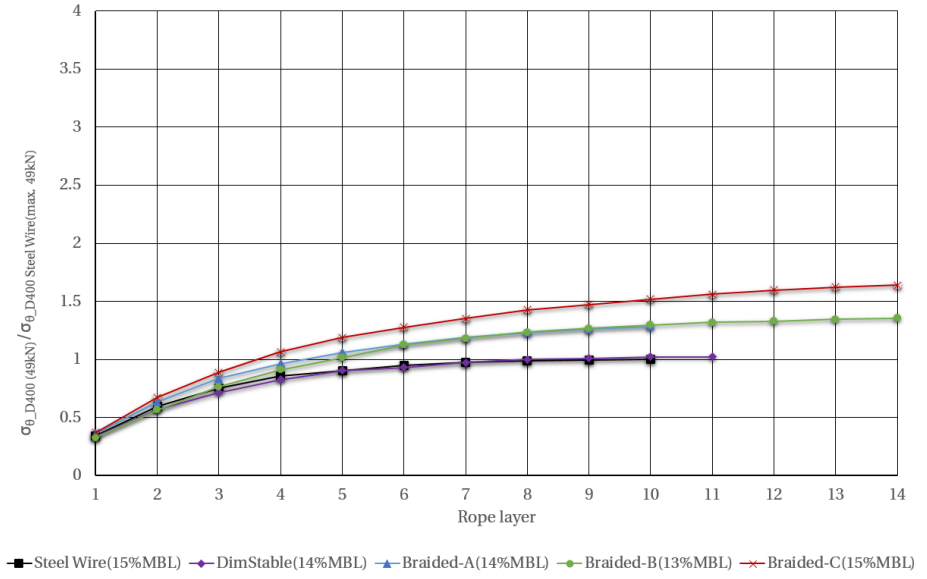

Figure 5.18: Tangential stress in D400 - 49.05 kN (5 Te) tension, Ø20 mm, (D/d=20)

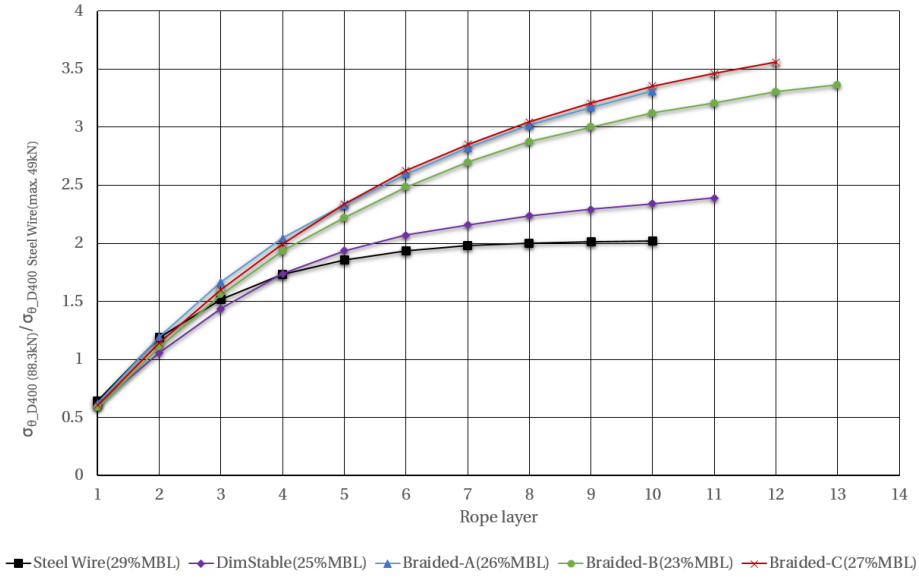

Figure 5.19: Tangential stress in D400 - 88.3 kN (9 Te) tension, Ø20 mm, (D/d=20)

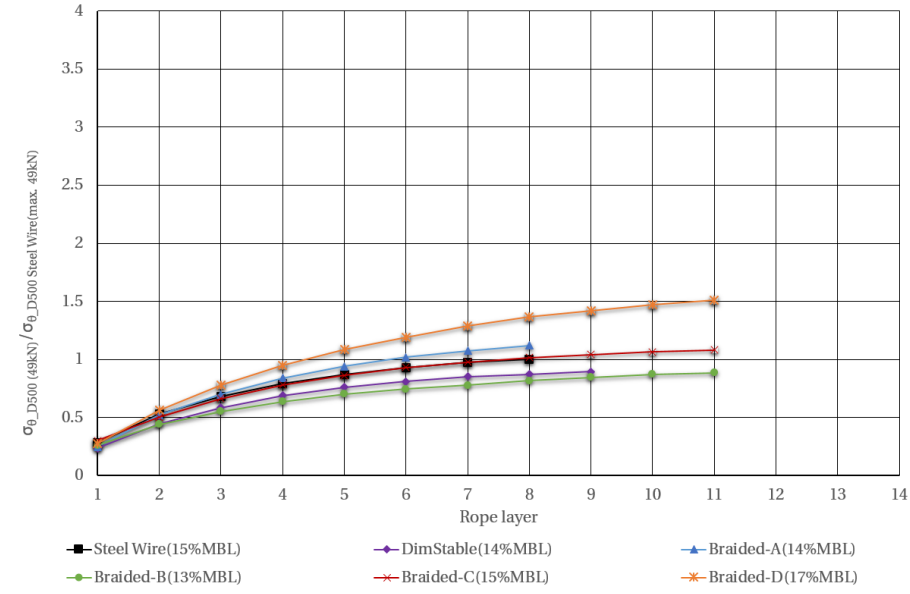

Figure 5.20: Tangential stress in D500 - 49.05 kN (5 Te) tension, Ø20 mm, (D/d=25)

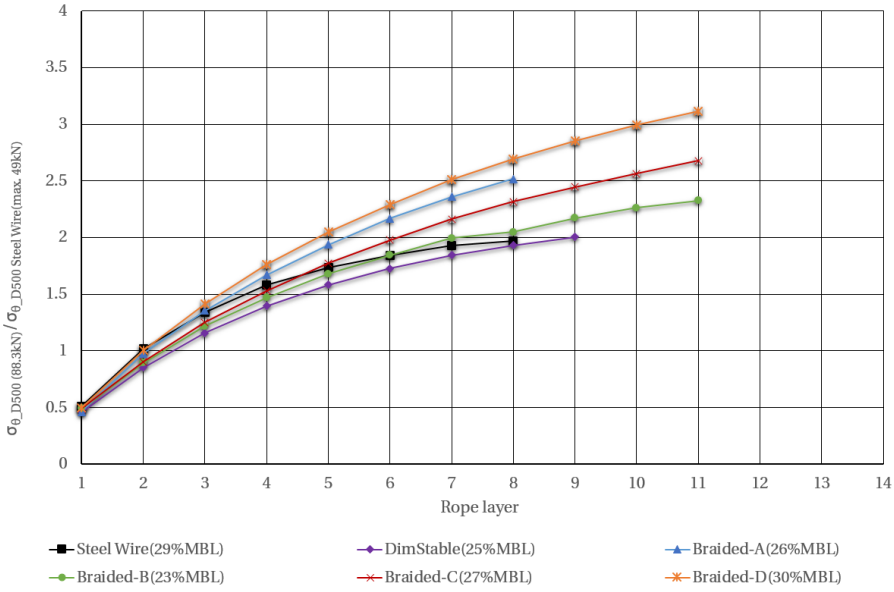

Figure 5.21: Tangential stress in D500 - 88.3 kN (9 Te) tension, Ø20 mm, (D/d=25)

Increasing spooling tension to 88.3 kN causes significant differences, Fig. 5.19. The plotted values are relative to the peak stress from the steel wire with 49 kN tension. The absence of a linear relationship between tension and stress level is noticeable. With a 1.8 times increase in rope tension, the stress induced by the steel wire is doubled. With ten layers, Braided-C induces 3.35 times higher stress than the steel wire and continues to grow with a steeper gradient compared to the values from 49 kN spooling tension. Stresses caused by the DimStable rope exceed the steel wire from five layers and beyond. At the same time, Braided-A now gives values nearly identical to Braided-C. Stresses from Braided-B are similar but still a bit lower.

On the D400 drum, the steel wire reaches a practically constant tangential stress level with 7-8 layers for both rope tension levels. This is also the case for DimStable with the lower tension, while more than eleven layers are required to reach a limit with the higher tension. Correspondingly, at least 13-14 layers are required for the pure braided ropes with the low tension level and even more with increased rope tension.

The stresses induced by the HPSFRs are reduced relative to the steel wire on the D500 drum (D/d=25), Figs. 5.20 and 5.21. The values are now plotted relative to the peak tangential stress induced by the steel wire on the D500 drum. With 49 kN

rope tension, stresses from Braided-C are close to the steel wire stresses. At the same time, DimStable and Braided-B induce lower stresses and stresses induced by Braided-A are only slightly higher than the steel wire. Braided-D gives the highest stresses, and with eight layers, the value is about 1.36 times the steel wire. Constant stress levels are achieved with 8-9 layers for the steel wire and DimStable ropes. The other ropes require approximately 10-13 layers.

With higher rope tension, stresses induced by the pure braided ropes exceed the steel wire values, but it requires more layers. It takes Braided-A four layers, Braided-B seven and Braided-C five to exceed the steel wire stresses. Braided-D still induces the highest stresses, and it takes only three layers until the steel wire values are exceeded. With eight layers, the stress level for Braided-D is 2.69 times the steel wire and still increasing significantly. Until nine layers, DimStable induces lower stresses than the steel wire.

Effect of D/d-ratio

Figure 5.22 compares tangential stresses for the different Ø20 mm rope designs on D500 relative to D400 with 88.3 kN rope tension.

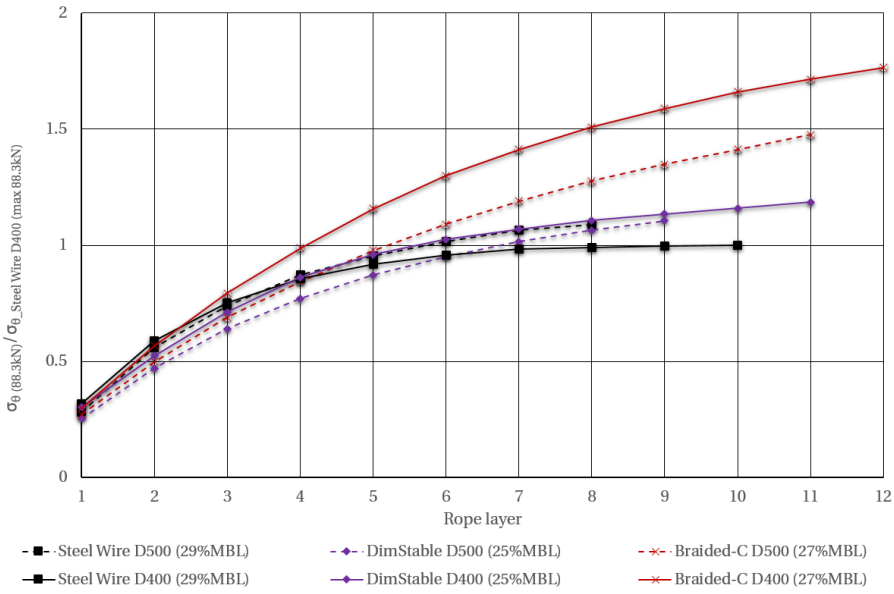

Figure 5.22: Tangential stress in D500 relative to D400 - 88.3 kN (9 Te) tension, Ø20mm

The pure braided rope, Braided-C, is relatively sensitive to D/d-ratio and induces significantly lower stresses in D500 compared to D400. On the other hand, DimStable and the steel wire are not very sensitive. With an increasing number of layers, the steel wire exhibits slightly higher stresses on D500 than D400.

Figure 5.23 shows the same tendencies for the smaller rope sizes. This figure shows stresses induced in the two drums with Ø12 mm DimStable and Braided-C ropes spooled with a rather high rope tension level of 39.24 kN. Further, DimStable is also spooled with a lower tension of 19.62 kN. The curves are normalized against the maximum measured stress (17 layers of Braided-C on D400).

Appendix E holds more figures showing that these trends are similar for lower tensions and the other braided ropes.

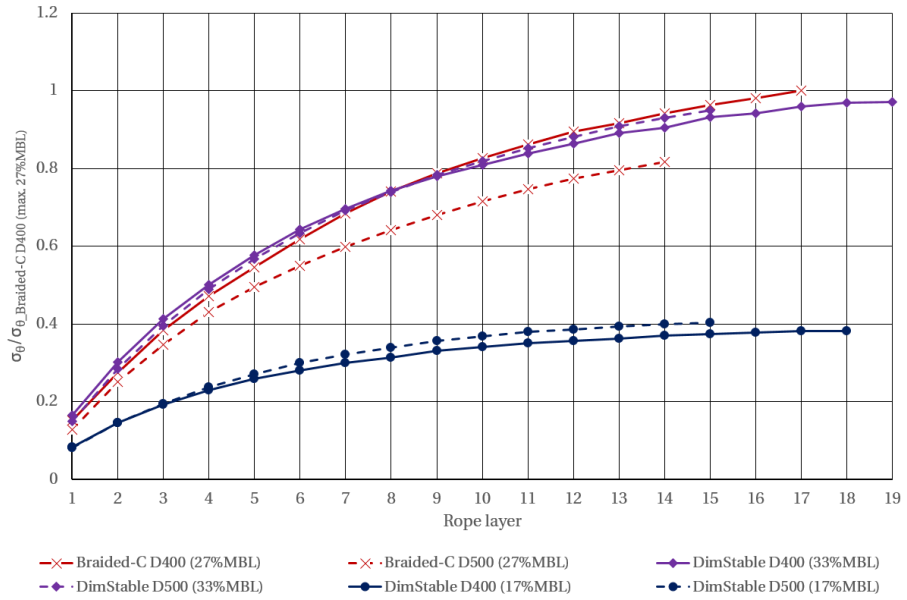

Figure 5.23: Tangential stress - Ø12 mm ropes on D400 (D/d=33.3) and D500 (D/d=41.7)

Effects of spooling speed

Figure 5.24 shows tangential stresses in D500 when ropes are spooled with 0.1 and 0.3 m/s. The values are normalized against the maximum measured stress, which is eleven layers of Braided-D.

For all of the ropes, the tangential stresses are higher for the lower speed. The differences are more prominent for Braided-C and Braided-D than for DimStable. It is assumed that this effect also is related to stiffness and deformability as slower

speed allows more time for the ropes to deform and adapt. DimStable exhibits higher dimensional stability and is, therefore, less affected.

It should be noticed that the applied spooling speeds are very low and considered irrelevant for many practical applications. The effect of speed should be further investigated with higher and more speed levels.

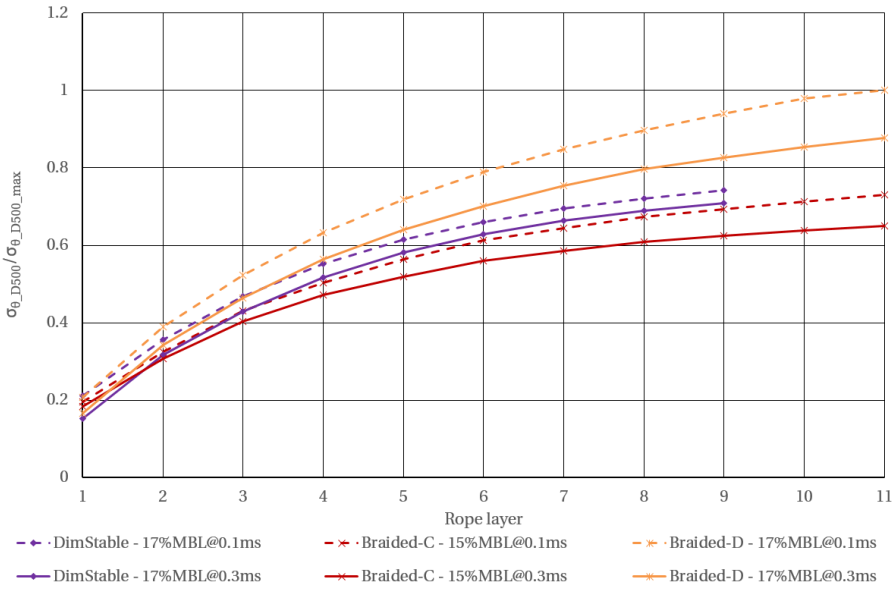

Figure 5.24: Tangential stress at different spooling speeds Ø20 mm, (D/d=25)

Circumferential stress variation in drums

The different sectors where the rope runs parallel or crosses cause differences in tangential stresses. This is apparent in Figs. 5.25 through 5.28 which show the circumferential tangential stress distribution (values from each strain gauge around the circumference) for the steel wire, DimStable, Braided-C and Braided-D.

The steel wire and DimStable ropes cause significant stress variations around the circumference. The variations increase with an increasing number of layers. These ropes exhibit relatively significant differences in layer radii around the circumference.

For the pure braided ropes, the layer radii vary less and result in more evenly distributed stresses. Consequently, the differences between average and peak stresses are smaller.

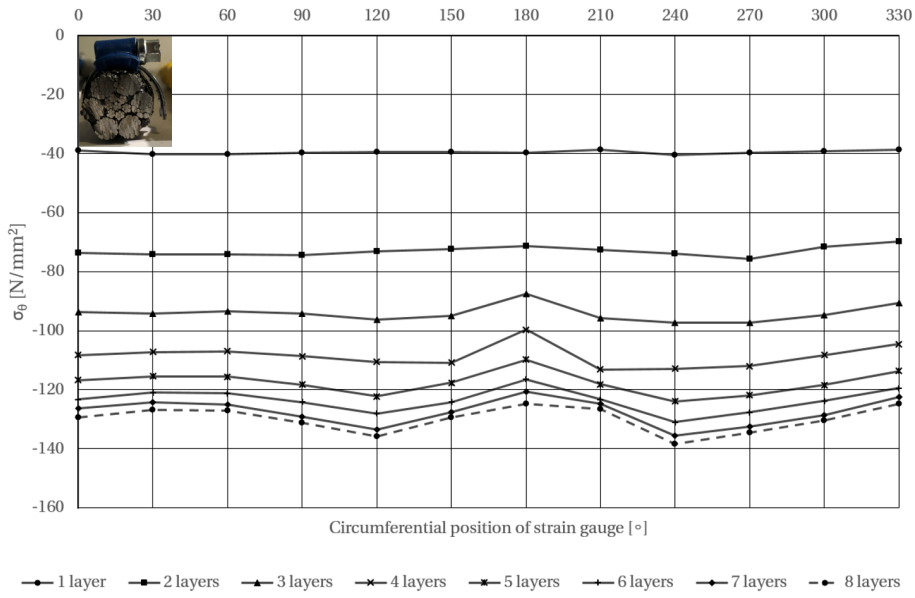

Figure 5.25: Circumferential stress variation - Steel wire, 20% MBL, (D/d=25)

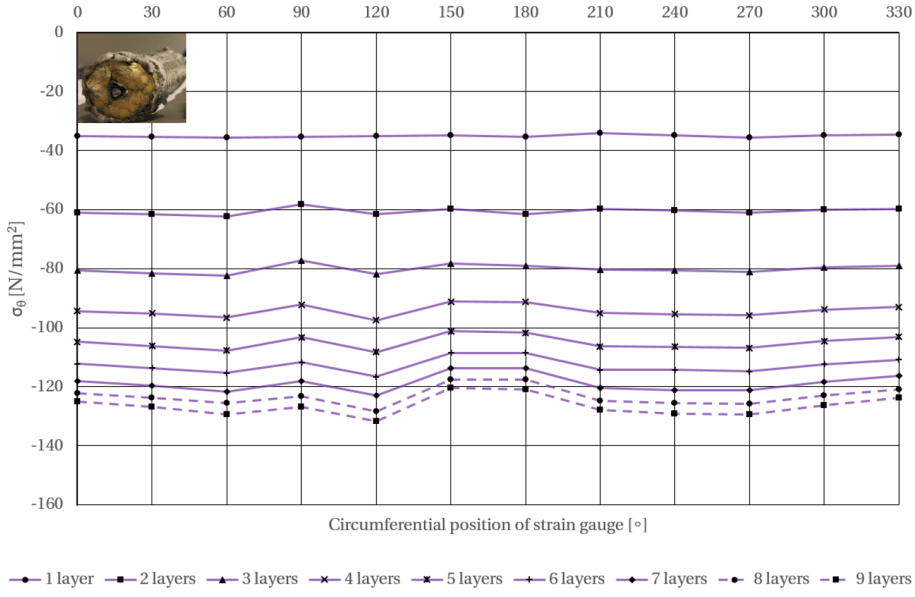

Figure 5.26: Circumferential stress variation - DimStable, 17% MBL, (D/d=25)

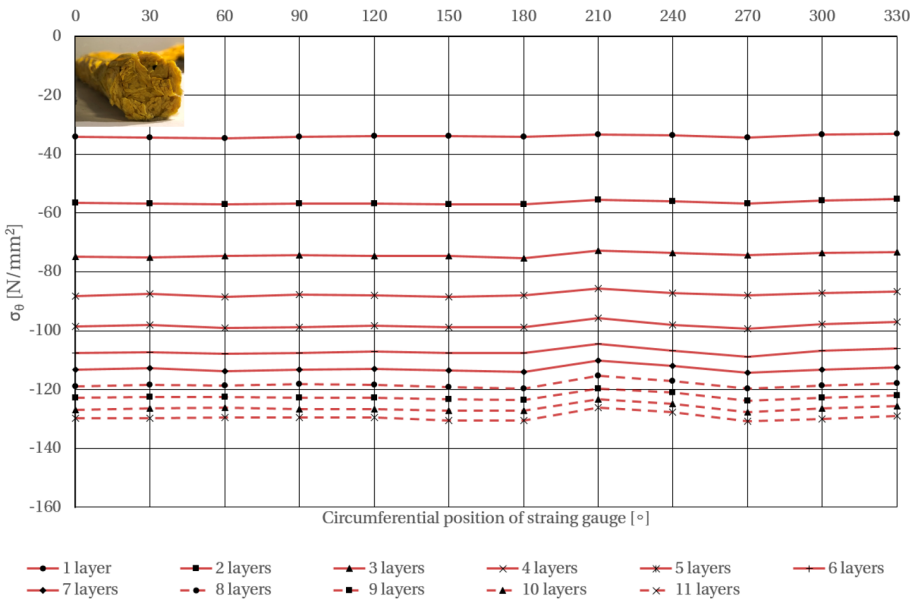

Figure 5.27: Circumferential stress variation - Braided-C, 15% MBL, (D/d=25)

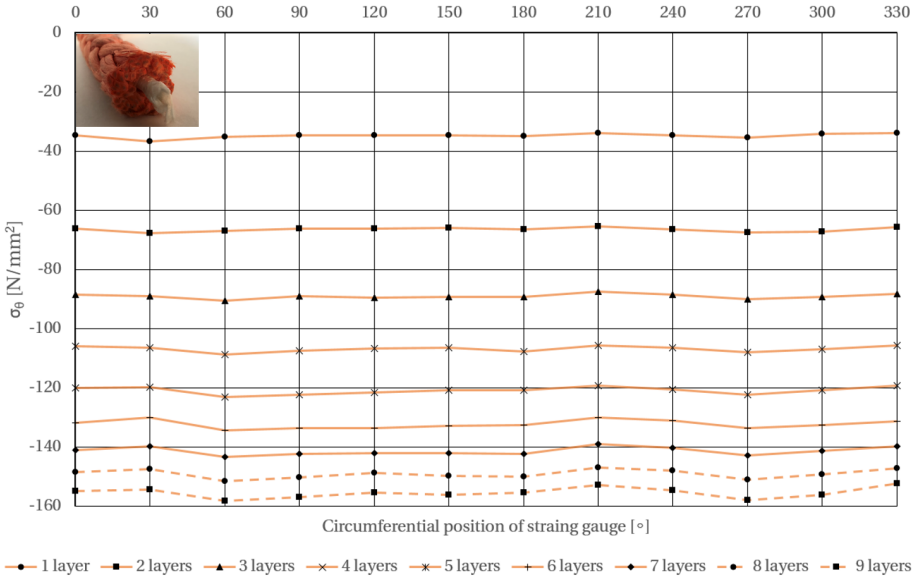

Figure 5.28: Circumferential stress variation - Braided-D, 17% MBL, (D/d=25)

5.2.2 Axial stress in drum structures

During multilayer spooling, the axial forces acting on the flanges induce axial stresses in the drums. Figures 5.29 and 5.30 show examples of measured maximum axial stresses in the D400 test drum with 49.05 kN and 88.3 kN rope tension.

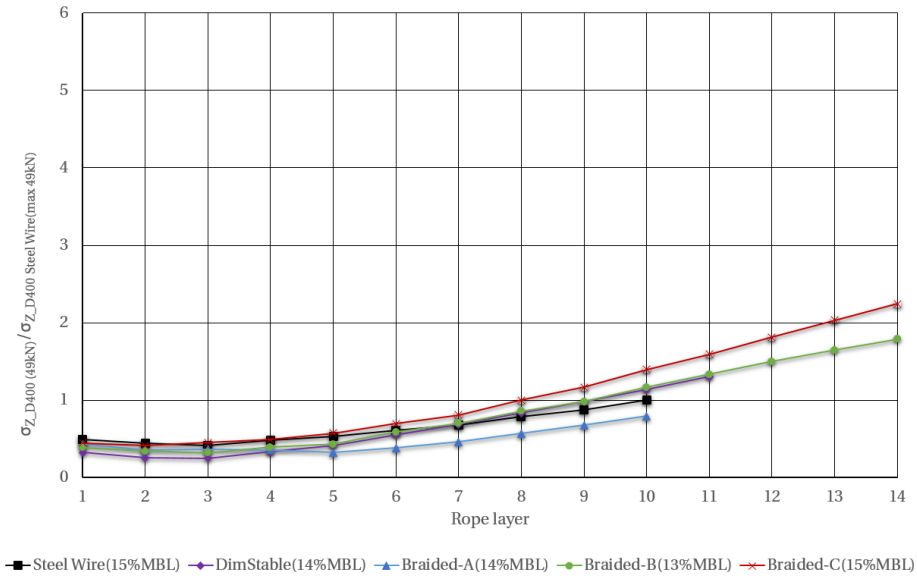

Figure 5.29: Axial stress in D400 - 49.05 kN (5 Te) tension, Ø20 mm, (D/d=20)

The values are normalized against the maximum stress measured for the steel wire rope with 49.05 kN rope tension. The axial stresses are relatively low for the first few layers until they increase from five layers and beyond. The differences between the ropes are relatively small. Braided-C causes the highest stresses and Braided-A the lowest. In contrast, stresses from DimStable and Braided-B are similar to the steel wire.

With 88.3 kN rope tension, stresses start to increase more significantly from three rope layers. With more than five to seven layers, stresses from all HPSFRs exceed the steel wire values. With an increasing number of layers, the growth becomes approximately linear. This linearity is an indication of more or less constant flange forces for each layer. Braided-B and Braided-C induce the highest axial stresses for both rope tension levels.

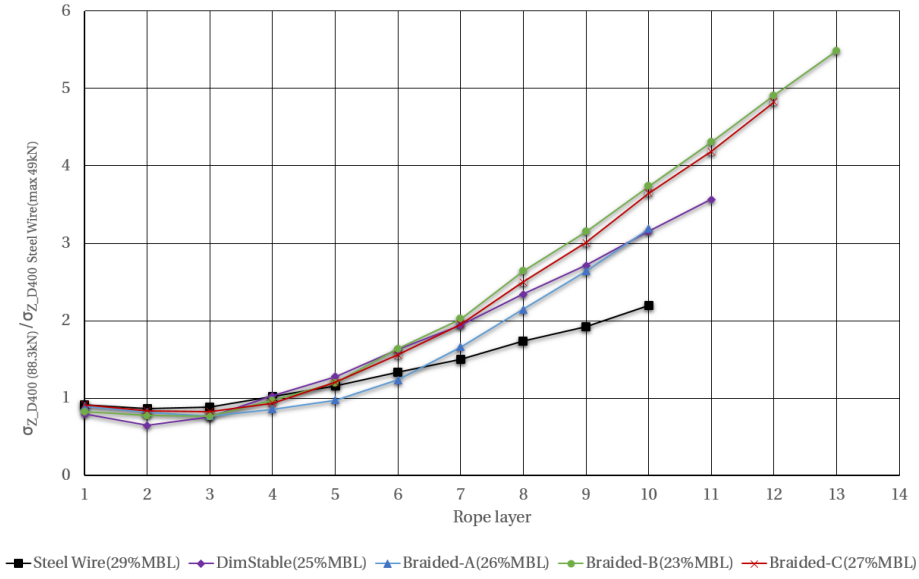

Figure 5.30: Axial stress in D400 - 88.3 kN (9 Te) tension, Ø20 mm, (D/d=20)

5.2.3 Stresses in flanges (B2)

Examples of von Mises stresses measured in the flanges of both drums are shown in Figs. 5.31 and 5.32. These plots show the ropes causing the highest stresses with 88.3 kN. The values are normalized against the maximum measured stress in the fixed-end flange of each drum.

Supplementary plots for the other ropes are enclosed in Appendix F.

The flanges are subjected to radial contraction from the radial pressure on the drum and shear forces and bending moments from the axial forces acting on the flanges. Due to higher constraints, stresses are higher in the fixed-end flange than in the free-end flange.

The HPSFRs induce higher stresses than the steel wire rope, but the differences are much smaller than stresses in the drums. In general, DimStable and Braided-D induce the highest stresses. Stresses from Braided-B are also relatively high and for D400 comparable to DimStable.

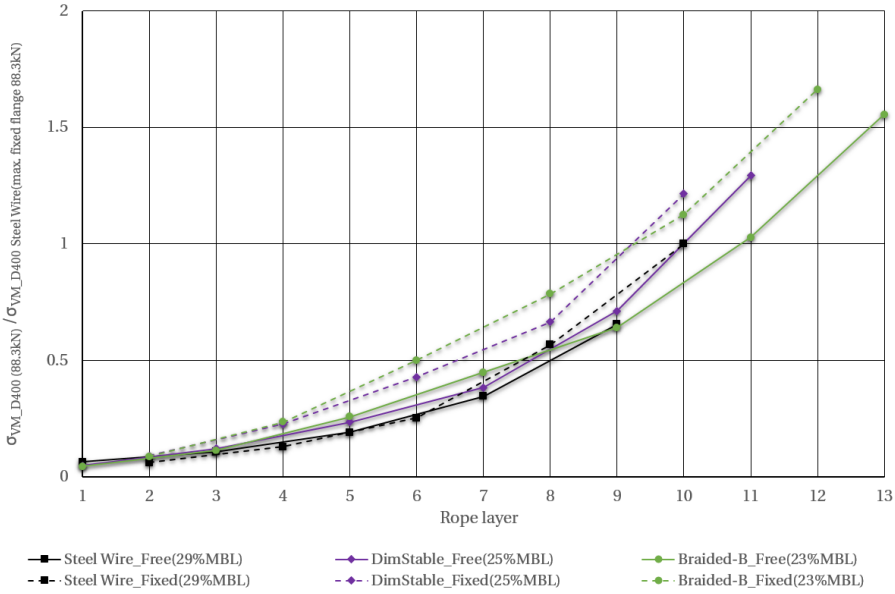

Figure 5.31: von Mises stress, D400 flanges - 88.3 kN (9 Te) tension, Ø20 mm

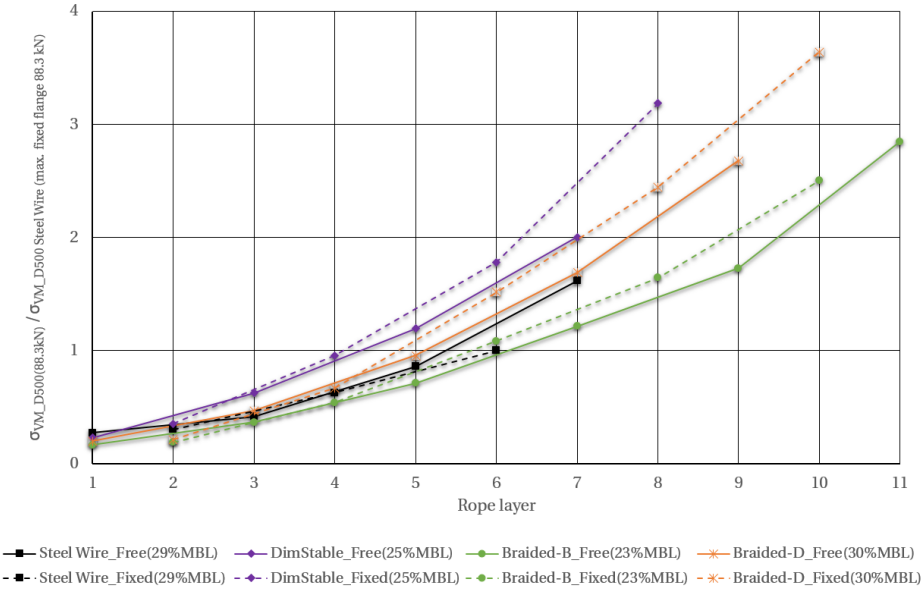

Figure 5.32: von Mises stress, D500 flanges - 88.3 kN (9 Te) tension, Ø20 mm

5.2.4 Effect of "protective" rope layers

A recommended way to reduce the maximum tangential stress in winch drums is to add "protective" layers, where the first layers are spooled with lower tension than the rest [3].

Figure 5.33 shows the effect of this for Braided-B on the D500 drum. The tangential stresses are normalized against the maximum stress measured when all eleven layers are spooled with a constant rope tension of 88.3 kN. When spooling the first layer with 39.24 kN and the other layers with 88.3 kN there is a reduction of peak stress of approximately 7%. Applying two "protective layers" with the same force ratio significantly reduces the peak stress by approximately 24%.

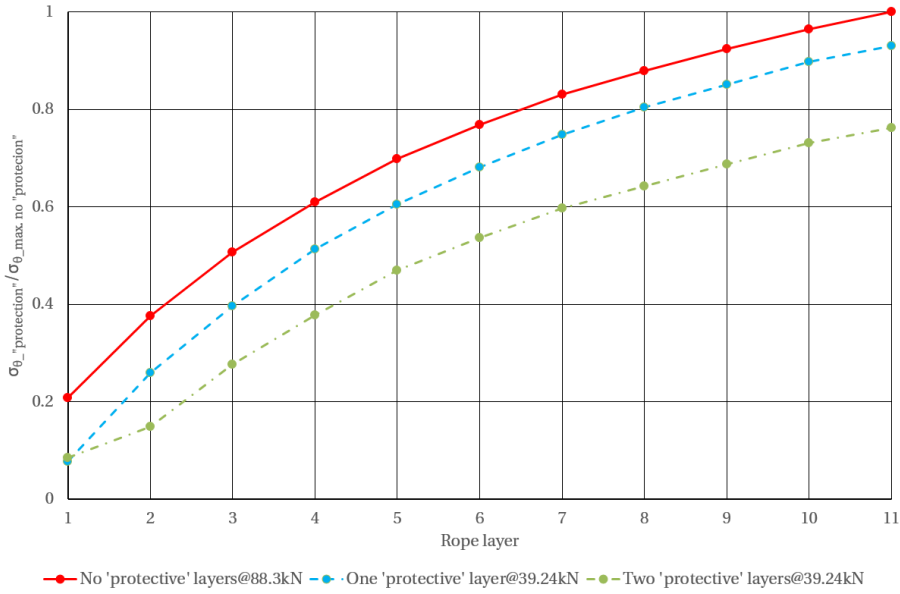

Figure 5.33: Effect of "protective" layers Ø20 mm Braided-B, (D/d=25)

The stress-reducing effect of "protective layers" is confirmed. However, when the lower layers are spooled with low tension followed by higher tensions in subsequent layers, it is important to know the risk of "rope knifing" effects. Thus, one needs to find an optimal balance between tension level and protection.

A certain degree of protection in the first layer are expected on drums in service. The first windings are usually spooled with lower tension due to the anchoring of the rope, and the first layer is also rarely used in operations. Consequently, dependent on tension level during spooling, the first layer might normally act as protective.

5.2.5 Long term stress development

Fibre ropes exhibit time-dependent (visco-elastic) properties. For the current experiments, an effect related to such properties were observed when releasing tension in ropes subjected to testing of transverse stiffness. After releasing the tension, it was partially recovered, and the ropes lifted from the floor. Figure 5.34 shows examples of this measured with the Ø12 mm Braided-C and DimStable ropes. The tension of Braided-C was reduced once, resulting in a continuous increase in tension. With DimStable, the rope tension was released three times. The curve shows a significant reduction in tension increase for each time. Compared to the tensions applied during testing of transverse stiffness, the magnitudes of recovered tensions are minor.

The potential effect of such properties on stresses in multilayer winches was investigated. Figures 5.35 and 5.36 show how the von Mises stress in the drum and flanges developed after spooling was completed and rope tension released. Each curve represents average stresses from all strain gauges around the centre of the drum and around each flange.

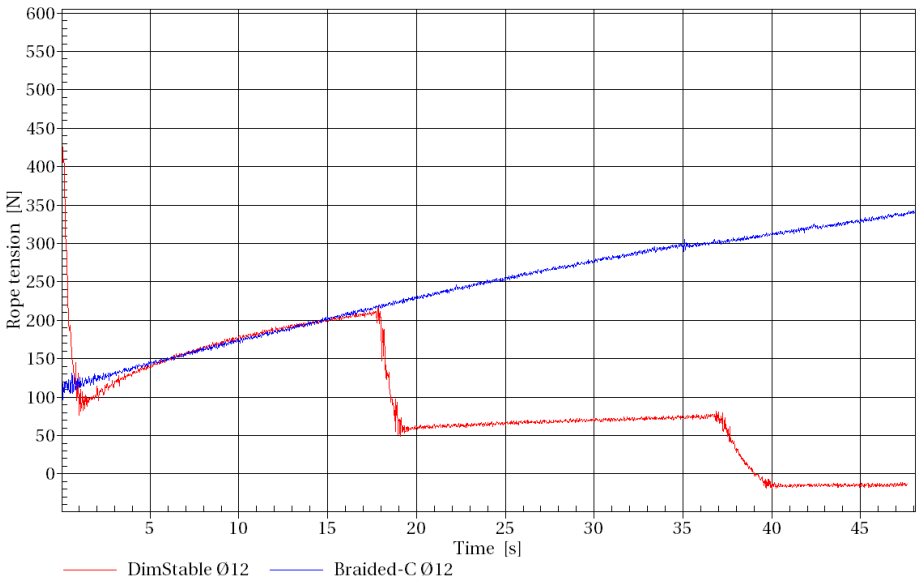

Figure 5.34: Load recovery after releasing of tension in ropes

With a single layer, the von Mises stress in the drum decreases continuously and gradually flattens out for almost two hours after tension is released. The trend is similar for the stress in the free-end flange. On the other hand, the stress in the

fixed-end flange shows an increasing tendency. However, the flanges are barely stressed with one single layer on the drum, and the small stresses are considered noise. Thus, the slight stress increase in the fixed-end flange is disregarded.

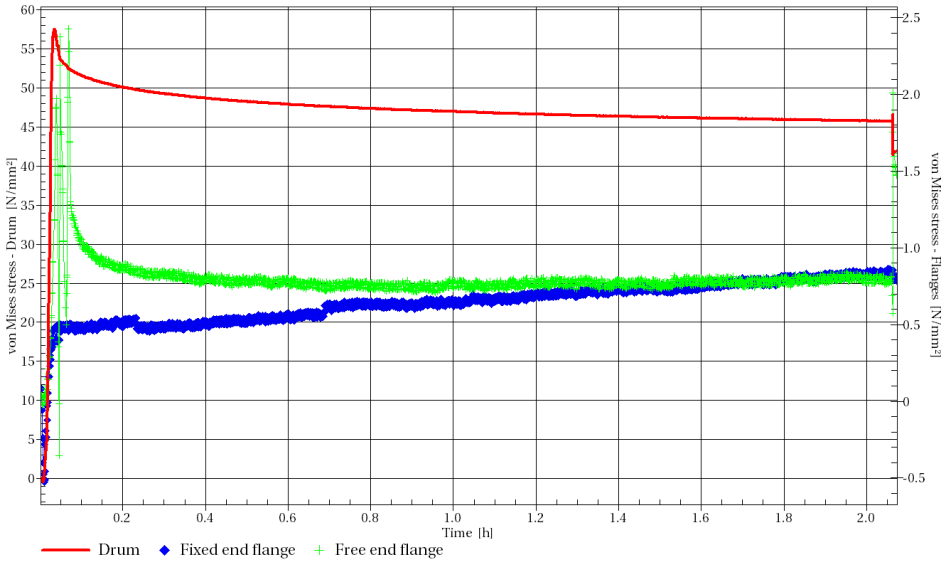

Figure 5.35: Stress development - one layer@88.3 kN - Ø20 mm Braided-B (D/d=25)

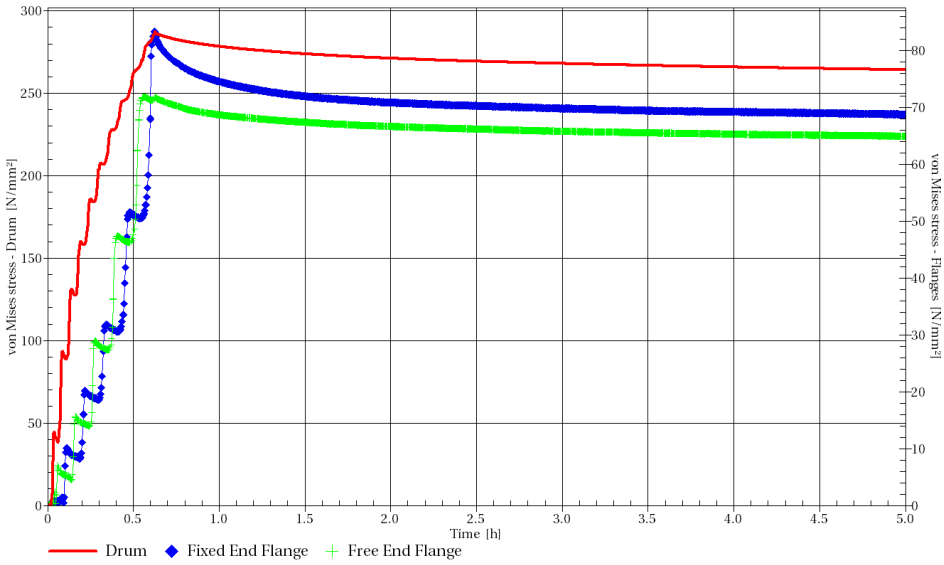

Figure 5.36: Stress development - ten layers@88.3 kN - Ø20 mm Braided-B (D/d=25)

When the number of layers is increased to ten and tension removed, stresses in both drum and flanges decrease continuously, slowly flattening out for nearly four and a half hours.

Based on these measurements, no indications of stresses increasing over time in HPSFR rope packages were found. Quite the contrary, stresses in both drum and flanges are slightly reduced when tension is released after spooling.

5.3 Rope properties' effects on stresses

The experiments show that all tested HPSFRs induce higher stresses in both multilayer winch drums than the steel wire rope. This applies particularly to the tangential stress in the drum but also to stresses in flanges. The differences increase with increasing tension.

In the following, the effects of rope properties on stresses in multilayer winch drums are further elaborated.

5.3.1 Effect of rope strength utilization

Figure 5.37 illustrates the relative tangential stresses in the drums induced by the various Ø20 mm ropes with eight layers and two levels of rope tension. Due to different breaking loads, the degree of rope utilization vary.

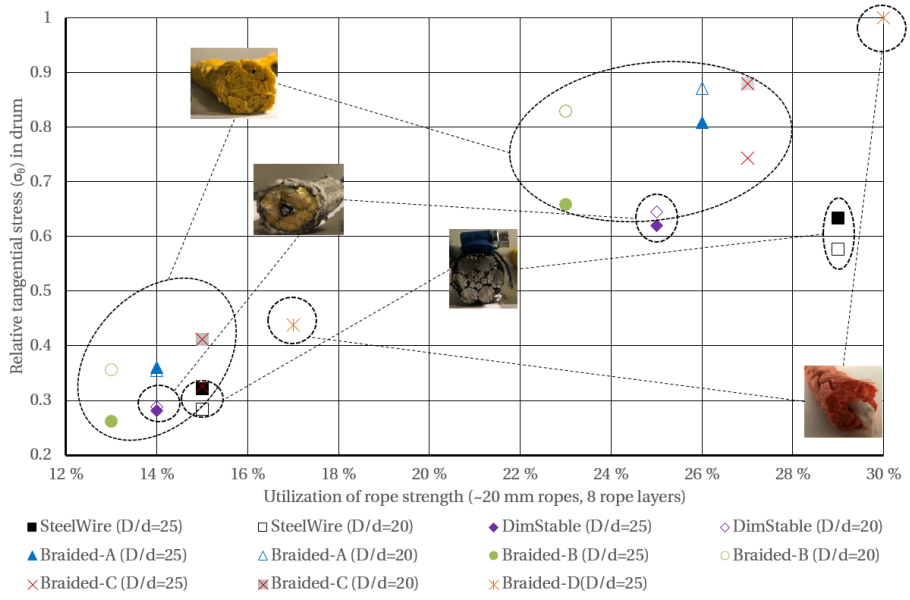

Figure 5.37: Tangential stresses in drums relative to the utilization of rope strength

On the smallest drum (D400, D/d=20), the pure braided fibre ropes induce higher stresses than the steel wire. The utilization of rope strength is also less or similar to the steel wire rope. Besides Braided-B with low tension, this is also the case for stresses in the larger drum (D500, D/d=25). The differences between the pure braided ropes and the steel wire are amplified with increasing rope tension.

Surprisingly, the effect of increased D/d-ratio is different for the steel wire rope as it causes higher stress in D500 than D400. The order of testing and altered rope stiffness can explain this effect. The steel wire rope was tested on D400 first, and a certain amount of increase in stiffness during usage is typical. Unfortunately, this was not verified by testing transverse stiffness before and after spooling tests on each drum. However, the differences between the two drums are relatively small, and effects related to measurement uncertainties cannot be disregarded.

The DimStable rope induces stress comparable to the steel wire but with lower utilization of rope strength. Like the steel wire, this rope also exhibits low sensitivity to D/d-ratio. The reason for this is uncertain, but it can be related to the higher dimensional stability of this rope.

The high stress induced by Braided-D is related to the high utilization of rope strength. Stress levels closer to the pure braided ropes are expected with more comparable utilization of strength.

In the case of multilayer spooling with equivalent utilization of rope strength, all HPSFRs are expected to induce higher stresses in the drums than the steel wire rope.

5.3.2 Effect of the rope's elasticity ratio

Figure 5.38 shows the relative tangential stresses in the drums plotted against the ratio of longitudinal and transverse moduli of elasticity measured with a single rope.

According to Dietz [7] and Lohrengel et al. [8], the tension reduction effect decrease with decreasing elasticity ratio (Eq. 3.99). Consequently, lower ratios should cause higher tangential stresses in the drum. The presented results do not reflect this unambiguously as the pure braided fibre ropes cause significant higher stresses with higher elasticity ratios than the steel wire. Further, the elasticity ratios for DimStable are higher than the steel wire, while the stress levels are comparable. This indicates that the elasticity ratio cannot predict the level of tangential stress in multilayer winch drums with HPSFRs. Consequently, accurate assessment of tangential stresses from multilayer spooling of such ropes requires the stiffness development in the complete rope package to be taken into account.

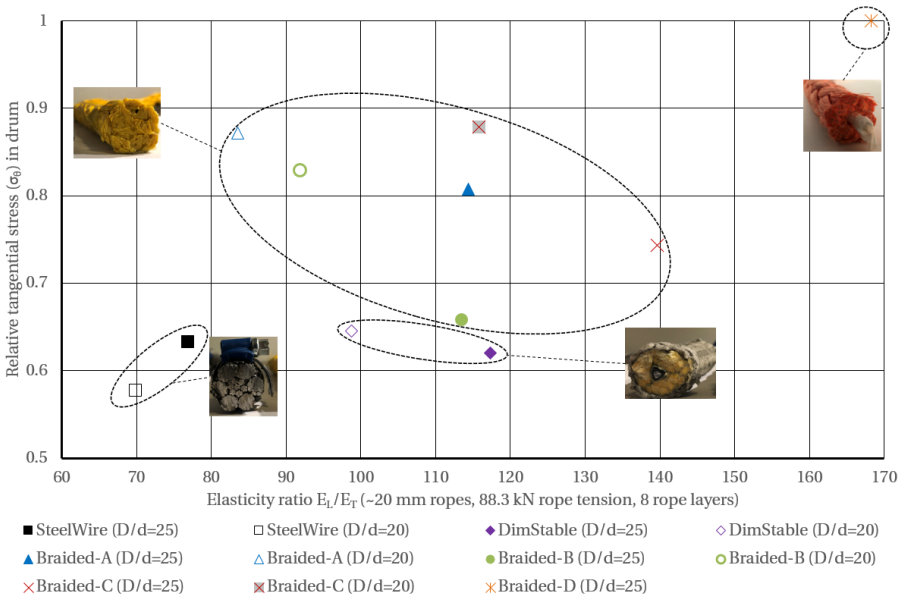

Figure 5.38: Tangential stresses in drums relative to the elasticity ratios of the ropes

5.3.3 Effect of rope deformation

Figure 5.39 shows relative stresses in the drums plotted against relative ovality (Eq. 3.98) for the different ropes.

Deformations are more significant for the pure braided ropes than for the steel wire rope and the dimensionally stable fibre ropes. Besides Braided-D, which causes the highest stress, stresses are also considerably higher for the pure braided ropes.

The correlations between deformations and stresses in the flanges are found less significant, Fig. 5.40. The DimStable and Braided-D cause the highest flange stresses. The higher dimensionally stability of these ropes causes larger layer radii and higher bending moments on the flanges. Compared to stresses induced by the steel wire, the stresses from the pure braided ropes are lower in the free-end flange and higher in the fixed-end flange.

The significant relative differences in stresses between the fixed- and free-end flanges are caused by a different number of layers. As the measurements are based on six complete rope layers, the rope has climbed to the seventh layer at the free end. Therefore, the fixed-end flange is exposed to forces from six rope layers and the free-end flange from seven layers.

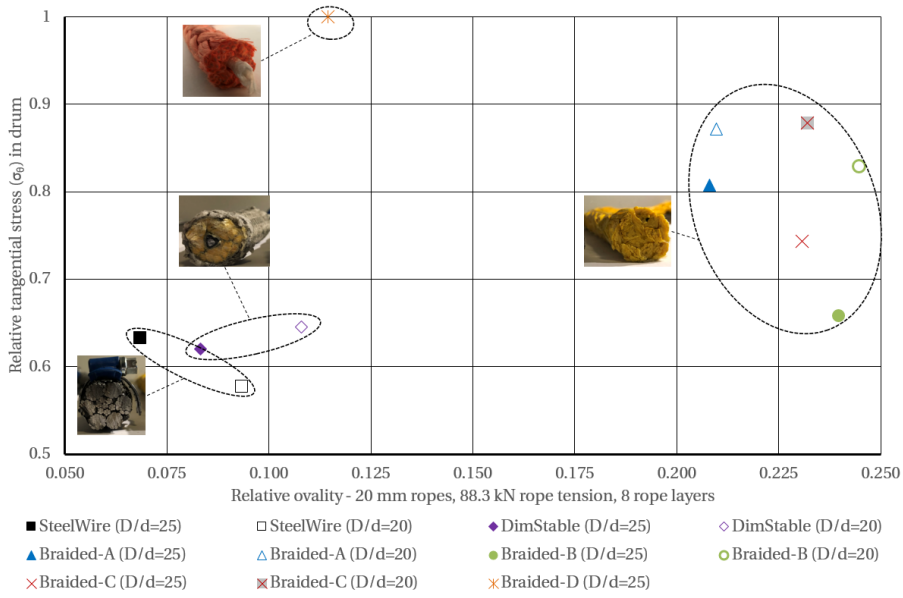

Figure 5.39: Tangential stresses in drums relative to rope deformability

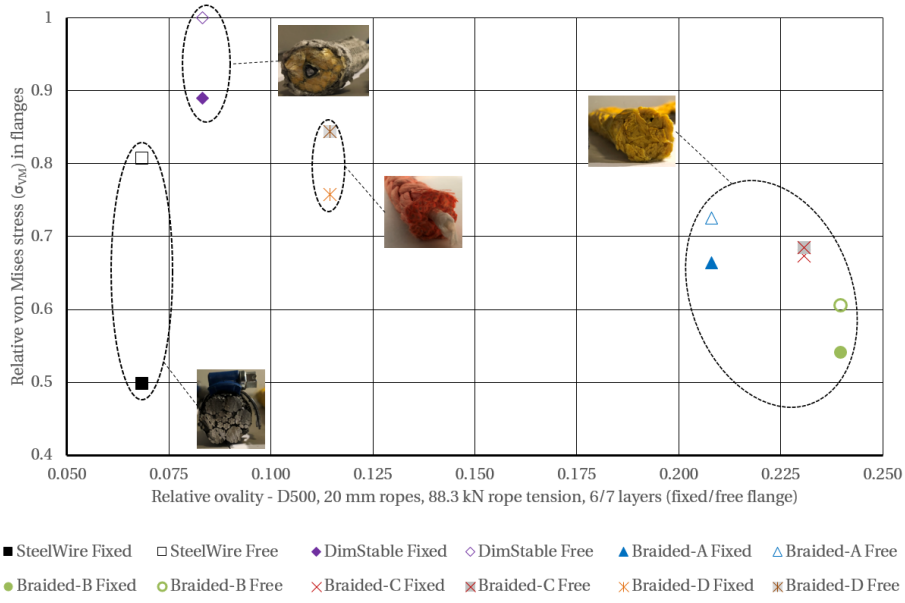

Figure 5.40: von Mises stresses in flanges relative to rope deformability - D500

5.3.4 Effect of rope friction

According to Dietz' theory of "the last climbing winding" [7] and Mupende [16] forces on flanges increase with decreasing coefficient of friction. Figures 5.41 and 5.42 show flange stresses plotted against coefficients of friction for D500 and D400, respectively. The friction coefficients are derived from the fitted curves in Fig. 4.37 applying average pressure in the first layer using Eq. 4.5.

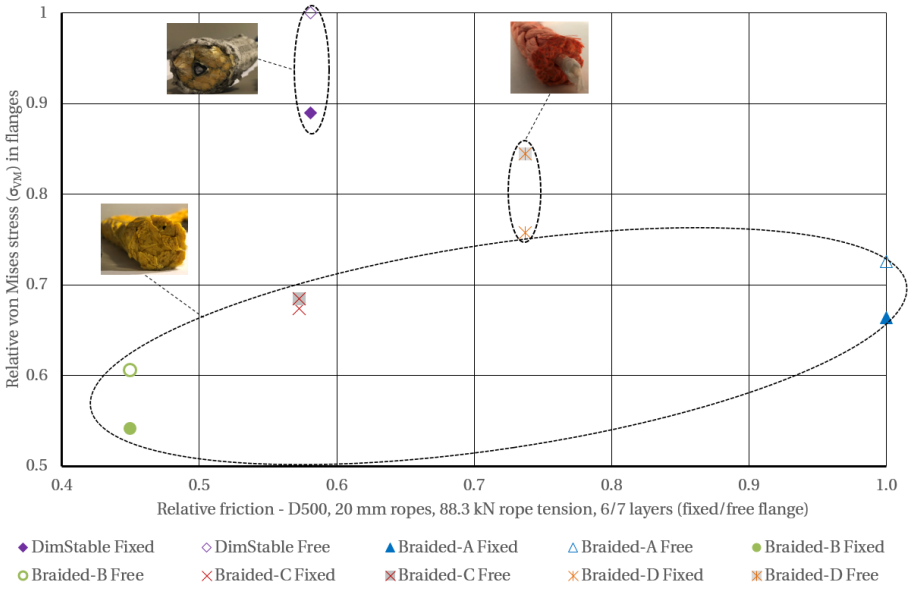

Figure 5.41: Stress in flanges relative to rope friction - D500

On D500, stresses from Braided-A and Braided-C are higher than Braided-B. Braided-B exhibits a lower coefficient of friction, and there is no apparent relation between low friction and high stress. The highest stresses in both flanges are induced by DimStable, whose friction properties are comparable to Braided-C. On D500, the number of layers was six and seven for the fixed and free ends, respectively. The situation on D400, with ten and nine layers, shows another picture more supporting the theory. Still, the highest stresses are caused by DimStable.

It is difficult to separate the different rope properties' effects on flange forces. The experiments show that flange forces are dependent on combinations of tension, rope deformation and friction. In addition, flange forces are possibly influenced by multilayer tension reduction effects.

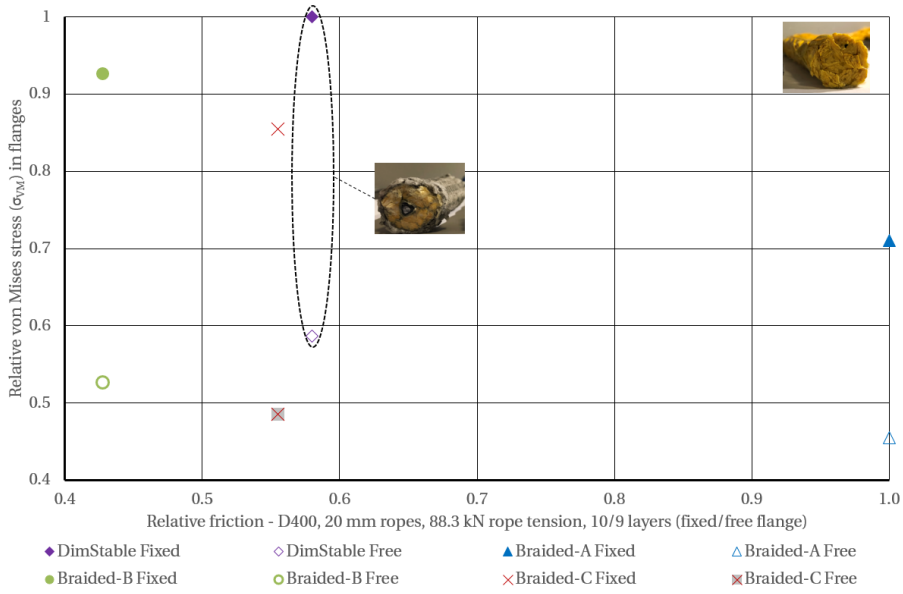

Figure 5.42: Stress in flanges relative to rope friction - D400

5.4 Summary - experimental test results

Investigations of rope properties are carried out for various 12-strand HPSFRs and a comparable steel wire rope. The investigated properties are transverse stiffness, deformation and friction. In addition, extensive multilayer spooling tests of these ropes are carried out on two different winch drums. Further, stresses in drums and flanges induced by the different ropes during multilayers spooling are analyzed and compared. The number of rope layers applied are significant and exceeds previous research.

The transverse rope stiffness, expressed by the transverse modulus, increases with increasing rope tension and rope constraint. The transverse moduli of HPSFRs are significantly lower than the transverse modulus of the steel wire rope. The dimensionally stable rope with a braided jacket and a stiff internal core exhibits transverse moduli between the pure braided HPSFRs and the steel wire rope. These results support findings from previous investigations by Lohrengel et al. [9].

Testing of transverse stiffness with up to eight ropes in a linearly stacked arrangement was not unambiguous. The results did not disclose any significant increase in rope package stiffness with an increasing number of layers. However, a novel experiment measuring transverse rope stiffness directly on the drum revealed such

possibilities when spooling with high tension. Compared to the steel wire rope, the fibre rope showed a relatively higher increase in rope package stiffness. Stress measurements support the existence of such an effect.

The test operator had to work close to the winch while compressing the ropes. Due to safety, tension was released during this process. Each layer was spooled entirely, and the rope entry point was at the flange when tension was released. Due to rope friction, the tension reduction is expected only to influence the very few windings closest to the flange. On the other hand, with reference to the long term stress development (Figs. 5.35 and 5.36), there is a gradual decrease in stress over time after tension is released. Such an effect is also expected to be present for the wire rope. However, the stress reduction gradients and possible effects on the measurements are unknown.

Friction coefficients of HPSFRs are low and decrease with increasing contact pressure. This also confirms previous findings by Lohrengel et al. [8]. The measurements confirmed that ropes designed for improved traction properties exhibit higher coefficients of friction.

There are significant differences in rope deformation for the various rope designs. Pure braided ropes exhibit significantly larger deformations than ropes with shape controlling measures. When the different rope designs are subjected to tension or spooled over sheaves and onto drums, they deform into different cross-sectional profiles. The pure 12-strand braided ropes deformed to a rounded rectangular profile, while a similar rope combined with an internal fibre core took a rounded hexafoil profile. However, a single shape controlling measure as this does not seem to increase transverse stiffness. The profile of ropes combining a stiff internal core with a braided jacket was hexagonal.

The radial deformation of pure braided 12-strand ropes is relatively large. For the current experiments, the deformed radial dimensions are roughly in the range of 70-85% of the nominal dimension. For these ropes, deformations increase with decreasing D/d-ratio. Evidence of additional compression from subsequent layers during spooling was also found.

The measurements prove that the HPSFRs induce significantly higher stresses in the winch drums than the steel wire rope. With low tension, few layers and higher D/d-ratio, the differences are relatively small while significantly amplified with increased tension, rope deformation and the number of layers. The number of layers before the tangential stresses in winch drums reach a limit is also considerably higher for the HPSFRs than for the steel wire. This is particularly significant for the pure braided ropes. In addition, decreased spooling speed can increase stresses

in the drum. This effect should be further elaborated with higher speeds and more speed levels.

In general, the sensitivity to D/d-ratio is also high for pure braided ropes. Stresses in multilayer winch drums can be reduced by increasing the D/d-ratio for such ropes. On the other hand, the effect of increased D/d-ratio was much less for the dimensionally stable fibre rope and the steel wire.

Compared to fibre ropes with shape controlling measures and the steel wire rope, stresses around the circumference of the winch drums are much more evenly distributed for the pure 12-strand braided ropes.

It is confirmed that tangential stresses in multilayer winch drums can be reduced by spooling the first few layers on the drum with lower tension. However, the tension in these layers needs to be high enough to avoid "rope knifing" effects when subsequent layers are spooled with higher tension. A consequence of such protection is that these layers need to remain on the drum and cannot be utilized. Thus, the functional length capacity of the winch will be somewhat reduced.

Concerning multilayer spooling, any signs of increased tension over time are not found. After spooling is stopped, the tangential stresses in the drum are slightly reduced until stabilized.

Due to higher rope layer radii, dimensionally stable HPSFRs induce higher stresses in winch drum flanges. With few rope layers on the drum, the differences between the various rope designs are minor. Flange forces also increase with increased tension, reduced friction and rope deformation (low radial rope deformation and high lateral expansion).

These investigations complete the fulfilment of research objective RO1 and answer research question RQ1.

Part III

Evaluation of calculation methods

Chapter 6

Evaluation of radial pressure on multilayer winch drums

In Section 3.3, the "modified Dietz" method was identified as state-of-the-art for assessing radial pressure on multilayer winch drums. In the following, the tangential stresses in drums resulting from this method and the calculations specified by DNV GL [3] are evaluated against measurements.

6.1 Tangential stress in multilayer winch drums

The accumulated transverse modulus for i number of layers, $E_{T(i)}$, is calculated employing Eq. 6.1, where η is the multilayer exponent, and $E_{T(1)}$ the transverse modulus determined from a single rope.

$$E_{T(i)} = E_{T(1)} i^{(\eta+1)}, i = 2, 3, 4...n-1, n \tag{6.1}$$

Calculations of radial pressures and the resulting tangential stresses in the drum are carried out for the various ropes on both drums. Both constant rope package stiffness ($\eta = -1$) and exponents approximated for the calculations to fit measurements are applied ($\eta \neq -1$).

Tangential stresses in winch drums can be calculated in various ways. Class societies apply the simple equation for tangential stress in thin-walled cylinders, Eq. 2.6. This equation is dependent on a relatively low ratio between drum thickness and radius to be sufficiently accurate (Fig. 4.16). The methods by Dietz [7] and Mupende [16] use the 1^{st} order differential equation for circular symmetric shells, Eq. 2.19. However, both test drums are confirmed as "long", and the tangential stresses

are not affected by flange forces and geometry at points of measurements (Section 4.6). Thus, peak tangential stresses can be calculated employing the equation for thick-walled cylinders (Eq. 2.7). This method is applied in the following as it is efficient and straightforward, with results comparable to finite element analysis [11].

Further, the calculations are based on the following:

- Friction is ignored, and stress ratio k_T is calculated according to Eq. 3.95.
- Transverse moduli are based on measurements with curved counterparts.
- Constant longitudinal moduli E_L are according to Table 5.1.
- Mean rope dimensions, d_x and d_y, are according to Table 5.3.
- Rope pitch is set equivalent to d_x.
- Rope fill factors f are according to Table 4.4.
- Layer radii are according to Eq. 3.100.

For the "modified Dietz" method, the radial deformation of the drum is also taken into account. The deformation is based on a unit load, δ_D, determined using FEA. The applied radial deformations are $2.13{\cdot}10^{-3}$ mm and $3.57{\cdot}10^{-3}$ mm for D400 and D500, respectively.

The calculations are compared with peak tangential stress values averaged from repeated experiments. The results are normalized against the peak measured values. The 10.2% estimated uncertainty (95% confidence interval) of the stress measurements is indicated by a light grey area in each figure.

Supplementary evaluations are enclosed in Appendix G.

6.1.1 Calculations with steel wire rope

The calculations for the Ø20 mm steel wire are carried out with constant transverse moduli for all layers ($\eta = -1$).

Figure 6.1 shows a good agreement between the calculated values and measurements for the D400 drum and 23% of MBL rope tension. The calculations for the D500 drum with corresponding rope tension level are also good, but with somewhat increasing deviations with an increasing number of layers, Fig. 6.2.

In general, the DNV GL method underestimates the measured stresses for both D400 and D500. However, for D400, the results can be considered reasonable.

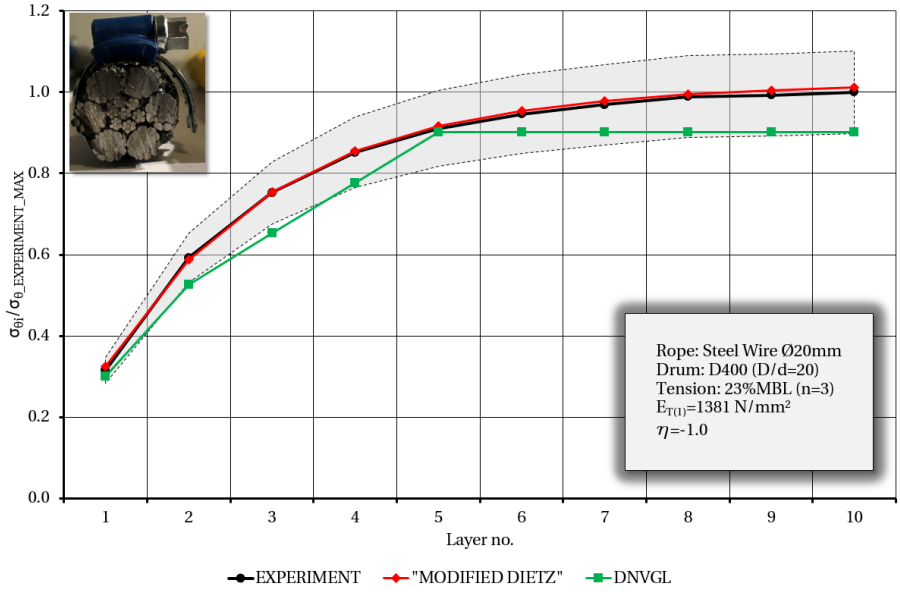

Figure 6.1: Calculations vs. experiment, σ_θ - Ø20 mm steel wire on D400, 23% MBL

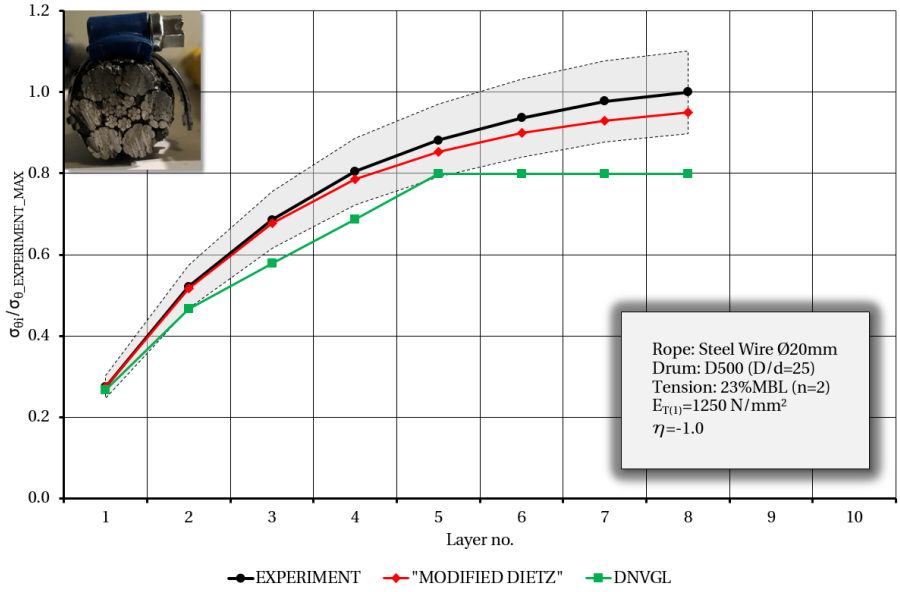

Figure 6.2: Calculations vs. experiment, σ_θ - Ø20 mm steel wire on D500, 23% MBL

There is a close match for five rope layers, and the stresses are within the measurement uncertainty for further layers. For D500, the deviations increase from five layers and are approximately 20% relative to the mean measured value with eight layers. It can also be noticed that the DNV GL method underestimates stresses calculated for less than five layers.

For both higher and lower rope tension levels, the compliance between calculations and measurements are relatively good and within the measurement uncertainty limits (Figs. G.3 - G.6 in Appendix G). With 15% of MBL rope tension, the calculated values are close to the mean measured values. Increasing the tension to 29% of MBL gives calculated stresses close to the upper uncertainty limit for D400 and ten rope layers. For D500, the calculated stresses are still close to the mean measured values for all layers.

The DNV GL method can be considered reasonable for up to five rope layers. However, the values are generally not conservative and close to the lower end of the measurement uncertainty band. With an increasing number of layers, the deviations relative to the mean measured values increase.

6.1.2 HPSFR - dimensionally stable ropes

For the Ø20 mm DimStable rope with 25% of MBL rope tension, Fig. 6.3, a multilayer exponent of -0.87 gives a close fit with the measured values for D400. With constant modulus, the calculated values are lower with increasing deviations from five layers and beyond. These trends are similar for D500, Fig. 6.4, where an exponent of -0.8 gives a good match with measurements.

Calculations according to DNV GL give relatively good results for up to five rope layers but underestimate stresses considerably with an increasing number of layers.

With lower rope tension, constant modulus calculations give pretty good results for both drums. However, further improvements are achieved with multilayer exponents of -0.91 and -0.92 for D400 and D500, respectively (Appendix G, Figs. G.7 and G.8). Stresses calculated by the DNV GL method can now be considered as reasonable for more than five layers for both load cases.

For rope tension levels between 18% and 46% of MBL, the smaller Ø12 mm DimStable rope requires calculations with multilayer exponents of -0.75 and -0.71 to match the mean measured values on D400. For D500, the corresponding exponents are -0.53 and -0.55. For this rope, the DNV GL method underestimates the stresses considerably for both drums, Fig. 6.5. The deviations increase with increasing rope tension and are larger for D500 than D400. (See Appendix G, Figs. G.9 - G.13)

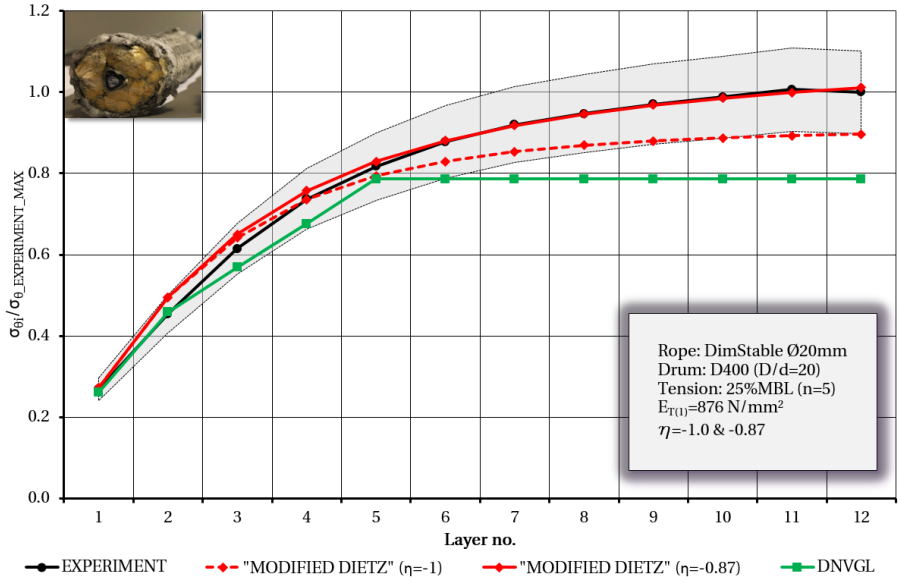

Figure 6.3: Calculations vs. experiment, σ_θ - Ø20 mm DimStable on D400, 25% MBL

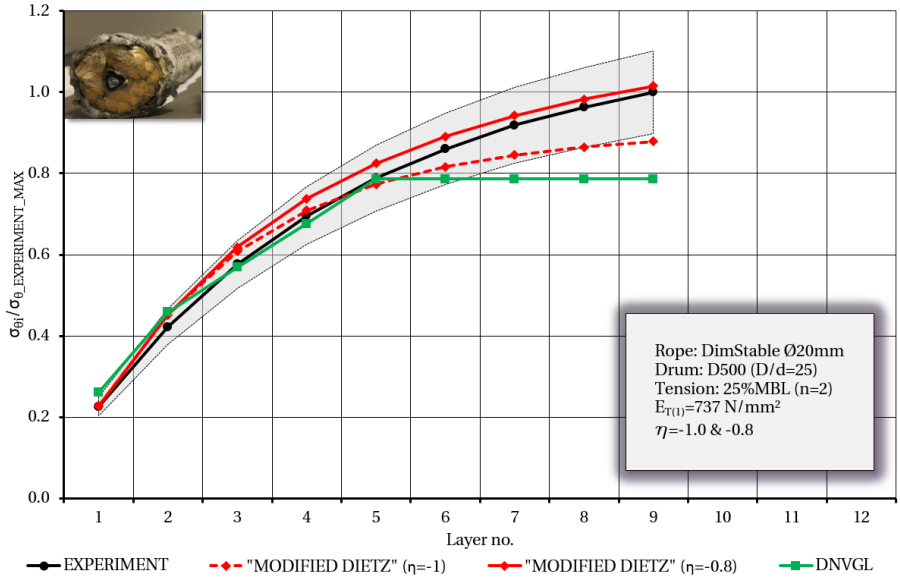

Figure 6.4: Calculations vs. experiment, σ_θ - Ø20 mm DimStable on D500, 25% MBL

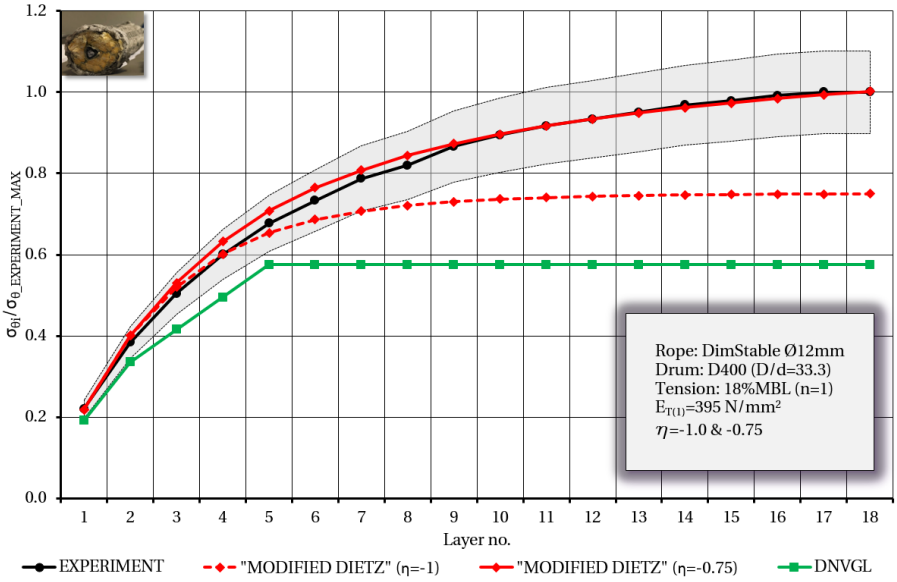

Figure 6.5: Calculations vs. experiment, σ_θ - Ø12 mm DimStable on D400, 18% MBL

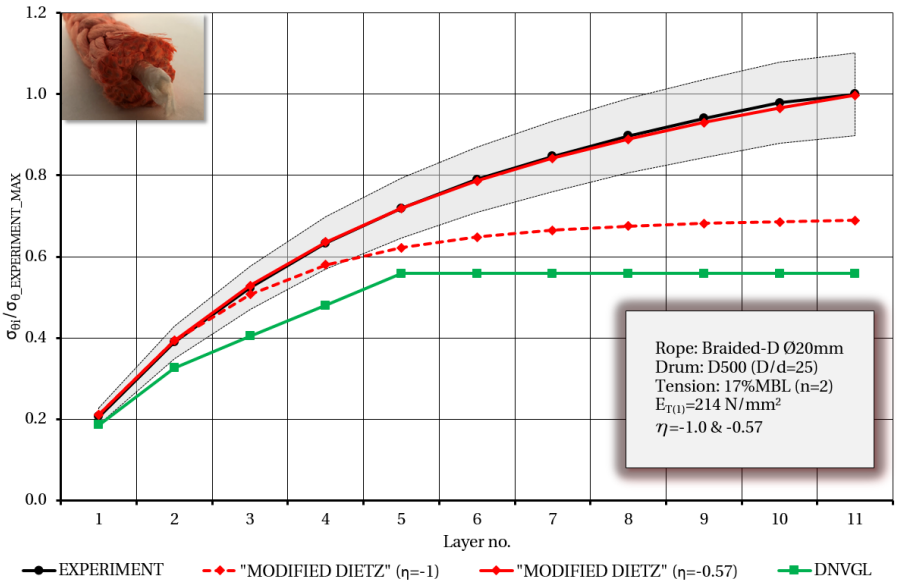

Figure 6.6: Calculations vs. experiment, σ_θ - Ø20 mm Braided-D on D500, 17% MBL

Braided-D, with its shape controlling fibre core in the centre, is also considered a dimensionally stable rope. For this rope and 15% of MBL rope tension on D500, a multilayer exponent of -0.57 gives good agreement with measurements, Fig. 6.6. This trend is similar to higher rope tension. For 30% of MBL, the multilayer exponent is practically unchanged (Ref. Appendix G, Fig. G.43).

Calculations with constant transverse moduli underestimate the stresses from four-five layers. At the same time, the DNV GL method results in too low stresses for practically all layers.

6.1.3 HPSFR - pure 12-strand braided ropes

Figures 6.7 and 6.8 show comparisons between calculations and experimental results for the Ø20 mm Braided-C rope, with 21% of MBL rope tension, on D400 and D500.

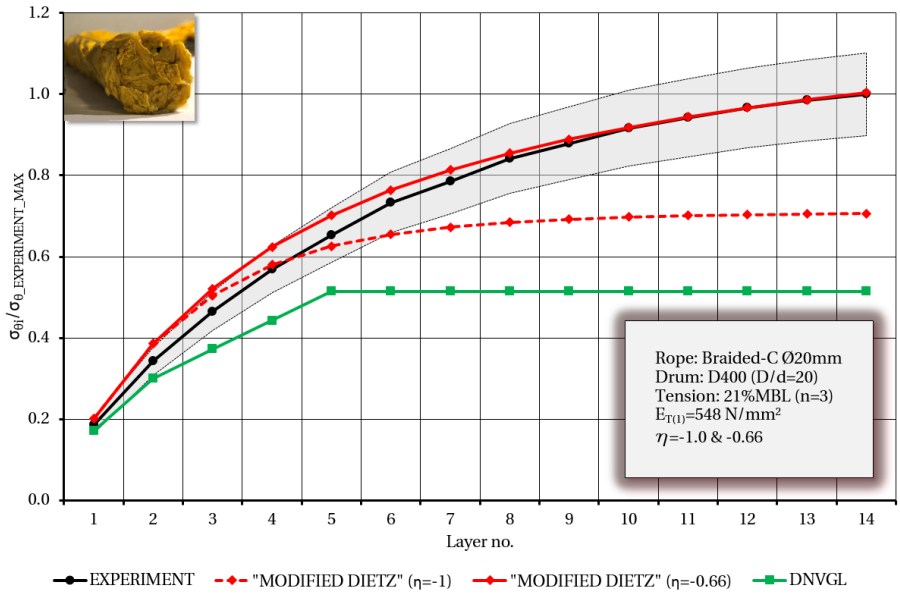

Figure 6.7: Calculations vs. experiment, σ_θ - Ø20 mm Braided-C on D400, 21% MBL

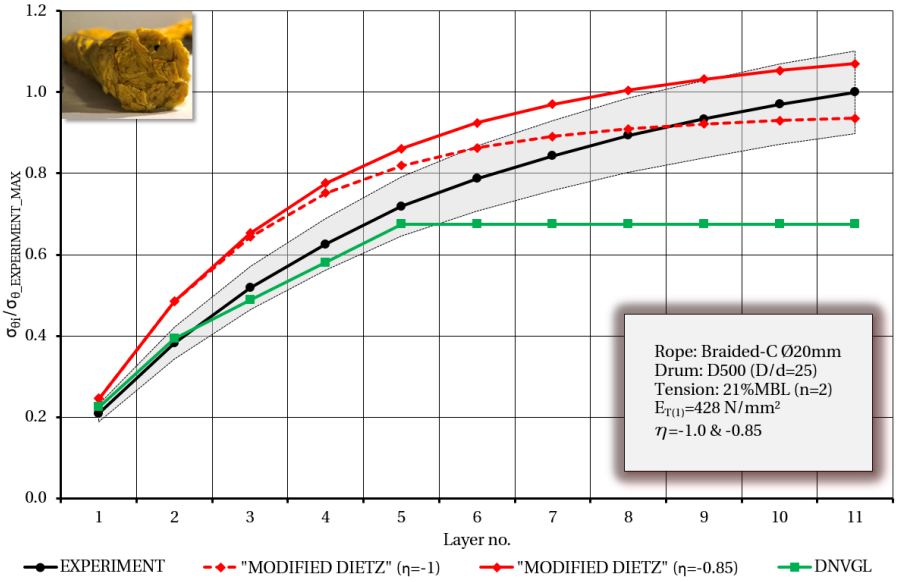

Figure 6.8: Calculations vs. experiment, σ_θ - Ø20 mm Braided-C on D500, 21% MBL

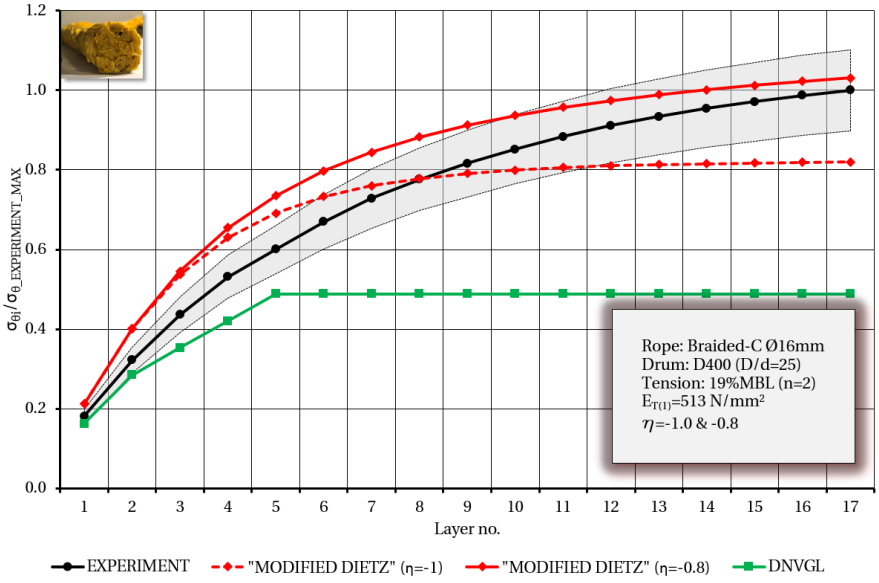

Figure 6.9: Calculations vs. experiment, σ_θ - Ø16 mm Braided-C on D400, 19% MBL

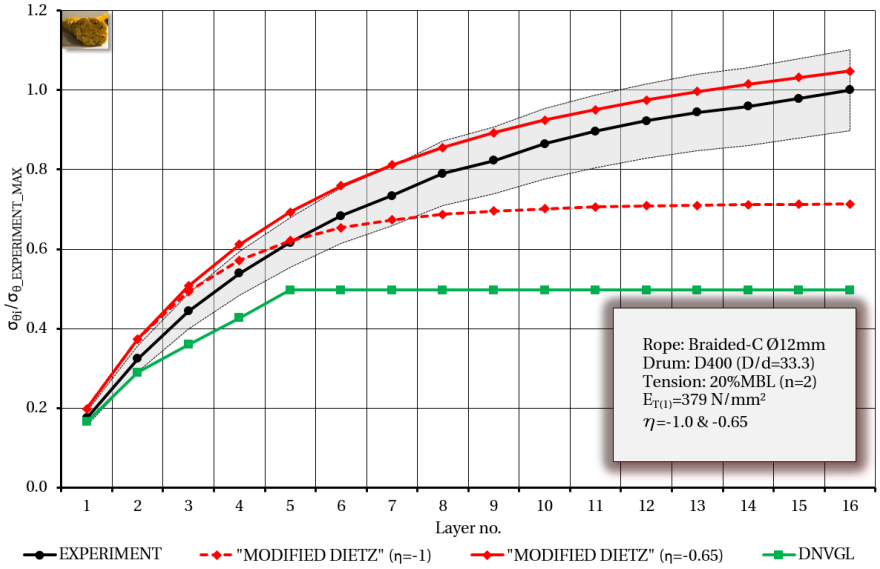

Figure 6.10: Calculations vs. experiment, σ_θ - Ø12 mm Braided-C on D400, 20% MBL

For D400, there are relatively good correspondences between calculations and the mean measured values when applying a multilayer exponent of -0.66. However, the calculations overestimate stresses slightly between two to seven layers on D400. For D500, the corresponding exponent is -0.85. On this drum, the overestimation is amplified and continues beyond eleven layers. Comparisons for Ø16 mm and Ø12 mm Braided-C with approximately 20% of MBL rope tension are shown in Figs. 6.9 and 6.10. The multilayer exponent for the Ø16 mm rope is -0.8 and not very different from the Ø20 mm rope. For the smallest rope, it is -0.65, which indicates a higher increase in rope package stiffness. These calculations overestimate the stresses for all rope layers.

In general, the "modified Dietz" method gives somewhat better results for D400 than D500 (see Appendix G). The accuracy of calculations also increases with increasing rope tension. The DNV GL method cannot assess stresses with reasonable accuracy for the pure braided ropes with more than 15-20% of MBL tension.

6.2 Discussion on tangential stress calculations

The evaluations show that the radial pressure on multilayer winch drums can be predicted reasonably by the "modified Dietz" method for ropes with relatively constant rope package stiffness ($\eta \approx -1$). The steel wire exhibits such properties, and to some extent, this method also yields good results for the Ø20 mm DimStable

rope. On the other hand, if constant rope package stiffness is assumed for the pure braided ropes, stresses are considerably underestimated when the number of layers exceeds four or five. Better agreement between calculations and measurements can be achieved by adjusting the multilayer exponent to account for a layer dependent, increasing rope package stiffness.

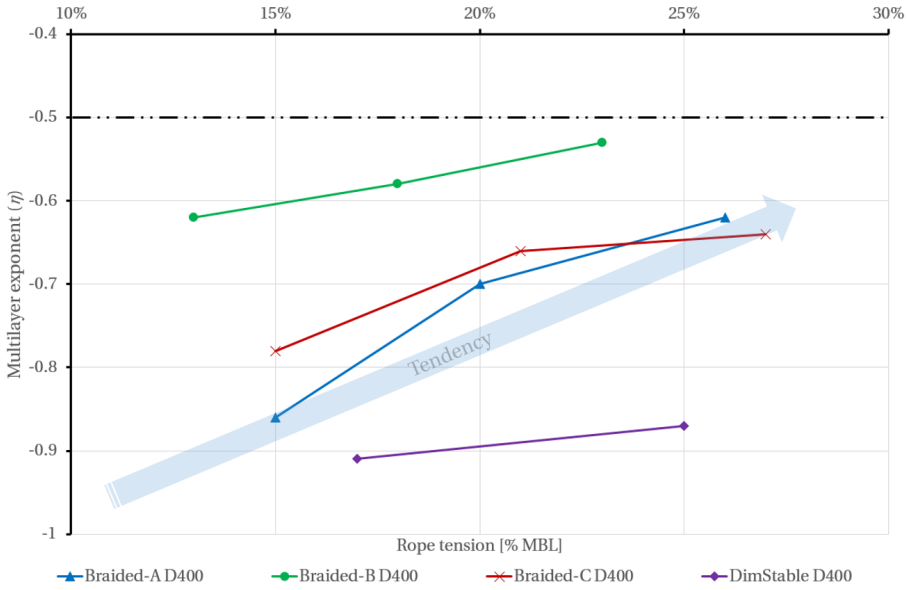

Figure 6.11: Multilayer exponents vs. rope tension - Ø20 mm HPSFR - D400 (D/d=20)

Figure 6.11 shows exponents matched to measurements at different rope tension levels for the Ø20 mm ropes on D400. These values are significantly different from the values from the experiments with linearly stacked ropes in Table 5.2. The tendency is similar for all ropes, and the rope package stiffness increases with increasing rope tension. The tendency is the same for these ropes on D500 (Appendix G, Fig. G.1). For some ropes on D500, there are only minor differences between multilayer exponents for different levels of rope tension. This can be a possible indication of the multilayer exponents converging.

The differences in multilayer exponents between rope sizes are illustrated in Fig. 6.12. For both DimStable and Braided-C, the smaller Ø12 mm ropes exhibit higher rope package stiffness than the larger ropes. Braided-C, with three rope sizes, discloses that this tendency is not unambiguous. The Ø16 mm rope exhibits lower exponents than the two other sizes, whose exponents are also relatively similar. The situation is similar on D500 but with smaller differences.

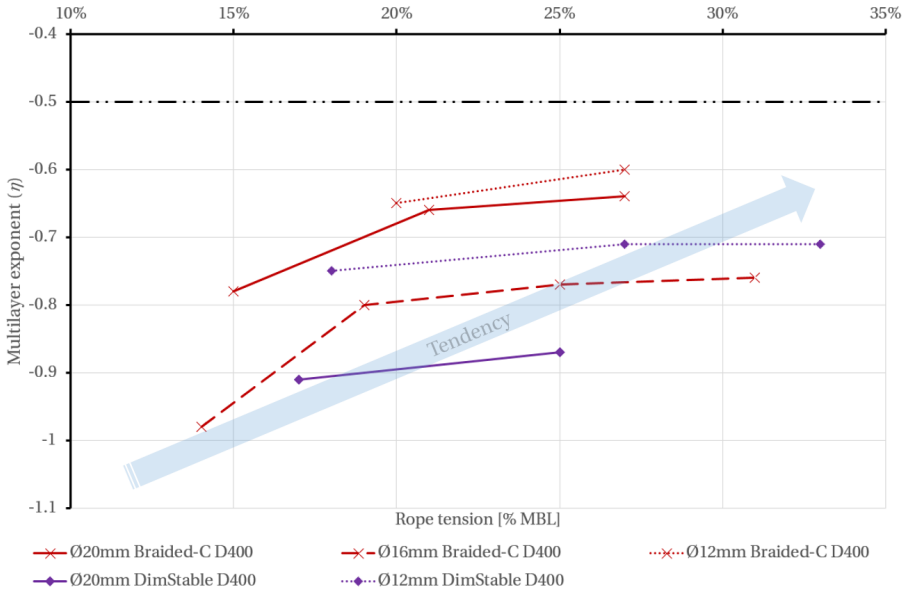

Figure 6.12: Multilayer exponents vs. rope tension - Ø12-Ø20 mm HPSFR - D400

The variation in multilayer exponents makes practical application of the "modified Dietz" method challenging for HPSFRs. Relevant multilayer exponents must be determined for different tension levels. This requires transverse stiffness testing of several rope layers in a configuration reflecting the actual conditions on the drum. Such a test arrangement is complicated. Possibly, a pyramid arrangement of linear ropes can give valid approximations. However, a significant, at present unknown number of layers are required to give valid information.

Figure 6.13 illustrates ropes as ideal springs with dampers in a pyramidal configuration. The ropes in each layer act parallelly, while the different layers act in series. The system stiffness and dampening can be described by the harmonic series, Eq. 6.2. Applying curve fitting using a power function gives an exponent of -0.5 for six layers and -0.6 for 20 layers which appear as reasonable magnitudes for the stiffness. However, no such situation is ideal due to, e.g. internal and external friction.

Based on observations from the experiments, a reasonable conservative limit for multilayer exponents is drawn at η=-0.5.

$$\frac{H_\infty}{n} = \Sigma_{k=1}^{\infty} \frac{1}{k} \tag{6.2}$$

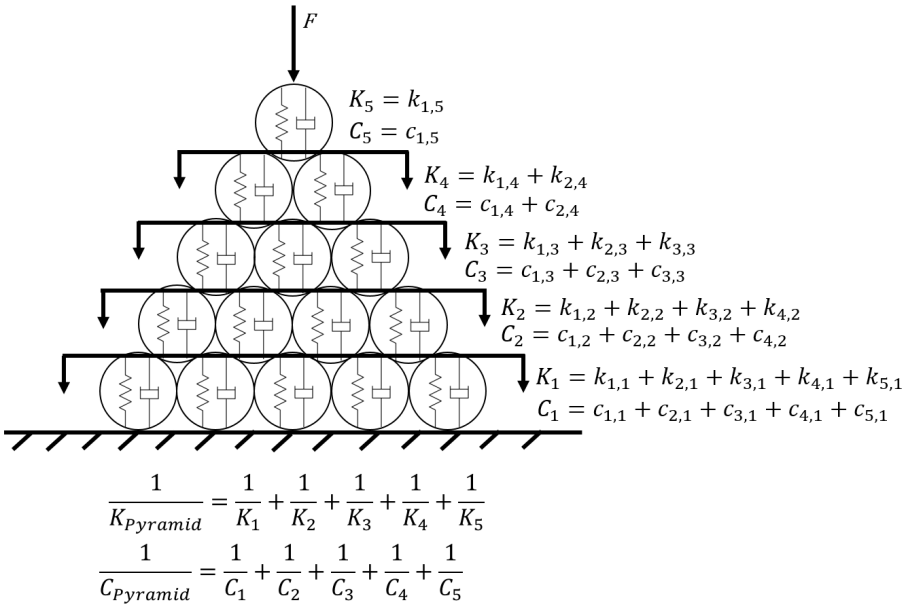

Figure 6.13: Ideal spring-dampers in ideal pyramidal configuration

Some of the adapted calculations with pure braided ropes result in relatively large deviations between calculated and measured stresses for a low number of layers. These deviations are particularly noticeable for the D500 drum, for smaller rope sizes and experiments with low rope tension levels. A possible explanation for this is that the applied transverse single rope moduli are too high. The moduli for the HPSFRs are determined by the same method as for steel wire ropes. In reality, during multilayer spooling, the relatively soft ropes are compressed by each other and not by rigid steel. Thus, it might be questioned if the applied measurements of transverse stiffness reflect the stiffness of HPSFRs during multilayer spooling realistically. On the other hand, a lower transverse modulus requires an even more aggressive stiffening of the rope package for the calculations to be comparable with the measurements.

Another non-linear development of rope package stiffness than the applied power-law function is also a possibility. Further, the evaluations are also based on the presumption that the "modified Dietz" method can assess the multilayer pressure with high accuracy for all cases. The deviations can, of course, be related to the complexity of spooling and the limitations of the calculation model itself.

Compared to the "modified Dietz" method, the DNV GL method is much simpler. This method is not dependent on knowledge of rope deformation and stiffness but

on relevant coefficients of rope layers. Generally, with a typical utilization factor of 20% of MBL or more, the DNV GL method underestimates the actual stresses for the pure braided fibre ropes. Remarkably, the DNV GL method, applying the equation for thin-walled cylinders (Eq. 2.6), calculates the stress in the first layer with reasonable accuracy for most cases. This is more or less by coincidence and related to the initial load-free windings and ramping of rope tension causing reduced stress in the first layer. On the other hand, one might argue that this reflects actual conditions on winches in service. However, it is expected that calculations based on classification rules should be conservative.

6.3 Summary - drum calculations

The evaluations of stress calculations show that current design guidelines specified by class societies are not applicable for multilayer winch drums with HPSFRs. The more sophisticated method by Dietz [7], modified for HPSFR by Lohrengel et al. [8], can assess the radial pressure with reasonable accuracy. However, this depends on a multilayer exponent relevant for th levels actual rope/drum system. At present, the determination of such relevant multilayer exponents is not considered possible without measurements of multilayer spooling tests of the actual rope/winch system.

The resulting peak tangential stress in the drum is effectively calculated employing the equation for thick-walled cylinders exposed to external radial pressure.

These evaluations partly fulfil research objectives RO2 and RO4 and answer RQ2 and RQ3 regarding radial pressure on multilayer winch drums.

Chapter 7

Evaluation of flange force calculations

Three methods for the assessment of flange forces are evaluated. These methods are; Dietz' "climbing of the last winding" [7], DNV GL's variable pressure distribution [3] and Mupende's method [16].

7.1 Stresses in flanges

The evaluations are based on von Mises stresses calculated using linear-elastic FEA. Calculated stresses are extracted from points equivalent to the locations of the strain gauges on the flanges and compared with average stresses derived from repeated experiments. Deformations measured at the outer end of the free-end flange and axial stresses derived from measured strains in the drum are also compared with calculations.

The flange loads are simplified, and in general 2D axisymmetric FEA is applied. However, the effects of more realistic asymmetric flange forces are investigated using 3D solid FEA for the steel wire rope.

Flange forces are applied as either axial line forces on the middle radius of each completed layer (Dietz & Mupende) or distributed pressures (DNV GL). Radial pressures on the drums are calculated by the "modified Dietz" method with multilayer exponents empirically adapted to measurements (Chapter 6).

Three different Ø20 mm ropes are subjected to investigation on both test drums; the steel wire, DimStable and Braided-C. Evaluations are carried out for each completely spooled rope layer.

7.1.1 Dietz' method - "climbing of the last winding"

With constant rope tension, T, Dietz' theory (Section 3.1.6) results in equivalent forces N_i for all layers i, Eq. 7.1.

$$N_i = 1.2\pi T \tag{7.1}$$

7.1.2 Flange forces according to DNV GL

DNV GL's pressure variation is described in Section 3.1.16 and the maximum pressure is calculated employing Eq. 3.102.

7.1.3 Mupendes' climbing and parallel sectors

Mupende's equations (Section 3.1.12) allow for varying forces for each layer in different sectors on the flanges. In the current calculations, multilayer tension reduction effects are included by applying tension reduction factors Ψ_i for each layer i, Eq. 7.2.

$$\Psi_i = \frac{T_i - \Delta T_i}{T_i} \tag{7.2}$$

The total flange force in each layer R_k is calculated by Eq. 7.3 employing Eq. 7.4 for elliptic rope profile shapes (Fig. 3.29).

$$\begin{aligned} R_k = \frac{T_k \Psi_k}{2\pi r_k} \int_0^{\varphi_c} \frac{(cot\alpha - \mu_r)}{(1 - \mu_r\mu + (\mu_r + \mu)cot\alpha)} d\varphi + \\ + \frac{\varphi_p}{2\pi} \frac{cot\alpha_0 - \mu_r}{(1 - \mu_r\mu + (\mu_r + \mu)cot\alpha_0)} \sum_{i=k}^{n} \frac{T_i \Psi_i}{r_i} \end{aligned} \tag{7.3}$$

$$tan\alpha_0 = \frac{d_y \sqrt{4d_x^2 - a^2}}{d_x a} \tag{7.4}$$

Friction coefficients for the HPSFRs are estimated from the fitted curves in Fig. 5.1.3 using the average pressure on the drum in the first layer. For the steel wire rope, a value of 0.18 is assumed and applied for both friction parameters.

The sizes of climbing and parallel sectors are estimated from the drum laser measurements. The climbing sectors are approximately 60° for all ropes, while there are more significant differences between the parallel sectors. The rigid construction of the steel wire ensures proper spooling resulting in a large parallel sector,

and the total contact angle is conservatively approximated to fully 360°. For the HPSFRs, the spooling patterns close to the flanges and during climbing were typically not perfect, particularly with many layers of pure braided ropes. Therefore, smaller parallel contact angles are applied for the HPSFRs. For the DimStable rope, the parallel sectors are estimated to 210°, while the corresponding value for Braided-C is 180°.

7.1.4 Transfer of reaction forces during rope climbing

During spooling on the test drums, contact between rope and the free-end flange occurs for every odd-numbered layer and contact with the fixed-end flange for every even-numbered layer. The measurements show that the axial stress increases for each layer, but no reactions are visible in the opposite flange during rope climbing, Fig. 7.1. This means that reaction forces are not distributed horizontally through the rope package. At least not through the layers at or above the radius of the strain gauges on the flanges. Thus, it is assumed that reaction forces are transferred through friction at the outer drum surface.

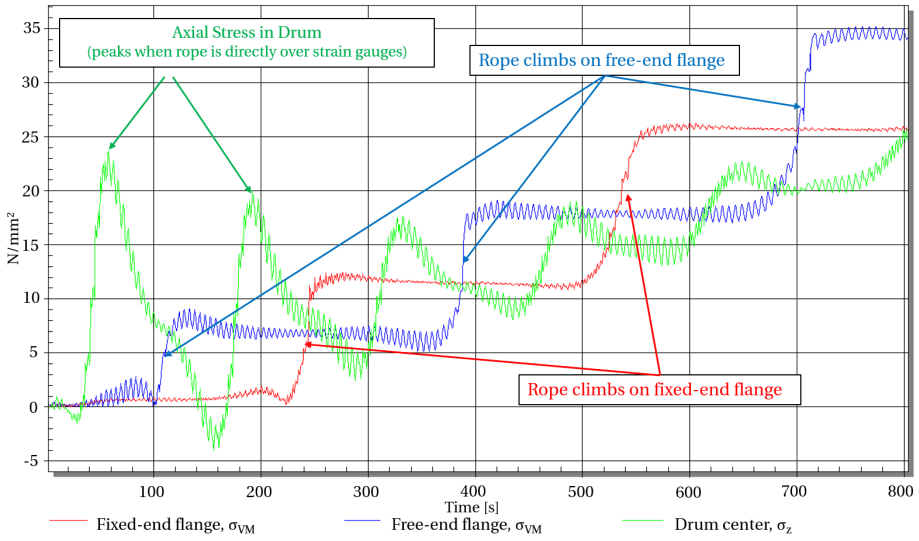

Figure 7.1: Example of stresses showing no force transfer between flanges

Concerning FEA, the rope package is not modelled. Due to differences in forces and force magnitudes on the flanges, the axial forces are not in equilibrium. Therefore, reaction forces equivalent to the force differences are applied at the drum surface. This applies to the calculation methods by Dietz and Mupende.

7.1.5 Flange stress calculations - steel wire rope

Figures 7.2 and 7.3 show stresses calculated according to Dietz' method compared with experimental results for the steel wire on D400. The stresses for each layer are plotted relative to the maximum stress derived from measured strain in the flange on the fixed end of the drum. The measured values are based on averages from n repeated experiments. The error bars indicate the estimated stress measurement uncertainty of 10.2%.

Asymmetric loading is evident for the flange at the fixed end of the drum but more discrete on the free end. The calculated stresses are reasonable and with a relatively good match from six layers and beyond. The results are somewhat better for the flange on the fixed end than on the free end with few rope layers.

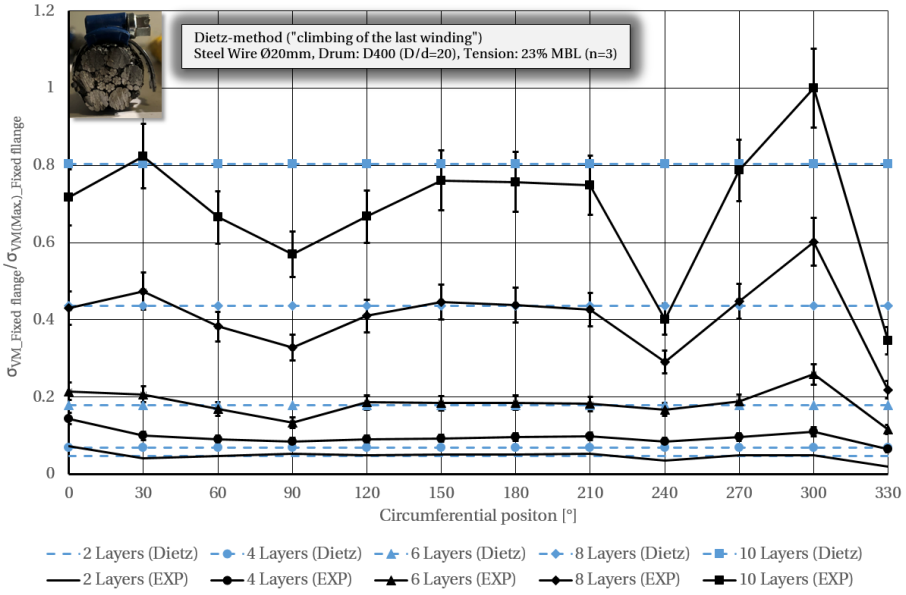

Figure 7.2: Calc. vs. exp. - σ_{VM} - Ø20 mm steel wire, D400, fixed end, 23% MBL

The three calculation methods are compared in Figs. 7.4 and 7.5 for D400 and D500, respectively. The figures show calculated von Mises stresses relative to both measured average stresses around the circumference and peak values for each layer. The dotted line indicates the experimental values for each layer (target values for each bar). It replaces numerous bars of unit magnitude in each plot.

With less than six layers, the results are relatively similar for all three methods. The more significant differences between average and maximum stresses in the fixed-end flange are also noticeable. However, the calculated values are, in general,

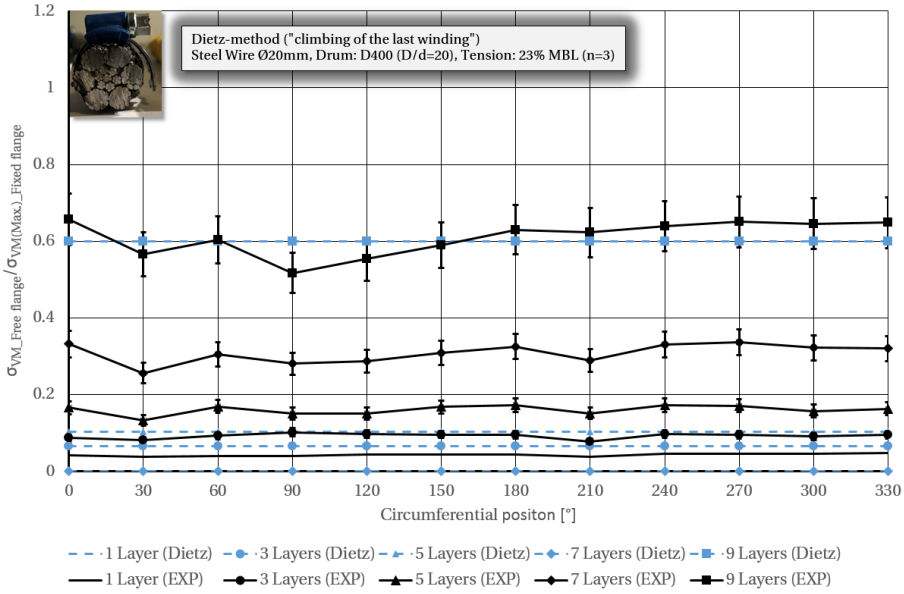

Figure 7.3: Calc. vs. exp. - σ_{VM} - Ø20 mm steel wire, D400, free end, 23% MBL

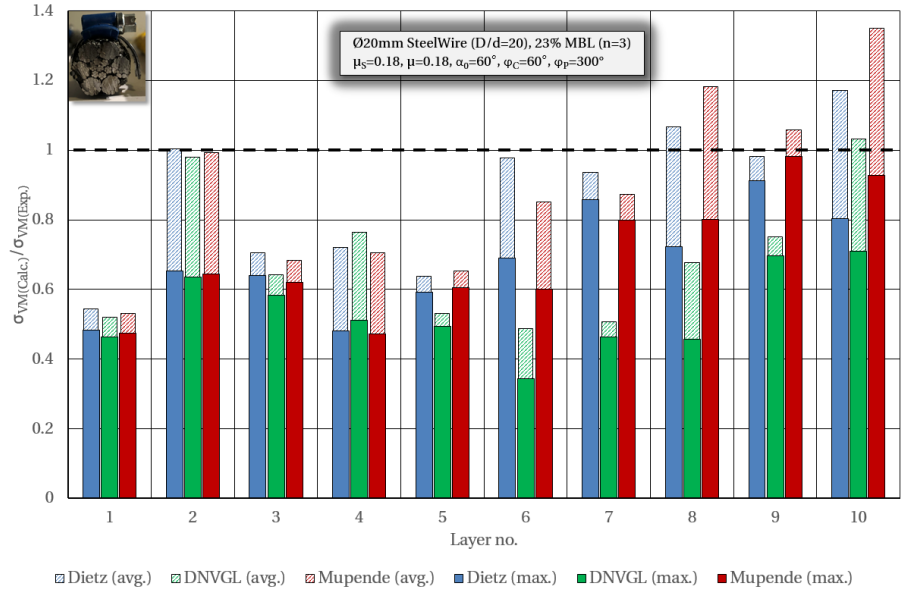

Figure 7.4: Calc. methods - σ_{VM} - Ø20 mm steel wire, D400, 23% MBL

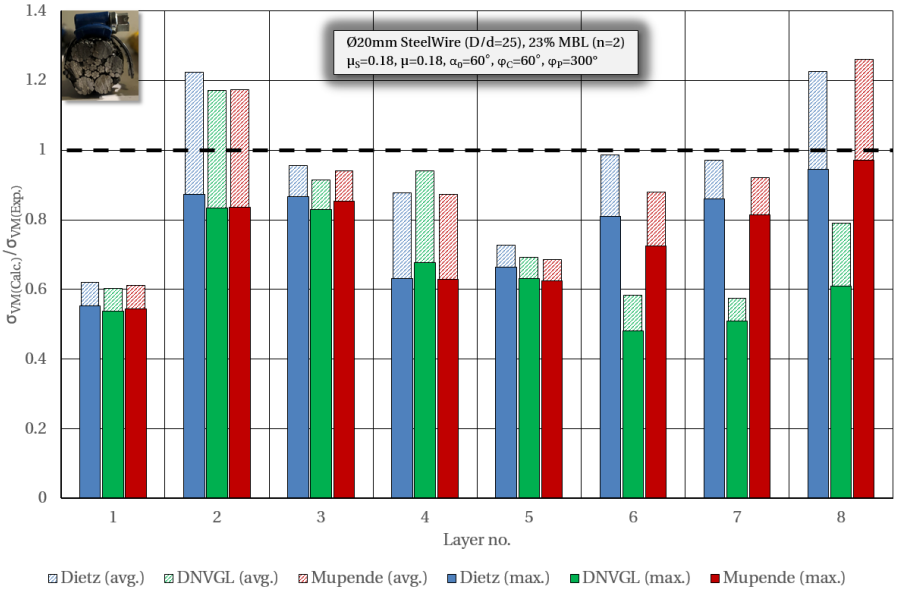

Figure 7.5: Calc. methods - σ_{VM} - Ø20 mm steel wire, D500, 23% MBL

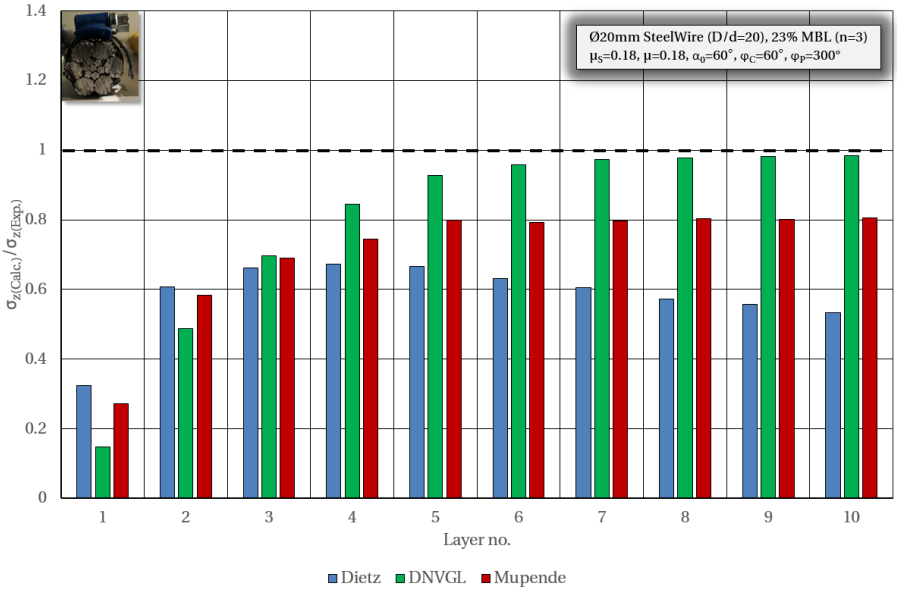

Figure 7.6: Calc. methods - σ_z - Ø20 mm steel wire, D400, 23% MBL

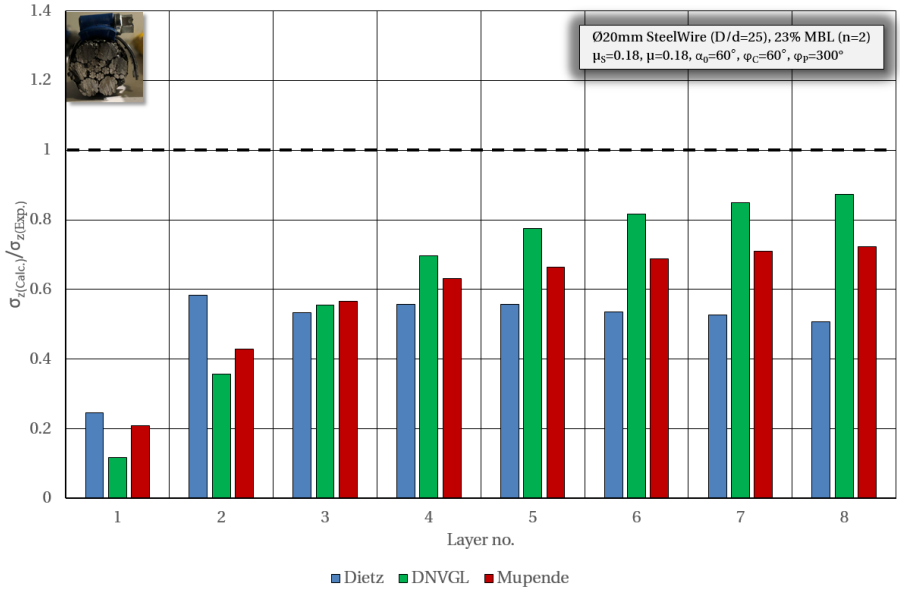

Figure 7.7: Calc. methods - σ_z - Ø20 mm steel wire, D500, 23% MBL

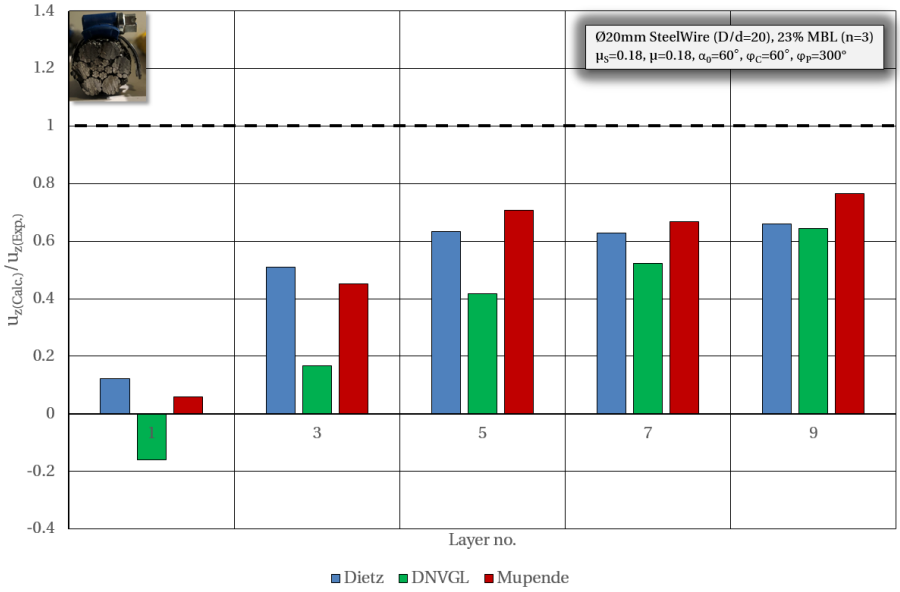

Figure 7.8: Calc. methods - u_z - Ø20 mm steel wire, D400, 23% MBL

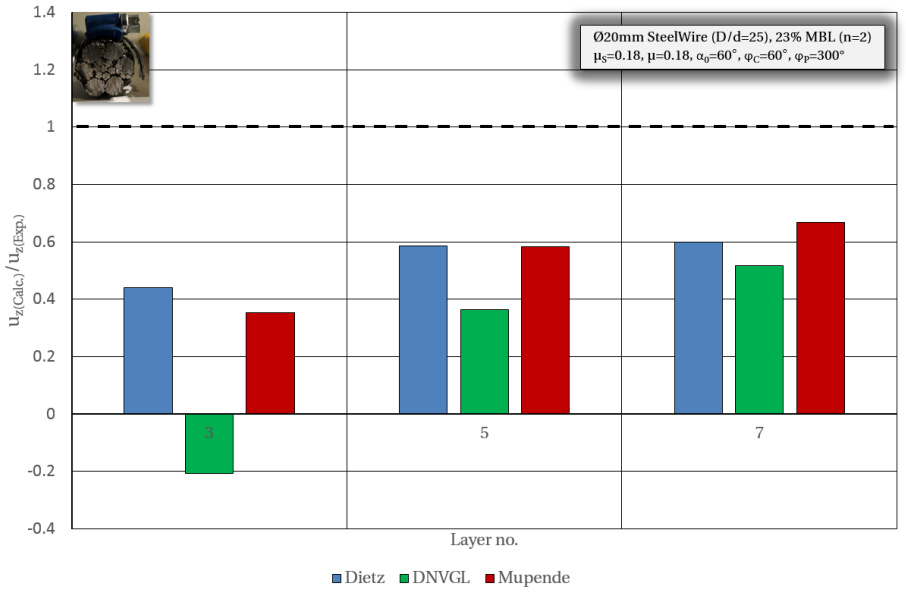

Figure 7.9: Calc. methods - u_z - Ø20 mm steel wire, D500, 23% MBL

too low. The match between Dietz' and Mupende's methods and measurements are better than the DNV GL method from five layers. The latter only calculates approximately 35-45% of the measured maximum stress with six and seven layers on D400. Deviations between calculations and measurements decrease with an increasing number of layers. With ten layers, Mupende's method overestimates the average stresses by approximately 35%. The tendency is similar for D500 but with somewhat reduced deviations.

Considering axial stresses in the drums, Figs. 7.6 and 7.7, DNV GL's and Mupende's methods yield better results than the Dietz method. For D400, the DNV GL method gives a close match from six layers and beyond, while the results from Mupende's equations underestimate the experimental results by approximately 20%. The deviations between axial stress calculations and measurements are larger for D500 than D400.

Displacements of the free-end flange are compared to measurements and shown in Figs. 7.8 and 7.9. As with the flange stresses, calculations based on Dietz and Mupende's theories give better results than the DNV GL method. However, neither of the methods calculate the average displacements with particularly high accuracy.

Asymmetric flange loading

An investigation of asymmetric loading according to Mupende's theory was carried out for the steel wire rope on D500. Figure 7.10 shows an example of flange deformations (up-scaled) where the asymmetry is apparent. Consequently, there is also asymmetry related to the tangential and radial stress tensors in the flanges.

The calculated stresses reflect the stress distribution tendencies relatively good for both flanges, Figs. 7.11 and 7.12. The match between experimental and calculated peak values are good.

Mupende's flange force equations applied with asymmetric loading prove their relevance, and further refinements can possibly increase accuracy.

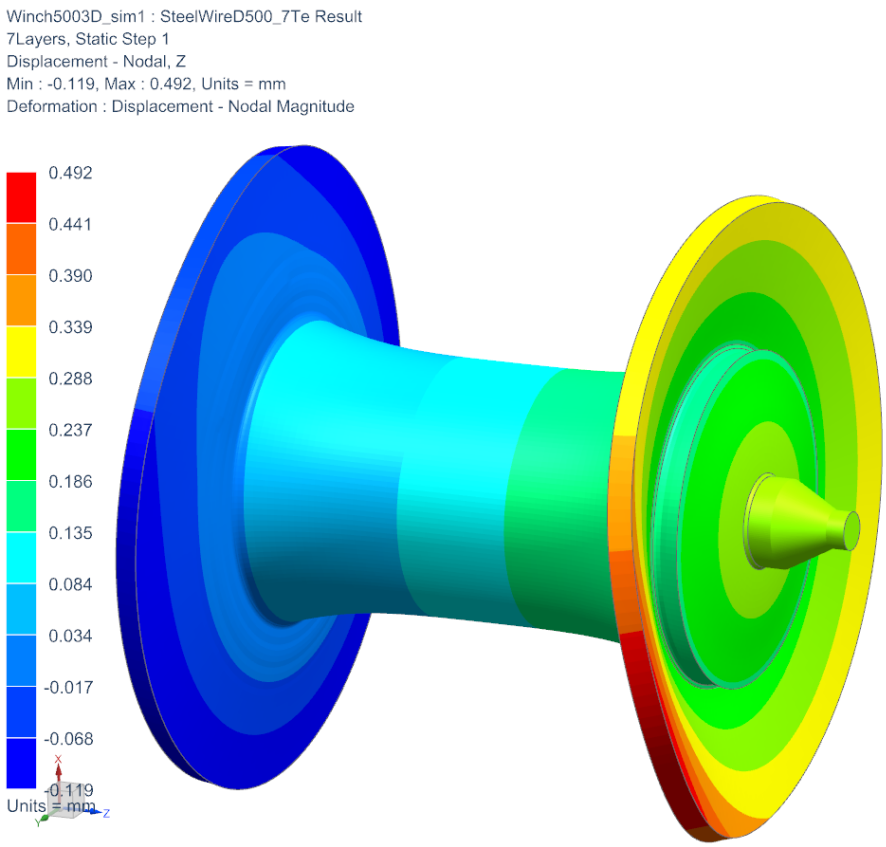

Figure 7.10: Asymmmetric flange loads - Ø20 mm steel wire, D500, 23% MBL

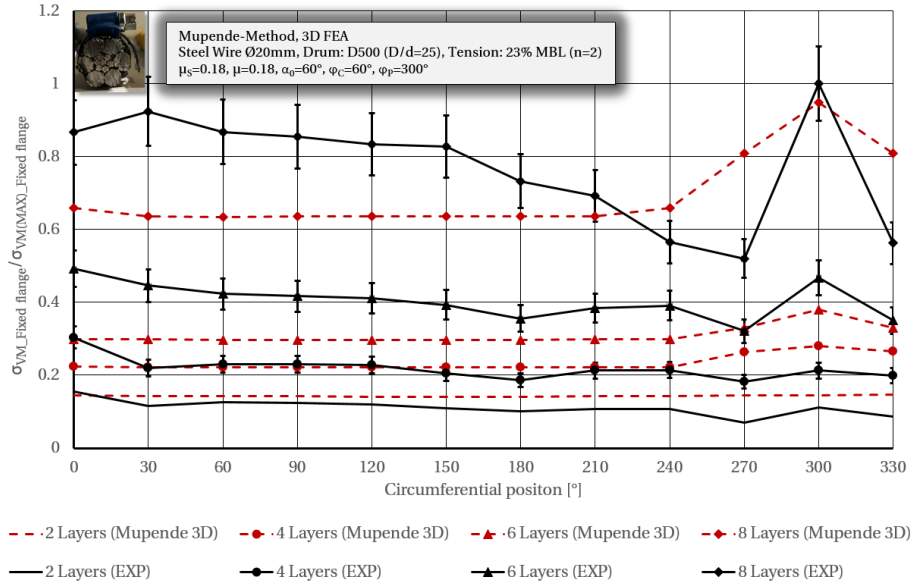

Figure 7.11: Mupende vs. exp. - σ_{VM} - Ø20 mm steel wire, D500, fixed end, 23% MBL

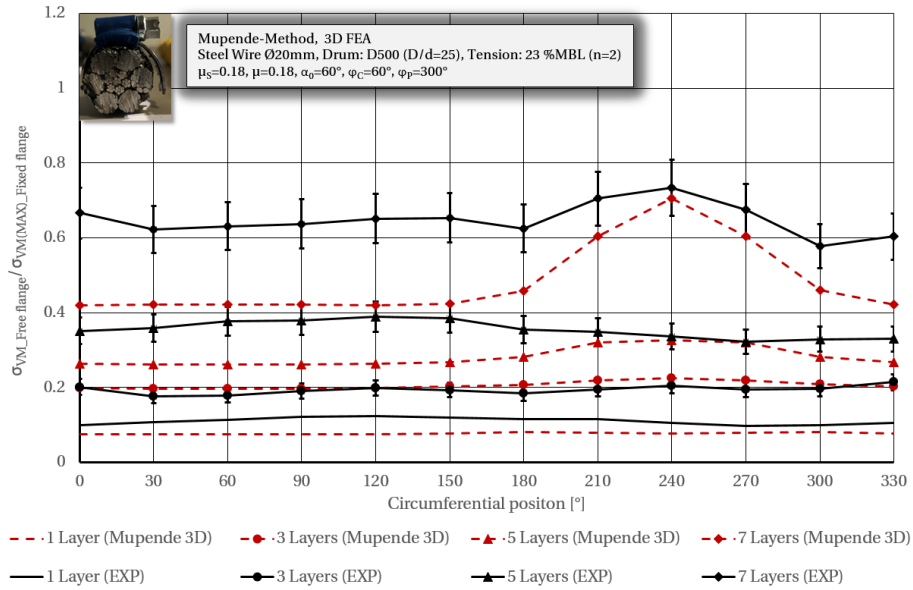

Figure 7.12: Mupende vs. exp. - σ_{VM} - Ø20mm steel wire, D500, free end, 23%MBL

7.1.6 Flange stress calculations - DimStable

Calculations according to DNV GL and measured stresses in flanges from the DimStable rope on D400 are shown in Figs. 7.13 and 7.14. The stress distribution around the circumference of the fixed-end flange is similar to the steel wire rope, while stresses in the free-end flange are more evenly distributed. The calculated stresses are about 60% of the measured maximum value for the fixed-end flange with ten rope layers and 40% for the free-end flange with nine rope layers.

None of the three methods yields good results compared with measurements, Figs. 7.15 and 7.16. As with the steel wire, the differences in stresses calculated by the three methods are relatively small for the first five layers on both drums. Calculations for the D500 drum are also somewhat closer to the measured stresses than for the D400 drum. With an increasing number of layers, Mupende's equations give better results than the others. However, approximately seven to nine layers are required to reach values conservative to the measured.

For the D400 drum, the Mupende-method calculates flange deformations within approximately 80% of the measured values, Fig. 7.17. The values for D500 are smaller, and there are also a couple of questionable outliers, Fig. 7.18.

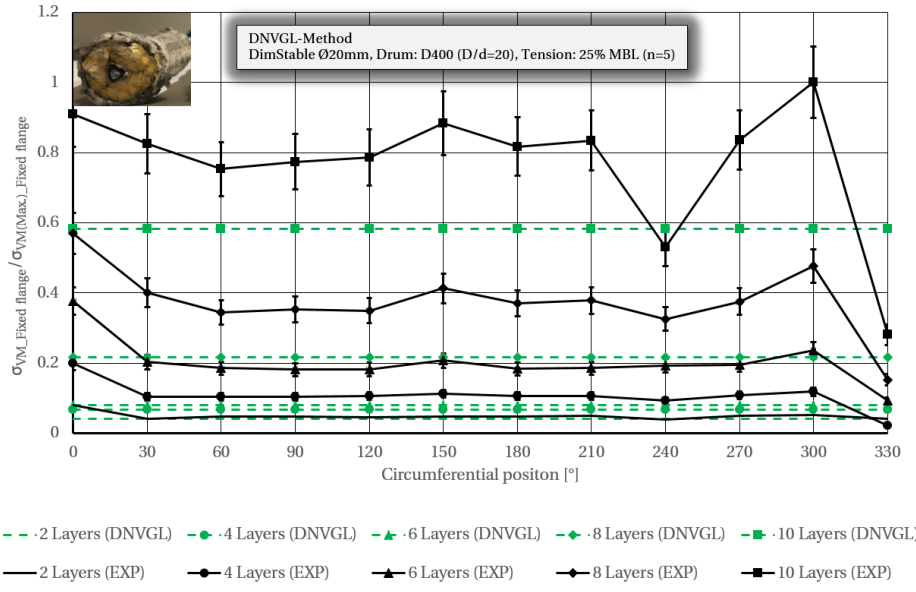

Figure 7.13: Calc. vs. exp. - σ_{VM} - Ø20 mm DimStable, D400, fixed end, 25% MBL

Considering axial stresses in the drums, the Mupende-method overestimates the values with few rope layers, Figs. 7.19 and 7.20. With an increasing number of

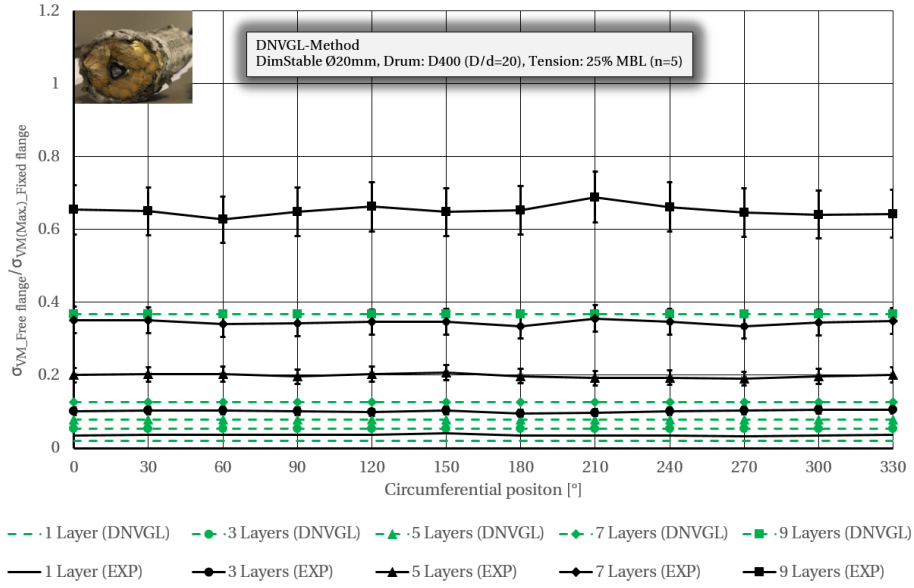

Figure 7.14: Calc. vs. exp. - σ_{VM} - Ø20 mm DimStable, D400, free end, 25% MBL

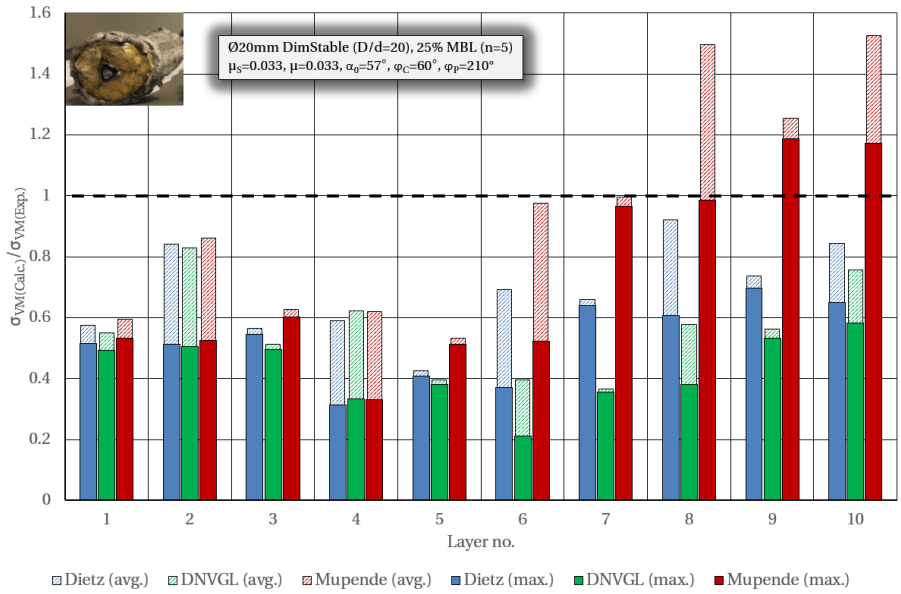

Figure 7.15: Calc. methods - σ_{VM} - Ø20 mm DimStable, D400, 25% MBL

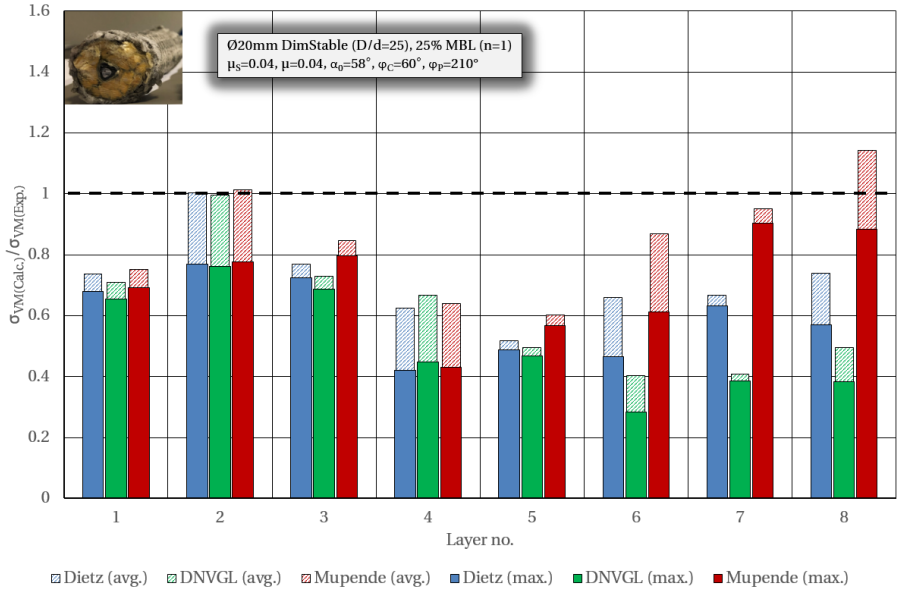

Figure 7.16: Calc. methods - σ_{VM} - Ø20 mm DimStable, D500, 25% MBL

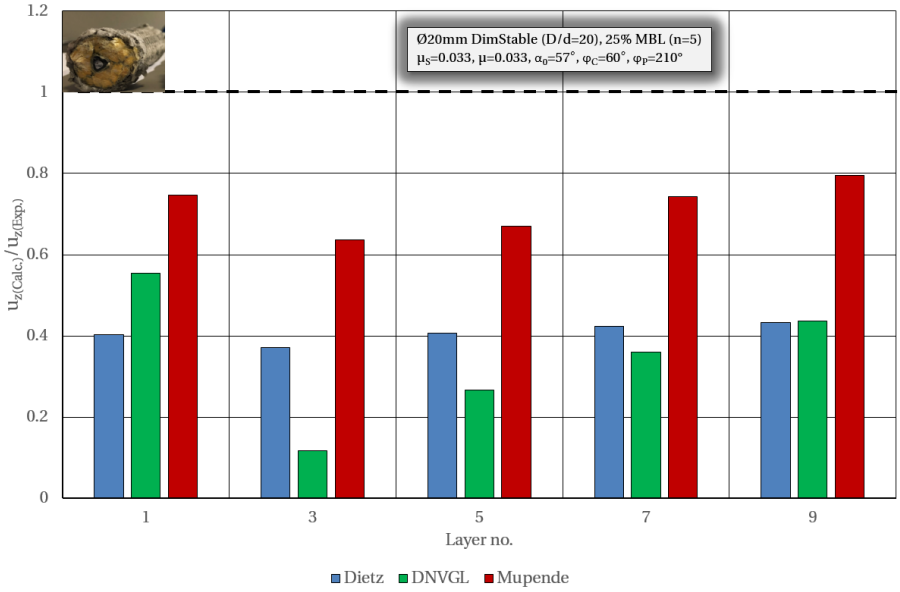

Figure 7.17: Calc. methods - u_z - Ø20 mm DimStable, D400, 25% MBL

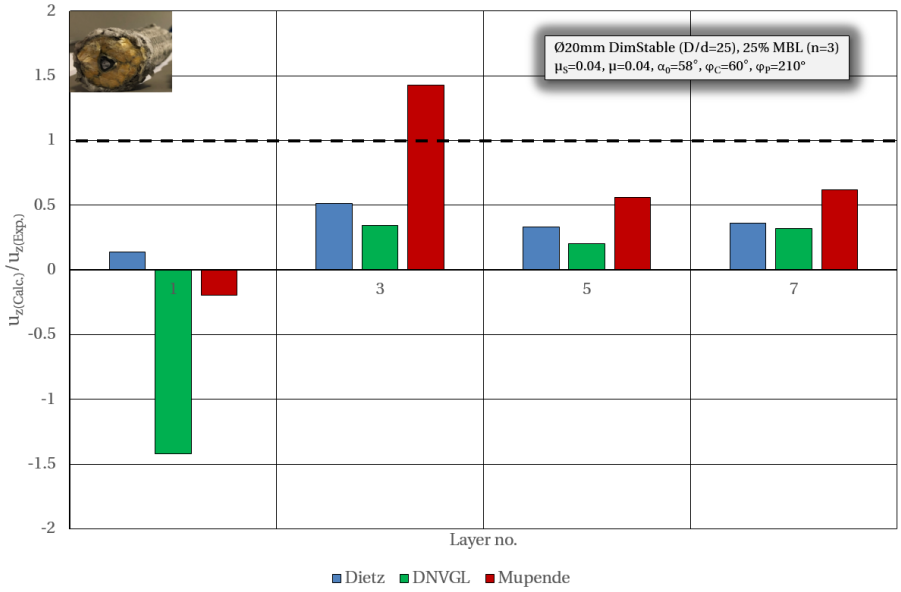

Figure 7.18: Calc. methods - u_z - Ø20 mm DimStable, D500, 25% MBL

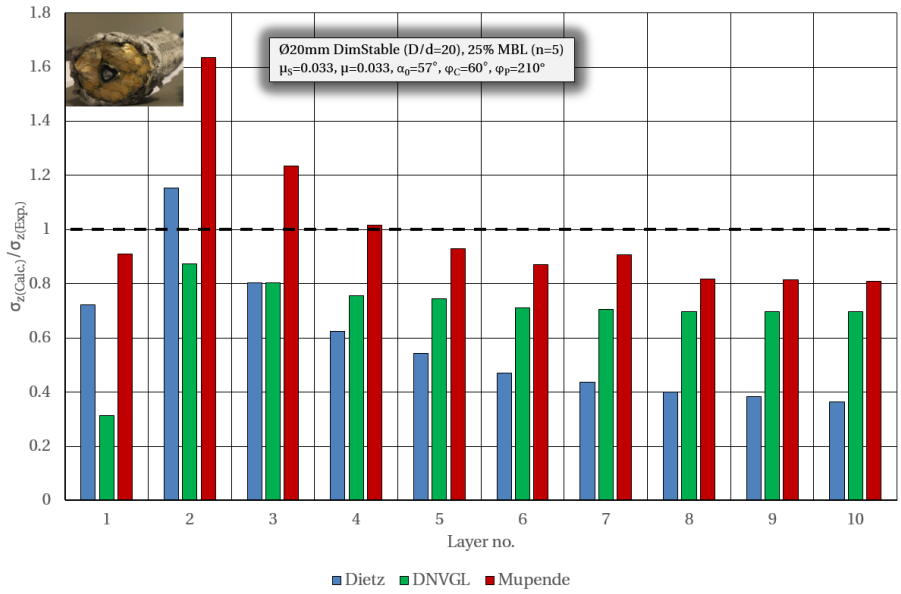

Figure 7.19: Calc. methods - σ_z - Ø20 mm DimStable, D400, 25% MBL

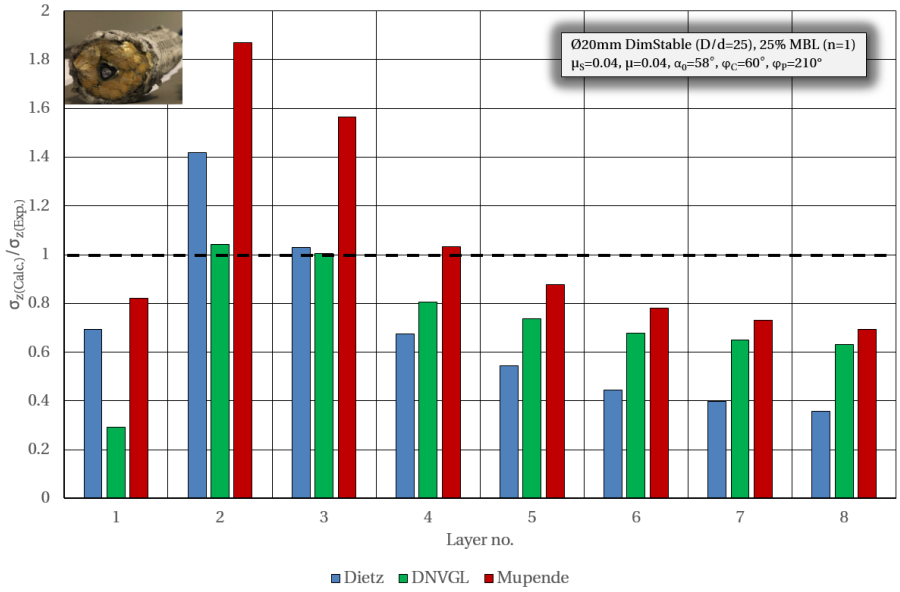

Figure 7.20: Calc. methods - σ_z - Ø20 mm DimStable, D500, 25% MBL

layers, this method gives results closer to the measured. However, all calculations underestimate the stresses when the number of layers increases.

7.1.7 Flange stress calculations - Braided-C

Figures 7.21 and 7.22 show stresses induced in the flanges of D400 and values calculated by Mupende's equations when subjected to spooling with the more deformable Braided-C rope. Compared to the two other ropes, stresses in the free-end flange of the drum are even more smoothly distributed. On the opposite flange, the stresses still show signs of distinct asymmetric load distribution.

The comparisons shown in Figs. 7.23 and 7.24 disclose that neither the DNV GL method, nor the Dietz method calculate stress values close to the measured values for D400. On the other hand, all methods yield better results for D500. With an increasing number of layers, Mupende's equations calculate too high stresses.

Comparisons of axial stresses are shown in Figs. 7.25 and 7.26. The results are similar to the DimStable results. At first, Mupende's equations overestimate the axial stresses. When the number of layers increases, there is a shift and stresses are underestimated. The two other methods underestimate the values for practically all layers.

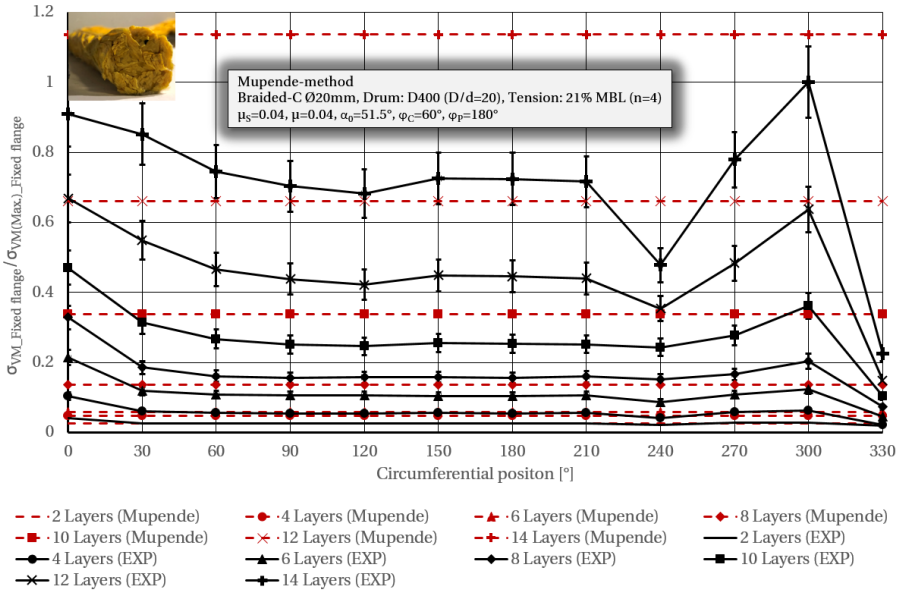

Figure 7.21: Calc. vs. exp. - σ_{VM} - Ø20 mm Braided-C, D400, fixed end, 21% MBL

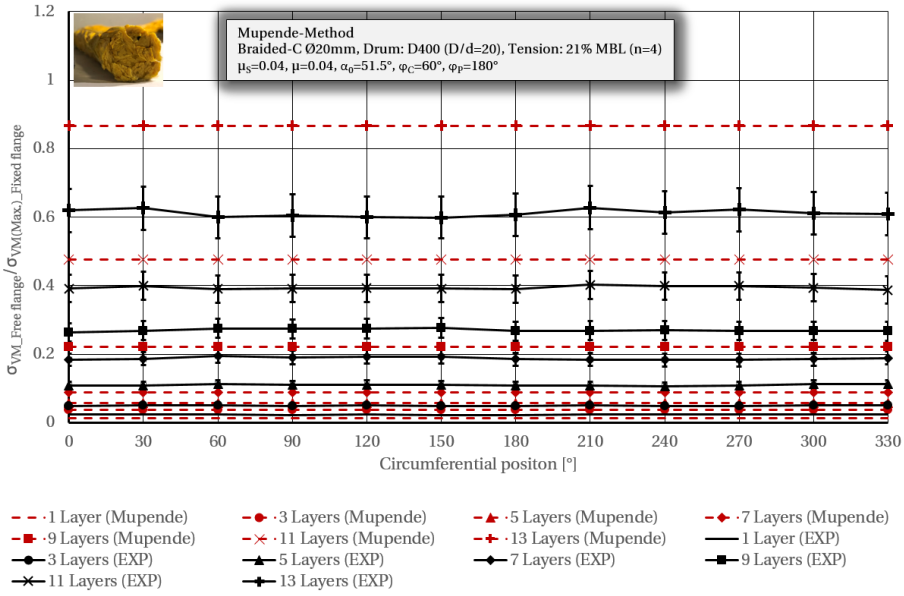

Figure 7.22: Calc. vs. exp. - σ_{VM} - Ø20 mm Braided-C, D400, free end, 21% MBL

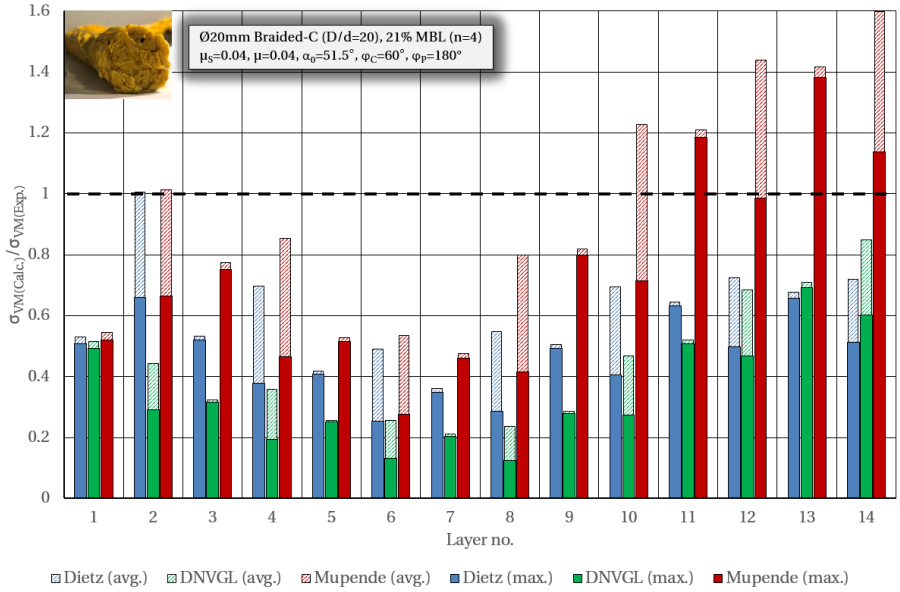

Figure 7.23: Calc. methods - σ_{VM} - Ø20 mm Braided-C, D400, 21% MBL

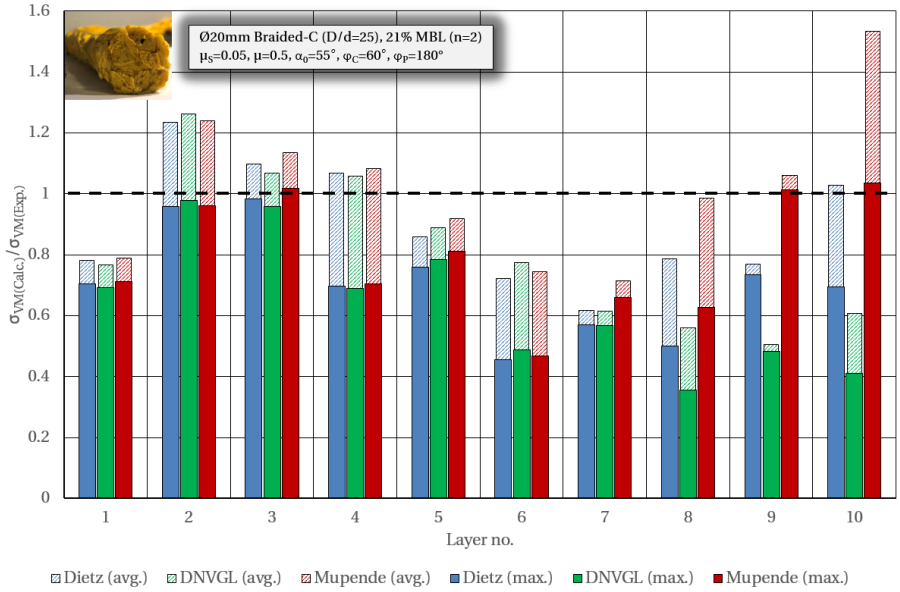

Figure 7.24: Calc. methods - σ_{VM} - Ø20 mm Braided-C, D500, 21% MBL

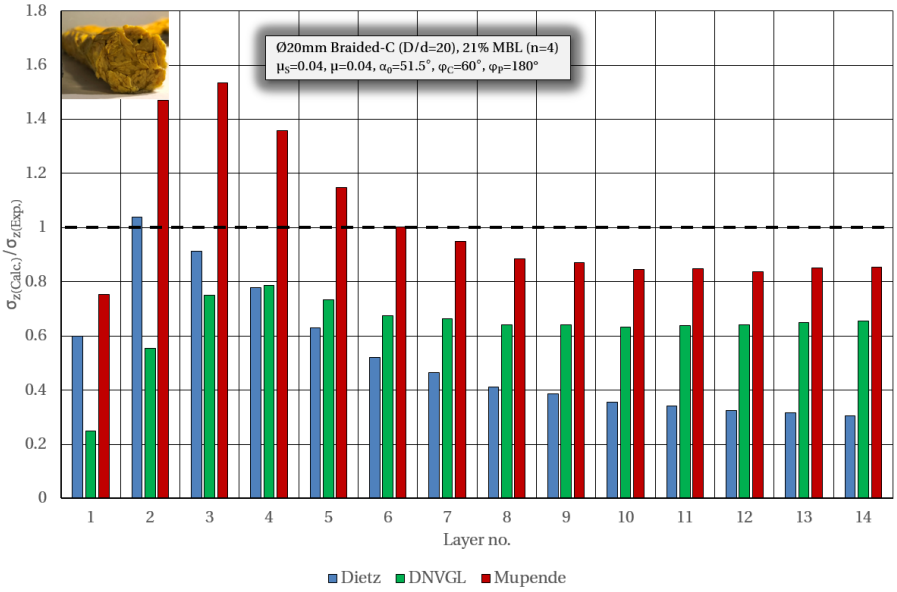

Figure 7.25: Calc. methods - σ_z - Ø20 mm Braided-C, D400, 21% MBL

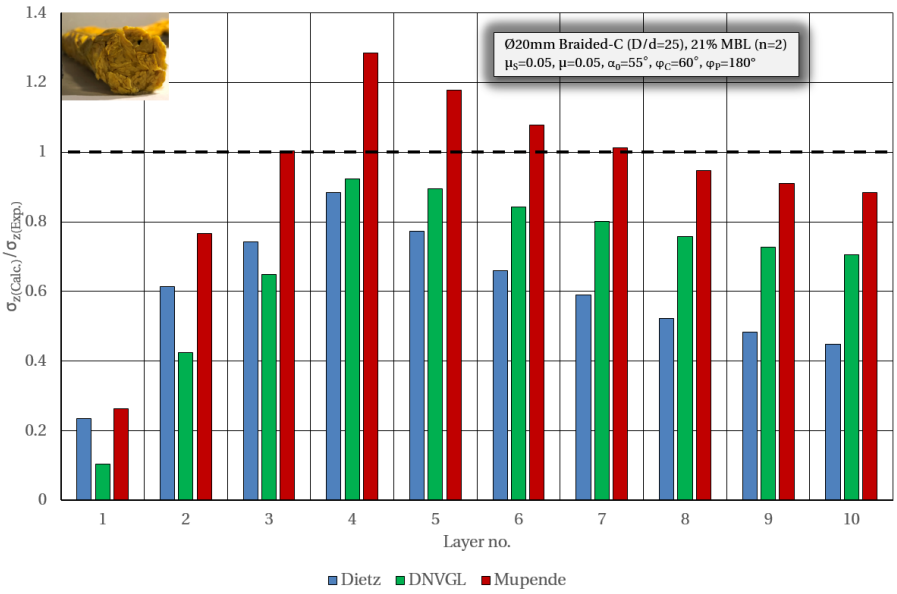

Figure 7.26: Calc. methods - σ_z - Ø20 mm Braided-C, D500, 21% MBL

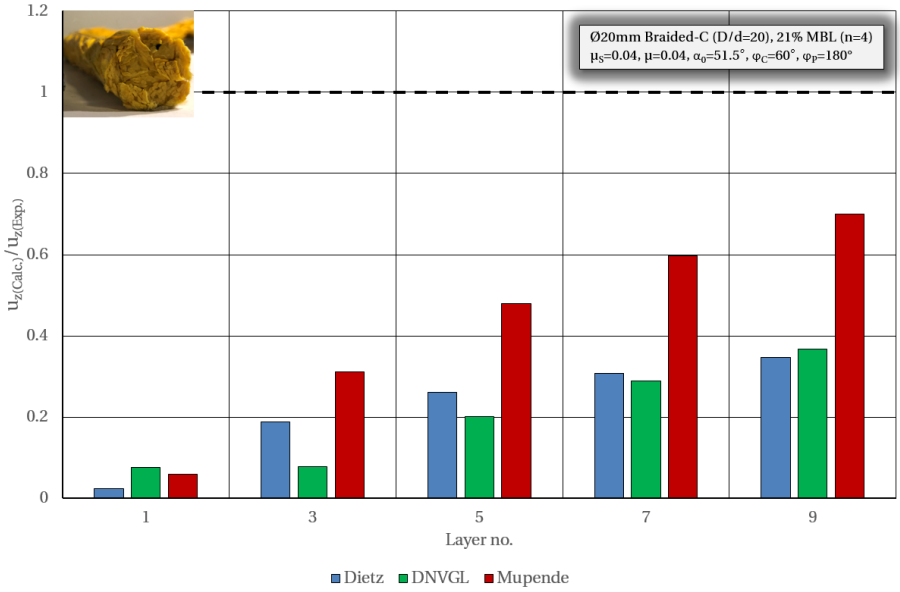

Figure 7.27: Calc. methods - u_z - Ø20 mm Braided-C, D400, 21% MBL

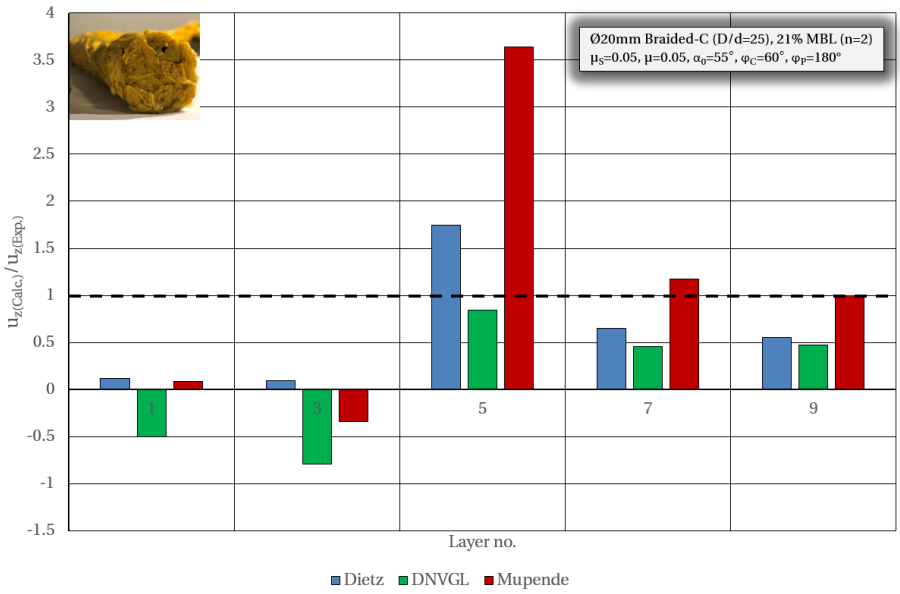

Figure 7.28: Calc. methods - u_z - Ø20 mm Braided-C, D500, 21% MBL

The differences between measured and calculated displacements decrease with an increasing number of layers for the D400 drum, Figs. 7.27. The values calculated by Mupende's equations are closest to the measured. At the same time, the values from the two other methods are smaller and more comparable. However, the match relative to the measured values is not good for any of the three methods. For the D500 drum, there are large discrepancies, and the results for this case are questionable, Fig. 7.28.

7.2 Discussion on flange stress calculations

None of the three calculation methods for flange forces yields good accuracy relative to the measured values for any of the ropes. There are relatively large discrepancies between the different layers, and the stresses for the first layers are consistently too low. There can be several reasons for this. The most obvious reason is the axisymmetric simplification of an asymmetric load condition. Further, there are limitations related to all calculation methods and the application of these. Neither variation in radius within each layer nor potential variation in parameters, e.g. friction, are considered. In addition, flange forces are calculated without considering potential effects from the deformation of drum, flanges or rope package. The results can also be influenced by variations in spooling quality close to the flanges.

The relatively poor results from Dietz's method when applied with fibre ropes are expected and related to too high friction coefficients relevant for such ropes. This method is also limited to forces during rope climbing only. Mupende's method directly allows for variation of parameters as friction, climbing- and parallel sectors and rope package angle. However, the applied friction values and the sizes of climbing- and parallel sectors are only estimates. Measurement of friction values below 0.05 is considered technically challenging. Some of the applied values for coefficients of friction can therefore be unrealistic.

However, the most suspicious is the strange wave-like tendencies of the calculations relative to the measured values. Investigation of principal stresses shows that disturbances from the flange-drum transitions might influence the strain gauge measurements on the flanges, Fig. 7.29. With increased loading, the "disturbed stress field" grows radially outwards from the notch at the drum-flange transition causing changed directions of principal stresses at the point of measurement. In the axisymmetric analysis, the principal stress directions are shifted by 90°.

The situation is different for the more realistic analysis applying non-symmetric loads, as shown in Fig. 7.30. This figure shows an example of principal stress tensors along a line from the notch to the locations of the strain gauges. With non-

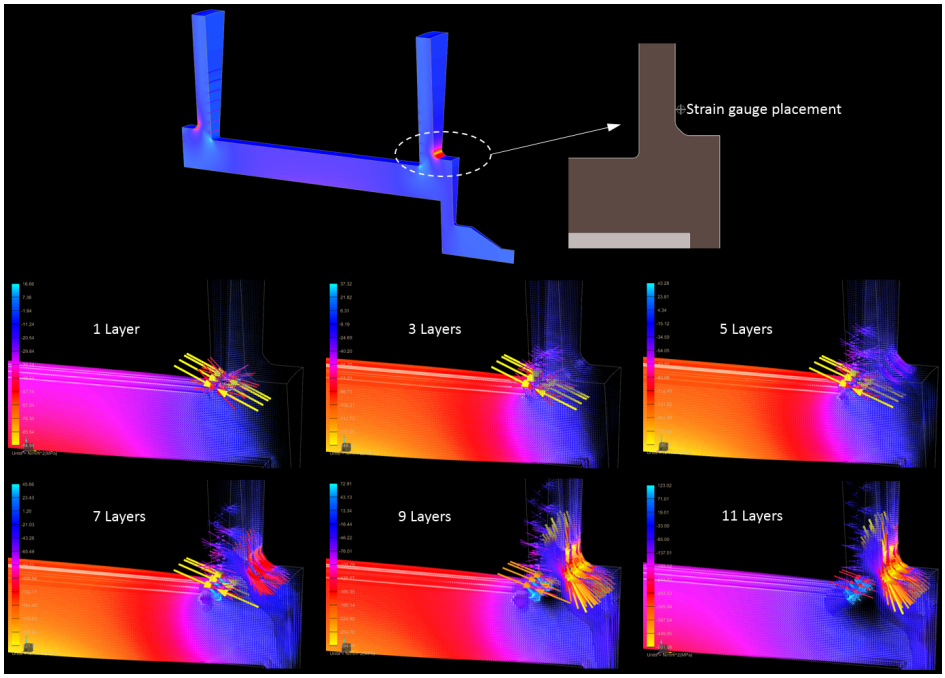

Figure 7.29: Minimum principal stresses in flange on D400

symmetric loading, the directions of principal stresses can deviate considerably from the radial and tangential directions. Consequently, the assumption of known principal stress directions seems to be invalid for the flanges. Because of this, there are uncertainties brought to the present strain measurements. Strain gauges with measurement grids in three directions (R-rosettes) should have been used instead of the applied biaxial T-rosettes. Such R-rosettes would have made the measurements more trustworthy.

$$R_\sigma = \frac{\sigma_1}{\sigma_2} \tag{7.5}$$

$$\sigma_1(R_\sigma) = \frac{1 - R_\sigma}{2R_\sigma}\left(1 - cos(2\beta)\right) \tag{7.6}$$

$$\sigma_2(R_\sigma) = \frac{R_\sigma - 1}{2}\left(1 - cos(2\beta)\right) \tag{7.7}$$

The measurement error depends on the ratio between the actual principal stresses and the misalignment angle [38]. Figure 7.31 shows errors for different principal stress ratios (Eq. 7.5) and misalignment angle β between 0 and 45° calculated for a biaxial stress state by Eqs. 7.6 and 7.7. The errors can be considerable with large differences between the magnitudes of principal stresses.

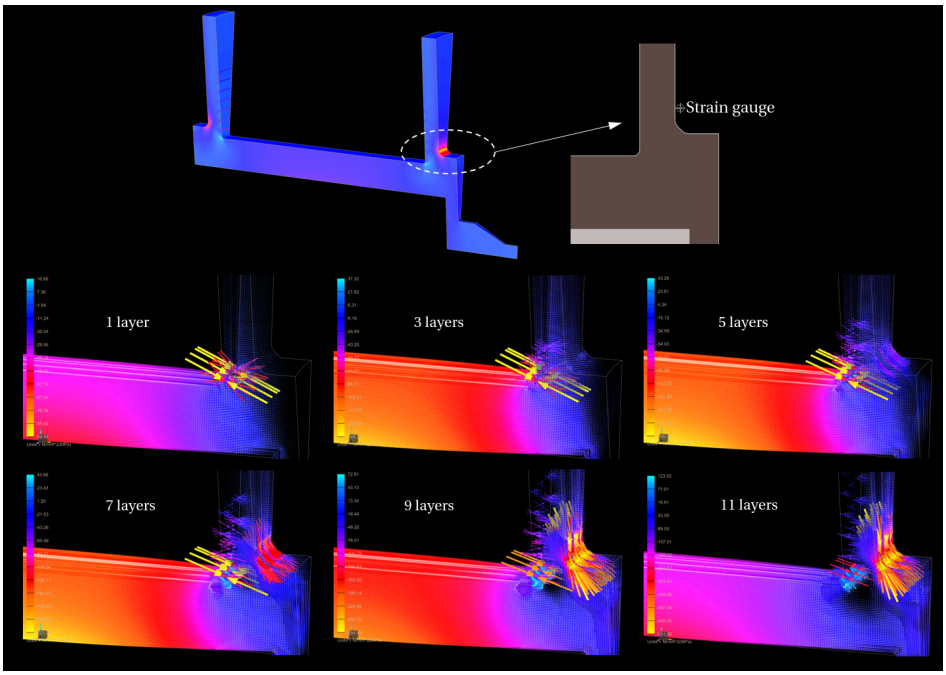

Figure 7.30: Principal stresses at elements close to strain gauge locations on D500

To determine the actual effect of the altered principal stress directions and to quantify the influence on the presented results, further research on flange forces are required. Nevertheless, the level of axial stress in the drum is still considered a valid indicator of the total forces on the flanges for the current investigations.

Compared to the measured axial stresses in the drums, the Dietz method consistently calculates too low flange forces. The DNV GL method calculates axial stresses relatively good for all ropes. However, the calculations from Mupende's equations are somewhat better even though this method (like the Dietz method) only apply forces for every second layer on each flange.

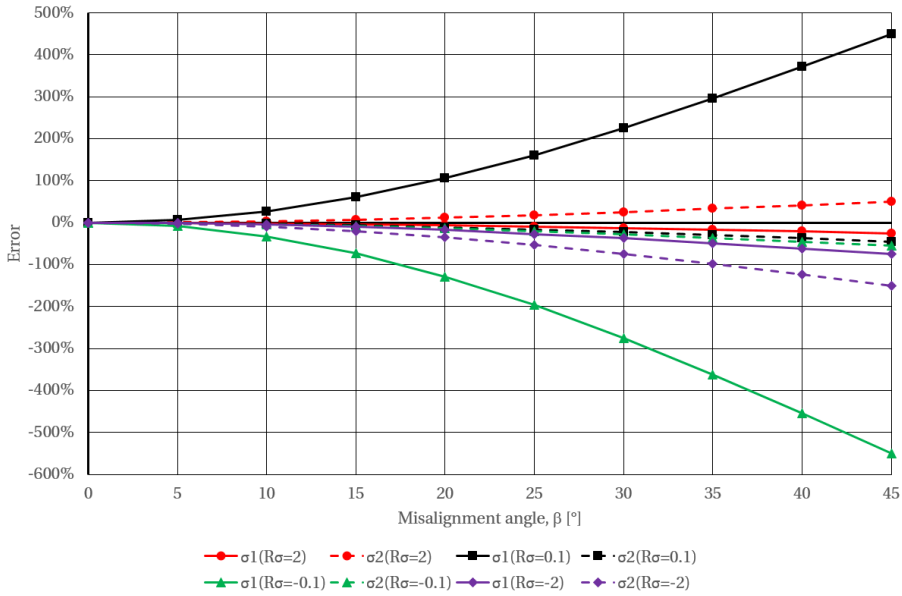

Figure 7.31: Measurement error due to strain gauge misalignment (biaxial stress state)

7.3 Summary - flange force calculations

There are significant variations in accuracy for all flange force calculation methods relative to the measured values, and none give good results.

The choice of applied strain gauges are questionable and a possible reason for measurement discrepancies. Despite this, a relative comparison of measurements and calculations on each drum is still considered valid.

Mupende's equations for climbing- and parallel sectors are considered the best and most flexible flange force calculations. This method is considered applicable for both steel wire ropes and HPSFRs. With detailed modelling, relevant parameters and solid 3D FEA, this method can potentially calculate flange forces with reasonable accuracy.

These evaluations fulfil research objectives RO2 and RO3. Due to the identified issues regarding measurements of flange forces, research questions RQ2 and RQ4 are only partially answered.

Part IV

Proposed improvements and summary of the research

Chapter 8

Assessment of tangential stress in multilayer winch drums with HPSFR

The doctoral work has disclosed challenges with existing methods for load assessment regarding multilayer winch drums with HPSFRs.

In theory, design optimization of winch drums is possible through the "modified Dietz" method for drum pressure calculations. However, the method is dependent on information about rope properties as deformation, moduli of elasticity and development of the rope package stiffness with an increasing number of layers. Unfortunately, the longitudinal modulus is the only parameter usually available from rope manufacturers. The "modified Dietz" method is, at present, considered impractical as the general application is impossible without particular tests and measurements as presented in this thesis. In most cases, this becomes excessively expensive.

On the other hand, the method specified in class rules is straightforward to use. However, with this method, design optimization is impossible. Moreover, the present calculation factors are proved insufficient for safe designs of winches with HPSFRs.

This chapter presents a method improving the assessment of tangential stress in multilayer winch drums with HPSFRs. The method is based on the same straightforward principle as the class rules. However, it applies calculation factors derived from the experiments relevant for HPSFRs.

8.1 Tangential stress ratios

Coefficients of rope layers, C- or K_{L}-factors are equivalent to ratios, $R_\theta(i)$, of calculated, empirical or measured tangential stresses in the drum induced by a given number of layers and a single layer, Fig.8.1. Such ratios from initial measurements on D400 were presented in [10]. These ratios were based on maximum stresses measured in the drum for each rope layer relative to the maximum measured stress caused by the first layer. Due to ramping of rope tension and initial load-free windings, the stresses caused by the first layer were relatively low. Consequently, these stress ratios are considered unreasonable and unpractical for calculations.

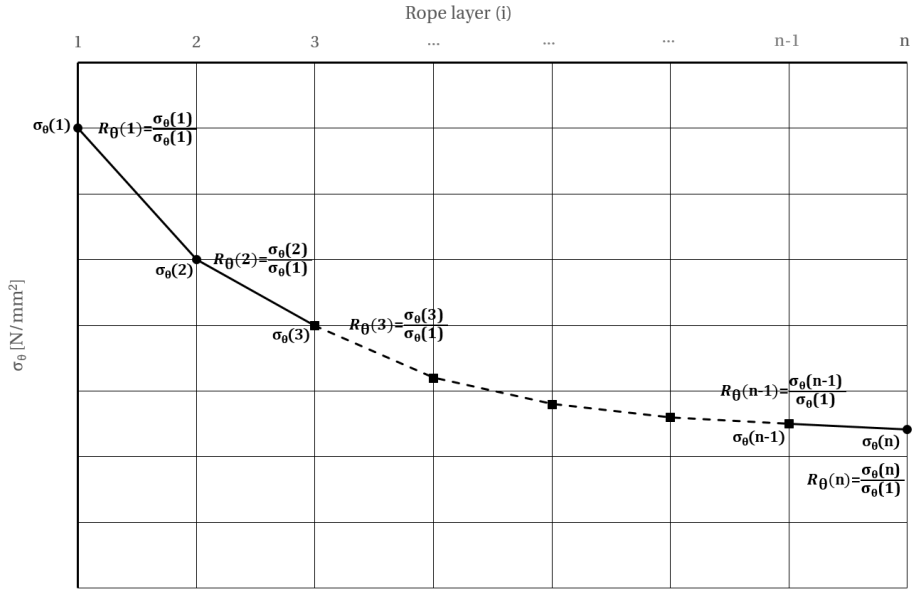

Figure 8.1: Principle of tangential stress ratios, C-factors and coefficients of rope layers

In the following, an approach more suitable for generalized design calculations is applied. The stress ratios are calculated relative to the theoretical maximum tangential stress induced in a thick-walled cylinder with a single rope layer, Eq. 2.7. For the first layer, the stress is conservatively considered equal to the calculated resulting in a stress ratio of one. From the second layer, the stress ratios are calculated by Eq. 8.1. These ratios are defined based on the average peak tangential stress, $\overline{\sigma_\theta}(i)$, from repetitive experiments with 0.3 m/s spooling speed.

$$R_\theta(i) = \frac{\overline{\sigma_\theta}(i)}{\sigma_\theta(1)} = -\frac{\overline{\sigma_\theta}(i)ta(D-t)}{DT}, i = 2, 3, 4..., n-1, n \qquad (8.1)$$

8.1.1 Stress ratios from pure 12-strand braided ropes

Figures 8.2, 8.3 and 8.4 show stress ratios for the Ø20 mm pure 12-strand braided ropes (Braided-A, Braided-B and Braided-C) spooled onto D400 and D500 with rope tension levels equal to 15%, 20% and 25% of MBL.

The stress ratios reflect earlier presented results in Chapters 5 and 6, with curves showing evident asymptotic growth and magnitudes increasing with increasing rope tension. The stress ratios for the smallest drum are highest, and there are relatively small differences between the different ropes, particularly with higher rope tension.

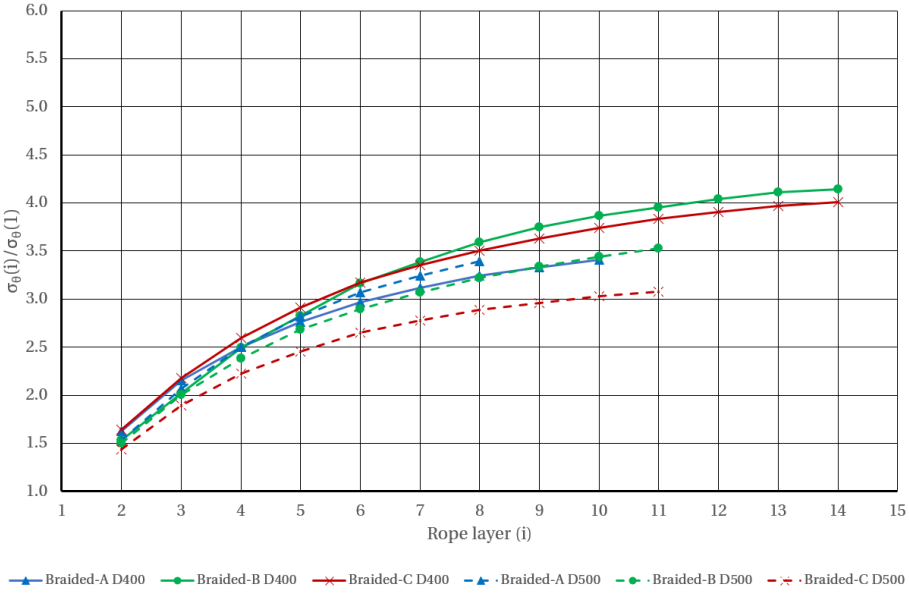

Figure 8.2: Stress ratios - Pure 12-strand braided ropes - 15% MBL

Figures 8.5 and 8.6 show stress ratios for the three different sizes (Ø12, Ø16 and Ø20 mm) of Braided-C when spooled with 20% and 25% MBL rope tension. The trends are identical for all rope sizes, with stress ratios increasing with decreasing D/d-ratios. Further, an effect related to rope size is identified when comparing stress ratios for different rope sizes with equal, or nearly equal, D/d-ratios. The smallest rope yields higher stress ratios than the larger.

Despite the differences in rope sizes and D/d-ratios, the stress ratios for each drum are not very different (solid lines indicate D400 and dotted lines D500).

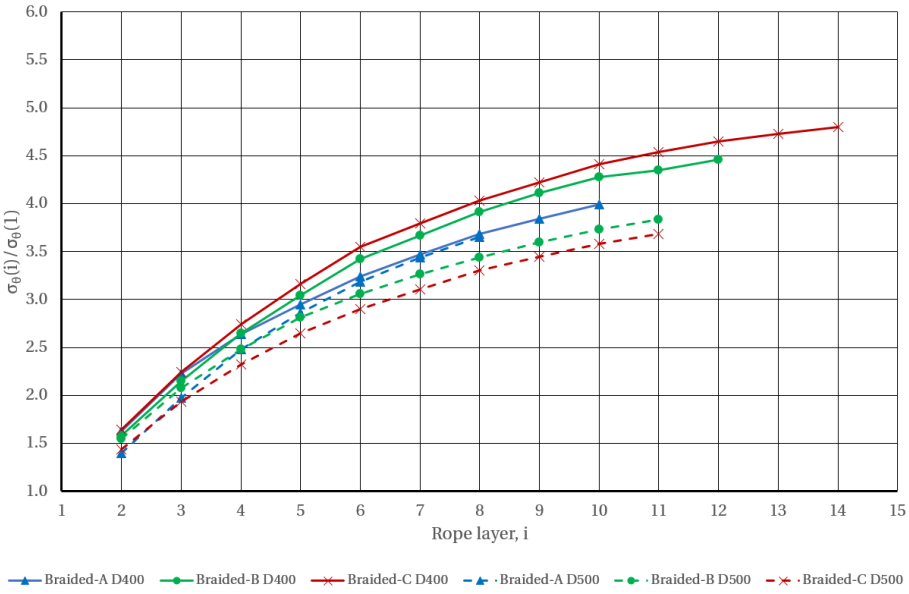

Figure 8.3: Stress ratios - Pure 12-strand braided ropes - 20% MBL

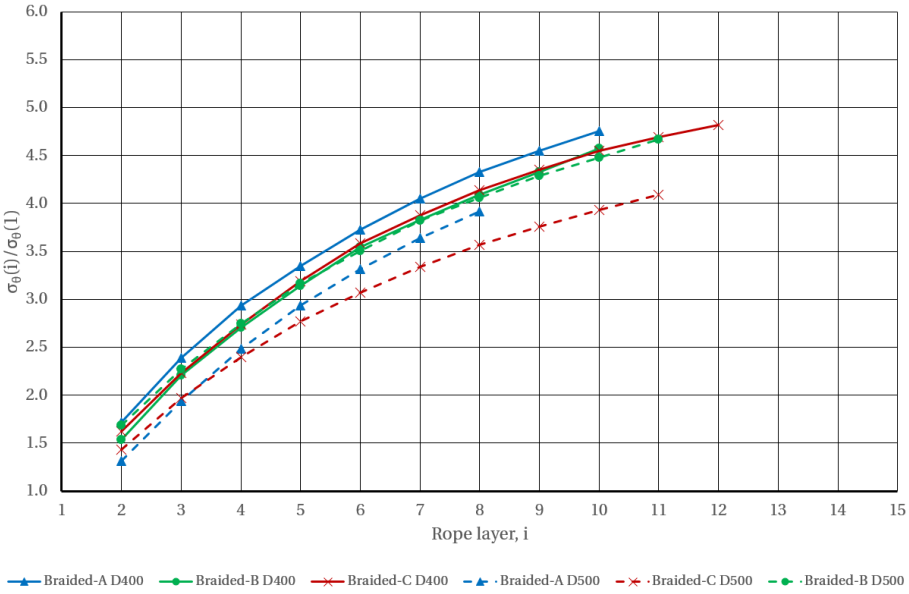

Figure 8.4: Stress ratios - Pure 12-strand braided ropes - 25% MBL

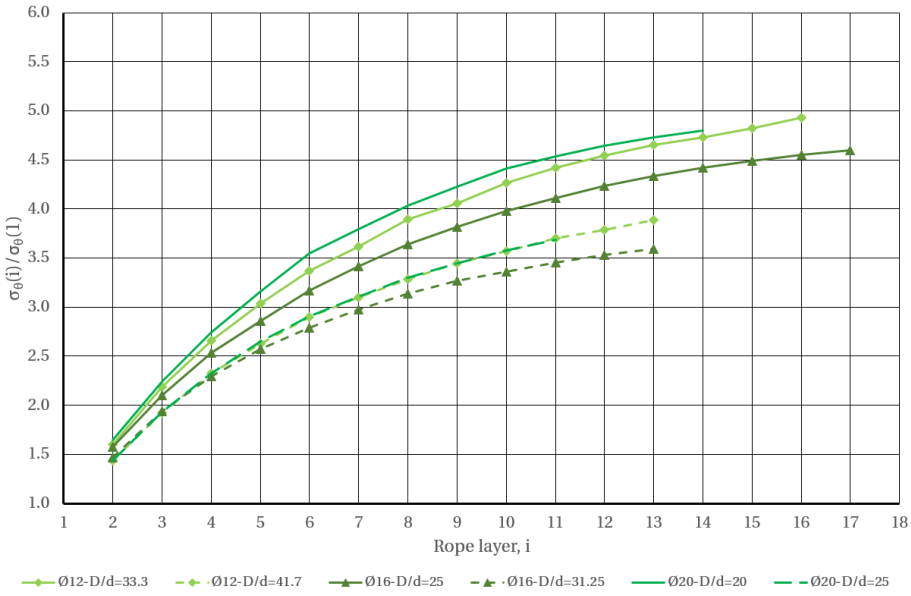

Figure 8.5: Stress ratios - Different sizes of Braided-C - 20% MBL

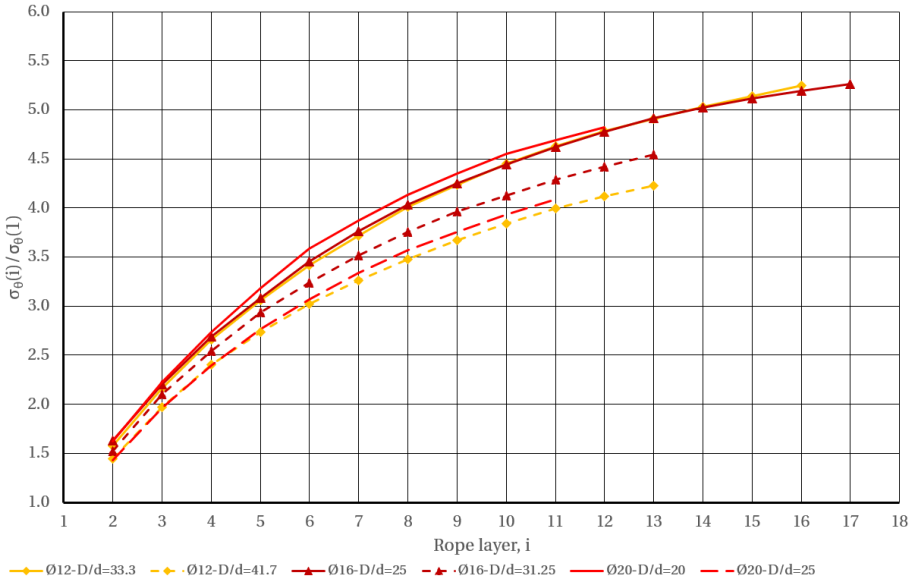

Figure 8.6: Stress ratios - Different sizes of Braided-C - 25% MBL

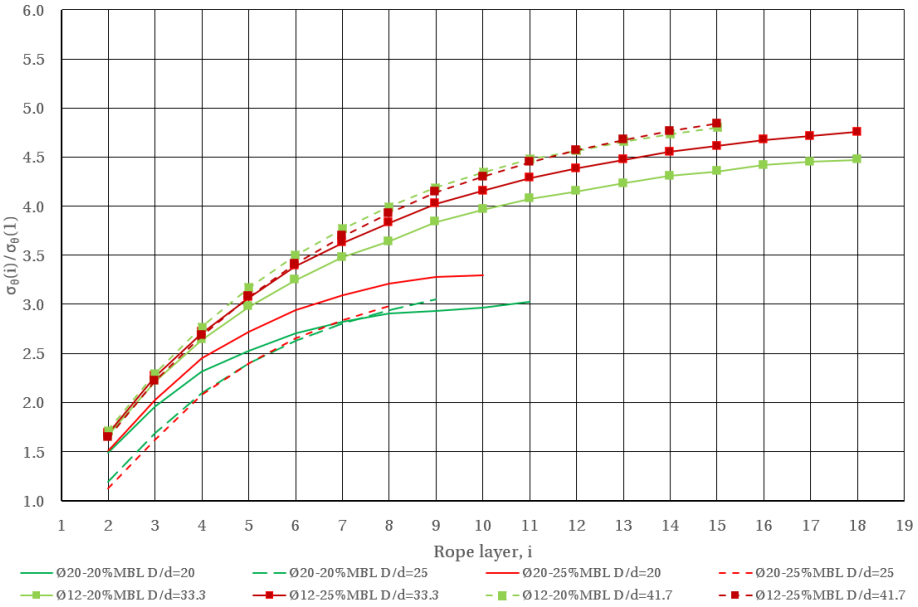

Figure 8.7: Stress ratios - DimStable ropes (Ø12 and Ø20 mm)

8.1.2 Stress ratios from dimensionally stable ropes

For the DimStable ropes (Ø12 and Ø20 mm), Fig. 8.7, the previously identified lower sensitivity to D/d-ratio is recognized for both rope sizes. For identical sizes, there are small differences between the stress ratios for the two drums. Further, the stress ratios are lower than the pure braided ropes. The effect of rope tension level also seems to be reduced with increasing D/d-ratio.

Considering the Braided-D rope on D500, Fig. H.1, there are only slight differences between the different rope tension levels. However, further investigations of this rope on other drum sizes are considered necessary. Therefore, the evaluation of calculation factors for this rope design is omitted.

8.2 Calculation of tangential stress in the drum

A calculation factor S_F, analogous to the layer dependent factors C and K_L in class rules, is introduced to calculate tangential stress in drums with HPSFRs.

The proposed calculation factors are derived from the maximum stress ratios for the Ø20 mm pure braided ropes and the Ø20 mm DimStable rope on the D400 drum (Figs. 8.2, 8.3, 8.4 and 8.7). Curves are fitted to the values using nonlinear regression analysis employing the equation for concave asymptotic growth, Eq.

8.2 (Mitscherlich law/von Bertalanffy growth function). Calculation factors are derived for three levels of rope tension, 15%, 20% and 25% of MBL.

$$\begin{aligned} S_F(1) &= 1 \\ S_F(i) &\approx \theta_1 - \theta_2 e^{-\theta_3 i}, i = 2, 3, 4...n-1, n \end{aligned} \tag{8.2}$$

Tables 8.1 and 8.2 hold coefficients θ_1, θ_2 and θ_3 from the regression analysis. Values for s, the standard deviation of the distance between the data values and the fitted values, are also given. The standard deviations are small, and the curve fitting is considered very good. Due to the known asymptotic nature of the curves, these parameters allow for estimating values beyond measured rope layers.

Table 8.1: Parameters for S_F - Ø20 mm DimStable

Rope tension level	θ_1	θ_2	θ_3	s
15% of MBL	2.671	2.730	0.399	0.010
20% of MBL	3.067	3.286	0.366	0.013
25% of MBL	3.496	3.768	0.318	0.021

Table 8.2: Parameters for S_F - Ø20 mm pure 12-strand braided ropes

Rope tension level	θ_1	θ_2	θ_3	s
15% of MBL	4.386	4.115	0.205	0.015
20% of MBL	5.173	5.165	0.190	0.014
25% of MBL	5.743	5.675	0.174	0.018

The proposed calculation factors are shown in Fig. 8.8. Due to the relatively small differences between the stress ratios for the different pure braided ropes, factors for these ropes are generalized. As the stress ratios for DimStable is considerable different from the pure braided ropes, this rope is treated separately. The dotted black lines indicate the values on which the regression analysis are based.

$$\sigma_\theta(i) = \frac{S_F(i)TD}{ta(D-t)} \tag{8.3}$$

The peak tangential stress in the drum is calculated by Eq. 8.3 applying a value for S_F relevant for the rope design, spooling tension and the maximum number of layers. Calculation factors for tension levels in between the given curves are estimated through linear interpolation.

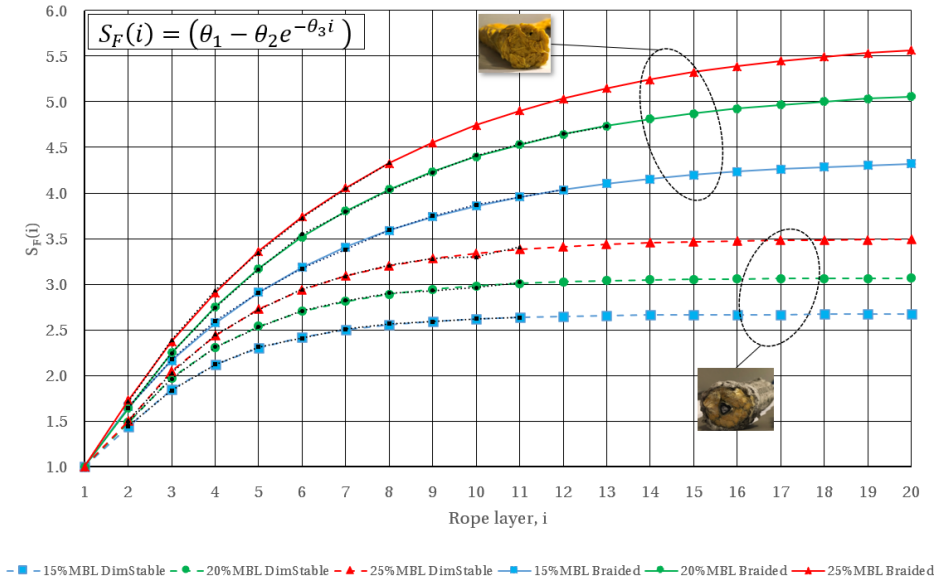

Figure 8.8: Proposed calculation factors for HPSFRs

8.3 Verification and validation of the calculation method

Validation and verification procedures are applied to check if a product, system, method or service meets defined requirements and specifications. These are independent procedures, however, often mixed up and misunderstood. For the calculation method, the differences between verification and validation might be described through the following two questions:

- Verification - is the calculation method derived correctly?
- Validation - is the correct calculation method derived?

The calculation factors are based on measurements on D400 for three specific rope tension levels. Consequently, good calculation results are trivial for these tension levels on D400, and for D500, the calculations should give more conservative results. However, valid results for other rope tension levels need to be confirmed. Further, to be generally applicable, the proposed calculation must be valid for multilayer spooling of the same or similar ropes on other drums. Thus, the questions to be answered through verification and validation of the proposed calculation method become:

- Does the calculation method give conservative results for tension levels other than those defined?
- Does the calculation method give valid results for other relevant rope/drum systems?

Figure 8.9 illustrates the concept for development, verification and validation of the proposed calculation method. This diagram is based on the principle of the "Sargent Circle" developed by the Society for Computer Simulation [39]. The proposed calculation method (*Calculation model*) is based on stress ratios (*Conceptual model*) derived from the physical tests and measurements presented in this thesis (*Current tests and measurements*).

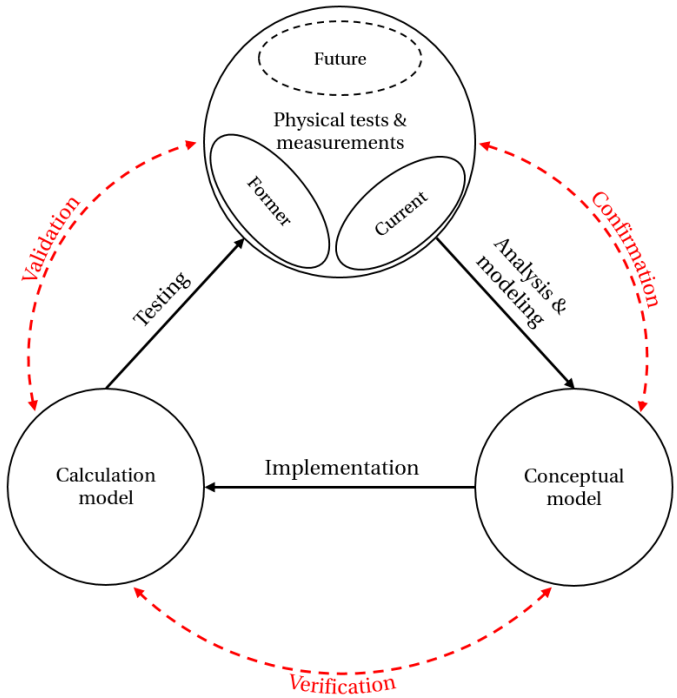

Figure 8.9: Model development with verification and validation

The first step in the verification and validation process is to verify the calculations for different rope tension levels applying linear interpolation. This verification is carried out by comparing calculations with measurement results from Ø20 mm ropes spooled onto D400 and D500 with rope tension levels different from 15%, 20% and 25% of MBL.

The second step is to validate calculations with measurement results from relevant similar physical tests. At present, such measurement results are limited to former measurements carried out in the test rig in 2014 in conjunction with the incident mentioned in Chapter 1 (Fig. 1.5). This validation and possible future validation results contribute to either confirmation, revision, or disposal of the proposed calculation method.

Direct comparisons to calculations based on the DNV GL method are included in the following figures. Some of the referenced figures are enclosed in Appendix H.

8.3.1 Verification against current measurements

Figures 8.10 and 8.11 show calculations and measurements for Ø20 mm Braided-B spooled with rope tension levels 23% and 18% of MBL. Compared to the measurements, the proposed calculations give conservative results. For the highest rope tension, the calculated stresses are, on average, 6.8% and 8.7% higher than the measured for D400 and D500, respectively. With the lower spooling tension, the calculations give values very close to the measured for D400. At the same time, the results for D500 are rather conservative. On average, 17.2% higher than the measured stresses.

For Braided-C on D400 with 21% of MBL spooling tension, Fig. 8.12, there is a close match between the calculations and measurements. The calculated values are slightly lower than the measured, on average 0.8%. For D500, the calculated values are much more conservative and, on average, 19.7% higher than the measured. For Braided-C with 15% MBL rope tension, Fig. H.4, the calculations give similar results (1.8% higher for D400 and 21.4% for D500). The calculations also yield conservative results for the smaller sizes of Braided-C, Figs. H.5 and H.6.

For Braided-A on D400 the proposed calculations give on average 6.8% and 0.02% higher stresses with tension equal to 20% and 25% of MBL. For D500, the corresponding values are 12.1% and 17.2%, Figs. H.2 and H.3.

Figure 8.13 and H.7 show similar results for the Ø20 mm DimStable rope.

The proposed calculations are superior to the DNV GL method for the pure braided ropes on D400. For D500, some of the DNV GL calculations are close to the measured for five rope layers or less. With an increasing number of layers and higher tension, the deviations increase, resulting in a very significant underestimation of the actual stresses compared to the proposed calculation.

For Dimstable, the DNV GL calculations give good results for the lowest tension. With higher tension, the deviations are more significant, particularly with more than five layers.

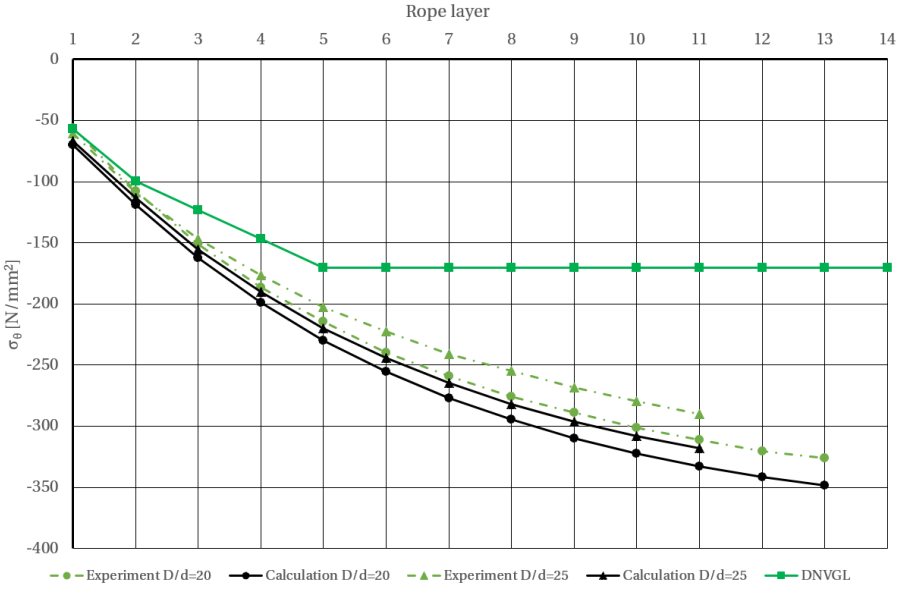

Figure 8.10: Eqs. 8.2 and 8.3 vs. measured stresses - Ø20 mm Braided-B, 23% MBL

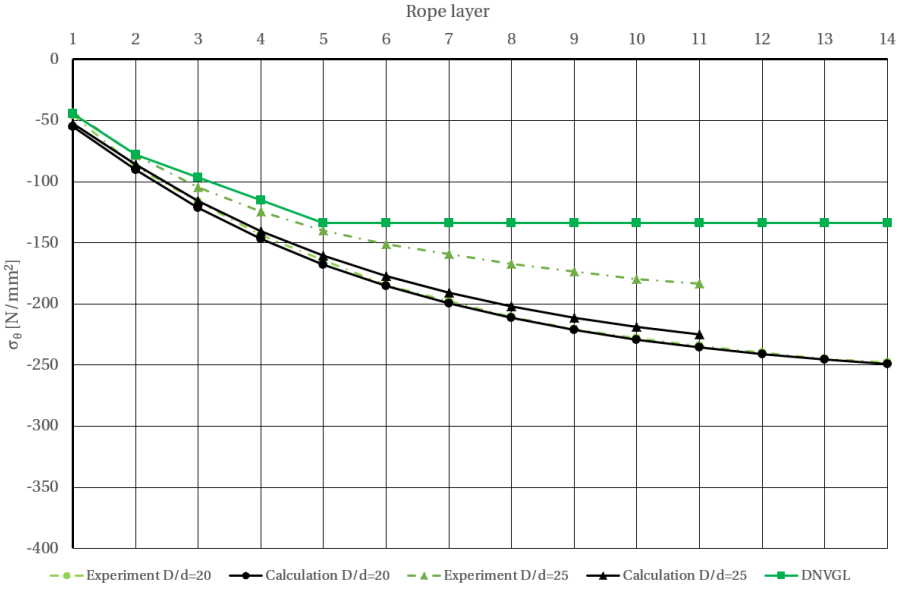

Figure 8.11: Eqs. 8.2 and 8.3 vs. measured stresses - Ø20 mm Braided-B, 18% MBL

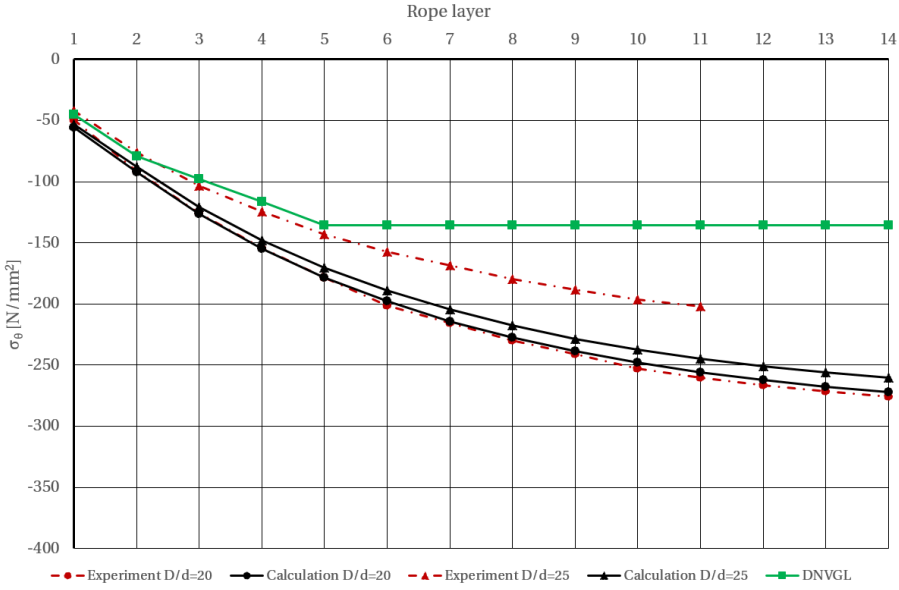

Figure 8.12: Eqs. 8.2 and 8.3 vs. measured stresses - Ø20 mm Braided-C, 21% MBL

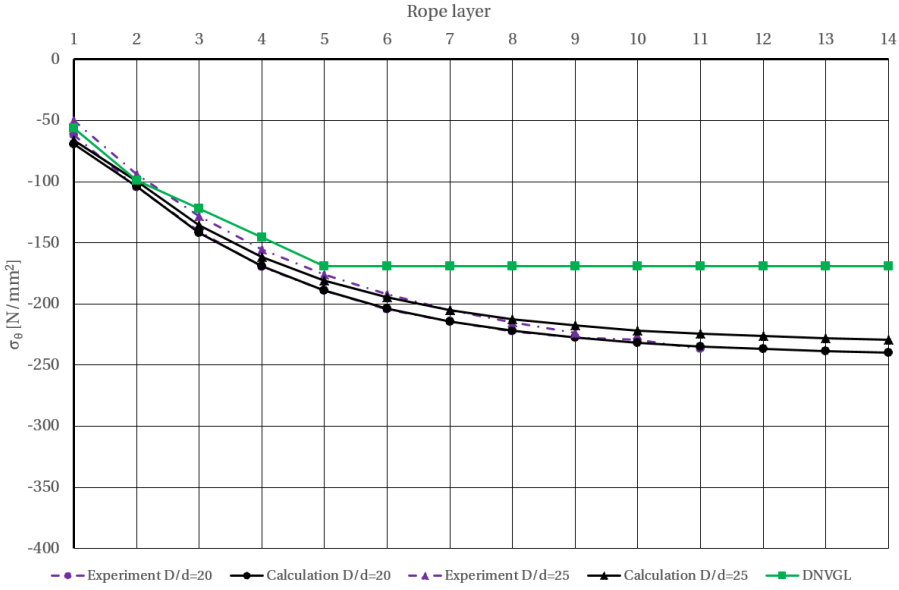

Figure 8.13: Eqs. 8.2 and 8.3 vs. measured stresses - Ø20 mm DimStable, 25% MBL

8.3.2 Validation against former measurements on D450 drum

The proposed calculation method is validated against former multilayer spooling experiments. These experiments applied another drum, D450, with 450 mm outer diameter, 45 mm drum core thickness, and 550 mm distance between Ø1000 mm flanges. Both drum and flanges were made of S355J2G3 steel. Strains were measured using twenty-one biaxial T-rosettes distributed around the circumference inside the drum, in the centre between the flanges. The measurement equipment was equivalent to the equipment used in the current experiments. The method and parameters used to derive stresses from strain measurements were also equivalent.

Results from equations 8.2 and 8.3 are validated against measurements of two Ø20 mm ropes on D450; DimStable and a 12-strand pure braided rope. This pure braided rope is made of Dyneema SK75 fibres and is very similar to Braided-A, Braided-B and Braided-C. The minimum spliced breaking strength is 386.5 kN.

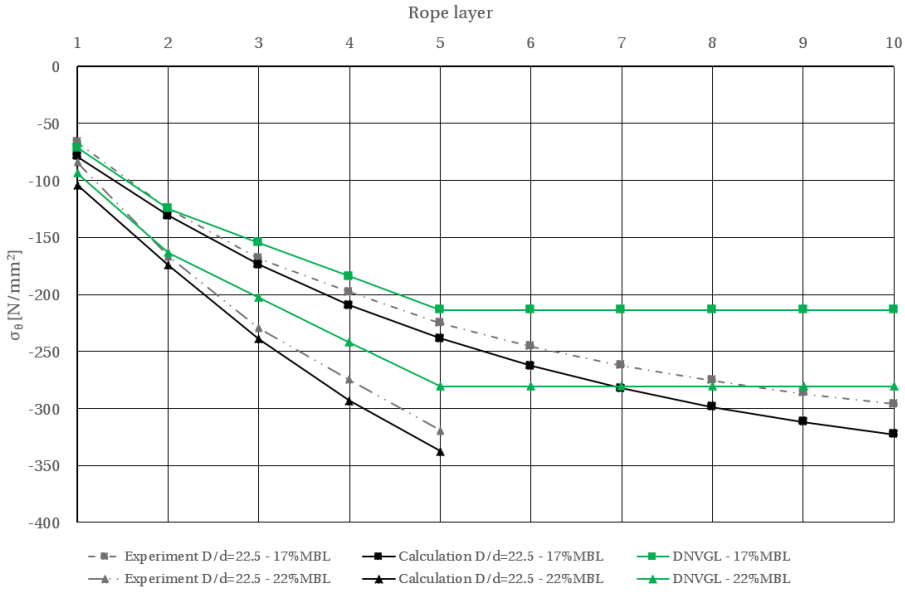

Figure 8.14: Eqs. 8.2 and 8.3 vs. measured stresses - Ø20 mm pure braided rope on D450

The proposed calculations also yield good results for both ropes on D450. The results are conservative for the pure braided rope, with average values for all layers equal to 12.1% and 11% for 17% and 22% of MBL rope tension. With DimStable, there is a relatively good match between calculations and measurements for the lowest tension (18% of MBL) and conservative values for the higher (25% of MBL). The average deviations for all layers are 5.6% and 9.5%, respectively.

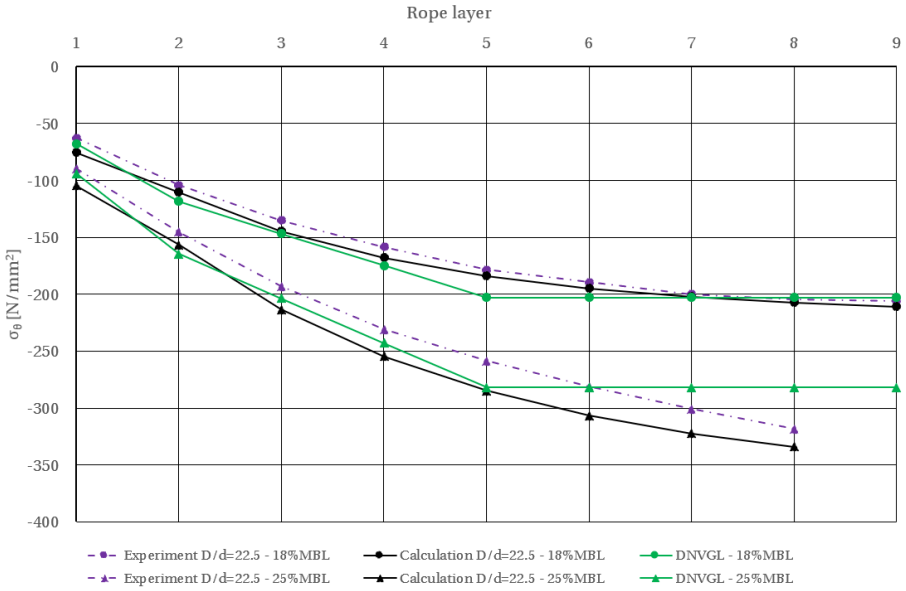

Figure 8.15: Eqs. 8.2 and 8.3 vs. measured stresses - Ø20 mm DimStable on D450

The results from the DNV GL calculations are also similar to D400 and D500 for both ropes. For the lower rope tension, the results are fair for less than six layers with the pure braided rope. For DimStable, the results are suitable for all nine layers with 18% MBL rope tension, but with increasing deviations for more than five layers when tension is raised to 25% of MBL.

8.4 Discussion of the proposed calculations

The verification and validation show that the proposed factors, in general, give good and conservative results and that the proposed linear interpolation between the curves is valid. The good calculation results for D400 and more conservative results for D500 are as expected. Possibly, the results for D500 can be considered too conservative.

Compared to the DNV GL calculations, the proposed calculations yield significantly improved and more conservative results.

The proposed calculation factors should be generally applicable and conservative for similar ropes larger than Ø20 mm on drums with D/d-ratios equal to twenty or higher.

This assumption is based on the following:

- For similar ropes, there are small differences between stress ratios for different fibre blends.
- The factors are based on the highest stress ratios derived for the Ø20 mm braided ropes with the smallest D/d-ratio.
- The stress ratios decrease with increasing rope size.

Consequently, the proposed factors can be used to ensure sufficient structural integrity against the radial pressure of multilayer winch drums with HPSFRs. The validations against former measurements on D450 confirms this hypothesis.

The calculation factors are based on average measured stresses without considering the measurement uncertainty. Including this uncertainty would either cause even more conservative values or better match the average values for higher D/d-ratios, as for D500. For lower D/d-ratios, this introduces a risk for the calculated values to be non-conservative in some cases. Concerning such generalized calculation factors, compromises as this are inevitable.

The specialized design of DimStable makes the general application of the related factors questionable. One might expect that the factors are relevant for ropes with very similar behaviour considering strength, stiffness and deformation. However, this needs to be verified by measurements.

Unfortunately, due to the nature of the proposed calculation, optimization of winch drum designs is impossible, and the risk of over dimensioning is still present.

Chapter 9

Summary and future work

9.1 Summary of the research

Comprehensive measurements of stresses induced in winch drums subjected to multilayer spooling of high-performance synthetic fibre ropes are carried out. The measurements exceed previous research when it comes to the number of rope layers. The measurements are also carried out with various rope tension levels on two different winch drums. Nine different ropes are tested, and rope properties as deformation, stiffness and friction are measured. Further, the effects of these properties on multilayer spooling loads are evaluated.

The HPSFRs can induce considerably larger stresses in the drums than the steel wire rope. While the tangential stress in the drums practically becomes constant within five to seven rope layers with the steel wire, more layers are required with the HPSFRs. The magnitude of stress levels is also strongly related to the rope tension. Further, the stress levels are related to the ratio between the drum and nominal rope size (D/d-ratio), rope design and stiffness. With an increased number of layers, the axial stress in the drum increases due to increased force on the flanges.

The measurements show that pure braided HPSFRs deform considerably during spooling. Dimensionally stable ropes are recognized by less deformation and behave more like steel wire with better spooling performance. The best effect is achieved if a stiff internal core is combined with an outer protective jacket. Due to more significant deformation, pure braided HPSFRs cause less variation in layer radius within each layer. Consequently, such ropes give a much more even stress distribution around the circumference of the drum.

The measurements show that the transverse moduli of ropes increase with rope tension. The transverse stiffness of a single HPSFR is also considerably lower than a single steel wire rope. These findings support previous research. Further, evaluations show that multilayer rope packages of HPSFR behave much stiffer than quantified by testing the stiffness of a single rope or multiple ropes in linearly stacked configurations. No significant differences considering the development of rope package stiffness were identified for the different fibre ropes when testing multiple linearly stacked ropes.

On the other hand, an experiment where rope package stiffness was measured directly on the drum indicated a more aggressive increase in accumulated stiffness for the fibre rope than the steel wire. However, the results were not unambiguous, and with lower spooling tension, the situation was opposite with much less difference. This method and the effects of identified uncertainties should be further investigated.

Increased rope package stiffness is a credible explanation of the higher stresses related to multilayer spooling of HPSFRs. However, the actual physics behind this is not proven. It is assumed that the more significant rope deformations and complexity of the vast number of contacts within the rope can increase the stiffness. The more extensive rope deformation can cause a more compact rope package with limited space for further deformation. Within the rope, considerable internal radial pressure, bending, and friction can potentially prevent relative motions of rope filaments. Consequently, the rope package becomes stiffer, and the effects of multilayer tension reduction are limited. This effect is possibly amplified by increased rope curvature (low D/d-ratio) or reduced by an external jacket and stiff internal core reducing rope deformation, internal pressure and friction.

Indications of inverse proportionality between tangential stress and spooling speed are also found. However, the applied spooling speeds are low and considered too low for many practical winch applications. The effects of spooling speed should be further investigated.

The development of stress in multilayer winch drums when releasing rope tension shows that the stresses are gradually reduced until stabilized. There are no signs of a subsequent increase in tension in the rope package again, as observed with straight ropes.

Further, the positive effect of "protective layers" was evaluated and confirmed. The peak stress level in the drum can be reduced by spooling the first layers with lower tension. To prevent the rope from subsequent layers to be pressed down in between underlying layers, the rope tension in the first layers must be high enough to give

sufficient radial stability. Practical tests are required for each rope type to find an adequate first level spooling tension.

Investigations of stresses in the flanges show much more varying and ambiguous results. For one of the drums, the steel wire rope and one of the dimensionally stable HPSFRs induce the highest stress. The results are similar for both high- and low rope tension levels. On the other drum, all ropes induce relatively similar stresses with low rope tension. With higher tension, a couple of the pure braided HPSFRs induce the highest stresses.

Possible influence on strain measurements due to varying principal strain directions in the flanges makes the measurements questionable. Flange measurements should be carried out with strain gauges with three independent measurement grids to allow for such variations.

Evaluations of calculation methods for multilayer radial pressure show that the simplified method specified by classification societies is not applicable for HPSFR. In some cases, this method can also underestimate stresses from the steel wire rope. A calculation method by Dietz [7] with modifications by Lohrengel et al. [8] was identified as state-of-the-art for radial pressure on multilayer drums. This method gives good agreement with measurements for the steel wire rope based on transverse stiffness determined from a single rope. For the HPSFRs, this method considerably underestimates the radial pressure on the drum unless a higher rope package stiffness is accounted for empirically.

In combination with a relevant multilayer pressure, the simple equation for tangential stress in externally loaded thick-walled cylinders gives good results. For more precise stress assessment of multilayer winch drums, 2D or 3D finite element analysis are recommended. However, in many cases, axisymmetric analysis is sufficient. At the same time, full solid 3D FEA gives possibilities for more realistic variations in radial pressure around the circumference of the drum and pressure against the flanges. Irrespective of the calculation method, relevant values for the radial pressure and flange forces are required as input.

The main contribution from the present work is a calculation method for the tangential stress in multilayer drums with HPSFR. This method is straightforward and based on the same principle as the methods specified in class rules. However, the proposed calculations are superior to the class rule calculations due to factors relevant for HPSFRs derived from the measurements and independent of the ratio between drum diameter and thickness. For pure 12-strand braided HPSFRs, the proposed factors are considered generally applicable for ropes larger than Ø20 mm on drums with D/d-ratios higher than twenty.

9.2 Lessons learned - experimental investigations

The test setup and execution of the test program worked well and according to the plan. The only exception is the rope against rope friction experiments. The effect of "rope knifing" was underestimated. The friction test drum should have been designed to prevent or reduce this effect.

Regarding the measurement of transverse rope elasticity, it was difficult to control the rope tension in the spooling rig. Preferably, measurements should have been carried out earlier in the cylinder arrangement and made the transverse stiffness measurements in the spooling rig superfluous. It would also have been interesting to investigate potential changes in transverse moduli during the test program. Such investigations could have been achieved by measuring transverse stiffness both before and after multilayer spooling tests.

Possibilities for measuring the transverse stiffness of several ropes in a pyramidal arrangement would have been very advantageous. The testing directly on the drum should preferably have been more investigated and carried out with more ropes on both drums. Unfortunately, this method was invented and introduced too late in the program.

The laser measurement with a single laser scanning a wide area of the drum worked very well. A more automated system for the rope profile measurements would have been advantageous. Continuous measurement of rope profiles is not considered necessary and would have caused massive amounts of data. However, a laser following the spooling device with a trigger for snapshot pictures would have improved the process. Further, a computerized method for the evaluation of rope profiles should have been developed.

The effects and consequences of the actual asymmetric loading on flanges were underestimated. As principal stress directions in flanges are not constant, robust measurements require strain gauges with three measuring grids (R-rosettes.)

9.3 Research contributions

The main objective of this research is as follows:

Improve understanding of structural loads and stresses in winch drums induced by multilayer spooling of HPSFRs, investigate rope properties effects and evaluate load assessment procedures for implementation in an improved process for multilayer winch drums.

The research objectives are fulfilled and research questions are answered through this work and the following specific contributions:

- C1: Measurements prove that HPSFRs can induce considerably higher tangential stresses in winch drums compared to steel wire. The stress level's dependence on the number of layers, rope design, rope deformation, D/d-ratio, spooling tension and speed is confirmed.
- C2: For HPSFRs, the state-of-the-art method for assessing radial pressure on multilayer winch drums requires higher transverse rope stiffness than quantifiable from a single rope or several linearly stacked ropes.
- C3: The calculation method for tangential stress in multilayer winch drums specified by classification societies underestimate actual stresses considerably for multilayer winch drums with HPSFRs. It is recommended that class rules are revised and adapted to the latest findings.
- C4: A calculation method for multilayer winches with 12-strand braided high-performance fibre ropes is developed. This method improves the assessment of tangential stress in multilayer winch drums significantly compared to class rule calculations.

9.4 Conclusion

The main hypothesis related to this work is confirmed. *Multilayer spooling with 12-strand high-performance synthetic ropes can induce higher loads in winch drums than steel wire ropes of comparable size and strength!*

With one exception, the results from this work fulfil the research objectives and answer the research questions. Until further, the accuracy of flange force calculations remains unanswered due to questions regarding the validity of the strain measurements on the flanges.

9.5 Recommendations for further work

Further work should prove the physics behind the increased stiffness of rope packages related to multilayer spooling of HPSFRs. Primarily, measurements of transverse moduli with a significant number of HPSFRs in pyramid arrangement should be carried out and evaluated. If this does not give satisfactory results, other test methods must be developed. Such methods should reflect the actual rope conditions, deformations and transverse rope stiffness when ropes are spooled onto a drum. Numerical simulation techniques effectively handling rope deformations, the vast number of internal rope contacts, external and internal friction would be particularly advantageous.

Further, the remaining question left from this work should be answered. Flange

force calculations should be evaluated against measurements from R-rosettes. The number of rosettes should also be increased to better capture effects from non-symmetric loading. Preferably, stresses should be measured on the inner side of the flanges.

The validation of the proposed calculation method supports the hypothesis that it is generally applicable and conservative within limits for pure braided ropes. However, further confirmation through validations of calculations against drums applying various high-performance synthetic fibre ropes should be carried out.

Bibliography

[1] P. Ingeberg et al. 'Development of a fiber rope based deployment system for deep water application'. In: *Proceedings of the Sixteenth International Offshore and Polar Engineering Conference*. The International Society of Offshore and Polar Engineers. San Fransisco, California, U.S.A, May 2006, pp. 126–133. ISBN: 1-880653-66-4.

[2] S. Torben et al. 'Fiber Rope Deployment System For Ultra Deep Water Installations'. In: *Offshore Technology Conference*. Houston, Texas, U.S.A, Apr. 2007. ISBN: 978-1-55563-254-0.

[3] *DNVGL-ST-0378 Standard for offshore and platform lifting appliances*. May 2016.

[4] *DNVGL-RP-N201 Lifting appliances used in subsea operations*. June 2017.

[5] E. O. Waters. 'Rational Design of Hoisting Drums'. In: *Mechanical Engineering* 42.12 (Dec. 1920), pp. 675–679.

[6] Tadashi Egawa and Motoharu Taneda. 'External pressure produced by multilayers of rope wound about a hoisting drum'. In: *Hitachi Review* (Mar. 1958), pp. 26–31.

[7] P. Dietz. 'Ein Verfahren zur Berechnung ein- und mehrlagig bewickelter Seiltrommeln'. (German). Dissertation. Germany: Technischen Hochschule Darmstadt, 1971.

[8] A. Lohrengel et al. 'Innovative drum construction for multi-layer winding with fibre ropes'. In: *Challenging rope applications*. OIPEEC Conference. Stuttgart, Germany, Mar. 2015, pp. 269–285. ISBN: 978-0-9552500-5-7. URL: www.oipeec.org.

[9] A. Lohrengel et al. 'The influence of high performance fibre rope designs on drum load and spooling performance in multi-layer drum equipment'. In: *Rope - Present and Future*. OIPEEC Conference. La Rochelle, France, Apr. 2017, pp. 1–21. ISBN: 978-0-9552500-4-0. URL: www.oipeec.org.

[10] R.A. Skarbøvik et al. 'Experimental Investigation of Stresses in Winch Drums Subjected to Multilayer Spooling Loads from Synthetic Fibre Ropes'. In: *Proceedings of the ASME 2019 38th International Conference on Ocean, Offshore and Arctic Engineering*. Vol. 7A: Ocean Engineering. Glasgow, Scotland, June 2019. ISBN: 978-0-7918-5884-4. URL: https://doi.org/10.1115/OMAE2019-95283.

[11] R.A. Skarbøvik, H. Piehl and V. Æsøy. 'Tangential stress in multilayer winch drums with high performance synthetic fibre ropes – analytical calculations versus experimental measurements'. In: *Ships and Offshore Structures* 15.sup1 (Mar. 2020), pp. 82–97. URL: https://doi.org/10.1080/17445302.2020.1739871.

[12] H.A. McKenna, J.W.S Hearle and N. O'Hear. *Handbook of fibre rope technology*. Woodhead Publishing Ltd and CRC Press LLC, 2004. ISBN: 1-85573-606-3.

[13] J.W.S Hearle, ed. *High-performance fibres*. Woodhead Publishing Ltd and CRC Press LLC, 2001. ISBN: 1-85573-539-3.

[14] C.M Leech. 'The Modelling and Analysis of the Mechanics of Ropes'. In: ed. by Canada G.M.L Gladwell Waterloo. Vol. 209. Solid Mechanics and its Applications. Springer, 2014. ISBN: 978-94-007-7840-5. URL: https://doi.org/10.1007/978-94-007-7841-2.

[15] C.M. Leech. 'The Modelling and Analysis of Splices Used in Synthetic Ropes'. In: *Mathematical, Physical and Engineering Sciences*. Vol. 459. 2035. The Royal Society. July 2003, pp. 1641–1659. URL: https://www.jstor.org/stable/3560166.

[16] Ilaka Mupende. 'Beanspruchungs- und Verformungsverhalten des Systems Trommelmantel - Bordscheiben bei mehrlagig bewickelten Seiltrommeln unter elastischem und teilplastischem Werkstoffverhalten'. (German). Dissertation. Germany: Technischen Universität Clausthal, 2001. ISBN: 3-89873-171-5.

[17] Ansel C. Ugural. *Stresses in Beams, Plates, and Shells*. 3rd ed. CRC Press, 2009. ISBN: 978-1-4398-0270-0.

[18] Warren C. Young and Richard G. Budynas. *Roark's Formulas for Stress and Strain*. 7th ed. McGraw-Hill, 2002. ISBN: 0-07-072542-X.

[19] H. Ernst. ‘Untersuchungen über die Beanspruchung der Seiltrommeln von Kranen und Winden’. (German). In: *Mitteilung der Forschungsanstalten des GHH-Konzerns* (Sept. 1938), pp. 195–215.

[20] J. Dolan. ‘Winder drum tread design investigation’. In: *The South African Mechanical Engineer* 13 (1963), pp. 97–138.

[21] B. Mck. Torrance. ‘The design of winding drums’. In: *The South African Mechanical Engineer* 15 (Dec. 1965), pp. 123–128.

[22] N. W. Bellamy and B. D. A. Phillips. ‘An investigation into flange forces in winch drums’. In: *Proceedings of the Institution of Mechanical Engineers* 183 (1968), pp. 579–590. URL: https://doi.org/10.1243/PIME_PROC_1968_183_049_02.

[23] H. Kraitschy. ‘Beitrag zur Berechnung und Konstruktion von mehrlagig bewickelten Seiltrommeln’. (German). In: *Schweißtechnik* 24.7 (1974), pp. 315–318.

[24] H. J. Neugebauer. ‘Berechnungsverfahren für ein- und mehrlagig bewickelte Seiltrommeln mit und ohne Seilrillen - Teil 1’. (German). In: *Hebezeuge und Fördermittel* 20.1 (1980), pp. 8–11.

[25] H. J. Neugebauer. ‘Berechnungsverfahren fûr ein- und mehrlagig bewickelte Seiltrommeln mit und ohne Seilrillen - Teil 2’. (German). In: *Hebezeuge und Fördermittel* 20.5 (1980), pp. 142–146.

[26] K.K. Song, G.P. Rao and Mark A. Childers. ‘Large Wire Rope Mooring Winch Drum Analysis and Design Criteria’. In: *Society of petroleum engineers journal* (Apr. 1980), pp. 63–74.

[27] D. Karbalai. ‘Stresses in winch barrels with particular reference to multilayering’. PhD Thesis. UK: Department of Mechanical Engineering, Sunderland Polytechnic, 1988.

[28] J. Henschel. ‘Dimensionierung von Windentrommeln’. (German). Dissertation. Germany: Technischen Universität Clausthal, 1999. ISBN: 3-934238-12-2.

[29] Steffen Otto. ‘Ein nicht-rotationssymmetrisches Belastungsmodell für die Ermittlung des Beanspruchungsverhaltens mehrlagig bewickelter Seiltrommeln’. (German). Dissertation. Germany: Technischen Universität Clausthal, 2003. ISBN: 3-89720-703-6.

[30] Tim Schwarzer. ‘Beitrag zur Gestaltung und Dimensionierung von Windentrommeln bei mehrlagiger Bewicklung mit Kunststoff- und Hybridseilen’. (German). Dissertation. Germany: Technischen Universität Clausthal, 2011. ISBN: 978-3-86948-199-9.

[31] P. Dietz et al. 'Problems related to the design of multi layer drums for synthetic and hybrid ropes'. In: *Innovative ropes and rope applications*. OIPEEC Conference. Stuttgart, Germany, Mar. 2009, pp. 125–138. ISBN: 978-0-9552500-2-6. URL: www.oipeec.org.

[32] A. Lohrengel, K. Stahr and M. Wächter. 'Safe use of hoisting drums wound with multiple layers of wire, hybrid, fibre and/or large diameter ropes'. In: *Safe use of ropes*. OIPEEC Conference. Texas, USA, Mar. 2011, pp. 21–50. ISBN: 978-0-9552500-3-3. URL: www.oipeec.org.

[33] A. Lohrengel, K. Stahr and M. Wächter. 'Simulation of fibre ropes and their effects on the strain scenario of multi-layer wound rope drums'. In: *Simulating rope applications*. OIPEEC Conference. Oxford, UK, Mar. 2013, pp. 141–157. ISBN: 978-0-9552500-4-0. URL: www.oipeec.org.

[34] *American Bureau of Shipping (ABS) - Guide for certification of lifting appliances*. Apr. 2019.

[35] *ISO 12076:2002 Steel wire ropes - Determination of the actual modulus of elasticity*. Aug. 2002. URL: https://www.iso.org/standard/32197.html.

[36] HBM Test and Measurement. *Measurement Uncertainty: Less Errors, Better Results*. URL: https://www.hbm.com/en/6021/measurement-uncertainty-experimental-stress-analysis.

[37] *ASTM E74, Standard Practice of Calibration of Force-Measuring Instruments for Verifying the Force Indication of Testing Machines*. 2004. URL: https://www.astm.org.

[38] VISHAY Precision Group Micro-Measurements. *Tech.Note TN-511 Errors Due to Misalignment of Strain Gauges*. URL: http://www.vishaypg.com/docs/11061/tn511tn5.pdf.

[39] S. Schlesinger. 'Terminology for Model Credibility'. In: *Simulation* 32.3 (1979), pp. 103–104. DOI: 10.1177/003754977903200304.

[40] Hüseyin AVCI et al. 'High performance fibers: a review on current state of art and future challenges'. In: *Journal of Engineering and Architecture* 27.2 (Aug. 2019), pp. 130–155.

[41] Gunnar Härkegård. *Dimensjonering av maskindeler*. Norwegian. Tapir, 2004. ISBN: 82-519-1970-3.

Part V

APPENDICES

Appendix A

Related publications

REVISED DRAFT

Proceedings of the ASME 2019 38th International Conference on Ocean, Offshore and Arctic Engineering
OMAE2019
June 9-14, 2019, Glasgow, Scotland

OMAE2019-95283

EXPERIMENTAL INVESTIGATION OF STRESSES IN WINCH DRUMS SUBJECTED TO MULTILAYER SPOOLING LOADS FROM SYNTHETIC FIBRE ROPES

Reidar André Skarbøvik[1],
Rolls-Royce Marine AS
Offshore Deck Machinery/
Dept. of Ocean Operations and Civil Engineering
Norwegian University of Science and Technology
Ålesund, Norway

Henry Piehl
Dept. of Ocean Operations and Civil Engineering
Norwegian University of Science and Technology
Ålesund, Norway

Sverre Torben
Rolls-Royce Marine AS
Systems & Deck Machinery
Ålesund, Norway

Mette Lokna Nedreberg
Rolls-Royce Marine AS
Research & Technology
Ulsteinvik, Norway

Vilmar Æsøy
Dept. of Ocean Operations and Civil Engineering
Norwegian University of Science and Technology
Ålesund, Norway

ABSTRACT

In many marine applications, modern high-performance synthetic fibre ropes have replaced, and are continuing to replace, well-known steel wire rope solutions due to the low weight of the synthetic ropes removing limitations for operations at large water depths. In some cases, replacement of steel wires with synthetic ropes have caused permanent deformations and damage to multilayer winch drums and indicated that synthetic fibre ropes can cause larger pressure on winch drums than steel wire. This paper presents the first results from a novel experimental investigation of a multilayer winch subjected to a selection of braided high-performance synthetic fibre ropes and a reference steel wire rope. The tested ropes, with nominal diameters between 12 and 20mm, are spooled at different tensile loads and with maximum number of layers in the range of 10 to 19. The experiments utilize a test rig with two winch drums, controllable spooling gear and sheaves with load cells to apply and control required force and speed during spooling. Measurements from twelve biaxial strain gauges on the inside of a thick high-strength drum are used to measure stresses in the structure. The results show that the selected fibre ropes induce considerably larger stress in the winch drum than the steel wire rope. This confirms that design of multilayer winch drums with high-performance synthetic fibre ropes requires special considerations and that the guidance for stress calculations, related to steel wire ropes, in DNV-GL-0378 "Standard for offshore and platform lifting appliances" is not applicable for synthetic fibre rope applications.

Keywords: Multilayer winch drums, synthetic fibre rope, stress ratio

NOMENCLATURE

ε_θ	Tangential strain
ε_a	Axial strain
σ_θ	Tangential stress
σ_a	Axial stress
σ_{vM}	von Mises stress
ν	Poisson's ratio
i	Layer index
p	Distance between ropes, c-c (pitch)
p_d	Pressure on drum
p_f	Maximum pressure on drum flange
t	Thickness of drum
C_i	Layer dependent load ratio

[1] Contact author: skarbovi@alumni.ntnu.no

$Ceqv_i$	Equivalent layer dependent load ratio
E	Modulus of elasticity
F_a	Tensile rope force
R	Outer radius of drum
MBL	Minimum Breaking Load
HBM	Hottinger Baldwin Messtechnik GmbH
HPFR	High Performance Fibre Rope
IWRC	Independent Wire Rope Core

INTRODUCTION

Multilayer winches are important in marine applications either as standalone products or as sub-components in larger handling/lifting arrangements. Use of steel wire ropes in such applications are widespread, while use of high performance synthetic fibre ropes (HPFR) are increasing due to the advantageous properties of such ropes compared to steel wires. In fact, subsea cranes performing lifting operations in large water depths benefit from such ropes, being practically neutrally buoyant in water, to avoid the rope weight to consume a major part of the lifting capacity.

Quantifying the loads acting on winch drum and flanges from rope spooled in multiple layers is important for proper and safe design of winches. The tangential stress in the drum is an important design parameter and design engineers often apply the method from DNV-GL [1] which is easy to use with a layer dependent factor (C-factor) scaling the stress caused by one single layer of rope on the drum. This method has been disputed and it is claimed by Lohrengel et.al. [2] that the load on the drum can be underestimated, as it does not take the stiffness of the winch-rope system into account. In later revisions, DNV-GL mentions this uncertainty, but also that a C-factor of three is normally acceptable for winches with five or more layers in subsea operations. However, there is no information about design requirements for winch drums with HPFR. A guideline for mobile cranes from the European Materials Handling Federation [3] states that HPFR can cause larger forces to winch drums and flanges than steel wire rope due to increased flattening of the rope and different rope stiffness. This guideline neither gives any more information about design requirements nor calculation methods, but states that design and calculations of drums need to consider the rope dependent effects and recommends verification of calculation models by testing.

The majority of former experimental studies on this matter relate to steel wire rope applications and with only a few layers of rope. An exception, however limited to five layers, is Schwarzer [4] who carried out experiments with hybrid ropes on a grooved drum and demonstrated that the hybrid ropes resulted in reduced asymmetry in the stress distribution, related to the cross-over zones in the spooling pattern of the rope, compared to a steel wire rope. However, there were no significant differences in the maximum absolute tangential stress values.

Figure 1, from unpublished experimental work by Rolls-Royce Marine AS, strongly indicates that HPFR spooled in multiple layers can cause significantly higher stresses in winch drums compared to steel wire ropes. This is further investigated and strain measurement results from novel experiments with high-performance braided synthetic fibre ropes of different types and sizes, spooled onto a winch drum in ten to nineteen layers at different spooling loads, are presented in this paper.

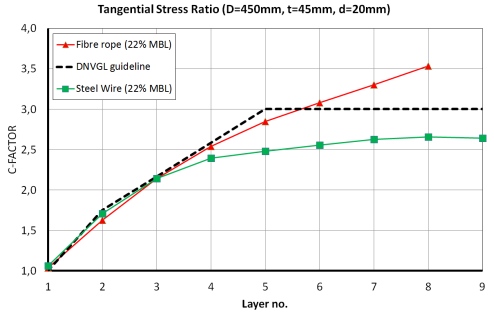

FIGURE 1: INITIAL EXPERIMENTS COMPARING C-FACTORS FOR Ø20MM STEEL WIRE AND SYNTHETIC FIBRE ROPE

The objectives of the experiments are to investigate the following:

1. Compare stresses in winch drum structure when spooled with HPFR and steel wire in multiple layers.
2. Investigate if the drum stresses grow asymptotically towards a limit, or continue to increase with increasing number of layers.
3. How does the degree of rope utilization affect stresses?
4. Evaluate results with the DNV-GL C-factor for steel wire.

The ropes in these experiments are mainly tested with tensile loads in the range of 10-30% of the minimum breaking load (MBL), but the smaller ropes even in the range of 10-53% of MBL. According to [5], safety factors less than five are rare for HPFR and 20% of MBL is a general recommendation for ropes under normal conditions. However, safety factors vary and depend on specific applications and requirements. For steel wires in running applications, DNV-GL [1] requires a factor of safety between five and three (20-33.3% of MBL).

STRESSES IN WINCH DRUMS

Winch drums are cylindrical shell structures and the stress state is biaxial with known principal stress directions. The rope spooled in multiple layers causes a compressive tangential stress (hoop stress), while the rope pushing against the flanges in each layer causes a tensile axial stress in the drum.

$$\sigma_\theta = \frac{E}{(1-\nu^2)}(\varepsilon_\theta + \nu\varepsilon_a) \quad (1)$$

$$\sigma_a = \frac{E}{(1-\nu^2)}(\varepsilon_a + \nu\varepsilon_\theta) \quad (2)$$

$$\sigma_{vM} = \sqrt{\sigma_\theta^2 + \sigma_a^2 - \sigma_\theta \sigma_a} \quad (3)$$

The tangential, σ_θ, and axial, σ_a, stresses are calculated from measured strains by means of the modified Hooke's law, Eq. 1 and Eq. 2, while the combined stress (von Mises criteria) is calculated by Eq. 3.

Considering a constant tensile load in the rope, Eq. 4 calculates the pressure acting on the drum, while Eq. 5 gives the corresponding tangential stress in the drum structure. C_i is a layer dependent factor, defined by the ratio of maximum stress caused by layer *i* relative to the maximum stress caused by the first layer, Eq. 6.

$$p_d = \frac{C_i F_a}{Rp} \quad (4)$$

$$\sigma_\theta = \frac{C_i F_a}{pt} \quad (5)$$

$$C_i = \frac{\sigma_{\theta_i}}{\sigma_{\theta_1}} \quad (6)$$

For one layer of rope C_1=1, DNV-GL [1] proposes C_2=1.75 for two layers of rope and an usually accepted value C_s=3 for five layers or more. The dotted line in Fig. 1 represents the proposed C-factor values.

DNV-GL does not give any formulas for the axial drum stress, but Eq. 7 gives the pressure acting on the flanges. The maximum flange pressure is assumed to act at the transition between the flange and the drum, with magnitude $^1/_3$ of the pressure acting on the drum surface, and linearly decrease to zero at the outer rope layer.

$$p_f = \frac{C_i F_a}{3Rp} \quad (7)$$

EXPERIMENTAL WORK

The experiments are conducted in a multi-functional test rig available in Rolls-Royce Marine's test facilities, shown in Fig. 2.

Test Rig

The test rig uses two high-pressure hydraulic driven winches, A and B. Hydraulic cylinders control the spooling devices for each winch, while a control system regulates the operation. With rope running from winch A to B, the control system receives information from a load cell, in the spooling device sheave of winch A, and an encoder, on the hydraulic motor of winch B, to regulate tension and speed. In addition, position and pressure sensors give information about spooling device position and hydraulic pressures. The system is bidirectional and can run in both directions with maximum rope tension in the range of 90-100kN. All data is captured in a log for each test run.

Winch Drums

The two winch drums are designed to handle high loads and stresses avoiding risk of any plastic deformations during tests. Drum A has outer diameter Ø500mm and 625mm distance between flanges, while drum B, Fig. 3, has 550mm flange distance and Ø400mm outer diameter. Both drums are smooth,

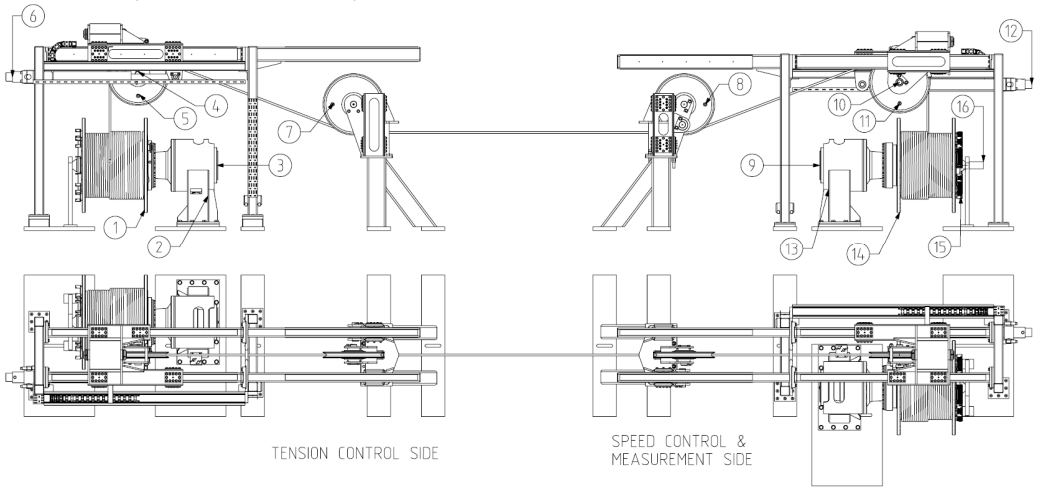

FIGURE 2: TEST RIG

Pos.1 – Winch drum A
Pos.2 – Hydraulic motor A
Pos.3 – Encoder A
Pos.4 – Load cell A
Pos.5 – Spooling sheave A
Pos.6 – Hydraulic cylinder A
Pos.7 – Guide sheave A
Pos.8 – Guide sheave B
Pos.9 – Encoder B
Pos.10 – Load cell B
Pos.11 – Spooling sheave B
Pos.12 – Hydraulic cylinder B
Pos.13 – Hydraulic motor B
Pos.14 – Winch drum B
Pos.15 – Data acquisition eq.
Pos.16 – Slip ring

without grooves, and with 75mm thick drum cores made of high-strength AISI4130 steel. The flanges, 36mm thick plates of high-strength JFE-Hiten780s steel, are welded to the drum core.

To control dimensions and prepare for mounting of strain gauges, flanges and drum cores are machined to tolerances on both the inside and the outside. The drums are post weld heat treated prior to machining.

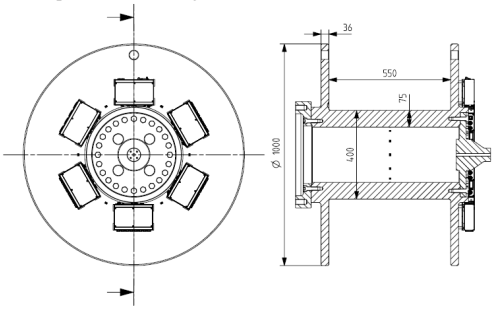

FIGURE 3: TEST DRUM B

Material properties for AIS4130 are typically varying through the thickness. In order to define a maximum stress limit, an abort criteria for the experiments to avoid overload and plastic deformations, tensile tests are conducted, both in axial and circumferential (tangential) direction, at three different radial positions. The results show that the yield stress is decreasing through the thickness from the outside to the inside of the drum core and that the largest drum is slightly stronger than the smallest. The inside yield stress, with an additional margin of 10%, giving 420 N/mm^2 is defined as a conservative maximum allowable stress in the drum for the experiments.

The minimum yield strength of the flange plates is 800 N/mm^2. 200 000 N/mm^2 and 0.3 are selected as relevant values for the elastic modulus and Poisson's ratio for both steel types.

Measurement Equipment

Fourteen biaxial strain gauges of type HBM K-CXY3-0030-1-350-4-030-N, Fig. 4, measure strains in drum B. Twelve gauges are glued, with equal spacing around the circumference, at the center between the flanges on the inside of the drum. In addition, two optional strain gauges are mounted 215mm to each side of the center, Fig. 5. The accuracy of the strain gauges, as installed, are estimated to ± 3%. All measurements are carried out indoor, with stable conditions and constant ambient temperature for each test run.

The drum is also equipped with 24 additional strain gauges, 12 on the outside of each flange. However, flange stresses and results from these strain gauges are not presented in this paper.

Five strain gauge amplifiers from HBM, four Quantum MX1615B and one MX840A, mounted on the outer side of the free end flange, together with a CX22B-W data recorder handle the strain data acquisition. All amplifiers are synchronized against a common time counter and 24V power is supplied to the equipment through a slip ring mounted on the axle at the free flange end, Fig. 6. HBM CatmanEasy-AP software controls the measurement equipment and recordings.

FIGURE 4: HBM BIAXIAL STRAIN GAUGE

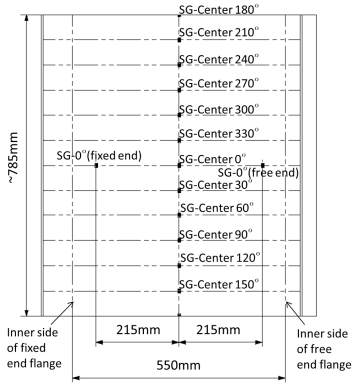

FIGURE 5: UNFOLDED VIEW OF TEST DRUM B WITH STRAIN GAUGE LOCATIONS

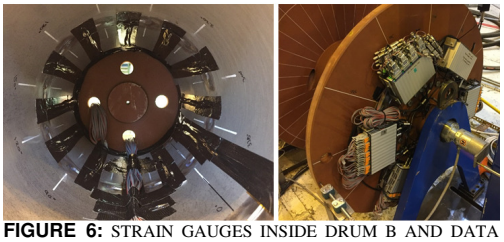

FIGURE 6: STRAIN GAUGES INSIDE DRUM B AND DATA ACQUSITION EQUIPMENT

Ropes

Eight ropes of five different designs, Fig. 7 and Table 1, are used in the experiments. The synthetic fibre ropes are 12 strand braided high performance ropes. Ropes 1 and 2 are two sizes (12 and 20mm) of same design with braided cover. Ropes 3, 4 and 5 are three sizes (12, 16 and 20mm) of another design with a portion of the main fibers replaced by polyester, while rope 6 is almost identical to rope 5, without polyester fibers. All ropes are made of Dyneema® fibers, except for rope 7, which is made of Spectra® and Vectran™ fibers, while rope 8 is an IWRC steel wire. Ropes 2, 7 and 8 are in used condition, and rope 2 and 8 are the ropes referenced in Fig. 1. The maximum number of

layers spooled onto the drum varies due to different available lengths for each rope, but at least 10 layers are reached on drum B for all ropes.

FIGURE 7: TEST ROPES

TABLE 1: Rope Properties

Rope	Fiber type	Design	Size [mm]	Cover	MBL [kN]
1	Dyneema®SK75	A	12	Yes	118
2			20	Yes	383
3	Dyneema®SK78 & Polyester	B	12	No	129
4			16	No	186
5			20	No	333
6	Dyneema®SK78	C	20	No	412
7	Spectra® & Vectran™	D	20	No	358
8	IWRC Steel wire	E	20	No	299

Test Procedure and Data Treatment

Each rope is spooled from drum A to drum B and back to drum A at 0.3m/s speed, while strains in drum B are being measured and recorded. The control system continuously regulates speed and tension against preset values during testing. The spooling pattern is programmable and the experiments use a basic and simple pattern, where the rope is displaced axially once per revolution. The axial displacement is typically of magnitude close to the rope nominal diameter, but adjusted for each rope to achieve proper spooling. Prior to each run, the winch is rotated to a defined initial position, with a few load free wraps of rope on the drum, and all strain gauges are zero balanced. Each rope is tested several times at different tensile forces with repetitions. The data presented in this paper is based on totally 123 test runs for the eight ropes.

Figure 8 shows an example of tensile rope loads and rope spooling speed. The tensile load on winch B varies more than the load on winch A. This is because the load is regulated on the A side of the test rig, which is a stiffer and more responsive subsystem than the complete test rig with the rope running through four sheaves to winch B.

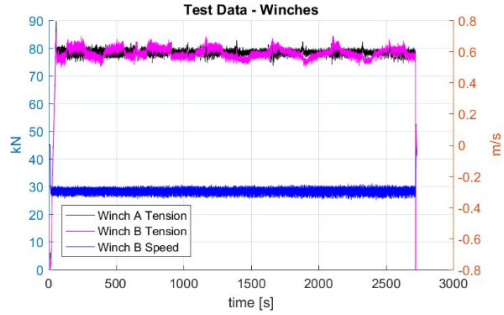

FIGURE 8: EXAMPLE OF WINCH TEST DATA, ROPE TENSION AND SPEED

The test-rig load cells (shear bolts holding the spooling device sheaves) are tuned and verified against a calibrated load cell spliced into the rope between the winches. Values from load cell B, being closest to the strain measurements, is defined as the relevant tensile spooling load.

The load during spooling of each layer is averaged to a uniform load for each layer. However, the load variations influence the measured stresses and spooling the different layers with larger or smaller tensile loads will result in larger or smaller stress increments compared to a uniform load. To compensate for this an equivalent layer dependent stress ratio is calculated by scaling the stress increments between two subsequent layers linearly with the ratio between the average tensile force in the first layer and the average tensile force in the relevant layer, Eq. 8.

$$C_{eqv_i} = \frac{(\sigma_{\theta_i} - \sigma_{\theta_{i-1}})\frac{\overline{F_1}}{\overline{F_i}} + \sigma_{\theta_{i-1}}}{\sigma_{\theta_1}}, \; i > 1 \quad (8)$$

RESULTS

Stress measurement results, stress distribution, stress variance and layer dependent stress ratios for the different ropes are presented and discussed in the following.

Drum Stresses

Figures 9, 10 and 11 are examples of stress curves showing tangential, axial and combined stresses in the winch drum structure caused by the different ropes spooled with tensile loads equal to 20% of MBL.

The first layers of rope are easily identified by distinct steps in the curves, but with increasing number of layers these steps diminish and the different layers become difficult to distinguish. The compressive tangential stress is dominating and (the absolute value) increases immediately when spooling of the first layer starts, while the axial stress is very low until 3-4 layers are spooled onto the drum. With additional layers, and increased forces acting on the flanges, the axial stress grows approximately linearly.

Rope 2, Fig. 9, shows a declining increase in tangential stress and seems to reach a limit around 200 N/mm^2 after 12-14 layers of rope on the drum. A similar trend is observed for rope 5, Fig. 10, but with higher stress, which does not reach a limit within 14 layers. There is an evident difference for rope 8 (steel wire), Fig. 11, which converges to a considerably lower tangential stress limit after eight layers.

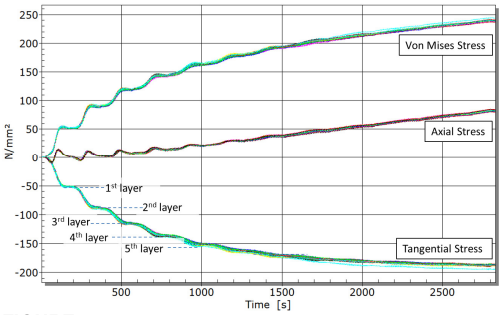

FIGURE 9: DRUM STRESSES – ROPE 2 – 20% MBL

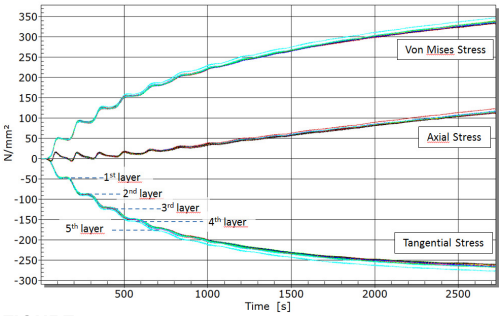

FIGURE 10: DRUM STRESSES – ROPE 5 – 20% MBL

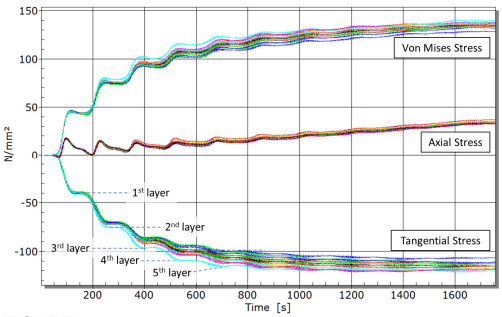

FIGURE 11: DRUM STRESSES – ROPE 8 – 20% MBL

Figures 12 and 13 show the extreme stress curves for all the 20mm ropes in the experiments when spooled onto the drum with two different tensile loads, 68.67kN (7 metric tons) and 88.29kN (9 metric tons). Stresses from all ropes are similar for the first two layers, but then the tangential stress and consequently the von Mises stress start to deviate. Ropes 5, 6 and 7 induce the highest stresses in the winch drum structure, while stresses from rope 2 is lower and closer to the steel wire (rope 8) than the others. The stress curves for rope 5, 6 and 7 follow each other relatively closely.

The large difference between rope 2 and the other synthetic ropes is assumed related to different deformability. The design of rope 2 with a braided cover constrains deformations more than the other ropes, and causes a behavior closer to the steel wire.

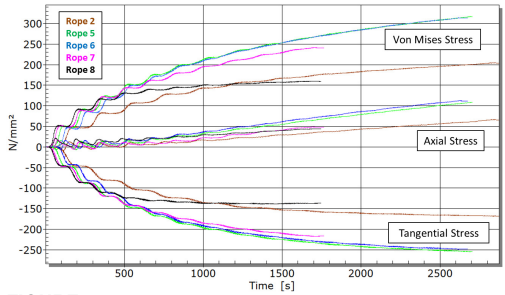

FIGURE 12: DRUM STRESSES – D/d=20 – 68.67kN (7 metric tons)

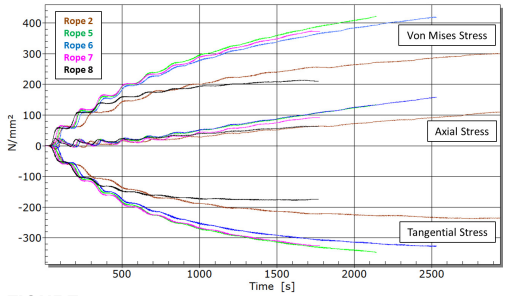

FIGURE 13: DRUM STRESSES – D/d=20 – 88.29kN (9 metric tons)

Stress Distribution

Dependent on type of spooling, and potential grooved drum design, each winding can be split into one or more parallel- and transition sections. In a parallel section, the rope winding has practically constant radius and is supported by the groove between to underlying layers, while it is displaced both axially and radially when it crosses the underlying rope in a transition section. This change in radius causes varying loads during spooling as the pressure from each layer, caused by the rope tension, is in inverse ratio to the rope radius (ref. Eq. 4) [6].

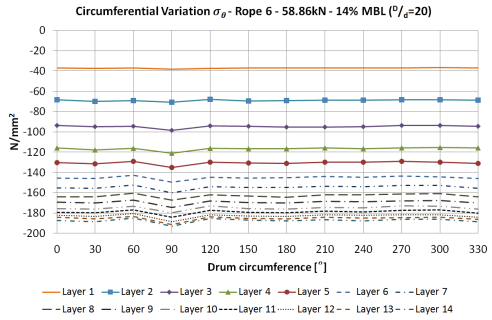

FIGURE 14: STRESS DISTRIBUTION WITH FIBRE ROPE

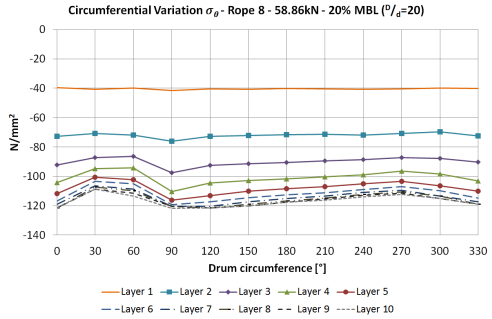

FIGURE 15: STRESS DISTRIBUTION WITH STEEL WIRE

Figures 14 and 15 show tangential stress distribution curves, created by plotting the results from all strain gauges around the circumference inside the drum, for rope 6 (HPFR) and rope 8 (steel wire) spooled with equivalent loads. Both ropes show an asymmetric stress distribution, but a clear difference is observed. Due to larger deformability, the synthetic rope causes a more even and less distorted stress distribution than the steel wire. This also indicates less variation in rope radius during spooling. In the first layer, where the rope is only displaced axially, the stress distribution is nearly symmetric for both ropes.

Schwarzer [4] found similar, but less distinct, effects with hybrid and steel wire ropes on a grooved drum.

Stress Variance

Figures 16 and 17 show examples of average tangential stress curves and related standard deviations from several equivalent test runs.

The standard deviations for the HPFR is considerably larger than the steel wire. This can be explained by the typical viscoelastic properties of HPFR [7]. The rope stiffness increases with tensile load and the highest load experienced by the rope can influence the properties and behavior of the rope. With time and unloading, the rope is relaxed again. This effect is observed in experiments where a high load test is followed by a test at lower load resulting in higher stresses than repeated experiments at the low load. This "memory effect" from previous test runs causes an element of autocorrelation to the measurements.

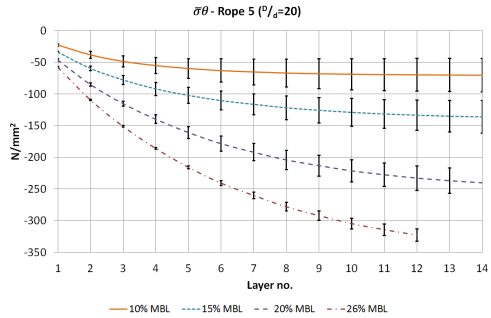

FIGURE 16: AVERAGE TANGENTIAL STRESS FOR ROPE 5

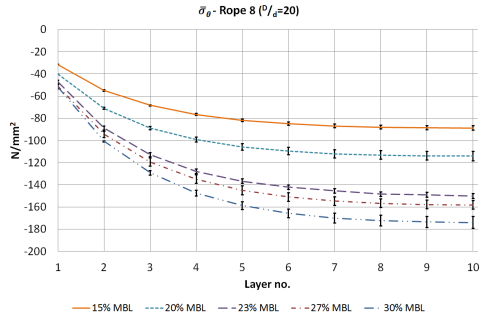

FIGURE 17: AVERAGE TANGENTIAL STRESS FOR ROPE 8

Note! The lines in the figures plotting stress or stress ratios against layers are for visualization purposes only, and do not represent continuous data between the discrete values for each layer.

An important observation is that stress results from the first runs of a new rope, prior to preconditioning (stabilizing properties by repeated loading to adjust and align fibers and strands), typically gives considerably lower stress values than measurements after several tests. Such initial measurements are too optimistic regarding actual stresses occurring in the drum structure.

Layer Dependent Stress Ratios

Layer dependent stress ratios, or C-factors, for different tensile spooling loads relative to rope strength are calculated and shown in Figures 18 through 22. Corresponding numeric values, rounded off to one decimal, are listed in Tables 2 through 5.

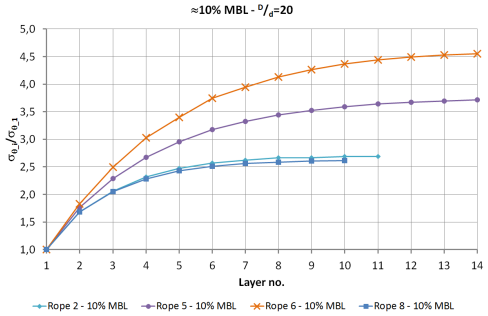

FIGURE 18: C-FACTOR WITH 10% MBL

TABLE 2: C-FACTOR WITH 10% MBL

Stress Ratio ($\sigma_{0\_i}/\sigma_{0\_1}$) 10% MBL				
Layer	**Rope 2** 10% MBL	**Rope 5** 10% MBL	**Rope 6** 10% MBL	**Rope 8** 10% MBL
2	1.7	1.8	1.8	1.7
3	2.1	2.3	2.5	2.1
4	2.3	2.7	3.0	2.3
5	2.5	3.0	3.4	2.4
6	2.6	3.2	3.7	2.5
7	2.6	3.3	3.9	2.6
8	2.7	3.4	4.1	2.6
9	2.7	3.5	4.3	2.6
10	2.7	3.6	4.4	2.6
11	2.7	3.6	4.4	
12		3.7	4.5	
13		3.7	4.5	
14		3.7	4.6	

With reference to Fig. 18 and Table 2 (10% of MBL), rope 2 and rope 8 follow each other closely and reach practically constant stress ratios of 2.7 and 2.6 after eight and seven layers, respectively. Stress ratios for rope 5 and 6 continue to grow slowly after 11 layers. With 14 layers of rope on the drum, the stress ratios for rope 5 and 6 are 3.7 and 4.6.

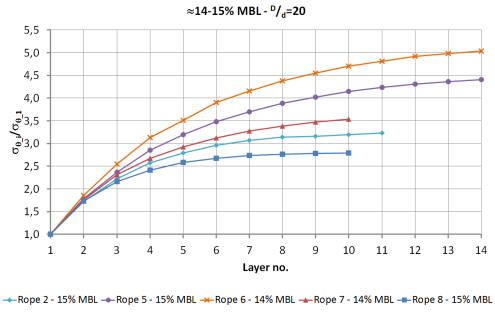

FIGURE 19: C-FACTOR WITH 14-15% MBL

TABLE 3: C-FACTOR WITH 14-15% MBL

Stress Ratio ($\sigma_{0\_i}/\sigma_{0\_1}$) 14-15% MBL					
Layer	**Rope 2** 15% MBL	**Rope 5** 15% MBL	**Rope 6** 14% MBL	**Rope 7** 14% MBL	**Rope 8** 15% MBL
2	1.7	1.8	1.9	1.8	1.7
3	2.2	2.4	2.6	2.3	2.2
4	2.6	2.9	3.1	2.7	2.4
5	2.8	3.2	3.5	2.9	2.6
6	3.0	3.5	3.9	3.1	2.7
7	3.1	3.7	4.2	3.3	2.7
8	3.1	3.9	4.4	3.4	2.8
9	3.2	4.0	4.6	3.5	2.8
10	3.2	4.1	4.7	3.5	2.8
11	3.2	4.2	4.8		
12		4.3	4.9		
13		4.4	5.0		
14		4.4	5.0		

Increasing the tensile spooling load to 14-15% of MBL, Fig. 19 and Table 3, shifts the maximum stress ratio for the steel wire slightly to 2.8, while rope 2 starts to deviate from the steel wire with a maximum stress ratio of 3.2. The curves for ropes 5 and 6 continue to increase beyond 14 layers, when the stress ratios are 4.4 and 5.0. The ratio for rope 7 is 3.5 with 10 layers of rope.

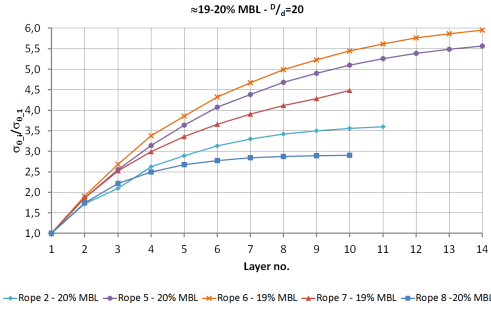

FIGURE 20: STRESS RATIO WITH 19-20% MBL

TABLE 4: STRESS RATIO WITH 19-20% MBL

Stress Ratio ($\sigma_{0\_i}/\sigma_{0\_1}$) 19-20% MBL					
Layer	**Rope 2** 20% MBL	**Rope 5** 20% MBL	**Rope 6** 19% MBL	**Rope 7** 19% MBL	**Rope 8** 20% MBL
2	1.7	1.9	1.9	1.9	1.7
3	2.1	2.6	2.7	2.5	2.2
4	2.6	3.1	3.4	3.0	2.5
5	2.9	3.6	3.9	3.4	2.7
6	3.1	4.1	4.3	3.7	2.8
7	3.3	4.4	4.7	3.9	2.8
8	3.4	4.7	5.0	4.1	2.9
9	3.5	4.9	5.2	4.3	2.9
10	3.6	5.1	5.4	4.5	2.9
11	3.6	5.3	5.6		
12		5.4	5.8		
13		5.5	5.9		
14		5.6	6.0		

Further stress ratio increase is observed with tensile load ~20% of MBL, Fig. 20 and table 4. Maximum stress ratio for rope 8 increases marginally again to 2.9 and still reaches a limit value after eight layers. The limit value for rope 2 is no longer present with 11 layers, when considering the curve strictly, and the maximum stress ratio increases to 3.6. With 14 layers, rope 5 and 6 have maximum stress ratios 5.6 and 6.0, while the ratio for rope 7 increases to 4.5 with 10 layers of rope on drum.

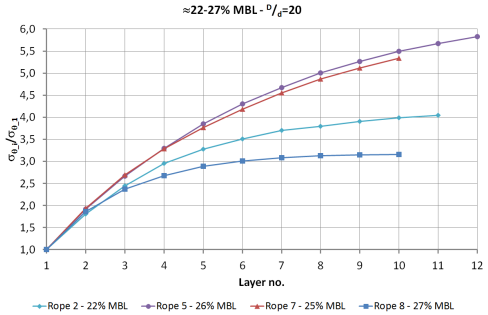

FIGURE 21: STRESS RATIO WITH 22-27% MBL

TABLE 5: STRESS RATIO WITH 22-27% MBL

Stress Ratio (σ_{θ_i}/ σ_{θ_1}) 22-27% MBL				
Layer	**Rope 2** 22% MBL	**Rope 5** 26% MBL	**Rope 7** 25% MBL	**Rope 8** 27% MBL
2	1.8	1.9	1.9	1.9
3	2.4	2.7	2.7	2.4
4	3.0	3.3	3.3	2.7
5	3.3	3.8	3.8	2.9
6	3.5	4.3	4.2	3.0
7	3.7	4.7	4.6	3.1
8	3.8	5.0	4.9	3.1
9	3.9	5.3	5.1	3.2
10	4.0	5.5	5.3	3.2
11	4.0	5.7		
12		5.8		

With 22-27% of MBL, the lowest number of layers for the steel wire to reach a practically constant tangential stress is nine with a corresponding stress ratio of 3.2, Fig. 21 and Table 5. With a slightly lower tensile spooling force, 22% MBL, rope 2 stress ratio is 4.0 and again shows a clear declining trend. Values for ropes 5 and 7 increase to 5.8 and 5.3 with 12 and 10 layers, respectively.

Extreme loads

The smaller ropes allowed for testing with many layers and extreme loads, in the range of 30-53% of MBL, Fig. 22 and Table 6. Rope 1, spooled with 33% of MBL, requires 17-18 layers of rope on the drum before a strong tendency to reach a stress ratio limit is observed. Then, the stress ratio is 5.8, while the same rope spooled with 41% of MBL gives a ratio of 5.9 with 16 layers of rope. Rope 3 seems to require at least 19-20 layers before converging and corresponding stress ratios for 30%, 38% and 53% of MBL are 6.6, 6.8 and 5.0, with 17, 16 and 7 layers of rope on the drum. Rope 4 shows a similar trend and follows the smaller rope of identical design (rope 3) closely.

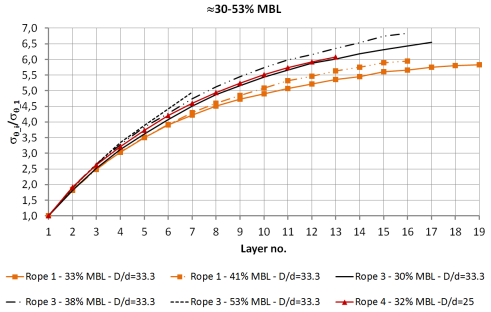

FIGURE 22: STRESS RATIO WITH EXTREME LOADING

TABLE 6: STRESS RATIO WITH 30-53% MBL

Stress Ratio (σ_{θ_i}/ σ_{θ_1}) 30-53% MBL						
Layer	**Rope 1** 33%MBL	**Rope 1** 41%MBL	**Rope 3** 30%MBL	**Rope 3** 38%MBL	**Rope 3** 53%MBL	**Rope 4** 32%MBL
2	1.8	1.8	1.8	1.9	1.9	1.9
3	2.5	2.5	2.5	2.7	2.6	2.6
4	3.0	3.0	3.1	3.3	3.3	3.2
5	3.5	3.5	3.6	3.8	3.9	3.7
6	3.9	3.9	4.1	4.3	4.4	4.2
7	4.2	4.3	4.5	4.7	5.0	4.6
8	4.5	4.6	4.9	5.1		4.9
9	4.7	4.9	5.2	5.5		5.2
10	4.9	5.1	5.4	5.7		5.5
11	5.1	5.3	5.7	6.0		5.7
12	5.2	5.5	5.9	6.2		5.9
13	5.4	5.6	6.0	6.3		6.1
14	5.5	5.7	6.2	6.5		
15	5.6	5.9	6.3	6.7		
16	5.7	5.9	6.4	6.8		
17	5.8		6.6			
18	5.8					
19	5.8					

DISCUSSION

It is evident for all results that the tangential stress decreases with increasing number of layers. According to Dietz [8], this effect is related to the stiffness of the drum and the rope's transverse and longitudinal modulus of elasticity. During spooling, radial deformation of underlying ropes, and the drum, reduces rope tension in each layer and consequently the pressure on the drum. Considering this theory, fibre ropes should cause lower tangential stress in the drum than wire ropes due to lower transverse and longitudinal modulus of elasticity. Lohrengel et. al. [9] modified the Dietz-theory and demonstrated the opposite by including the larger deformability and reduced spooling

radius related to HPFR. Further assessment of this theory against the presented, and additional, experiments is interesting.

The C-factors proposed by DNV-GL [1] are reasonable for the steel wire, but using these values for design of winches with HPFR can induce a considerable risk for underestimating the actual stresses, and potentially cause overload, plastic deformation and collapse of winch drums. Replacing steel wire with HPFR on winches in service can be equally critical, without thorough analysis and calculations, if the increased effective capacity of the lifting appliance, due to the saved weight of steel wire, is utilized.

The number of layers required to reach constant stress ratios increases with increasing spooling loads. At low loads, the covered rope requires at least eight layers on the drum to reach a constant tangential stress ratio and the uncovered ropes are close to constant stress ratios with 14 layers. With normal utilization (20% of MBL), constant stress ratios require more than 11 and 14 layers for the covered and uncovered ropes, respectively.

The C-factors presented in this paper are not necessarily valid for any other winch drum as stresses in winch drums are dependent on the interaction of rope properties and drum stiffness. The consequences of the load free wraps in the first layer and rope spooling speed also need further investigation. However, it is expected that the rope tendencies are valid in general and that dimensionally stable ropes induce lower stresses in multilayer winch drums than more deformable ropes.

CONCLUSIONS

The experiments proves that synthetic fibre ropes can cause larger stresses in winch drums than steel wire ropes of comparable size and strength. The compressive tangential stress is dominating and therefore the most important stress regarding design of winch drums. For the current drum, the axial stress increases linearly after 3-4 layers of rope and consequently causes an increase in von Mises stress with increasing number of layers, even if the tangential stress converges towards a limit.

All the synthetic ropes show tendencies to converge towards a tangential stress limit, but the number of layers before this occurs is dependent on rope design and spooling load. The wire rope and the covered fibre rope reach a stress limit before the other ropes, and in general, the covered rope demonstrates behavior and stresses closest to the wire rope. The synthetic fibre ropes also cause a more even, less asymmetric, stress distribution around the circumference of the drum than the steel wire.

Lifting appliances and winch drums need to fulfill rated capacities with safety margins. The presented experiments demonstrate that design standards and regulations need to be updated with information about special requirements for stress calculations of winch drums with HPFR. In addition, guidance for proper calculation methods, considering both wire rope and synthetic fibre rope properties, should be included.

SUMMARY

Novel results from ongoing experimental investigations of stresses in winch drums caused by different HPFR and a steel wire are presented. Considerable differences are shown and it is proved that fibre ropes can cause higher stresses in winch drums than wire ropes. Present design rules and regulations do not give sufficient information and there is a risk for winch drum damage if design requirements for steel wire winch drums are applied for HPFR applications.

FUTURE WORK

Further stress measurements and assessment of stress results, including flange stresses, against calculation theories and methods will be carried out. This includes testing of the ropes on test drum A, which is equipped with strain gauges in the same manner as drum B.

ACKNOWLEDGEMENTS

This work is carried out in relation to an industrial-PhD project for Rolls-Royce Marine AS and the Department of Ocean Operations and Civil Engineering at the Norwegian University of Science and Technology. The Norwegian Research Council funds the project, project no. 278450.

The authors would like to acknowledge HBM Norge AS for mounting the strain measurement equipment, Geir-Kåre Øverlid and Terje Kvangardsnes, Rolls-Royce Marine AS, for operating the test rig and assistance related to test rig control system.

REFERENCES

[1] DNVGL, "*ST-0378 Standard for offshore and platform lifting appliances*," DNVGL AS, 2016.

[2] Lohrengel, A., Stahr, K.,Wächter, M., "*Safe use of hoisting drums wound with multiple layers of wire hybrid, fibre and/or large diamater ropes*," OIPEEC Conference - Safe use of ropes, Offshore Technology Research Centre, Texas A&M University, College Station, Texas, USA, pp. 21-49, 2011.

[3] Federation, E. M. H., "*FEM 5.024 Guideline - Safe Use of High Performance Fibre Ropes in Mobile Crane Applications*," Cranes & Lifting Equipment, European Materials Handling Federation, 2017.

[4] Schwarzer, T., "*Beitrag zur Gestaltung und Dimensionierung von Windentrommeln bei mehrlagiger Bewicklung mit Kunststoff- und Hybridseilen*," Technischen Universität Clausthal, 2012.

[5] McKenna, H. A., Hearle, J.W.S, O'Near, N., *Handbook of fibre rope technology,* Woodhead Publishing Limited, 2004.

[6] Otto, S., "*Ein nicht-rotationssymmetrisches Belastungsmodell für die Ermittlung des Beanspruchungsverhaltens mehrlagig bewickelter Seiltrommeln*," Technischen Universität Clausthal, 2004.

[7] DNVGL, "*DNVGL-RP-E305 Design, testing and analysis of offshore fibre ropes*," 2015.

[8] Dietz, P., "*Ein verfahren zur berechnung ein- und mehrlagig bewickelter seiltrommeln*," Dr.-Ing., Technischen Hochschule Darmstadt, 1972.

[9] Lohrengel, A., Stahr, K.,Schulze, M.,Wächter, M., "*Innovative drum construction for multi-layer winding with fibre ropes*," OIPEEC Conference 2015/5th International Stuttgart Ropedays - Challenging Rope Applications, Alte Stuttgarter Reithalle, Stuttgart, Germany, pp. 269-285, 2015.

Taylor & Francis
Taylor & Francis Group

Ships and Offshore Structures

ISSN: 1744-5302 (Print) 1754-212X (Online) Journal homepage: https://www.tandfonline.com/loi/tsos20

Tangential stress in multilayer winch drums with high performance synthetic fibre ropes – analytical calculations versus experimental measurements

Reidar André Skarbøvik, Henry Piehl & Vilmar Æsøy

To cite this article: Reidar André Skarbøvik, Henry Piehl & Vilmar Æsøy (2020): Tangential stress in multilayer winch drums with high performance synthetic fibre ropes – analytical calculations versus experimental measurements, Ships and Offshore Structures, DOI: 10.1080/17445302.2020.1739871

To link to this article: https://doi.org/10.1080/17445302.2020.1739871

SHIPS AND OFFSHORE STRUCTURES
https://doi.org/10.1080/17445302.2020.1739871

Tangential stress in multilayer winch drums with high performance synthetic fibre ropes – analytical calculations versus experimental measurements

Reidar André Skarbøvik[a,b], Henry Piehl[b] and Vilmar Æsøy[b]

[a]Kongsberg Maritime Commercial Marine AS – Deck Machinery, Ålesund, Norway; [b]Department of Ocean Operations and Civil Engineering, Norwegian University of Science and Technology, Ålesund, Norway

ABSTRACT

Use of high performance fibre ropes (HPFR) is attractive in subsea operations due to high strength and low weight making lifting operations in deep waters possible with practically no reduced lifting capacity. However, experiments show that HPFRs can cause higher loads on multilayer winch drums compared to steel wire ropes. This paper presents comparisons between experimental stress measurements and calculation methods for a steel wire and two different HPFRs, wound in 10–14 layers at different rope tensions. The results show that the tangential stresses in the drum are reasonably assessed for the steel wire and a dimensionally stable HPFR, but considerably underestimated for a more deformable HPFR with more than 3–7 layers of rope, dependent on rope tension. The results also show that the method specified by class-societies is not capable of calculating relevant tangential stress in multilayer winch drums with HPFRs.

ARTICLE HISTORY
Received 27 November 2019
Accepted 4 March 2020

KEYWORDS
Multilayer winch drum; synthetic fibre rope; steel wire; tangential stress

Nomenclature

A_r	effective load carrying cross-section area of rope [mm^2]
B_i	integration constants [–]
C_i	layer dependent load factor [–]
E	modulus of elasticity of drum material [N/mm^2]
E_L	longitudinal modulus of elasticity of rope [N/mm^2]
E_T	transverse modulus of elasticity of rope [N/mm^2]
F_T	transverse force [N]
HPFR	high performance synthetic fibre rope [–]
IWRC	independent wire rope core [–]
K	bending stiffness [Nmm]
L	drum length, inside flange to inside flange [mm]
MBL	minimum breaking load [kN]
N_x	axial force [N]
O_r	relative ovality of rope [–]
T_i	rope tension in layer i [N]
$\overline{T}$	average rope tension from all rope spooled onto drum [N]
ΔT_i	relaxed tension in layer i [N]
$X_{k,n}$	partial pressure from layer k with n layers in rope pile [N/mm^2]
d	rope diameter [mm]
d_x	major axis of elliptic cross-section [mm]
d_y	minor axis of elliptic cross-section [mm]
Δd	reduction in rope diameter due to transverse pressure [mm]
e_R	distance between rope windings, c–c (pitch) [mm]
f_i	pressure reduction in winding i [N/mm^2]
i	layer index [–]
$k_{T,\mu}$	ratio of compressive and longitudinal stress with friction [–]
l_p	length of piston [mm]
n	number of rope wraps [–]
p_d	total pressure on drum [N/mm^2]
$p_{\mathrm{d\_max}}$	total pressure from full length of rope on drum [N/mm^2]
p_i	pressure on layer i [N/mm^2]
q	fill factor, ratio between effective and nominal cross-section [–]
r_D	outer drum radius [mm]
r_F	outer flange radius [mm]
$r_{i,c}$	middle radius of winding i in crossing-section [mm]
$r_{i,p}$	middle radius of winding i in parallel-section [mm]
r_m	middle drum radius [mm]
s	length of substitute cross-section [mm]
t	drum thickness [mm]
t_F	flange thickness [mm]
w	shell deformation [mm]
δ_i	compression of rope winding due to unit pressure [mm]
δ_T	compression of drum due to unit pressure [mm]
ε_L	longitudinal strain [mm/mm]
ε_T	compressive strain [mm/mm]
ν	Poisson's ratio of drum material [–]
σ_L	longitudinal stress in rope [N/mm^2]
σ_T	compressive stress in rope [N/mm^2]
σ_θ	tangential stress in drum [N/mm^2]
μ_D	coefficient of friction between rope and drum [–]
χ	dampening constant [1/mm]

1. Introduction

Experimental investigations (Skarbøvik et al. 2019) show that high performance fibre rope (HPFR) can induce considerably larger stresses in multilayer winch drums than steel wire rope. The dominating design parameter for such drums is the compressive tangential stress which increases

CONTACT Reidar André Skarbøvik reidar_andre.skarbovik@km.kongsberg.com Kongsberg Maritime Commercial Marine AS – Deck Machinery, Ålesund 6025, Norway

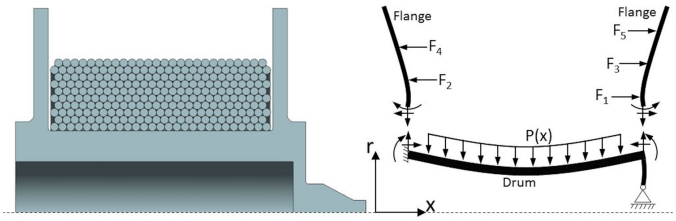

Figure 1. Multilayer winch drum. This figure is available in colour online.

towards a limit with the increasing number of rope layers. The magnitude of the tangential stress limit, and number of rope layers required to reach it, is dependent on rope properties and tensile load in the rope. As an example, a drum with steel wire rope wound with rope tension equal to 15% of minimum breaking load (MBL) can reach a practically constant tangential stress within eight layers, while a comparable HPFR, with equivalent utilisation of rope strength, requires more than 14 layers to reach a limit at a considerably higher stress level.

This paper presents calculations of tangential stress in a multilayer winch drum compared with experimental stress measurements. The method developed by Dietz (1971), referenced by DNV-GL (2017), is considered as best-practice for detailed assessment of radial pressure from multiple layers of steel wire rope, while a more recent modification of this theory (Lohrengel et al. 2015) is adapted to HPFR by taking the larger rope deformability of such ropes into account. These theories are applied to calculate the resulting radial pressure on a drum from multiple layers of steel wire and two HPFRs. Further, these pressures are used to calculate the tangential stresses in the drum structure by means of different methods; the coupled method using a differential equation for axisymmetric cylindrical shells (Mupende 2001), the classical closed form equation for tangential stress in thick-walled cylinders and two dimensional axisymmetric finite element analysis. In addition, the results are compared to the prevailing method for calculation of tangential stress in winch drums specified by class societies, DNV-GL (2019) and ABS (2019), and a modification of this method more suitable for thick-walled drums.

The objectives of the present study are:

- Evaluate best-practice multilayer calculation method against experimental measurements with steel wire and HPFRs.
- Assess applicability and accuracy of different calculation methods for tangential stress in the drum structure.

The calculations and measurements are based on four different tensile load levels ranging from 10-30% of the MBL. Rope deformations are measured by means of laser technology (Lohrengel et al. 2017) and relevant transverse moduli of elasticity are determined by experimental testing according to the method developed by Dietz (1971).

2. Theory & methods

Multilayer winch drums (Figure 1) experience radial pressure from multiple layers of rope and axial forces from the flanges keeping the rope package in place. The radial pressure from each rope layer varies and is in general dependent on the elastic interaction between rope and drum resulting from system design and stiffness, number of rope layers, rope tension and rope properties. The radial deformation of the drum contracts the flanges radially and induces bending moments to the flanges, while the forces from each layer acting on the flanges create a tensile axial force in the drum and opposite bending moments to the drum ends.

The rope radius varies within each layer as the rope climbs over underlying ropes when displaced axially during winding, thus the radial pressure also varies with the rotational angle. The contact between rope and flange is also limited to an angle sector and in reality, neither the drum pressure nor the flange forces are axisymmetric loads. However, for analytical stress calculations, the loads acting on multilayer winch drums are often simplified as such.

2.1. Radial pressure on multilayer winch drums (Dietz 1971)

The radial pressure acting on the drum is calculated by taking drum and rope deformations into consideration. Figure 2 shows the idealised 'Dietz-model' with an axisymmetric winch drum and rope windings modelled as separate, closed and stacked concentric rings with square cross-sections. As each ring is closed and only the radial pressure between ropes are considered in the model, friction between the ropes are neglected and rope tension in each ring is constant with respect to rotational angle.

The resulting radial pressure from each stack, Equation (1), is calculated by the sum of all partial pressures in a linear system of equations, Equation (2). The original tension applied to the rope windings in each layer is relaxed due to compression forces from subsequent layers causing deformations to the rope cross-sections and reduction of the winding radii. Equation (4) gives the side lengths of the square cross-section, while rope deformation and resulting pressure reduction, due to unit load pressure, are calculated by Equations (5) and (6), respectively. The layer radius, Equation (7), and ratio of the rope's longitudinal and transverse moduli of elasticity are important quantities related to the tension relaxation and

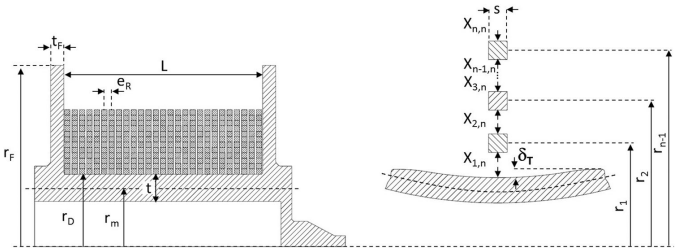

Figure 2. Applied principle of the method for calculation of pressure on multilayer winch drums.

pressure reduction. The radial pressure from the outer layer, as defined by Dietz, is given by Equation (8).

The total pressure on the drum is determined by sequential calculations, starting with one layer and repeated until all layers are included. If radial deformation of the drum is taken into account, the calculations are repeated for each rope stack as the radial deformation is not constant along with the drum.

$$p_D = \sum_{i=1}^{n} X_{1,i} \tag{1}$$

$$\begin{bmatrix} \alpha_i & \delta_1 & 0 & 0 & 0 & 0 & 0 \\ \delta_1 & \alpha_2 & \delta_2 & 0 & 0 & 0 & 0 \\ 0 & \delta_2 & \alpha_3 & \delta_3 & 0 & 0 & 0 \\ . & . & . & . & . & . & . \\ 0 & 0 & 0 & \delta_k & \alpha_{k+1} & \delta_{k+1} & 0 \\ . & . & . & . & . & . & . \\ 0 & 0 & 0 & 0 & 0 & \delta_{n-2} & \alpha_{n-1} \end{bmatrix} \begin{bmatrix} X_{1,n} \\ X_{2,n} \\ X_{3,n} \\ . \\ X_{k,n} \\ 0 \\ X_{n-1,n} \end{bmatrix} = \begin{bmatrix} 0 \\ 0 \\ 0 \\ . \\ 0 \\ . \\ -\delta_{n-1} X_{n,n} \end{bmatrix} \tag{2}$$

$$\begin{aligned} \alpha_1 &= [\delta_T - (1 + f_1)\delta_1] \\ \alpha_i &= -[(1 + f_{i-1})\delta_{i-1} + (1 + f_i)\delta_i] \\ i &= 1, 2, \ldots, n-1 \end{aligned} \tag{3}$$

$$s = \frac{d}{2}\sqrt{\pi q} \tag{4}$$

$$\delta_i = -\frac{r_i^2}{sE_L} \tag{5}$$

$$f_i = \frac{s^2}{2r_i^2}\left(\frac{E_L}{E_T}\right)_i \tag{6}$$

$$r_i = r_D + \left(i - \frac{1}{2}\right)s \tag{7}$$

$$X_{n,n} = \frac{T_n}{r_n s} \tag{8}$$

2.2. Equation for radial pressure

Calculating the tangential stress in a drum with one single layer of rope by means of the pressure from Equation (8) results in too high stress compared with experiments. Considering force equilibrium of a drum with one single layer of rope with n wraps with tension T (Figure 3), results in an equation for the radial pressure more comparable with experiments, Equation (9).

$$2r_D n e_R p_D = 2T_1 n \Leftrightarrow p_D = \frac{T_1}{r_D e_R} \Rightarrow X_{n,n} = \frac{T_n}{r_n e_R} \tag{9}$$

2.3. Modification for fibre rope deformation

Lohrengel et al. (2015) modified the original method by Dietz to better incorporate the larger deformation related to HPFR using elliptical rope shapes (Figure 4). Equation (10) gives the tension reduction in each layer considering the major and minor diameters of an ellipse. The degree of deformation is described by the relative ovality, Equation (11), and corresponding layer radii for parallel- and crossing sections are given by Equations (12) and (13), respectively.

$$\Delta T_i = p_i \frac{\sqrt{\frac{\pi}{4} d_x d_y q}}{2r_i} \frac{E_L}{E_T} A_r \tag{10}$$

$$O_r = \frac{|d_x - d_y|}{\max(d_x; d_y)} \tag{11}$$

$$r_{i,p} = r_D + \frac{d_y}{2} + \frac{i-1}{2}\sqrt{d_y^2\left(4 - \frac{e_R^2}{d_x^2}\right)} \tag{12}$$

$$r_{i,c} = r_D + \frac{d_y}{2} + \left(i - \frac{1}{2}\right)d_y \tag{13}$$

2.4. Stress calculation method – the coupled method

Mupende (2001) developed an analytical axisymmetric model with rings coupling forces and moments between the drum and flanges (Figure 5). This resulted in an integrated analytical model where the reciprocal effects between flanges and drum are taken into account. Assuming small deformations, the radial deformation of an axisymmetric cylindrical shell exposed to radial pressure and axial force is given by Equation (14), the

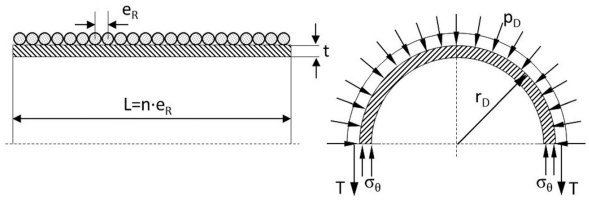

Figure 3. Rope pressure on drum.

dampening constant, Equation (15), and the bending stiffness, Equation (16).

The general solution of the differential equation is given by Equation (17) from which rotation, bending moment and shear force are deduced from the derivatives.

$$\frac{\partial^4 w}{\partial x^4} + 4\chi^4 w = \frac{1}{K}\left(p(x) - \frac{\nu}{r_m}N_x\right) \tag{14}$$

$$\chi = \frac{1}{\sqrt{r_m t}}\sqrt[4]{3(1-\nu^2)} \tag{15}$$

$$K = \frac{Et^3}{12(1-\nu^2)} \tag{16}$$

$$\begin{aligned} w(x) = {} & B_1\cosh(\chi x)\cos(\chi x) + B_2\mathrm{Sinh}(\chi x)\sin(\chi x) \\ & + B_3\mathrm{Cosh}(\chi x)\sin(\chi x) + B_4\sinh(\chi x)\cos(\chi x) \\ & + \frac{1}{4\chi^4 K}\left(p(x) - \frac{\nu}{r_m}N_x\right) \end{aligned} \tag{17}$$

2.5. Stress calculation method – thick shell equation (Irgens 2008)

Winch drums with $t > 0.1r_m$ are considered as thick, for which the error using thin shell theory can be significant. Equation (18) calculates the compressive tangential stress on the inside of a thick drum.

$$\sigma_\theta = -\frac{2p_D}{1 - \left(\frac{(r_D - t)^2}{r_D^2}\right)} \tag{18}$$

2.6. Stress calculation methods – DNVGL and MOD*

Class societies, DNV-GL (2019) and ABS (2019) calculate the tangential drum stress using a thin-shell equation, applying the rope tension in the first layer multiplied by an empirical, layer dependent factor C_i, Equation (19). The tangential stress in the winch drum is considered to be constant from five layers with a maximum C-factor of 3. The pressure on a drum with i layers is given by Equation (20).

Current rules and regulations do not differentiate between thin- and thick drums and a proposed modification denoted MOD*, more relevant for thick drums, is given by Equation (21).

$$\begin{aligned} \sigma_\theta = {} & -C_i\frac{T_1}{td} \\ & C_1 = 1,\ C_2 = 1.75,\ C_3 \approx 2.17,\ C_4 \approx 2.58,\ C_5 \\ & = 3 \ldots C_n = 3 \end{aligned} \tag{19}$$

$$p_D = \frac{C_i T_1}{r_D e_R} \tag{20}$$

$$\sigma_\theta = -C_i\frac{2T_1}{\left(r_D - \frac{(r_D - t)^2}{r_D}\right)e_R} \tag{21}$$

2.7. Stress calculation method – 2D axisymmetric finite element method

A static linear elastic 2D axisymmetric finite element model of the experimental test drum (Figure 6) is used for numerical calculations. The calculated pressure, from the theories described in sections 2.1 through 2.3, is applied as an evenly distributed radial load on the outer drum surface. The drum is fully

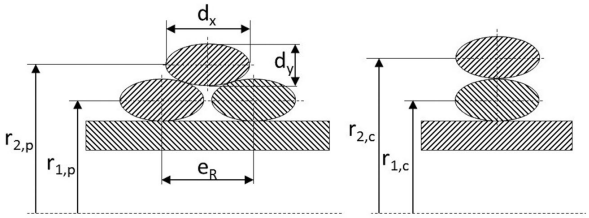

Figure 4. Elliptic rope cross-sections – parallel sections (left), crossing sections (right).

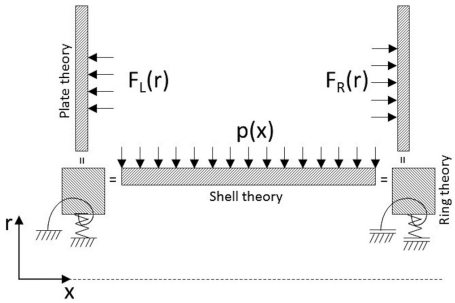

Figure 5. Principle of the coupled method.

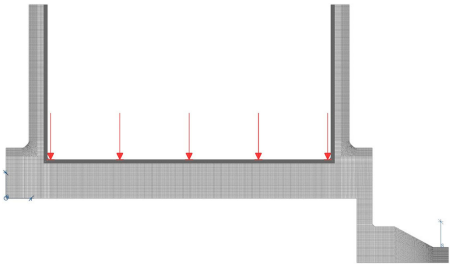

Figure 6. Axisymmetric finite element model. This figure is available in colour online.

constrained at the drive interface on the left side and supported by a radial constraint on the axle end on the right side.

A fine structured mesh with 8-node axisymmetric elements and material properties E = 200 GPa and $\nu = 0.3$, equivalent to the strain measurement calculations (Skarbøvik et al. 2019), are used with the NX Nastran SOL101 solver.

3. Experimental setup & calculation data

The experimental stress measurements from Skarbøvik et al. (2019) are used in the evaluations. The following section gives a brief introduction to the rope test arrangement with supplemented information about the measurement of rope shape and transverse modulus of elasticity.

3.1. Experimental stress measurement

Figure 7 shows the test arrangement in Kongsberg Maritime Commercial Marine's multilayer winch test rig. The test rope (red curve) runs between two winch drums (pos.1 and 14) driven by high-pressure hydraulic motors (pos.2 and 13). A control system continuously controls the rope tension and winch speed, using input from load cells (pos.4 and 10) and encoders (pos.3 and 9), as well as the linear motion of the spooling sheaves (pos.5 and 11) driven by hydraulic cylinders (pos.6 and 12). Guide sheaves (pos.7 and 8) bring the rope down to working height for potential testing of rope's transverse modulus of elasticity (pos.17) or rope-friction using a driven drum with two different diameters equal to the test drums (pos.18). Pos. 19 and 20 are laser scanners for measuring rope profiles on the drum and rope shapes.

The strain measurements are controlled by QuantumX equipment from HBM (Figure 7, Pos.15), five strain gauge amplifiers and a data recorder, attached to the flange with 24 V power supply through a slip-ring on the free end axle (Figure 7, Pos.16). During testing, the measurements are remotely controlled and monitored using Wi-Fi.

The stresses are calculated from twelve biaxial strain gauges glued, with equal circumferential spacing, on the inside of the drum in the centre between the flanges (Figure 8).

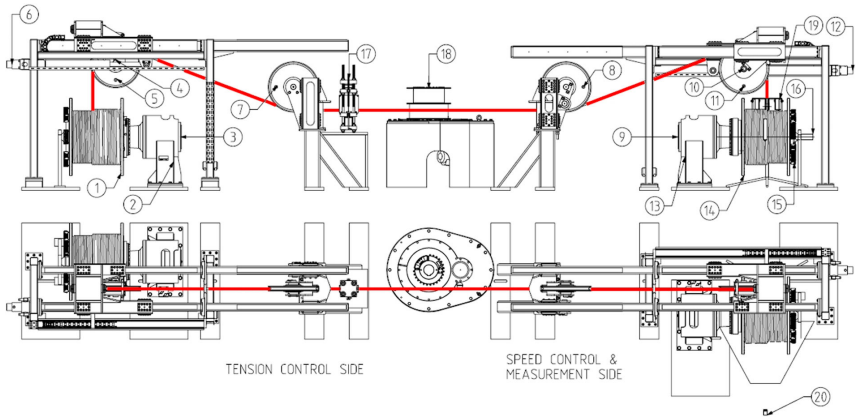

Figure 7. Arrangement in Kongsberg Maritime Commercial Marine's multilayer winch test rig. This figure is available in colour online.

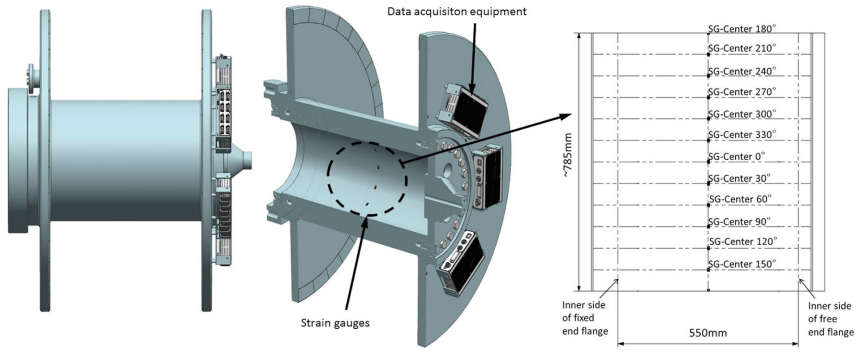

Figure 8. Test drum with strain gauge locations, strain gauge amplifiers and data recorder on the outer side of the flange. This figure is available in colour online.

3.2. Test drum

The experiments use two drums of different sizes. Drum A with Ø500 mm outer diameter and 625 mm distance between flanges and drum B with outer diameter Ø400 and 550 mm length. Due to the limited availability of strain measurement equipment, measurement of only one drum is possible for each test run. The present analysis is based on results from drum B, Figure 8 and Table 1.

3.3. Ropes

The calculations and measurements are based on three different ropes of same nominal size. One independent wire rope core (IWRC) steel wire, one 12-strand braided HPFR with cover and core (dimensionally stable rope) and one 12-strand braided HPFR (deformable rope). The different ropes, with related minimum breaking loads, are listed in Table 2.

3.4. Laser measurement

One LMI Gocator 2380B laser scanner (Figure 9), taking 36 pictures per revolution, measures rope layer profiles on the drum during winding, while three LMI Gocator 2130C scanners (Figure 10) are used to take snapshots of rope shapes when wound off the drum.

Examples of the three different rope shapes are shown in Figure 11. The steel wire rope (rope 1) maintains a close to circular shape, while the dimensionally stable HPFR (rope 2) takes a more hexagonal shape without considerable deformations. The deformation of the deformable HPFR (rope 3) is considerably larger resulting in a rectangular-like shape.

Figures 12 and 13 show examples of rope profiles on the drum for ropes 2 and 3 during winding. The differences in rope shapes can be recognised with a more uneven curve for the dimensionally stable HPFR and a smoother, more flattened curve for the deformable HPFR.

Table 1. Test drum dimensions.

Drum	r_D [mm]	t [mm]	L [mm]	r_F [mm]	t_F [mm]	t/r_m	Materials (drum/ flanges)
A	250	75	625	500	36	0.35	AISI4130/JFE-Hiten780s
B	200	75	550	500	36	0.46	AISI4130/JFE-Hiten780s

Table 2. Ropes.

Rope	Size [mm]	Fibre type	Design	MBL [kN]
1	Ø20	IWRC Steel Wire	6 × 26WS with extruded steel core	299
2	Ø20	Dyneema®SK75	12-strand braided with cover and core	383
3	Ø20	Dyneema®SK78 & Polyester	12-strand braided	353

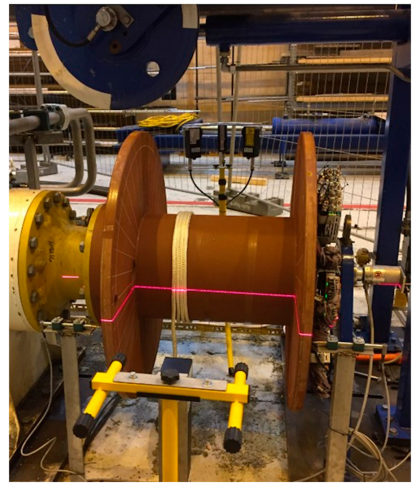

Figure 9. Drum laser scanner. This figure is available in colour online.

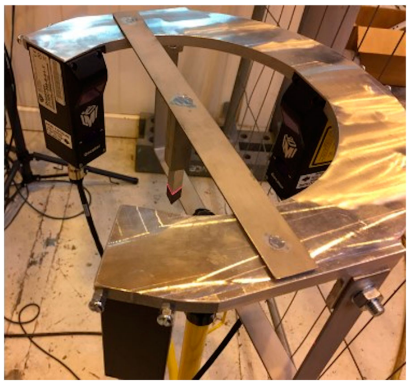

Figure 10. Rope shape scanners with calibration piece. This figure is available in colour online.

The cross-section and layer profile scans allow for measuring the closed profile cross-sectional area, profile dimensions and estimate rope radiuses in each layer.

3.5. Rope elasticity

The transverse modulus of elasticity is defined according to Dietz (1971), Equation (22). The ropes are tested in the rope test rig with a calibrated tension load-cell spliced into the rope (Figure 14) or in an available calibrated rope test machine (Figure 15) giving possibilities for testing of transverse elasticity with more than one single rope, longitudinal modulus, Equation (23), at different axial rope loads and breaking strength.

$$E_T = \frac{\sigma_T}{\varepsilon_T} = \frac{\frac{F_T}{s l_p}}{\frac{\Delta d}{s}} \tag{22}$$

$$E_L = \frac{\sigma_L}{\varepsilon_L} = \frac{\frac{T}{s^2}}{\frac{\Delta l}{l}} \tag{23}$$

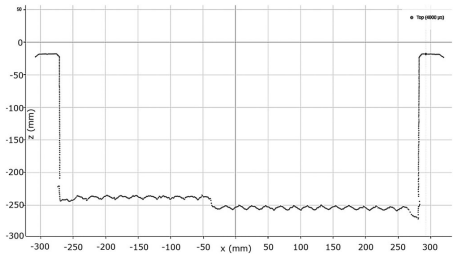

Figure 12. Profile of dimensionally stable HPFR on drum.

For testing of the transverse modulus, the rope is routed through a compression device (Figure 7, Pos.17) and a specified tensile load is applied before the rope is repeatedly compressed to a specified transverse load. When the hysteresis effect stabilises, after 5–10 cycles, a valid force-displacement curve is obtained. Testing is carried out for different tensile loads, typically in the range of 10-40% MBL, while the transverse loads are in the range of 10-150% of the tensile loads.

Polynomial curve-fitting is applied to calculate transverse moduli, for different ratios of transverse and longitudinal stress, from the derivative of stress–strain curves generated from the measured force-elongation curves (Figure 16). Longitudinal moduli are supplied by manufacturer for rope 1 and calculated from measurements for rope 3, while an estimated value for rope 2 is extracted from literature (Lohrengel et al. 2017).

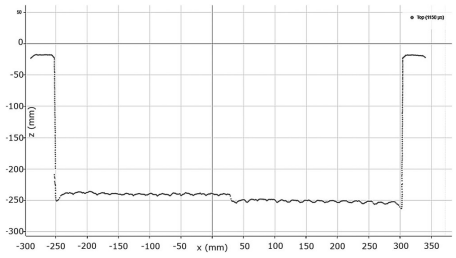

Figure 13. Profile of deformable HPFR on drum.

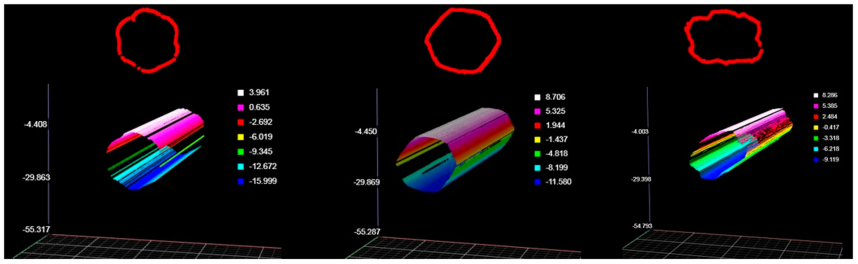

Figure 11. Example of rope shapes: steel wire rope (left), dimensionally stable HPFR (centre) and deformable HPFR (right). This figure is available in colour online.

Figure 14. Testing of transverse modulus in multilayer test rig. This figure is available in colour online.

Figure 15. Testing of transverse modulus in rope tension machine. This figure is available in colour online.

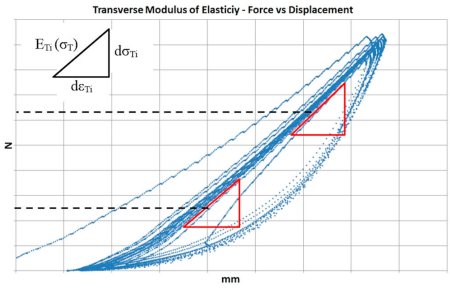

Figure 16. Example of force/displacement curve and rope modulus. This figure is available in colour online.

Selection of a transverse modulus from test data, relevant for the actual rope-drum system, is based on an equivalent ratio between transverse and longitudinal stress calculated by Equation (24) (Mupende 2001).

$$k_{T,\mu} = \frac{\sigma_T}{\sigma_L} = \frac{\sqrt{A_r}}{\pi \mu_D r_D}\left(e^{-\pi\mu_D} - 1\right) \tag{24}$$

3.6. Calculation data

The analytical calculations are based on the different tensile loads, transverse and longitudinal moduli, friction coefficients and the number of layers given in Table 3.

Due to a required number of practically load-free wraps of rope in the first layer and rope tension being ramped up over a given time in the test rig, the resulting rope tension in the first layer is not uniform and lower than in subsequent layers. Applying this low rope tension in calculations based on a constant tension and a layer dependent factor (e.g. DNVGL and MOD* methods) would result in too low stresses. To compensate for this, the average tension in the complete rope package is applied for these calculation methods. For the other calculation methods, which are based on calculated pressure from each layer, the measured average tensions in each layer are applied.

Dietz (1971) and Mupende (2001) applied friction coefficients in the range of 0.18-0.2 for steel wire ropes on winch drums, while dry experiments with a Dyneema® SK75 rope by Lohrengel et al. (2015) resulted in friction coefficients in ranges 0.042–0.097 for self-contact and 0.053–0.118 for contact with steel. Based on this, friction coefficients of 0.1 and 0.2 are applied in the calculations for the fibre ropes and the steel wire, respectively.

The values for transverse modulus of elasticity are based on tests using one single rope for all three rope designs. The rope dimensions for the HPFRs, d_x and d_y, are estimated from cross-section profiles, while the nominal rope dimensions are used for the steel wire. The distance between each winding, e_R, is taken as the average distance between the ropes in all layers measured over a length at the centre of the drum.

Deformation of the drum structure is neglected in the calculations, $\delta_T = 0$, radial pressure, p_D, and the radius for the different layers are calculated by Equations (9) and (12), respectively. The effective cross-sectional area of each rope is calculated by the nominal cross-section multiplied with the fill factor q.

Table 3. Calculation data.

Rope #	$\overline{T}$ [kN]	MBL %	E_L [N/mm^2]	E_T [N/mm^2]	$\overline{d}_x$ [mm]	$\overline{d}_y$ [mm]	$\bar{e}_R$ [mm]	μ_D [–]	q [–]	p_{D_max} [N/mm^2]	Layers #
1	29.12	~10	90000	548	20	20	20	0.2	0.649	15.9	10
1	43.75	~15	98000	774	20	20	20	0.2	0.649	25.8	10
1	58.23	~20	104000	974	20	20	20	0.2	0.649	36.5	10
1	87.17	~30	113000	1314	20	20	20	0.2	0.649	58.5	10
2	38.73	~10	39100	395	20.8	18.7	21.1	0.1	0.620	25.3	11
2	58.17	~15	39100	511	20.9	18.7	21.1	0.1	0.620	41.7	11
2	77.26	~20	39100	628	21.3	18.7	21.1	0.1	0.620	59.7	11
2	85.15	~22	39100	677	21.3	18.7	21.1	0.1	0.620	68.9	11
3	33.99	~10	46200	316	18.1	12.1	19.8	0.1	0.689	24.8	14
3	48.73	~14	49800	367	17.7	12.3	19.7	0.1	0.689	36.6	14
3	68.04	~19	53400	423	17.8	12.4	19.5	0.1	0.689	52.1	14
3	88.25	~25	55750	466	17.6	12.4	19.7	0.1	0.689	66.4	11

4. Results

In the following, influence from flange forces on tangential stress is first presented. Further, measured peak tangential stress values are compared with calculated stresses using different calculation methods. The figures show the ratios between stresses for each layer against the maximum measured value for each experiment.

4.1. Flange force influence on tangential stress in drum

The stress calculations are exclusively considering radial pressure loads, which in reality is impossible as multiple layers of rope cause inevitable axial forces to the flanges. The effect of flange forces are dependent on structure stiffness and it is expected that the flange forces have most significance on the tangential stress close to the flanges. In addition, increased von Mises stress in the drum is expected due to the combination of tensile axial stress and compressive tangential stress. This is confirmed by the results from a finite element analysis, Figures 17 and 18, comparing stresses from simulations with radial pressure load only and radial pressure load in combination with flange forces. The applied multilayer winch loads are according to DNV-GL (2019).

Due to geometry and change in stiffness, axial stresses are induced in the vicinity of the flanges even without flange forces. Considering the tangential stress, influence from flange forces is very small at the centre of the drum where the experimental stresses are measured. At this location, the difference in tangential stress, with and without flange forces, is about 0.7%. This justifies the simplification of applying pure radial pressure loads in the evaluation of calculations versus measurements.

4.2. Tangential stress with rope 1 – steel wire rope

For rope 1 with low tension (Figure 19), all methods based on the calculated 'Dietz-pressure' underestimate the tangential stresses for more than two layers of rope. The respective stress ratios with 10 layers for the coupled method, thick shell equation and FEM are 0.81, 0.86 and 0.88. The DNVGL method is closest to the measurements with a maximum stress ratio of 0.96, but in general, also underestimates the stresses for most layers. The MOD* method is conservative and overestimates the stresses for all layers with a maximum stress ratio of 1.18.

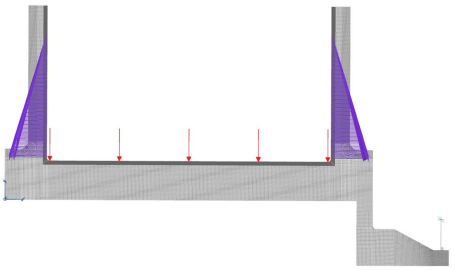

Figure 17. Finite element model with radial pressure and flange forces. This figure is available in colour online.

Increasing the tension to 15% MBL (Figure 20) reduces the deviations and the stress ratios with 10 layers for the thick shell equation and FEM increase to 0.93 and 0.95. The coupled method and MOD* method still under- and overestimates the stresses with respective 10-layer stress ratios of 0.87 and 1.18.

With 20% MBL rope tension (Figure 21) the FEM calculation, in particular, but also the thick shell equation follow the measured stresses closely, while the stresses are still underestimated by the coupled method. The respective 10-layer stress ratios for these three methods are 1.01, 0.98 and 0.93. The DNVGL method also still underestimates the stresses for practically all layers with a 10-layer stress ratio of 0.96 and the MOD* remains overly conservative with a 1.18 stress ratio.

With 30% MBL (Figure 22) all calculations give relatively good agreement with the measurements, except for the MOD* method which is too conservative. The 10-layer stress ratios for the different methods, in the order listed on the figures, are 0.98, 1.04, 0.95, 1.16 and 1.07.

4.3. Tangential stress with rope 2 – dimensionally stable HPFR

With rope 2 and low rope tension (Figure 23), all calculations based on 'Dietz-pressure' are conservative for all layers. The DNVGL method is closest to the measurements with an exact stress ratio of 1.00 for 11 layers, while the MOD* method is very conservative with a stress ratio of 1.23.

With 15% and 20% MBL rope tension (Figures 24 and 25) the DNVGL method underestimates the stresses considerably for all layers with respective 11-layer stress ratios of 0.84 and 0.75. The MOD* method gives better results for all layers with 15% MBL tension and up to seven layers with 20% MBL tension. The thick shell equation and FEM give slightly conservative results for all layers. The stress ratios for these two load levels are 1.04 and 1.01 for the thick shell equation, and 1.07 and 1.04 for FEM. The coupled method gives the closest fit with 15% MBL, but underestimates the stresses with 20% MBL tension and more than seven layers.

Increasing the rope tension further (Figure 26) results in stress ratios of 0.9, 0.96, 0.68, 0.84 and 0.98 for the different methods. The fit is good for the thick shell and FEM, while the coupled method now underestimates the stresses with more than four layers of rope. The DNVGL method results in too low stresses for all layers, while the MOD* method gives reasonable results up to 5–6 layers.

4.4. Tangential stress with rope 3 – deformable HPFR

Larger deviations are observed for all calculations with the more deformable HPFR. The DNVGL method considerably underestimates the stresses for all rope tensions and all layers. For the lowest rope tension (Figure 27) the MOD* method is the most conservative, but underestimates the stresses with more than seven layers. With 14% MBL rope tension FEM gives slightly higher stress ratios than the MOD* method.

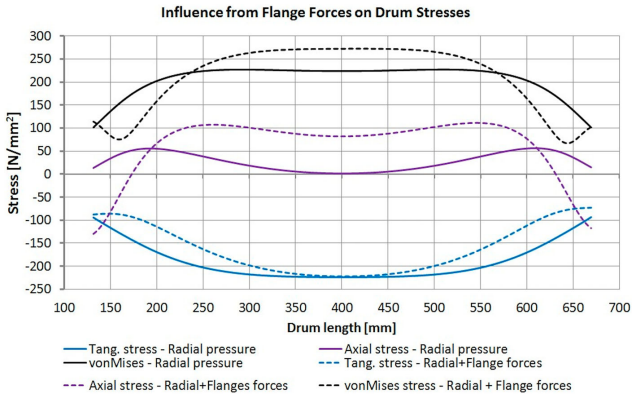

Figure 18. Drum stresses with/without flange forces. This figure is available in colour online.

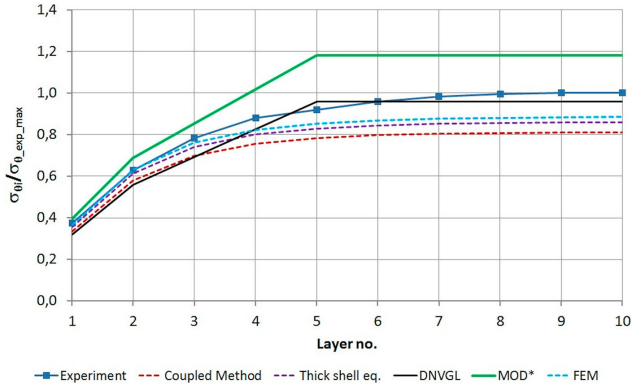

Figure 19. Rope 1 – tangential stress ratio – 10% MBL. This figure is available in colour online.

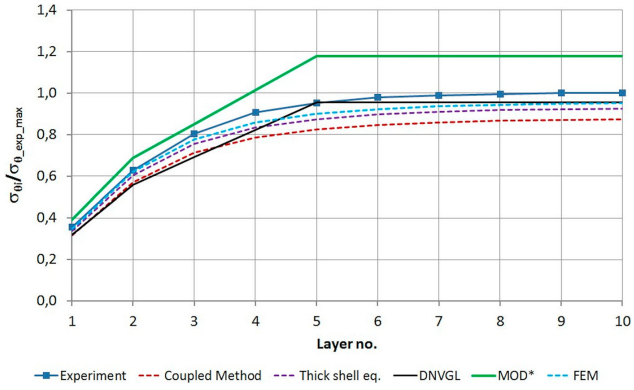

Figure 20. Rope 1 – tangential stress ratio – 15% MBL. This figure is available in colour online.

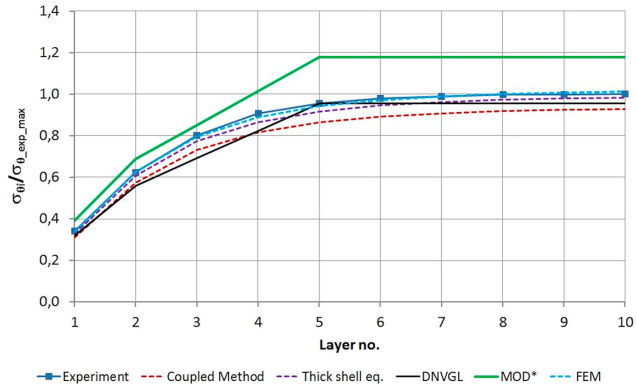

Figure 21. Rope 1 – tangential stress ratio – 20% MBL. This figure is available in colour online.

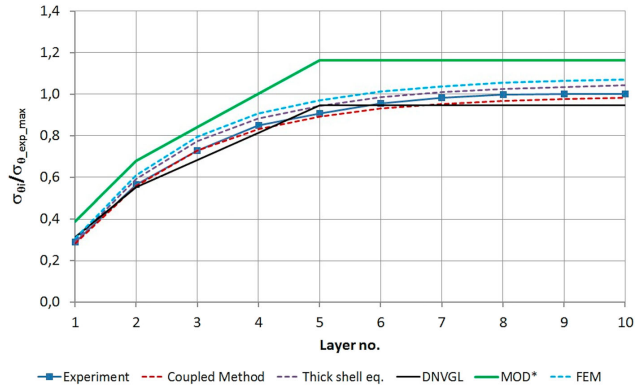

Figure 22. Rope 1 – tangential stress ratio – 30% MBL. This figure is available in colour online.

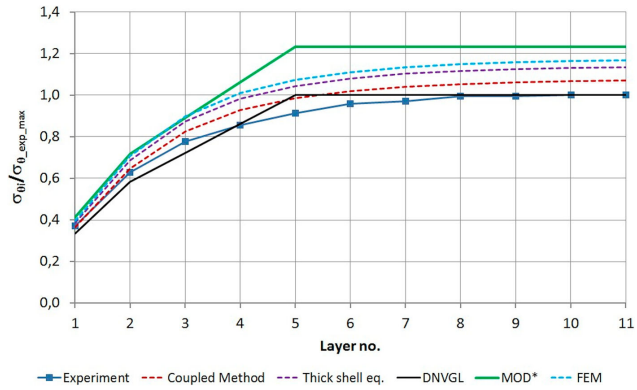

Figure 23. Rope 2 – tangential stress ratio – 10% MBL. This figure is available in colour online.

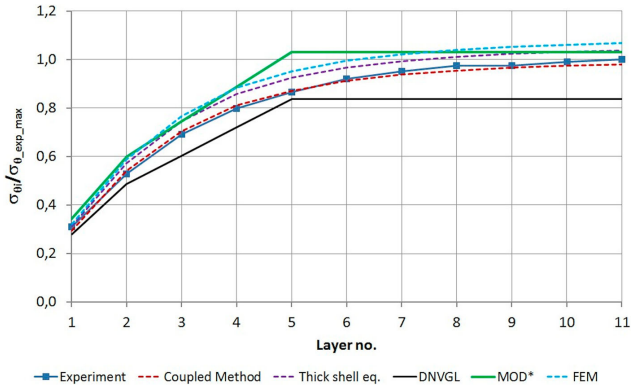

Figure 24. Rope 2 – tangential stress ratio – 15% MBL. This figure is available in colour online.

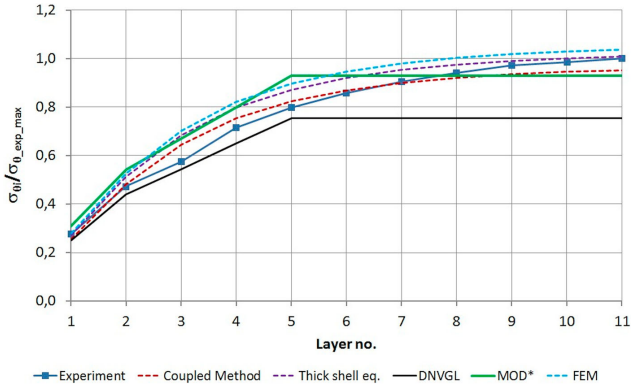

Figure 25. Rope 2 – tangential stress ratio – 20% MBL. This figure is available in colour online.

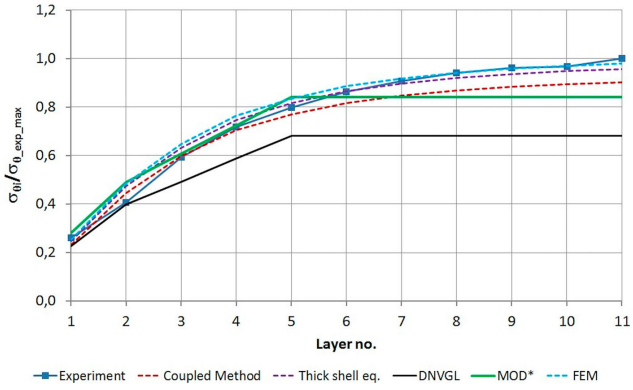

Figure 26. Rope 2 – tangential stress ratio – 22% MBL. This figure is available in colour online.

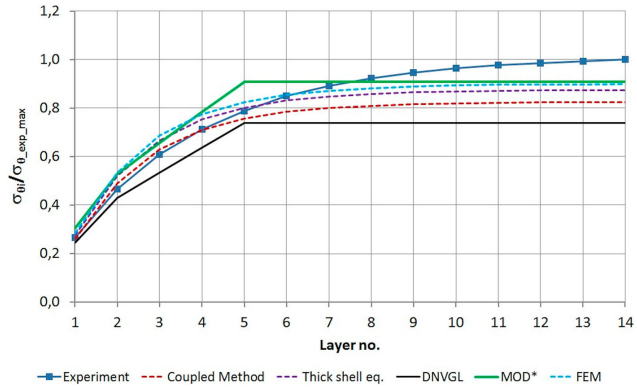

Figure 27. Rope 3 – tangential stress ratio – 10% MBL. This figure is available in colour online.

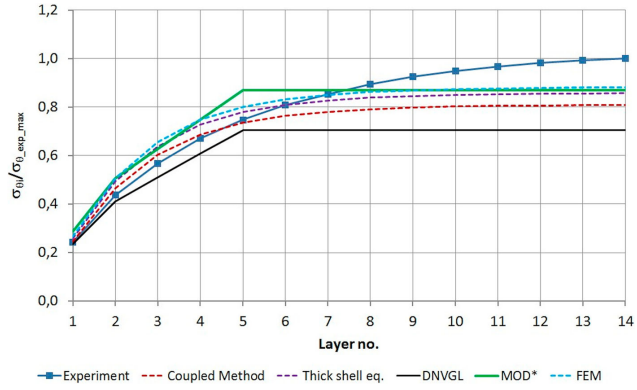

Figure 28. Rope 3 – tangential stress ratio – 14% MBL. This figure is available in colour online.

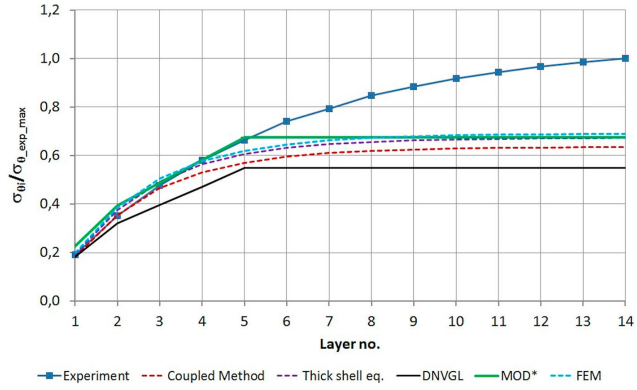

Figure 29. Rope 3 – tangential stress ratio – 19% MBL. This figure is available in colour online.

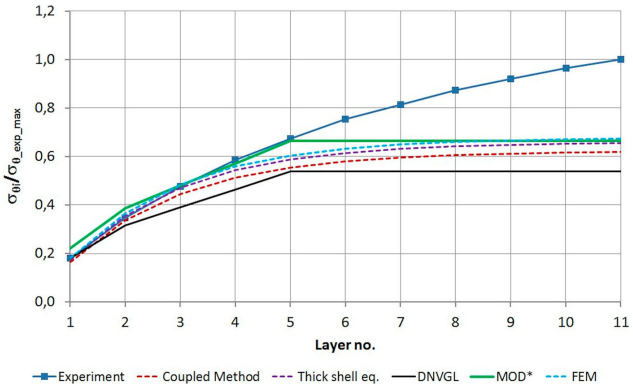

Figure 30. Rope 3 – tangential stress ratio – 25% MBL. This figure is available in colour online.

The calculations based on the 'Dietz-method', including modifications for larger rope deformations, are not able to follow the trends of the measured stress curves and the deviations increase with increasing rope tension. For the two lowest rope tensions (Figures 27 and 28) FEM calculates too-low stresses from eight to seven layers and with the two higher rope tensions from five to four layers (Figures 29 and 30). The extreme stress ratios with 14 layers of rope are 0.71 and 0.91 for 10% MBL tension, 0.71 and 0.88 for 14% MBL and 0.55 and 0.69 for 19% MBL. With 25% MBL the number of layers are limited to 11 due to stress level in the drum reaching the abort criteria for the experiments. The extreme stress ratios with 30% MBL and only 11 layers are 0.54 and 0.67.

Figures 31 and 32 show the differences between experiments and calculations for the three ropes with 10 and 20% MBL rope tension and five and ten layers on the drum.

5. Discussion

On winch drums in general, and also with experimental testing, sufficient fastening of rope in the first layer is required. Therefore, for all test runs, a number of practically load-free wraps are applied to ensure sufficient friction to transmit the rope load and prevent overload to the anchor point. In addition, the rope tension is ramped up to the specified test load during some rotations after the test starts and consequently, the pressure in the first layer is not uniform over the length of the drum. Even though compensated for in the calculations, there are variations and slight deviations between some measurements and analytical calculations with one layer of rope.

The presented calculations are based on pure radial pressure acting on the drum, justified by finite element calculations for the current drum dimensions. Relevant to this, is also the limit between short and long shells defined by Mupende

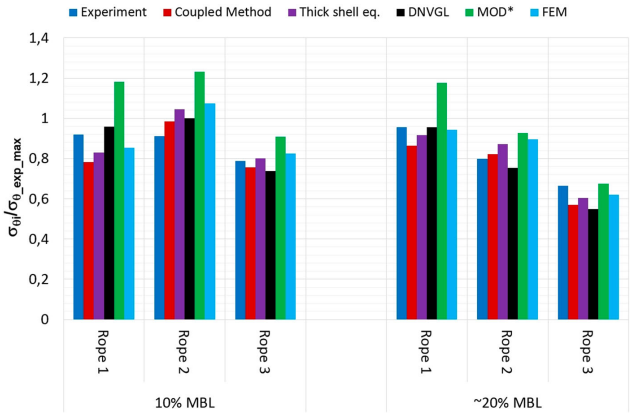

Figure 31. Comparisons between the ropes with five layers. This figure is available in colour online.

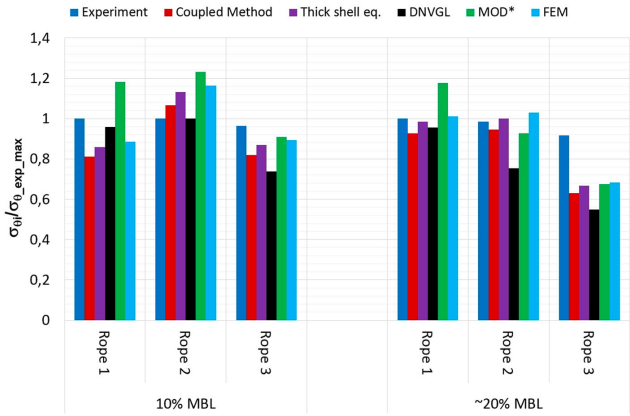

Figure 32. Comparisons between the ropes with ten layers. This figure is available in colour online.

(2001) using the reduced shell length χ_L. Long shells, with a reduced length of at least six, can be assessed without accurate knowledge of boundary conditions. The reduced length of the test drum is 6.4 and by definition a long shell. With reference to Figure 17, the tangential stress curves, with and without flange forces, are closing in on each other just at the centre of the drum. Thus, for a drum defined as a short shell, boundary conditions and flange forces would most probably result in larger deviations between measured and calculated tangential stress also at centre of the drum.

The comparisons between measured and calculated stresses show that the analytical methods can predict tangential stress levels. Considering the curves related to the calculations based on the 'Dietz-method' and 'modified Dietz-method', these follow the trends of the measurements well for the steel wire and the dimensionally stable HPFR. For such ropes, precise calculations of the tangential stress are plausible, but accuracy is dependent on available relevant longitudinal and transverse moduli for the rope and tensile load. According to the calculations, the ratio between longitudinal and transverse modulus of elasticity seems too high for the steel wire in combination with low tension resulting in an exaggerated load relaxation effect. For the highest tension, the situation is opposite as the calculations give somewhat larger stresses than the measurements. For the dimensionally stable HPFR, the elasticity ratios give similar results as the steel wire.

For the deformable HPFR, there are considerable deviations between analytical calculations and measurements. For low tensions, the calculations give comparable results up to 6–7 layers and for higher tensions up to 3–4 layers. With an increased number of layers, the calculations underestimate the actual tangential stresses considerably. With this type of rope, there seems to be an effect present in the rope package reducing the relaxation of tension and pressure in lower layers further and beyond the increased deformations already taken into account in the calculations. A hypothesis potentially explaining this is related to 'constraint stiffening' preventing further compression of the ropes in lower layers due to a very tightly-spooled, self-constraining rope package with close to rectangular rope shapes and limited space for deformation and further load relaxation. However, further investigations are required and this effect is not, at present, reproducible in testing of transverse rope stiffness.

There are deviations between the rope dimension, d_x, and the distance between windings, e_R, particularly for the deformable rope. Using the smaller d_x as the distance between windings would increase the calculated stresses somewhat, but also result in more rope windings in each layer than actually present. This indicates that the rope shape changes during the relative short distance between the drum and the rope shape scanners, and that the accuracy of the rope shape dimensions are somewhat uncertain. The rope shape is probably influenced by the 90° change in direction of rope cross-section compression caused by the orientation of the spooling sheave. Accuracy of measurements and data evaluation can also be reasons for this. However, the inaccuracies are expected to be limited to a few millimetres and more precise rope shape dimensions would not close the gaps between measurements and calculations for the deformable rope.

Considering the different methods for calculation of tangential stress, the simple and quick analytical method using the thick shell equation gives very good results compared with the finite element method. The deviation between these two methods is considered related to the geometric properties of the drum being different from a long unconstrained pipe for which the thick shell equation is based. In general, the differential equation used by the coupled method also gives good estimates, but with somewhat larger deviations relative to the two other methods also using the calculated 'Dietz-pressure'. This is probably related to limited relevance for the differential equation with very thick shells. The coupled method is applied without axial forces in the calculations, as the flange forces are neglected.

The DNVGL method, specified for classification of winch drums, seems fairly comparable for the steel rope, but this

method is in general not capable of calculating stresses with reasonable accuracy for HPFR and should be used with care. The MOD* method is conservative for the steel wire and for the two lowest rope tension levels with the dimensionally stable HPFR.

In relation to actual multilayer winch drums, the calculations are simplified by using axisymmetric models and the change in pressure related to different layer radii in parallel- and crossing-sections are neglected. However, the evaluations compare peak measured values against calculations based on parallel-section radius, which should give conservative drum pressures.

The experiments are conducted in dry conditions, but potential influence of water is obviously of significant interest in relation to equipment as ropes in marine applications. Some fibres loose strength and change characteristics when submerged in water (e.g. nylon and aramid), while the fibres relevant for this study (high-modulus polyethylene and polyester) exhibit hydrophobic properties with zero or less than 0.1% water absorption. Consequently, these fibre ropes don't swell or change mechanical properties when wet. In addition, water penetrating into the voids between strands and yarns are considered free to escape when the ropes are deformed over sheaves or spooled onto a drum. However, moisture can influence, and typically increase friction. While flange forces on multilayer winch drums are relatively strongly influenced by friction, influence on radial pressure is small and limited to selection of transverse modulus in the calculations. Thus, no significant differences in radial multilayer pressures, and consequently tangential stresses in the drum structure, are expected whether these ropes are wet or dry.

6. Conclusions

In combination with multilayer pressure calculated by the 'Dietz-method', the analytical methods are able to assess the tangential stress in the multilayer winch drum with the steel wire rope and the dimensionally stable HPFR. With the more deformable HPFR, the calculations underestimate the tangential stresses for more than 3–7 layers of rope on the drum, even if the larger rope deformation of HPFR is taken into account.

For the present drum, the method specified by class-societies is only sufficiently accurate for the steel wire rope and the dimensionally stable HPFR with low rope tension. Better results, however in some cases overly conservative, can be achieved by modifying the class society equation for tangential stress to account for thick-walled cylinders.

In case of pure tangential stress calculations, the quick and simple equation for thick-walled cylinders in combination with calculated multilayer pressure gives very good results, close to numerical calculations. The differential equation used by the coupled method (Mupende 2001) gives results good enough to make parameter studies of winch drums useful also for thick winch drums.

The presented analytical methods are useful for preliminary design work, but for final design verifications, allowable stresses should be evaluated against von Mises stress calculated by 3D FEM giving possibilities for more realistic asymmetrical load distributions, both for drum pressure and flange forces.

7. Further work

In relation to the presented work, further evaluations of analytical calculation methods for multilayer winch drums will be carried out. This includes more rope types and sizes, different drum dimensions and flange forces.

Acknowledgements

The authors would like to acknowledge Eirik Homlong and Offshore & Trawl Supply AS (OTS) for access to rope test facilities, support and assistance with testing of rope properties, HBM Norge AS for mounting the strain gauges, Geir-Kåre Øvrelid and Terje Kvangardsnes, Kongsberg Maritime Commercial Marine AS, for operating the test equipment and assistance related to test rig control system.

Disclosure statement

No potential conflict of interest was reported by the author(s).

Funding

This work is carried out in relation to an Industrial-PhD project for Kongsberg Maritime Commercial Marine AS and the Department of Ocean Operations and Civil Engineering at the Norwegian University of Science and Technology with funding by the Norwegian Research Council [grant number 278450].

References

ABS. 2019. Guide for certification of lifting appliances. Spring, Texas, USA: American Bureau of Shipping.

Dietz P. 1971. Ein Verfahren zur Berechnung ein- und mehrlagig bewickelter Seiltrommeln. Darmstadt, Germany: Technischen Hochschule Darmstadt.

DNV GL. 2017. DNVGL-RP-N201 Lifting appliances used in subsea operations.

DNV GL. 2019. DNVGL-ST-0378 Offshore and platform lifting appliances.

Irgens F. 2008. Continuum mechanics. Berlin Heidelberg, Germany: Springer-Verlag.

Lohrengel A, Schulze M, Erlendsson H, Magnusson J, Smeets P, Tacken B. 2017. The influence of high performance fibre rope designs on drum load and spooling perfomance in multi-layer drum equipment. OIPEEC Conference 2017 Rope-Present and Future; La Rochelle.

Lohrengel A, Stahr K, Schulze M, Wächter M. 2015. Innovative drum construction for multi-layer winding with fibre ropes. OIPEEC Conference 2015/5th International Stuttgart Ropedays – Challenging Rope Applications; Mar 24–26, Stuttgart: Alte Stuttgarter Reithalle.

Mupende I. 2001. Beanspruchungs- und Verformungsverhalten des Systems Trommelmantel - Bordscheiben bei mehrlagig bewickelten Seiltrommeln unter elastischem und teilplastischem Werkstoffverhalten. Göttingen, Germany: Cuvillier Verlag.

Skarbøvik RA, Piehl H, Torben S, Nedreberg ML, Æsøy V. 2019. Experimental investigation of stresses in winch drums subjected to multilayer spooling loads from synthetic fibre ropes. ASME 2019 OMAE 38th International Conference on Ocean, Offshore & Arctic Engineering; Glasgow, Scotland, UK.

Appendix B

Fibre rope technology

This appendix holds an introduction of terminology related to fibre ropes, properties and designs, as well as fibre materials and manufacturing methods. The information is based on Hearle, McKenna and O'Hear [12], Hearle [13] and Huseyin et al. [40]. .

B.1 Basic properties, terminology and units

Due to history, cultural and technical factors, there are different units used in fibre rope technology. Within rope structures, there are voids of varying volume resulting in undefined cross-sectional areas. There can also be differences in rope shapes, and altogether this causes conventional engineering quantities based on area or diameter to be inaccurate. However, in some applications, such definitions still need to be used.

B.1.1 Rope dimensions

Rope size is often specified as *mass per unit length* [kg/m] or in *tex* [g/km]. The easiest measurement of rope size is to measure the circumference by wrapping a string around the rope. However, the volume is related to the "fill factor" (fraction of cross-section occupied by fibre), and the linear density, or specific rope weight (mass per unit length), is therefore preferred for characterising rope sizes. The silk unit *denier* is also sometimes used, but the SI unit *tex* [g/km] is now preferred and more common.

The diameter or circumference of a rope must correspond to a specific linear density within limits of about +/-5%.

Some important relations between different rope weight units and definitions are:

- tex=g/km
- Megatex=kg/m
- decitex=0.1 g/km
- denier=g/9000 m
- lb/100ft=1.488 kg/100 m
- Rope area=linear density/density
- Rope density=fibre density $\times$ fill factor
- Fill factor=rope density/fibre density
- Total rope mass=linear density$\times$length

B.1.2 Breaking load

Minimum breaking load (MBL) is the maximum force a free length of rope can be exposed to under a straight pull before it breaks. The minimum breaking load is usually specified for spliced ropes and in accordance with either ISO 2307 or CI 1500 (Cordage Institute). Typically, in tensile strength tests, rupture occurs at the end of a splice, and the strength of a rope with a splice is about 90% of an unspliced rope.

B.1.3 Specific stress

Due to the difficulties of defining the actual cross-sectional area of fibre ropes, specific stress is commonly used instead of the common engineering definition of stress (force divided by area). The preferred unit for specific stress is N/tex, but there are also other units for stress in use, e.g. g/den, cN/dtex and Km-Force.

Tenacity is specific strength [N/tex] defined as *force per unit linear density* of an unstrained specimen. In some cases, tenacity is imprecisely used in the meaning of specific stress. Specific stress can be converted to conventional stress in GPa by multiplying a value in [N/tex] with density in [g/cm^3].

B.1.4 Elongation, stabilisation and modulus

When a load is applied to a rope, the rope is compacted due to structure and fibres rearranging (bedding-in) and adapting to the load—the elongation consist of both plastic, visco-elastic and elastic elements. The plastic elongation is unrecoverable and permanent, while elastic elongation is immediately recovered when the load is removed. The visco-elastic elongation is gradually recovered when tension is removed.

In order to measure strength and elongation with sufficient accuracy, new ropes need to be sufficiently stabilised (bedded-in or pre-conditioned) prior to measurement. This is done by repeated cycling of the rope to 20% (typical maximum working load) or 50% (maximum stabilisation) of the assumed breaking strength.

The rope is usually stabilised after ten load cycles.

If a previously stabilised rope is relaxed over time, new cycling is required to re-stabilise it again. Then, fewer cycles are usually required compared to a new rope.

When the rope is stabilised, the modulus can be determined from the last cycle of the stress-strain curve. The non-linearity of the curve is taken into account by determining a tangent modulus, the slope at any point, or a secant modulus, the slope between two points on the curve. In computer modelling, polynomial representation of the stress-strain curve through curve fitting (regression analysis) is common. The principles of stabilisation and approximation of modulus are illustrated in Fig. B.1.

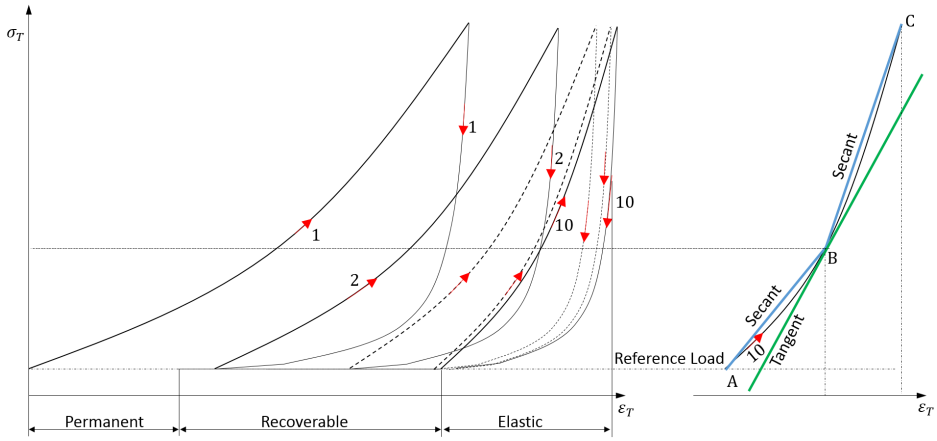

Figure B.1: Stabilisation and Modulus

B.2 Failure modes

B.2.1 Fatigue

Cyclic, or long term static loading, induces progressive damage to fibres and consequently loss of strength. There are different forms of fatigue failures related to fibre ropes.

Tensile fatigue

Repeated loading and unloading, at working loads below thresholds initiating other forms of fatigue (approx. 20% MBL), causes inter-fibre abrasion and loss of strength due to damaged and broken fibres over time.

Creep

Creep is the slow deformation of the material when loaded over time and caused by two mechanisms at the molecular level. A usually recoverable creep occurs at low stresses due to progressive straightening of molecules and potentially changes in links between segments. Recoverable creep does not affect strength, while creep rupture occurs at higher stresses when the creep limit is exceeded, causing molecules to slide past one another.

B.2.2 Relaxation

If creep is induced in a rope and the length is kept constant, as when a rope is tensioned between two fixed points, tension will gradually decrease. The rate of this relaxation decreases with decreasing tension.

B.2.3 Thermal damage and hysteresis heating

All materials exhibit temperature limits for melting or decomposition. Fibre ropes cannot be utilized at temperatures close to such limits. There are relatively significant differences between fibre types. However, the general temperature limits are low, and the maximum temperature is about 90°C. Long-term use or storage at higher temperatures should also be avoided.

Load cycling at high tensions causes increased temperature in ropes due to internal fibre energy loss and friction due to relative motion between fibres. The hysteresis loss can be quantified by the area enclosed by the loading and unloading curves for each cycle (Fig. B.1). The generated heat dissipates through the rope from the most heavily loaded elements, usually in the centre of strands. Heat dissipation decrease with increasing rope size but is improved in wet ropes. If submerged, the rope surface temperature will be the same as the surrounding water temperature.

Good performance in cyclic bending over sheaves (CBOS) is often a desirable property for fibre ropes. However, there are challenges of accelerated failure under such conditions. This is due to the relatively low melting point and thermal conductivity, causing friction and heat build-up in the rope core.

Some fibre materials exhibit a negative thermal expansion coefficient, e.g. Dyneema with a coefficient of $-12 \cdot 10^{-6}$ m/K. This means that ropes with such fibres which are free to retract become shorter with increasing temperature. On the other hand, some tension is induced in the rope structure if the rope is constrained.

Flex fatigue

Fatigue due to flexing can occur even at relatively low tensions and is a common source of failure. This failure mode is usually related to ropes running over pulleys,

winding and unwinding on fixed surfaces (e.g. fairleads and pins) and continuous flexing at low loads. Ratios between pulley or fixed surface and rope diameter (D/d) should always be made as large as possible and not less than three for nearly static applications.

Axial compression fatigue

In highly bent ropes, axial compression occurs on the inside with tension on the outside. This can cause rope components and fibres to buckle and create Z-shaped kinks within the rope structure. Further, continuous flexing of such kinks can cause fatigue and rupture. This failure mechanism is most commonly related to ropes exposed to low tension and twisting. Mismatch of fibre lengths can also cause some components to go into compression.

B.2.4 Abrasion

External abrasion is damages to fibres due to friction and rubbing against external surfaces, while internal abrasion is related to relative motion between fibres within the rope structure. Different fibres exhibit different abrasive resistance in dry and wet conditions.

B.2.5 Ultra-violet (UV) radiation

Synthetic fibre ropes can be damaged due to UV radiation from sunlight or fluorescent lightening. Thus, UV-inhibitors are frequently used in rope fibres. Smaller ropes are more affected than larger ropes as penetration of UV radiation is limited to small depths and thus only affects filaments in or close to the rope surface. Ropes larger than 24mm is not expected to experience damages of any significance unless used for a long time in sub-tropical areas. Ropes protected by covers (jackets) are not affected, neither are load-bearing cores.

B.2.6 Chemical and biological degradation

In contrast to natural fibre ropes, synthetic ropes are not attacked by common micro-organisms. However, synthetic fibre ropes can be damaged by chemicals, especially if the temperature is high or if the chemicals are highly corrosive.

B.3 Rope constructions

Figure B.2 shows examples of common types of rope constructions. However, other constructions also exist, and many manufacturers have developed their special designs.

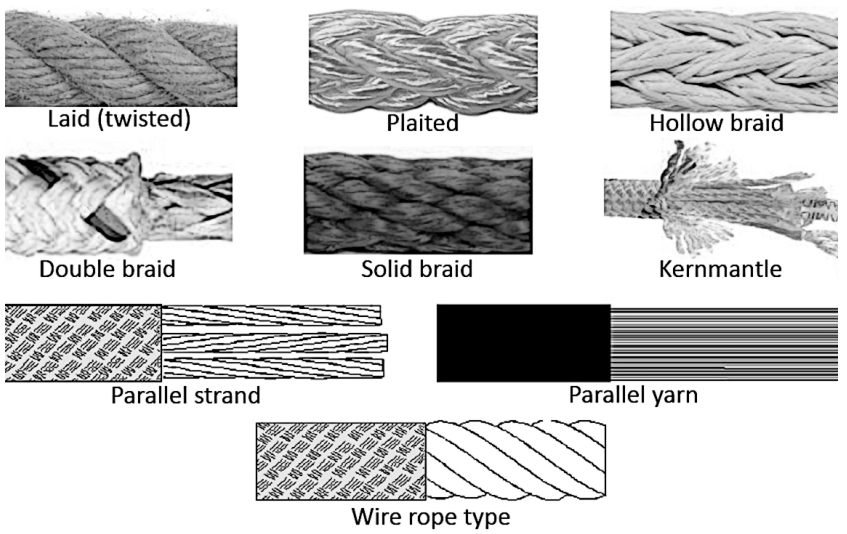

Figure B.2: Rope Types

B.3.1 Laid ropes

With three strands twisted together, the three-strand rope structure is the most used, oldest and simplest structure. Such ropes can be made with long or soft lay length. Long lay length increases strength and reduces elongation at the cost of resistance to snagging. Tight, hard lay length gives higher elongation and lower strength but improved resistance to abrasion and snagging. The size range is vast, from very small to huge ropes and the splice-ability is very good. However, the structure gives no torque balance. Due to poor load-sharing properties, such rope structures are not common with high modulus fibres.

There are also four- and six-strand laid ropes. The first is rare and similar to three-strand structures, while the latter is similar to wire rope constructions and typical for 50-80 mm mooring ropes.

B.3.2 Plaited ropes

Eight-strand plaited rope is braided with four strands and called "square braid" rope. All strands cross the centre and separate from each other if the rope is compressed. This rope structure can utilize all types of fibre materials, but ropes made of high modulus fibres are very soft due to a required long braid pitch.

Plaited ropes are general purpose ropes in small to large sizes (>160 mm). The structure gives a torque balanced rope with good abrasion resistance and splice-ability.

B.3.3 Hollow single-braid ropes

The most common type of single-braid ropes is made with 12-strands. For small rope sizes (<12 mm), 8-strand ropes are also common, while some ropes come with 16-strands or even more. Unless the pitch length is small, the structure is recognized by a void, or hole, in the centre. When such rope structures are under tension, this hole closes to a gap no larger than the gap between the strands in the structure. For ropes with 16-strands or more, the centre hole is larger. Unless the braid length is very long, hollow single-braid ropes become flat under tension. The most common braid pattern is called "twill", with each strand going under and over two strands in opposite directions. The rope structure can utilize all types of fibre materials. However, it also requires a relatively long braid pitch length for high-modulus fibres, giving soft ropes.

Single-braid ropes are round in shape, torque-balanced, and, unless the braid pitch is too small, exhibit very good splice-ability. Typically, strength and stiffness are somewhat higher than for laid and plaited ropes. However, they are also more exposed to internal fibre damage and loss in strength when subjected to high variation in load. The structure gives a significant transverse pressure when the rope is under tension and forces are effectively transferred between fibres due to friction. This can be utilized to make very long ropes by overlapping fibres in the structure.

Single-braid ropes can also have an internal core to improve shape stability and dimensions when running over sheaves or spooled onto drums. In addition, they are often covered by a non-load supporting cover of polyester fibres to improve abrasion resistance.

B.3.4 Double-braid (braid-on-braid)

In double-braid ropes, the load is shared between a braided cover over a braided core. Such ropes are typically made of nylon, polyester, polypropylene or combinations of these. The core gives high strength and stiffness due to a long braid pitch. In contrast, the cover typically is braided with a shorter pitch to improve resistance to snagging and give proper firmness over the core. Thus, the core takes more tension and before the cover. The cover also needs to compensate for elongation as the core diameter is reduced when the rope is under tension. Due to poor load sharing between high-modulus fibres, such fibres are not very suitable for double-braided ropes.

Double-braided ropes are strong and stiff with very stable shapes and dimensions. They can be spliced and made in substantial sizes. Such ropes are often used for mooring large vessels to buoys in the open sea.

B.3.5 Solid braid ropes

Solid braid ropes are very round and resilient with significant elongation but with limited mechanical properties. The strength conversion efficiency is relatively low, and such ropes can wear off if only one strand is broken. They are typically made of cotton, nylon, polyester or polypropylene and is typically used for decorative purposes. Industrial applications are limited.

B.3.6 Kernmantle ropes

These ropes are either dynamic or static ropes and are made with a core and a very thin cover made of very many small twisted yarns. The core can be made of parallel or twisted yarns, laid sub-ropes or many braids with long pitch distances. Static ropes are stiff and used for applications where high energy absorption is essential. In contrast, dynamic kernmantle ropes are made of nylon and used for, e.g. mountaineering, where high energy absorption and elongation are important properties in case of fall arrest.

Kernmantle ropes are round, firm, light and easy to handle. Sizes are limited and typically between 8 and 11 mm. Terminations are made by knotting, special clamps or multiple wraps..

B.3.7 Parallel strand ropes

Parallel strand ropes are stiff, low-twist ropes with high strength conversion from fibres to rope. The load is taken by the core, which is built up from several individual elements, sub-ropes or twisted bundles of yarn, enclosed by a braided cover.

Splicing this type of rope is straightforward in laid or braided sub-ropes, while twisted yarns require special techniques. The ropes can be very large with excellent cyclic tension fatigue properties, even better than wire rope in a marine environment. Due to high stiffness, very large radii are required to bend these ropes over sheaves or onto drums.

B.3.8 Parallel yarn ropes

This type of rope, with zero twists, is similar to parallel strand ropes but made with large amounts of parallel filaments or yarns enclosed by an extruded plastic cover. Splicing requires special techniques and skills, and potted sockets or unique termination designs typically do rope terminations. As with parallel strand ropes, bending requires large radii.

B.3.9 Wire like ropes

Some special fibre ropes are also built like wire rope structures. Six-strands around a centre strand is the most common, but several other constructions exist. The load conversion from fibre to rope is good for high- and low-modulus fibres as aramid and polyester. The length of rope is limited to the size of production machinery, but the same techniques can splice the ropes as wire ropes.

Tension-tension fatigue properties are excellent, and flex fatigue resistance is also good. Thirty-six strand ropes can be close to torque-free, while six- and eighteen-strand ropes are not.

B.4 Synthetic fibre rope materials

In contrast to natural fibres like, e.g. cotton, silk and hemp, synthetic fibres are manufactured materials designed with specific properties. The development started with the invention of Nylon and accelerated during the last century with new fibre types. Improvements and developments are still ongoing.

Ropes utilizing synthetic fibres have advantageous strength/weight ratios relative to steel wire ropes of comparable size and strength. Some ropes are also buoyant in water. This is attractive for marine lifting appliances to utilize lifting capacity or potentially reduce the size and weight of cranes, winches and related structures.

B.4.1 Production methods

The advantageous properties of fibres are achieved by combining fibre materials and different suitable production processes. The critical element is to orient long lengths of molecules parallel to the fibre axis.

Melt-spinning

In the melt-spinning process, the fibre-forming substance is melted and fibres oriented through extrusion before cooling and solidification, Fig.B.3. This is the most economical and most straightforward method for polymer fibre manufacturing with no recovered or evaporated solvents. However, a quickly melted polymer material is required.

Solution-spinning

There are different types of solution spinning processes. Common to these is applying a suitable volatile solvent to dissolve the polymer material before extrusion and solidification.

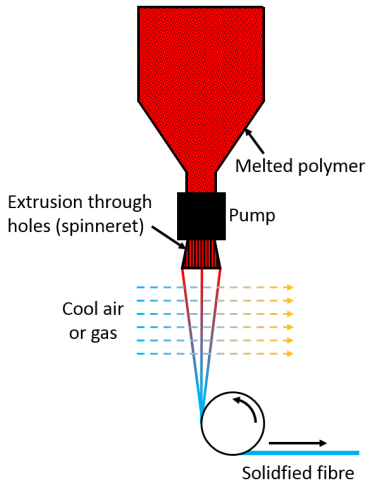

Figure B.3: Principle of melt-spinning

In wet-spinning, the dissolved material is pressed and extruded through holes using a pump while submerged in a bath coagulating the fibre material, Fig.B.4.

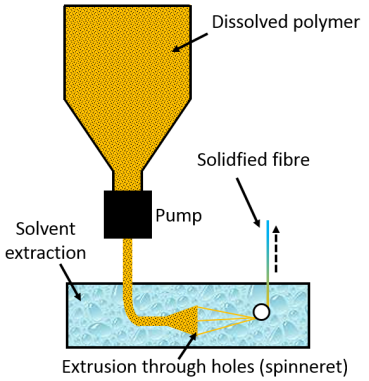

Figure B.4: Principle of wet-spinning

Dry-spinning is faster but requires large amounts of heat to evaporate the solvent, Fig.B.5. This method is typically used for materials like PVC and acrylics.

Dry-jet wet-spinning, Fig.B.6, is similar to wet-spinning. However, the polymer is extruded through the spinneret, stretched and elongated in an air gap before solidification in a coagulation bath.

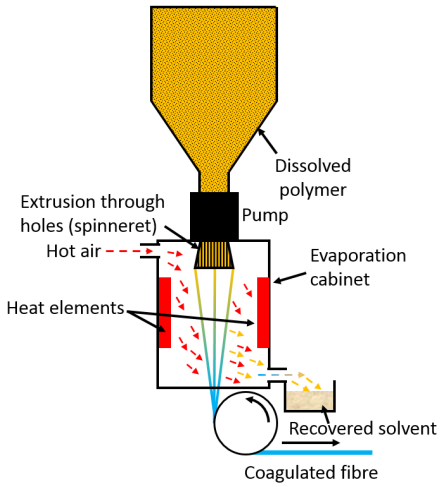

Figure B.5: Principle of dry-spinning

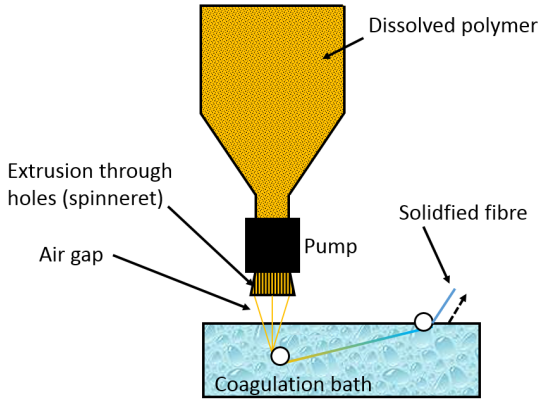

Figure B.6: Principle of dry-spinning

In the gel-spinning process, a solution of ultra-high-molecular-weight polyethylene (UHMWPE) is continuously extruded, cooled in a bath, super-drawn (up to 100 times in length) and crystallized by heat in an oven, Fig.B.7. At the expense of increased costs, mechanical properties can be improved by a subsequent treatment where fibres are further stretched slowly at a temperature close to the melting point.

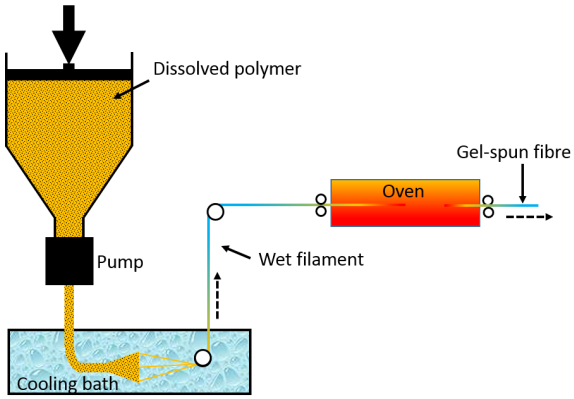

Figure B.7: Principle of dry-spinning

B.4.2 Fiber types

Nylon

Nylon is a polyamide and comes in two types used for ropes; Nylon 6 and Nylon 6.6. These fibres are produced by melt-spinning, exhibit good internal and external resistance against abrasion when dry but poor in wet conditions. Due to water absorption, Nylon also shrinks and loses strength (10-15%) in wet conditions due to water absorption. It is not buoyant in water. The elastic energy absorption is high with 15-20% elongation and a low modulus. Nylon is resistant to most chemicals, and the resistance against ultraviolet (UV) radiation is good due to inhibitors. The creep rate of Nylon 6.6 is lower than Nylon 6, which also has a lower melting temperature.

Polyester

Polyester (PET) is produced by the same method as Nylon. However, it is stiffer with elongation in the range of 5-10% under normal working conditions. Polyester does not absorb water (hydrophobic) and do not lose strength or shrink when wet. The resistance against ultraviolet radiation is good, and abrasion resistance is better than Nylon in wet conditions. The strength/weight ratio is somewhat lower than Nylon.

With certain polymer materials, high stiffness and strength are possible. This is achieved by manufacturing fibres with an extreme parallel orientation of long molecules. So far, this has not been possible with Nylon and Polyester. The following fibres are such high modulus-high tenacity (HMHT) fibres.

Aramids

Kevlar and Twaron (para-phenylene-terephthalamide, PPTA) are relatively expensive aromatic polyamide fibre brands. Technora is another similar fibre with a better balance between price and mechanical and thermal properties compared to other high modulus fibres. A dry-jet wet-spinning production process makes these fibres.

Aramid ropes decompose (above 500°C) before they melt. They also exhibit a low level of creep, good microbial resistance, but are sensitive to UV radiation, absorbs moisture (without losing strength) and sink when immersed in water. The strength-weight ratio is high, but elongation and capability to handle shock-loads are low. Abrasion resistance and axial compression fatigue properties are poor.

Another fibre in the aramid family (meta-aramid) is Nomex, with considerably lower modulus and strength.

Liquid-crystal polymers

Vectran is a liquid-crystal polymer (LCP), or aromatic polyester, fibre produced by melt-spinning. This is a cheaper process than the process used for aramid fibres. Unfortunately, the cost is increased by a required long heat treatment process to increase molecular weight. Vectran has good abrasion resistance (fibre on fibre), good CBOS performance and a low level of creep, but is very sensitive to UV radiation. Chemical resistance is good, and it is hydrophobic (<1% water absorption). It is not buoyant in water.

In this family, there are also Zylon (PBO) and M5 (Rigid-Rod Polymer) fibres produced by dry-jet wet spinning. PBO (poly-p-phenyelenebenzobisozazole) is similar to aramids in structure, character and production with excellent thermal stability (decomposition at 650°C) and chemical resistance. Both tensile strength and modulus are very high, but compressive strength and UV resistance are poor.

M5 has a unique crystal structure and is developed to enhance shear modulus, transverse and compressive strength.

The price of LCP fibres is high even compared to other fibre types considered as expensive.

High-modulus polyethylene

Ultra-high molecular weight polyethylene (UHMWPE) has long lengths of molecules. High-modulus polyethylene (HMPE)/high-performance polyethylene (HPPE) is created through a gel-spinning process. Due to very long lengths of extremely parallel and oriented molecules, these fibres achieve low weight, high strength and tensile stiffness. Spectra and Dyneema are commercial brands of such fibre types.

These come in different grades to balance properties and costs. Creep performance has been a drawback for some of these fibre types. However, continuous development has resulted in improved properties and new grades. UV Resistance is very good. The fibres are buoyant in water with very good abrasion, bending- and tensile fatigue properties. The chemical resistance is also very good, but the melting temperature is relatively low. The friction coefficient is low, with only small differences between dry and wet conditions.

Certran and Tensylon are other brands in such fibres, however with limited prevalence compared to Spectra and Dyneema which are widely used in ropes.

B.5 Coatings

Different coatings can impregnate individual fibres or finished ropes to protect against UV radiation, abrasion and wear, or improve friction, heat, and CBOS fatigue properties. Coatings are also applied to improve resistance against water and mould, fire retardant and colouring. Coatings can mitigate even the negative effect of softness related to plaited and single-braided ropes. Typical coating materials are polyurethane, silicons, wax and acrylates.

Appendix C

Transverse modulus of ropes

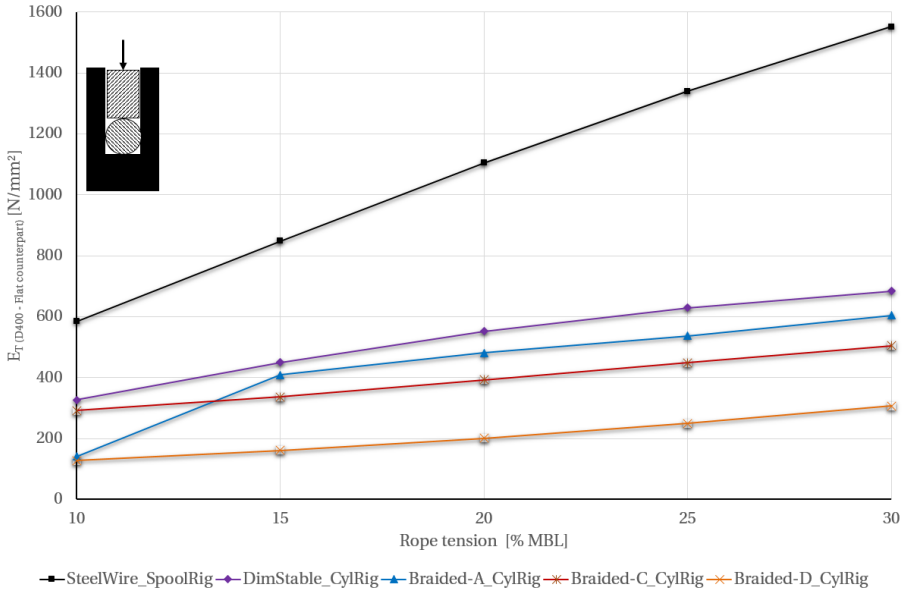

Figure C.1: Transverse modulus, flat counterpart, Ø20 mm ropes, D500 - CylRig

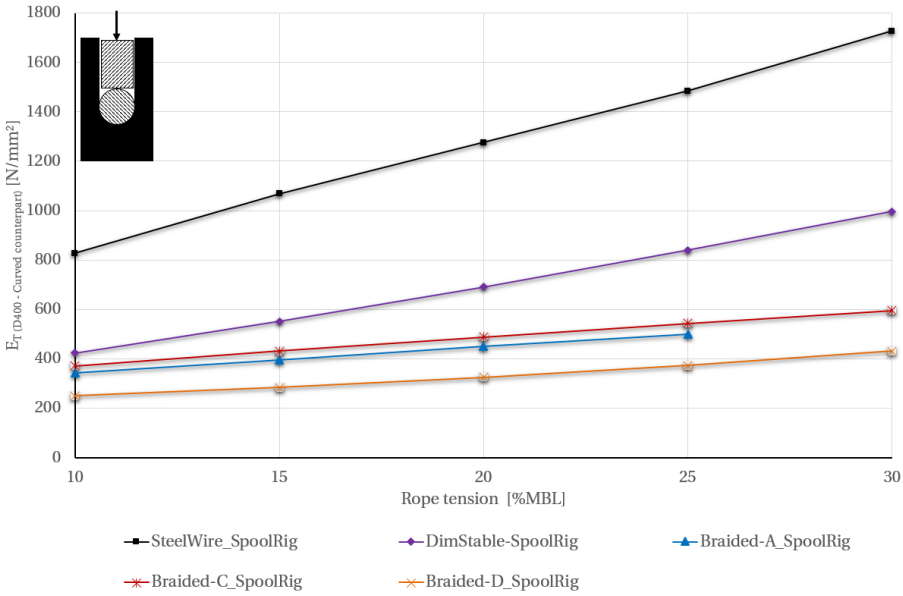

Figure C.2: Transverse modulus, curved counterpart, Ø20 mm ropes, D400 - SpolRig

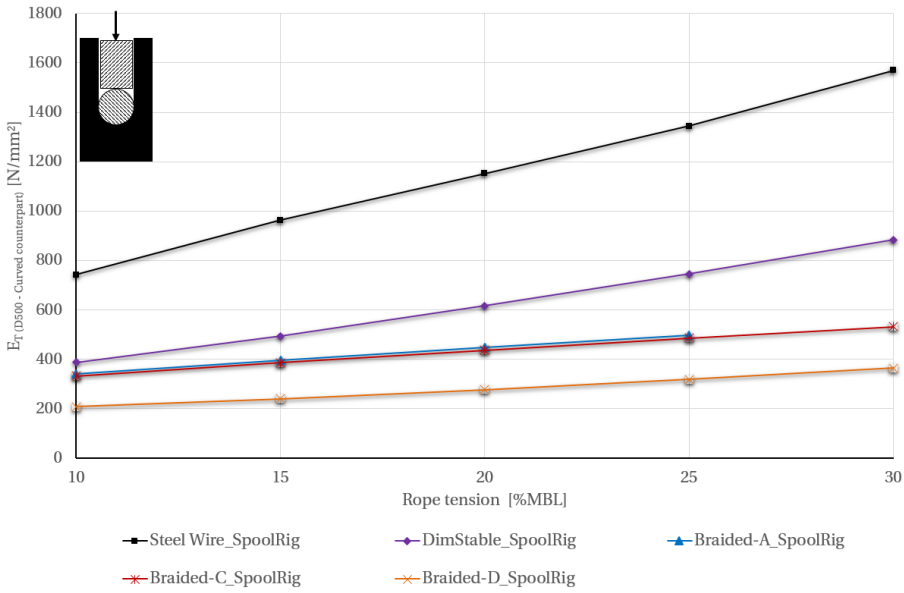

Figure C.3: Transverse modulus, curved counterpart, Ø20 mm ropes, D500 - SpolRig

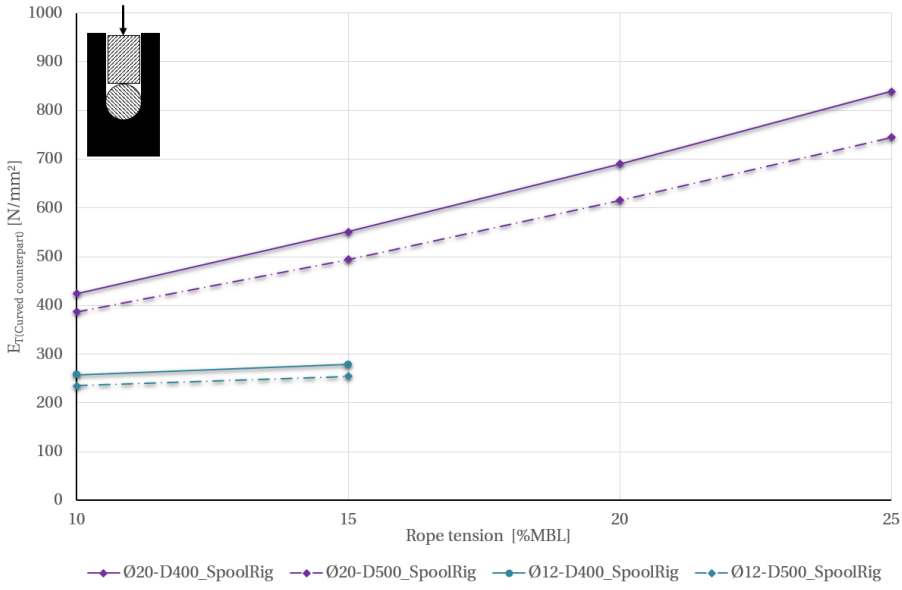

Figure C.4: Transv. modulus, curved cp., Ø12 and Ø20 mm DimStable - SpolRig

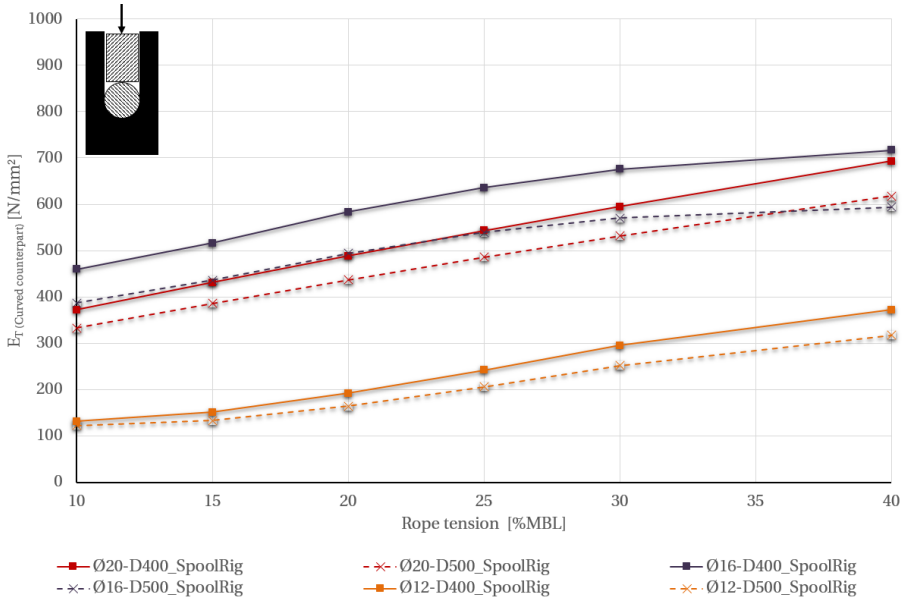

Figure C.5: Transv. modulus, curved cp., Ø12, Ø16 and Ø20 mm Braided-C - SpolRig

Appendix D

Rope dimension data

Table D.1: Mean outer layer radius with standard deviations [mm] Ø20 mm - D400

Layer	Tension [kN]	SteelWire	DimStable	Braided			
				A	B	C	D
1	49.05	219.7(0.03) n=3	220.5(-) n=1	213.7(0.09) n=3	213.4(0.01) n=3	213.0(0.04) n=3	- -
	88.3	219.7(0.02) n=3	220.3(0.10) n=2	213.8(0.48) n=3	213.3(0.18) n=3	212.8(-) n=1	- -
2	49.05	236.1(0.14) n=3	236.7(-) n=1	226.2(0.16) n=3	226.4(1.06) n=3	224.4(0.09) n=3	- -
	88.3	235.8(0.03) n=3	235.6(0.21) n=2	224.7(0.01) n=3	224.9(0.19) n=3	223.8(-) n=1	- -
3	49.05	252.5(0.17) n=3	252.4(-) n=1	238.6(0.12) n=3	238.3(0.03) n=3	236.5(0.36) n=3	- -
	88.3	252.0(0.04) n=3	251.7(0.09) n=2	237.0(0.05) n=3	237.3(0.95) n=3	234.9(-) n=1	- -
4	49.05	269.0(0.25) n=3	268.2(0.10) n=1	249.6(0.15) n=3	250.0(0.26) n=3	247.4(-) n=3	- -
	88.3	268.2(0.08) n=3	267.0(0.17) n=2	247.8(0.48) n=3	248.7(0.63) n=3	245.9(-) n=1	- -
5	49.05	285.4(0.21) n=3	284.0(0.13) n=1	261.6(0.11) n=3	261.4(0.20) n=3	258.9(-) n=3	-
	88.3	284.3(0.03) n=3	282.9(0.05) n=2	259.2(1.15) n=3	260.8(1.20) n=3	257.1(-) n=1	- -
6	49.05	301.8(0.20) n=3	299.9(-) n=1	272.6(0.17) n=3	274.1(0.77) n=3	270.5(0.14) n=3	- -
	88.3	300.2(0.74) n=3	298.4(0.24) n=2	269.9(0.97) n=3	272.5(0.80) n=3	268.3(-) n=1	- -
7	49.05	318.2(0.21) n=3	315.6(0.38) n=1	283.4(0.86) n=3	285.6(0.36) n=3	281.7(-) n=3	- -
	88.3	315.9(1.51) n=3	314.2(0.31) n=2	281.2(0.70) n=3	284.4(1.10) n=3	279.2(-) n=1	- -

Table D.2: Mean outer layer radius with standard deviations [mm] Ø20 mm - D500

Layer	Tension [kN]	SteelWire	DimStable	Braided			
				A	B	C	D
1	49.05	269.7(0.01) n=2	270.4(0.09) n=2	264.4(0.01) n=2	263.8(0.39) n=3	263.8(0.03) n=3	265.7(0.13) n=4
	88.3	269.6(0.05) n=2	270.2(0.31) n=4	264.3(0.20) n=4	263.5(0.15) n=2	263.7(0.18) n=3	265.8(0.06) n=3
2	49.05	286.2(0.03) n=2	286.9(0.01) n=2	276.3(0.05) n=2	275.7(0.17) n=3	275.6(0.18) n=3	279.4(0.18) n=4
	88.3	285.9(0.15) n=2	286.0(0.26) n=4	275.7(0.23) n=4	275.3(0.37) n=2	274.8(0.14) n=3	278.8(0.14) n=3
3	49.05	302.8(0.02) n=2	303.3(0.09) n=2	288.1(0.22) n=2	287.5(0.37) n=3	287.0(0.24) n=3	292.6(0.27) n=4
	88.3	302.3(0.10) n=2	302.1(0.20) n=4	287.1(0.24) n=4	286.9(0.05) n=2	286.3(0.61) n=3	291.6(0.13) n=3
4	49.05	319.2(0.08) n=2	319.7(0.07) n=2	299.0(0.32) n=2	299.3(0.07) n=3	298.2(0.46) n=3	305.7(0.24) n=4
	88.3	318.5(0.13) n=2	318.0(0.32) n=4	298.2(0.26) n=4	298.8(0.10) n=2	297.0(0.22) n=3	304.6(0.09) n=3
5	49.05	335.7(0.03) n=2	335.8(0.09) n=2	310.1(0.73) n=2	311.0(0.10) n=3	309.1(0.35) n=3	318.8(0.32) n=4
	88.3	334.8(0.20) n=2	333.8(0.20) n=4	309.5(0.26) n=4	310.3(0.03) n=2	307.9(0.72) n=3	317.3(0.04) n=3
6	49.05	352.2(0.06) n=2	352.1(0.04) n=2	323.0(1.15) n=2	323.1(0.21) n=3	321.4(0.30) n=3	331.9(0.28) n=4
	88.3	351.0(0.17) n=2	349.7(0.36) n=4	321.7(0.25) n=4	322.0(0.26) n=2	319.4(0.84) n=3	330.2(0.10) n=3
7	49.05	368.6(0.09) n=2	368.2(0.05) n=2	334.1(0.95) n=2	334.5(0.59) n=3	332.2(0.38) n=3	345.0(0.75) n=3
	88.3	367.2(0.11) n=2	365.4(0.35) n=4	332.3(0.62) n=4	333.0(0.24) n=2	330.0(0.85) n=3	342.9(0.24) n=3

Table D.3: Mean 1^{st} layer rope height [mm] during on and off spooling, Ø20 mm - D400

	Tension [kN]	SteelWire	DimStable	Braided			
				A	B	C	D
ON	49.05	19.70(0.03) n=3	20.54(-) n=1	13.72(0.09) n=3	13.44(0.01) n=3	13.04(0.04) n=3	- -
	88.3	19.67(0.02) n=3	20.26(0.10) n=2	13.79(0.48) n=3	13.26(0.18) n=3	12.81(-) n=1	- -
OFF	49.05	19.46(0.09) n=3	19.40(-) n=2	13.05(0.12) n=3	13.01(0.12) n=3	12.44(0.09) n=3	- -
	88.3	19.29(0.08) n=3	19.27(0.04) n=2	12.58(0.45) n=3	12.78(0.10) n=3	12.29(-) n=1	- -

Appendix E

Supplementary drum stress measurement results

Table E.1 holds values related to Figs. 5.25 through 5.28. The values are mean values for each layer with standard deviations in brackets. The values in square brackets are peak values.

Table E.1: Mean circumf. tangential stress [N/mm^2] - Ø20 mm - D500

Layer	Steel wire (20% MBL)	DimStable (17% MBL)	Braided-C (15% MBL)	Braided-D (17% MBL)
1	-40(0.6) [-41]	-35(0.4) [-35.7]	-34(0.4) [-35]	-35(0.8) [-37]
2	-73(1.5) [-76]	-61(1.1) [-62.4]	-56(0.6) [-57]	-67(0.7) [-68]
3	-94(2.7) [-97]	-80(1.5) [-82.4]	-74(0.7) [-75]	-89(0.8) [-91]
4	-109(3.7) [113]	-94(1.9) [-97.5]	-88(0.8) [-88]	-107(0.9) [-109]
5	-118(3.8) [-124]	-105(2.2) [-108]	-98(1.0) [-99]	-121(1.2) [-123]
6	-124(3.8) [-131]	-113(2.5) [-117]	-107(1.0) [-109]	-132(1.4) [-134]
7	-128(4.4) [-136]	-119(2.9) [-123]	-113(1.1) [-114]	-141(1.4) [-144]
8	-130(4.2) [-138]	-123(3.1) [-128]	-118(1.2) [-120]	-149(1.4) [-152]
9	-	-126(3.3) [-132]	-122(1.1) [-124]	-156(1.7) [-158]
10	-	-	-126(1.1) [-128]	-161(2.1) [-164]
11	-	-	-129(1.2) [-131]	-164(2.2) [-168]

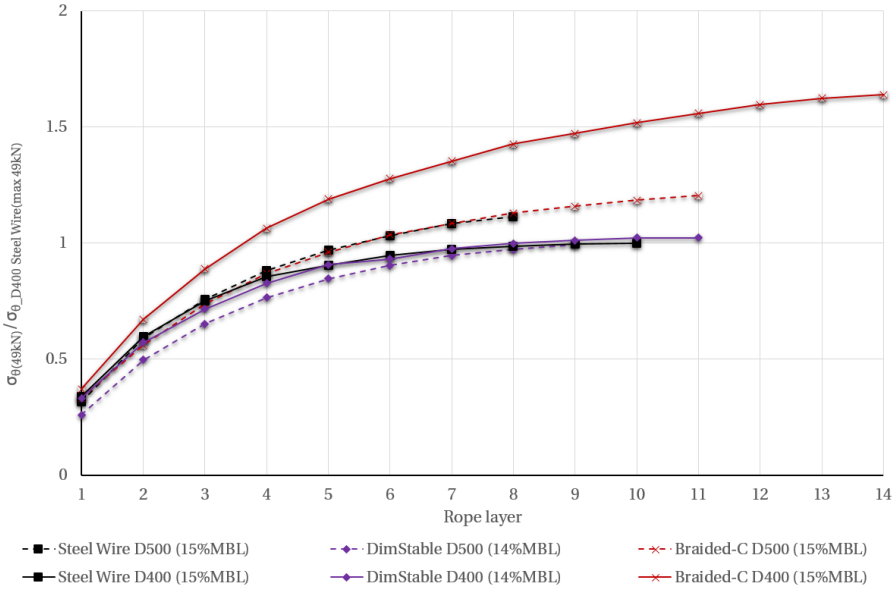

Figure E.1: Tangential stress in D500 relative to D400 - 49 kN (5 Te) tension, Ø20 mm

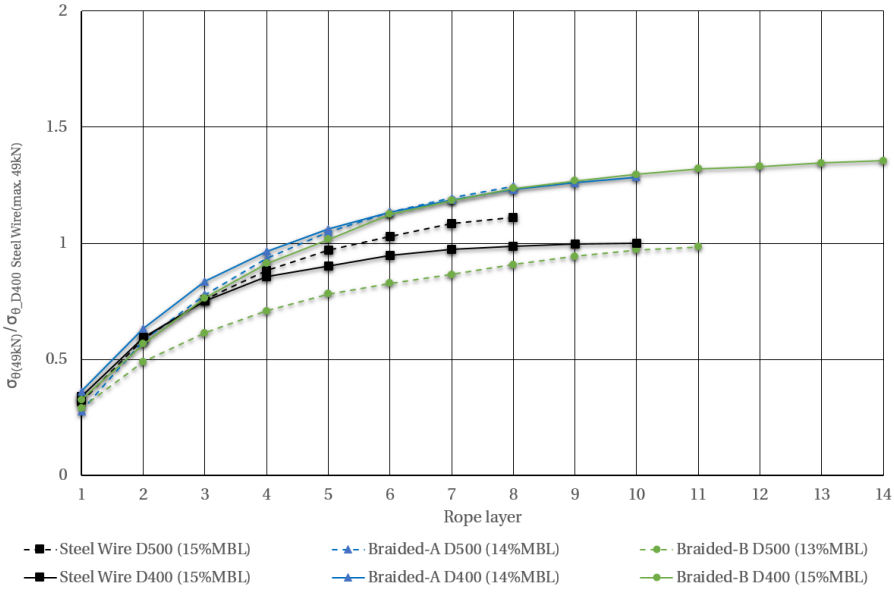

Figure E.2: Tangential stress in D500 relative to D400 - 49 kN (5 Te) tension, Ø20 mm

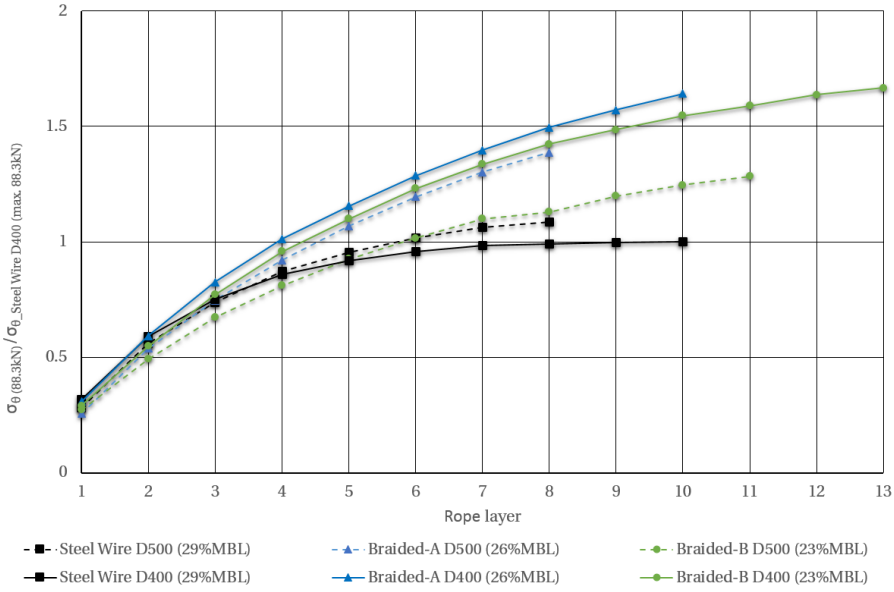

Figure E.3: Tangential stress in D500 relative to D400 - 88.3 kN (9 Te) tension, Ø20mm

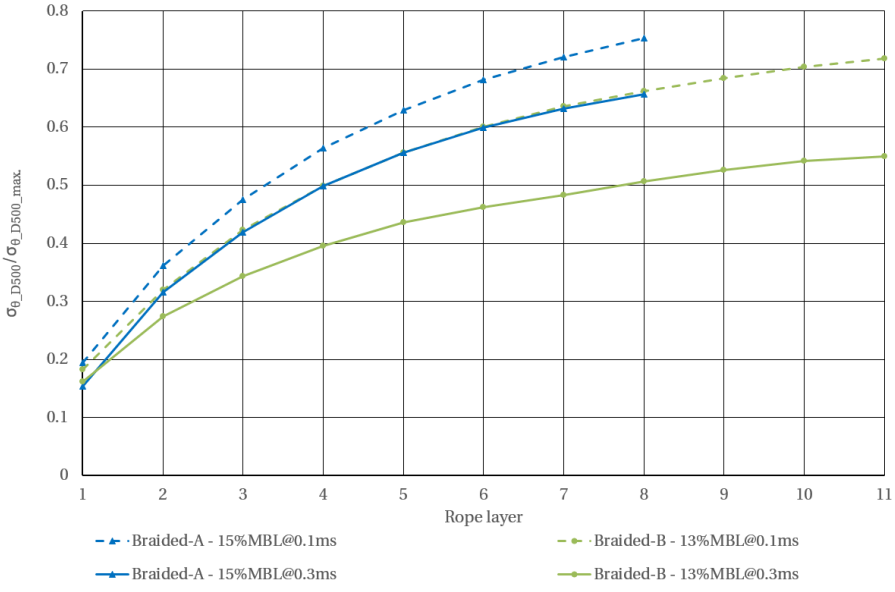

Figure E.4: Tangential stress at different spooling speeds Ø20 mm, (D/d=25)

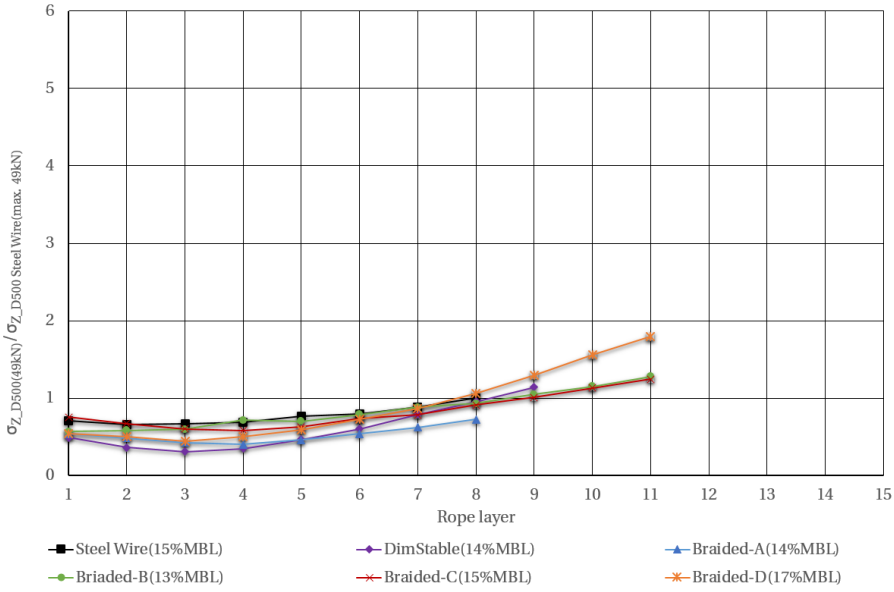

Figure E.5: Axial stress in D500 - 49.05 kN (5 Te) tension, Ø20 mm, (D/d=25)

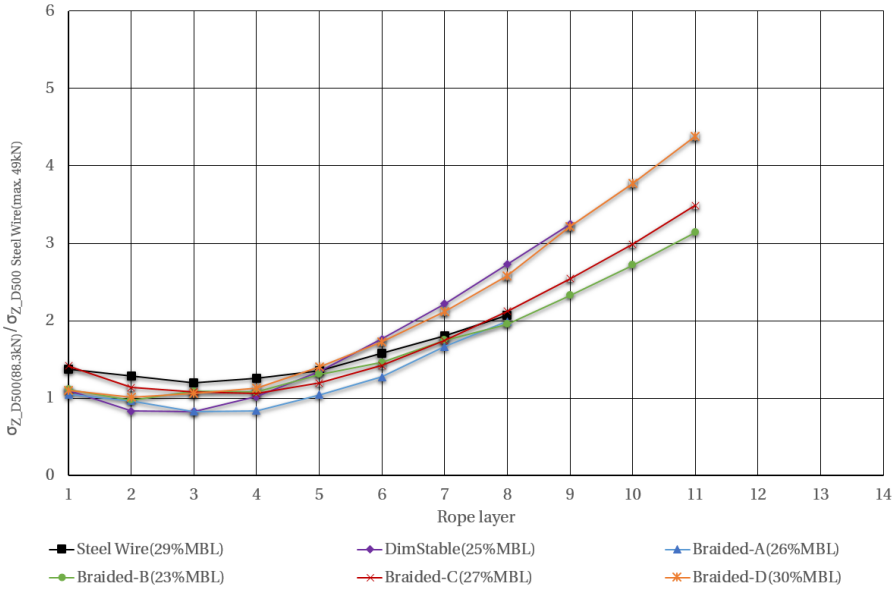

Figure E.6: Axial stress in D500 - 88.3 kN (9 Te) tension, Ø20 mm, (D/d=25)

Appendix F

Supplementary flange stress measurement results

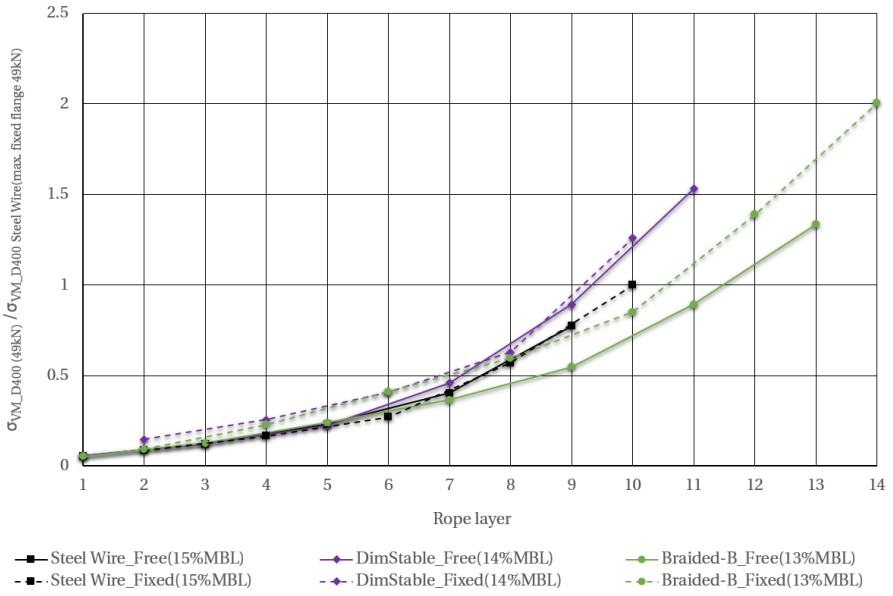

Figure F.1: von Mises stress, D400 flanges - 49.05 kN (5 Te) tension, Ø20 mm

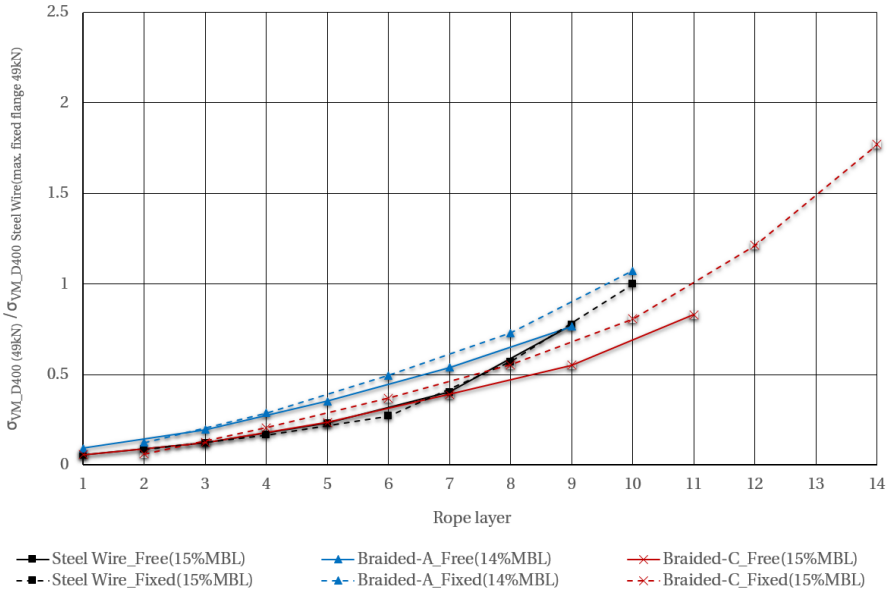

Figure F.2: von Mises stress, D400 flanges - 49.05 kN (5 Te) tension, Ø20 mm

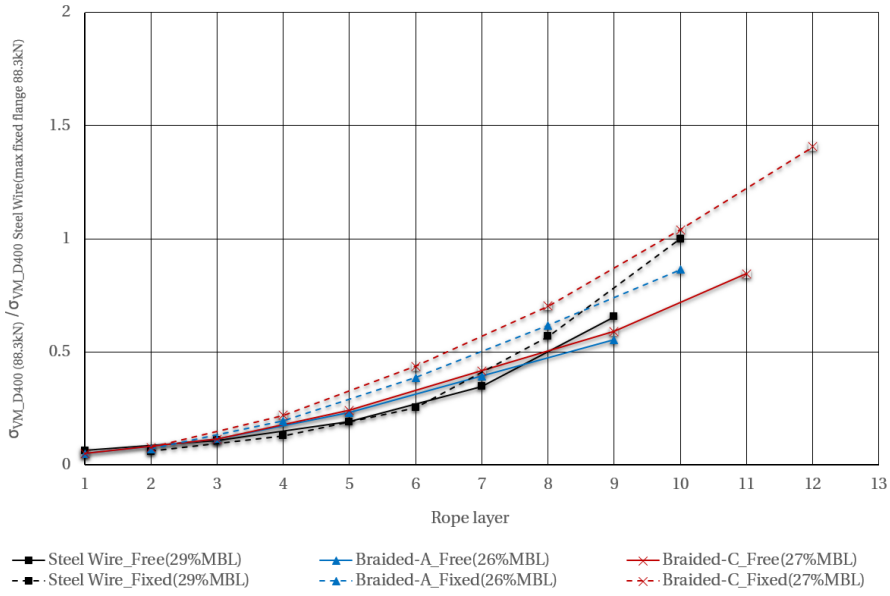

Figure F.3: von Mises stress, D400 flanges - 88.3 kN (9 Te) tension, Ø20 mm

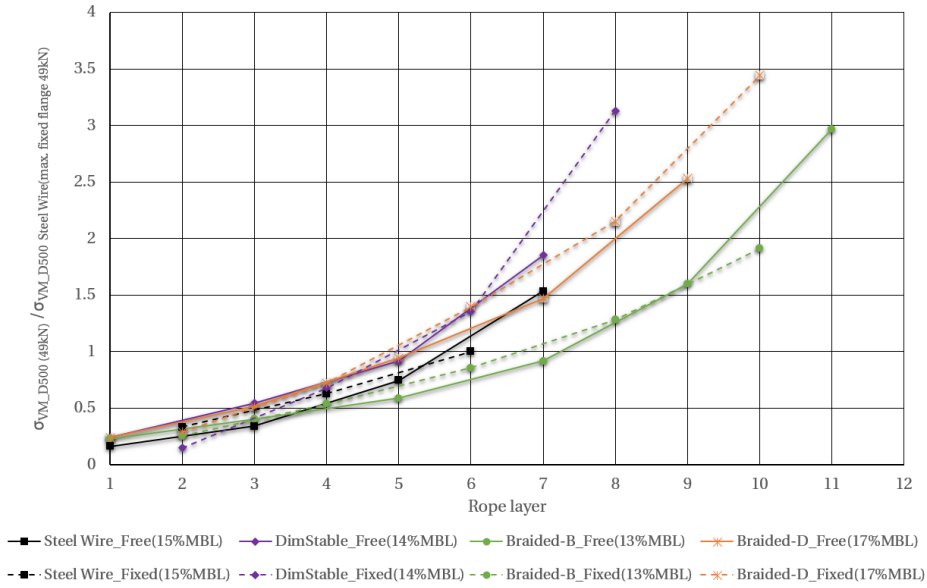

Figure F.4: von Mises stress, D500 flanges - 49.05 kN (5 Te) tension, Ø20 mm

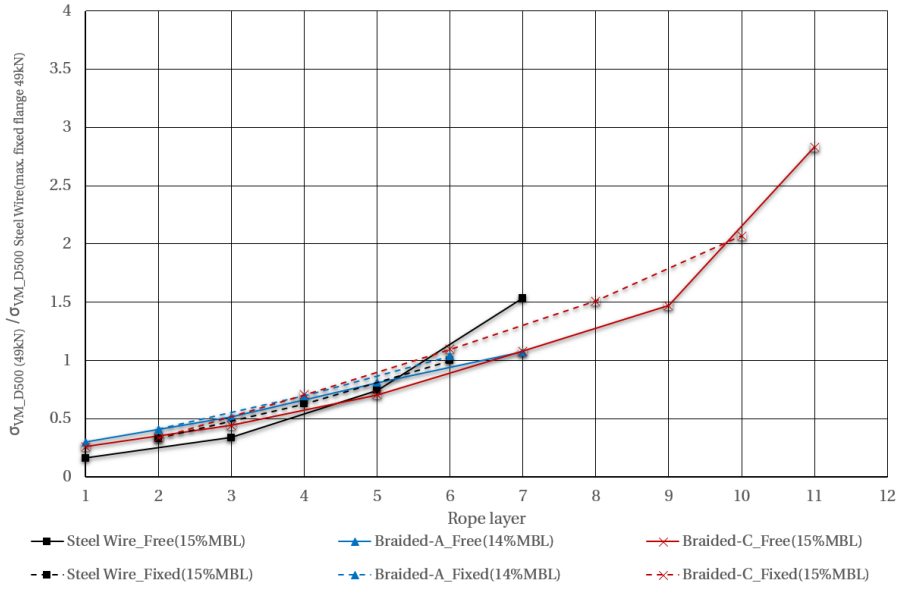

Figure F.5: von Mises stress, D500 flanges - 49.05 kN (5 Te) tension, Ø20 mm

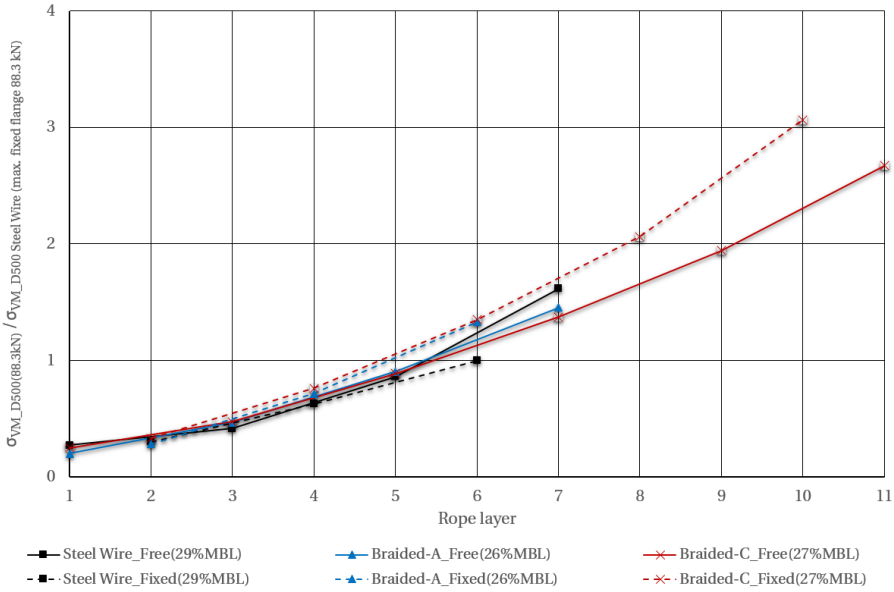

Figure F.6: von Mises stress, D500 flanges - 88.3 kN (9 Te) tension, Ø20 mm

Appendix G

Supplementary drum stress calculation results

G.1 Multilayer exponents

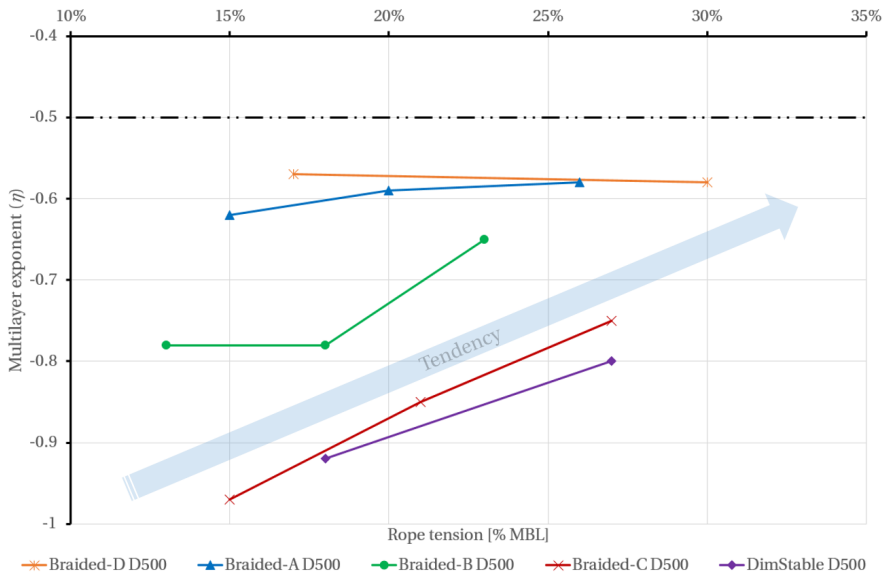

Figure G.1: Multilayer exponents vs. rope tension - Ø20 mm HPSFR - D500 (D/d=25)

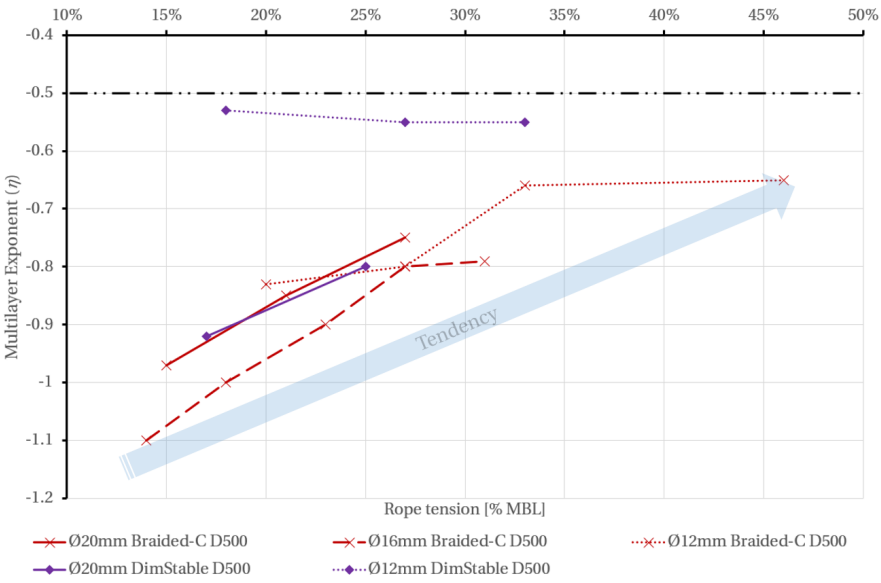

Figure G.2: Multilayer exponents vs. rope tension - Ø12-Ø20 mm HPSFR - D500

G.2 Steel wire rope - Ø20 mm

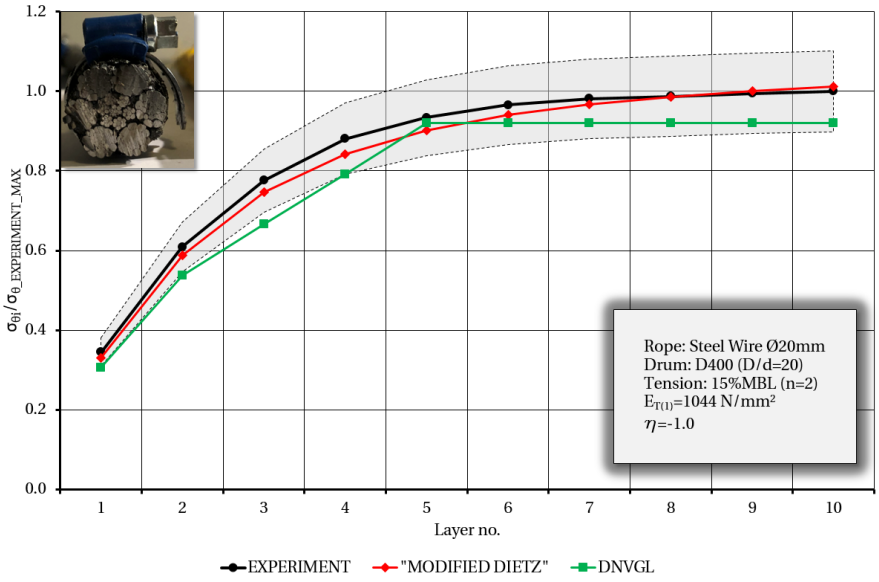

Figure G.3: Calculations vs. experiment, σ_θ - steel wire on D400, 15% MBL

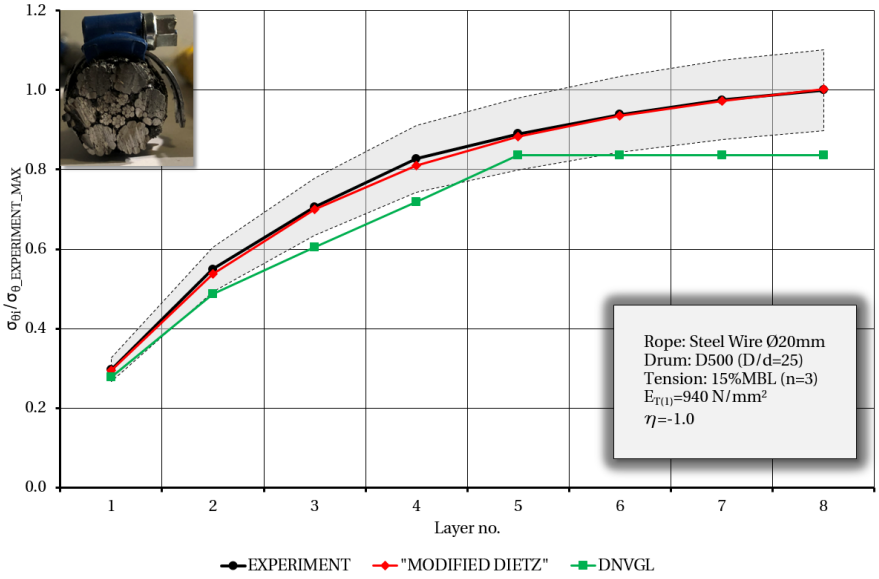

Figure G.4: Calculations vs. experiment, σ_θ - steel wire on D500, 15% MBL

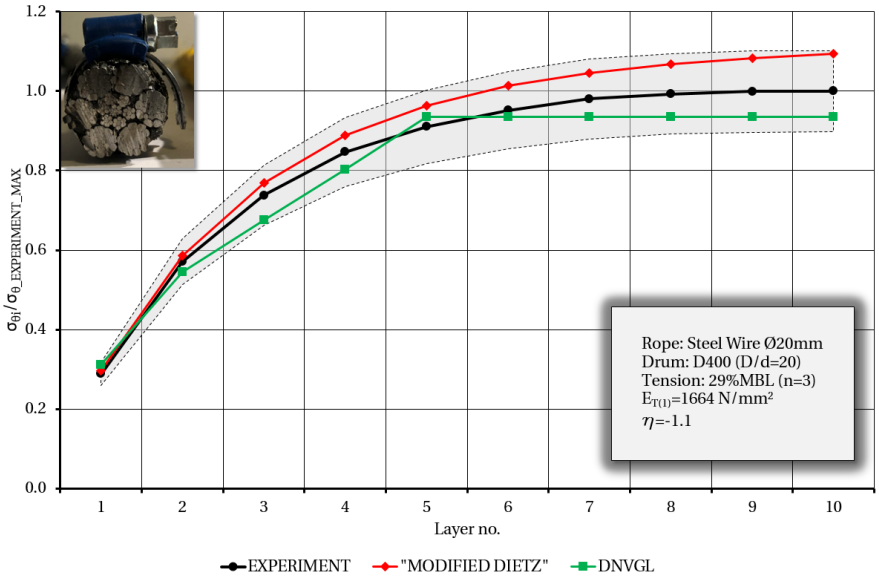

Figure G.5: Calculations vs. experiment, σ_θ - steel wire on D400, 29% MBL

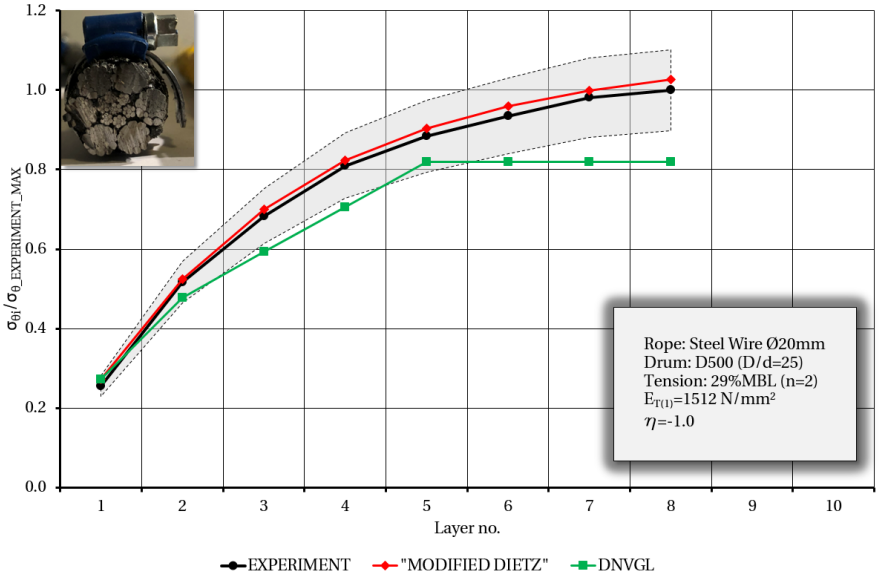

Figure G.6: Calculations vs. experiment, σ_θ - steel wire on D500, 29% MBL

G.3 DimStable - Ø20 mm

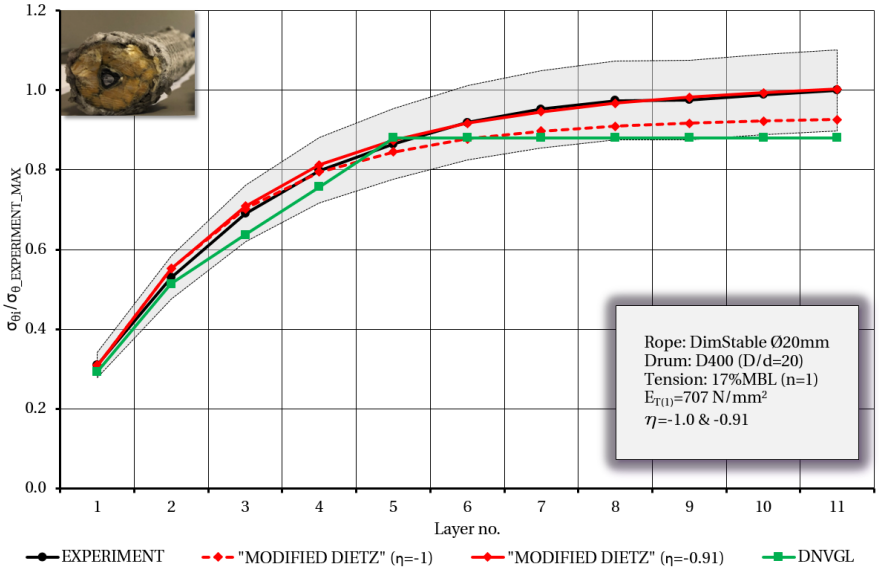

Figure G.7: Calculations vs. experiment, σ_θ - Ø20 mm DimStable on D400, 17% MBL

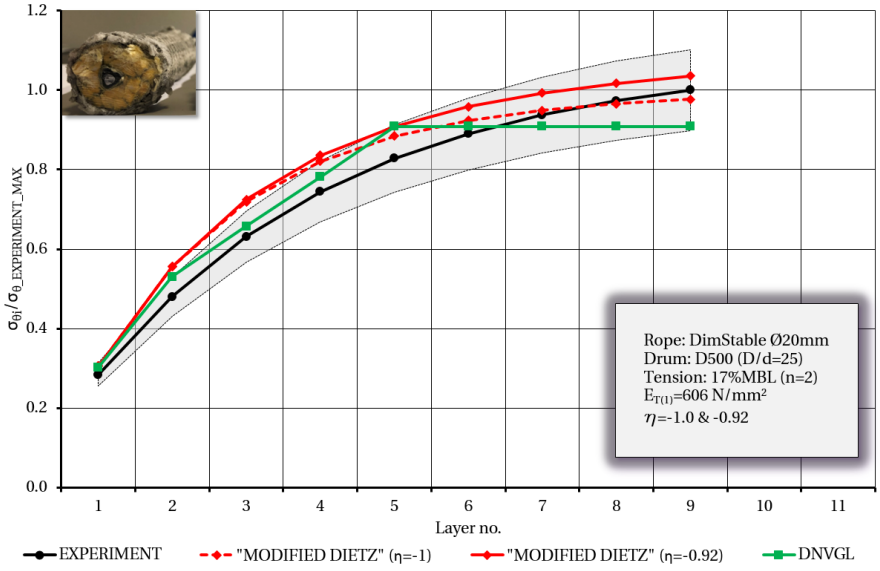

Figure G.8: Calculations vs. experiment, σ_θ - Ø20 mm DimStable on D500, 17% MBL

G.4 DimStable - Ø12 mm

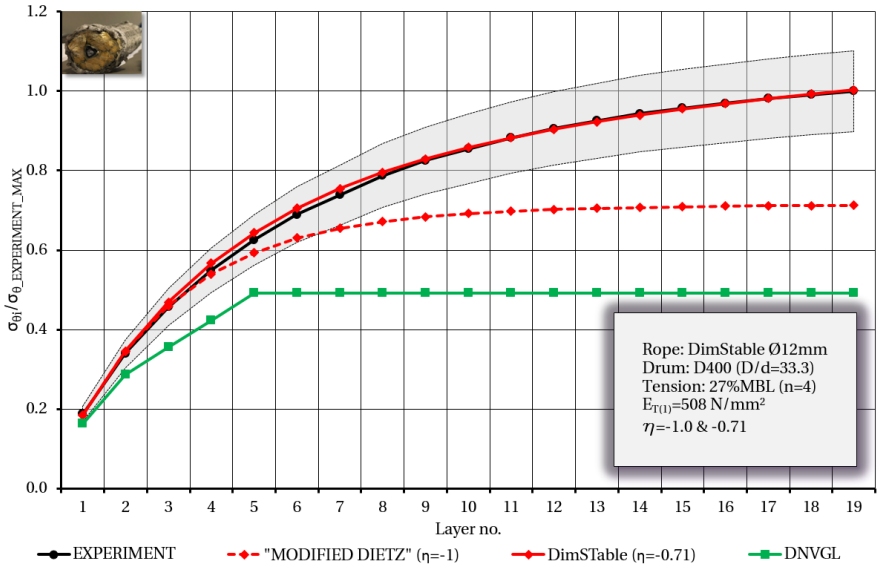

Figure G.9: Calculations vs. experiment, σ_θ - Ø12 mm DimStable on D400, 27% MBL

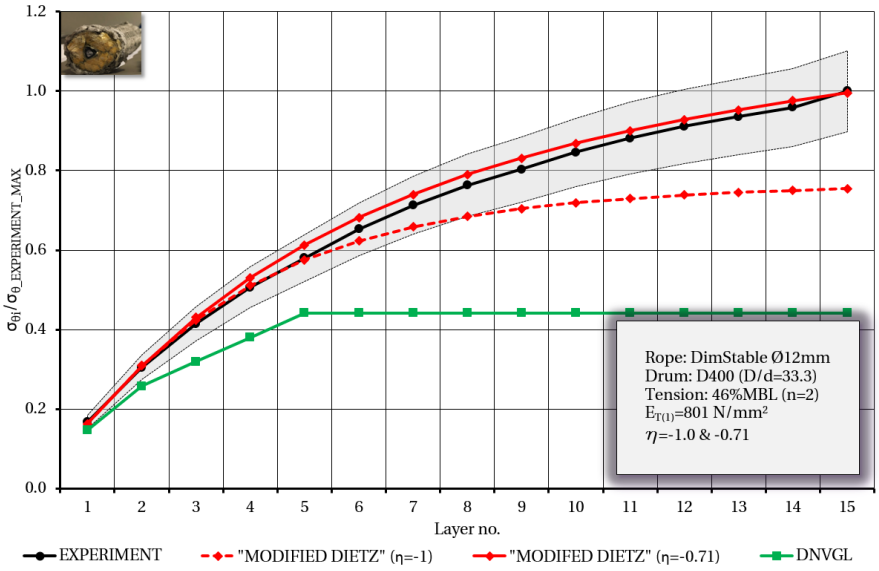

Figure G.10: Calculations vs. experiment, σ_θ - Ø12 mm DimStable on D400, 46% MBL

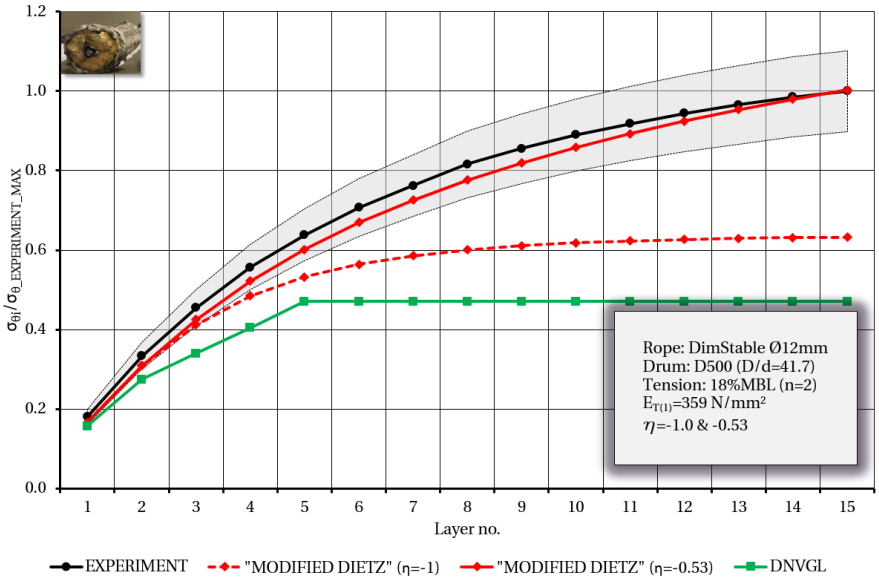

Figure G.11: Calculations vs. experiment, σ_θ - Ø12 mm DimStable on D500, 18% MBL

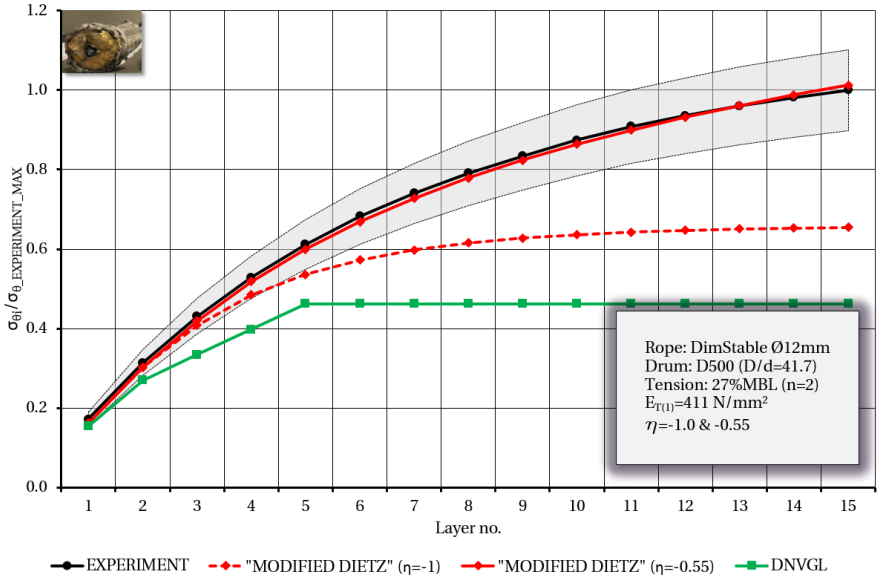

Figure G.12: Calculations vs. experiment, σ_θ - Ø12 mm DimStable on D500, 27% MBL

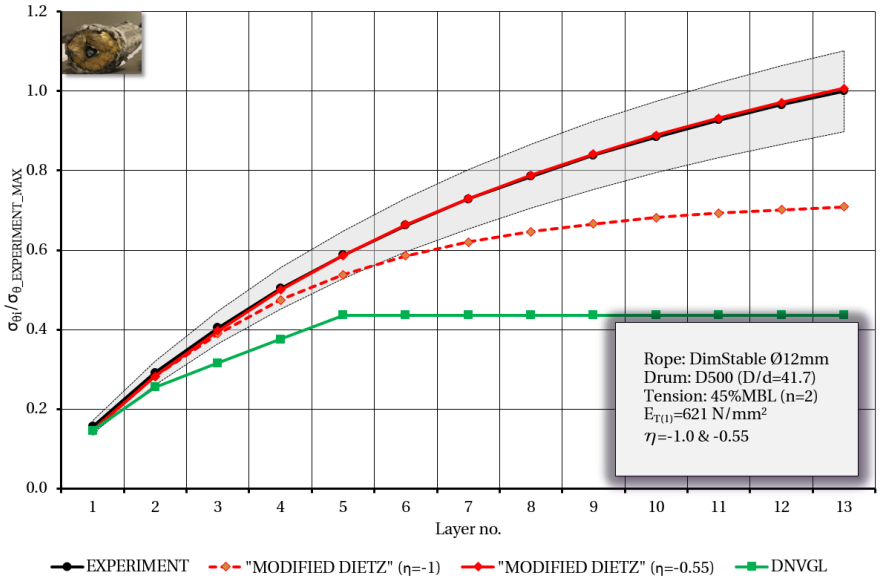

Figure G.13: Calculations vs. experiment, σ_θ - Ø12 mm DimStable on D500, 45% MBL

G.5 Braided-A - Ø20 mm

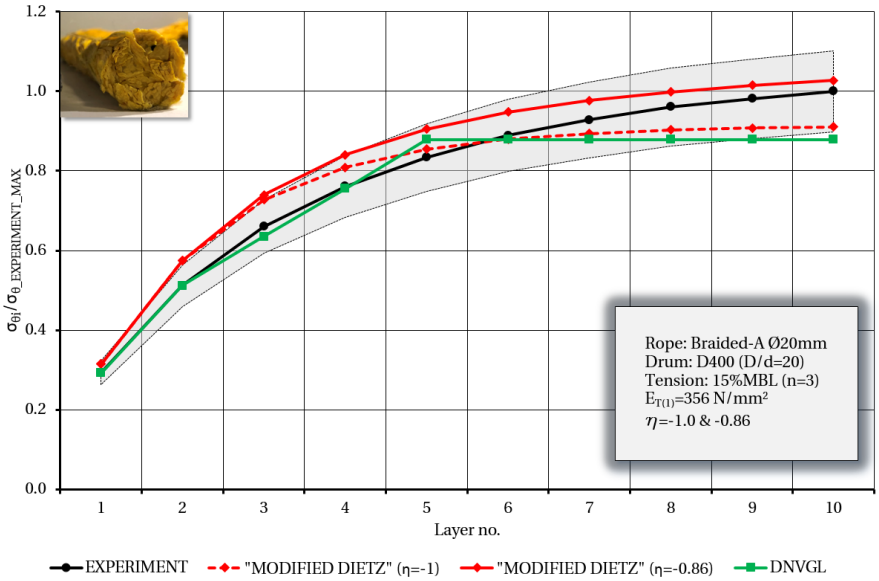

Figure G.14: Calculations vs. experiment, σ_θ - Ø20 mm Braided-A on D400, 15% MBL

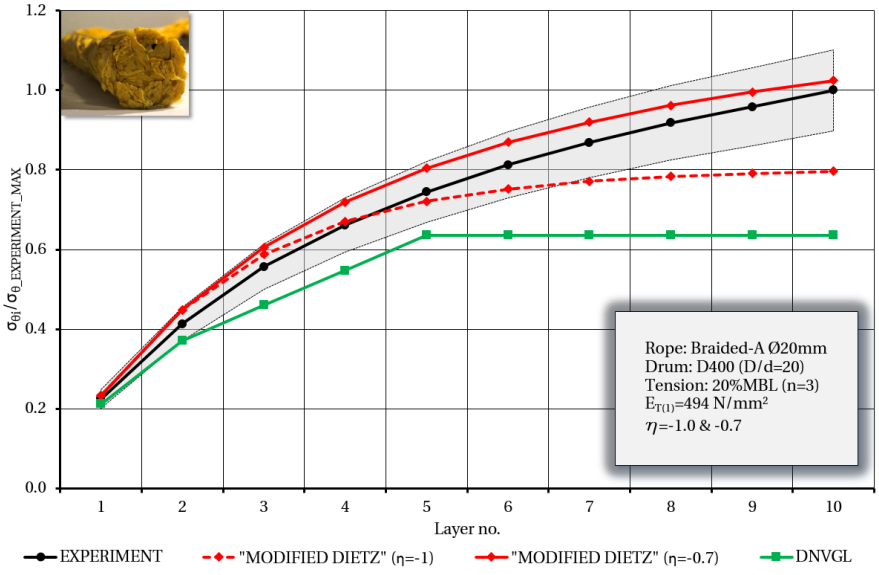

Figure G.15: Calculations vs. experiment, σ_θ - Ø20 mm Braided-A on D400, 20% MBL

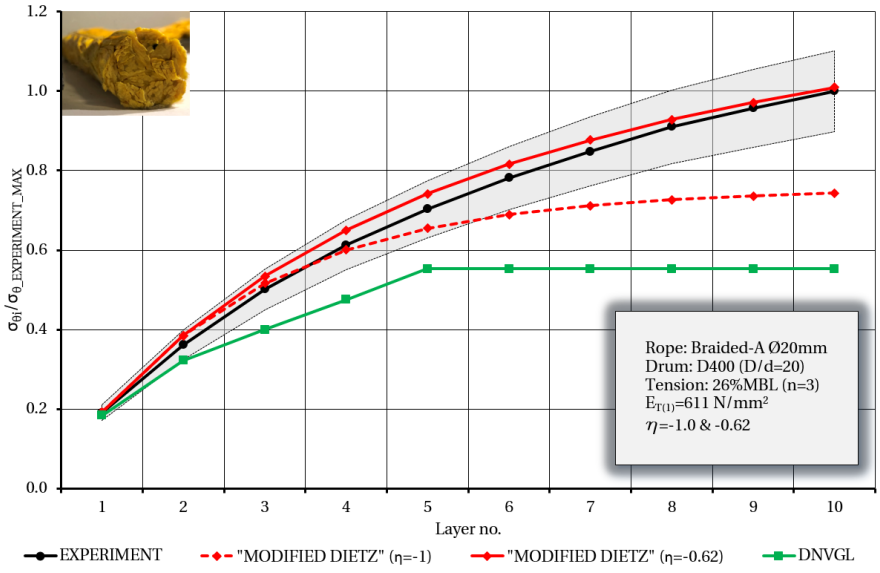

Figure G.16: Calculations vs. experiment, σ_θ - Ø20 mm Braided-A on D400, 26% MBL

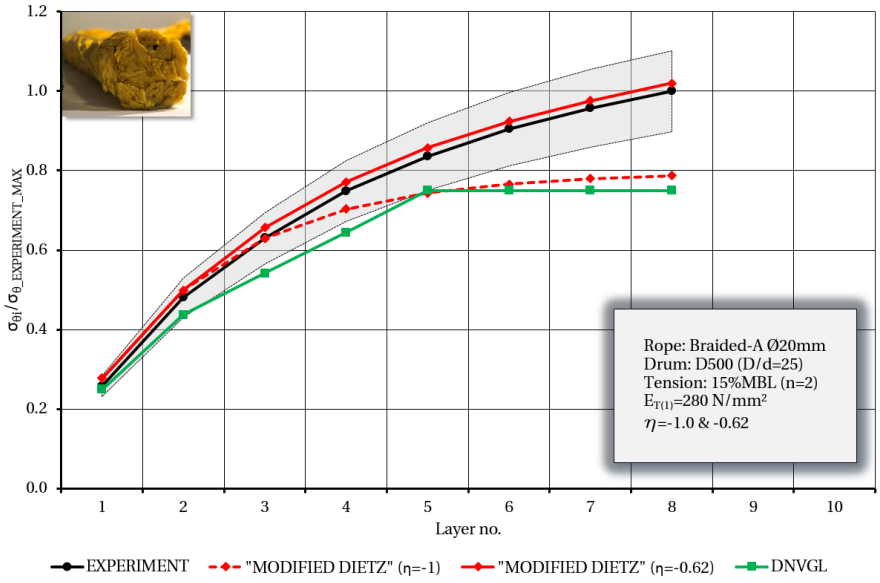

Figure G.17: Calculations vs. experiment, σ_θ - Ø20 mm Braided-A on D500, 15% MBL

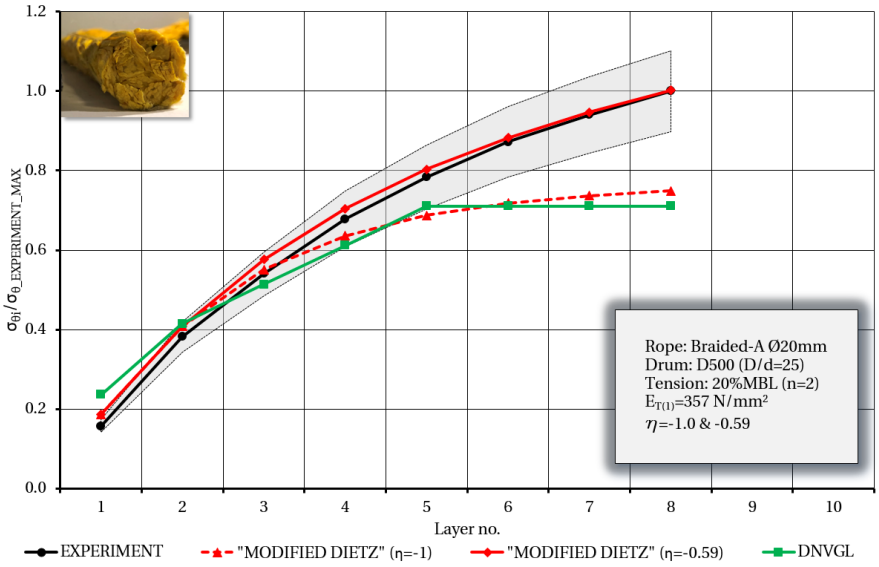

Figure G.18: Calculations vs. experiment, σ_θ - Ø20 mm Braided-A on D500, 20% MBL

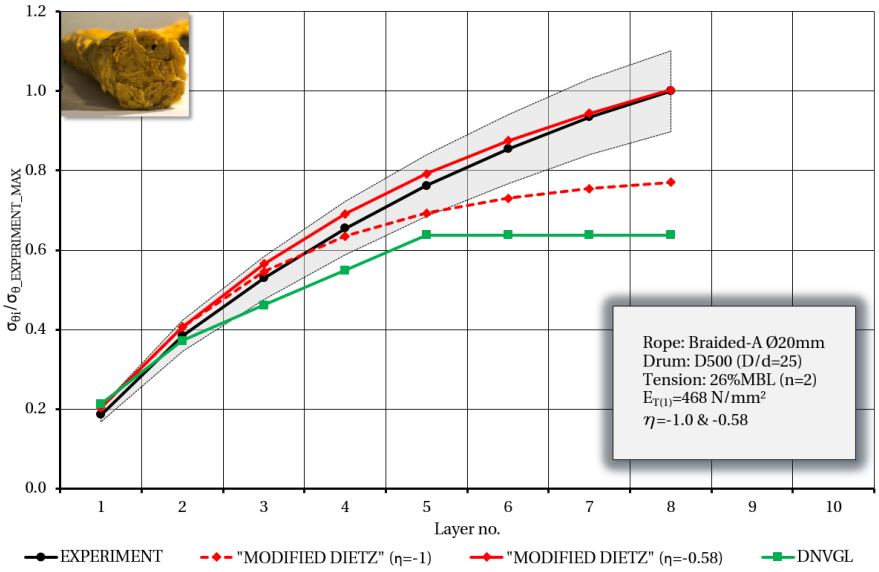

Figure G.19: Calculations vs. experiment, σ_θ - Ø20 mm Braided-A on D500, 26% MBL

G.6 Braided-B - Ø20 mm

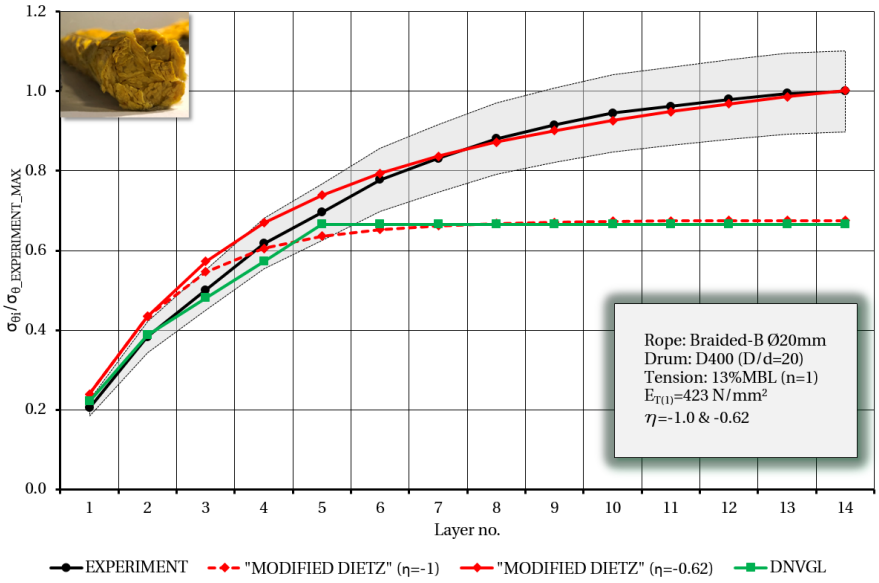

Figure G.20: Calculations vs. experiment, σ_θ - Ø20 mm Braided-B on D400, 13% MBL

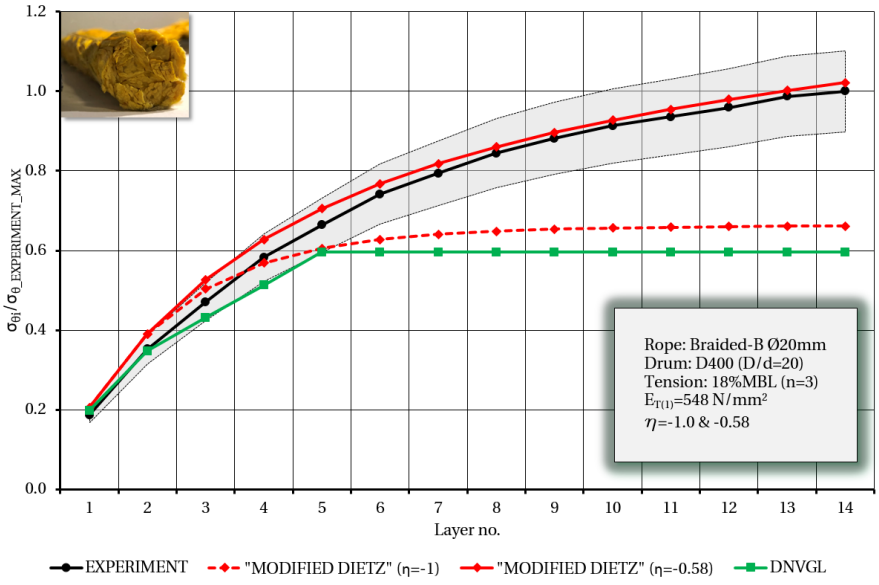

Figure G.21: Calculations vs. experiment, σ_θ - Ø20 mm Braided-B on D400, 18% MBL

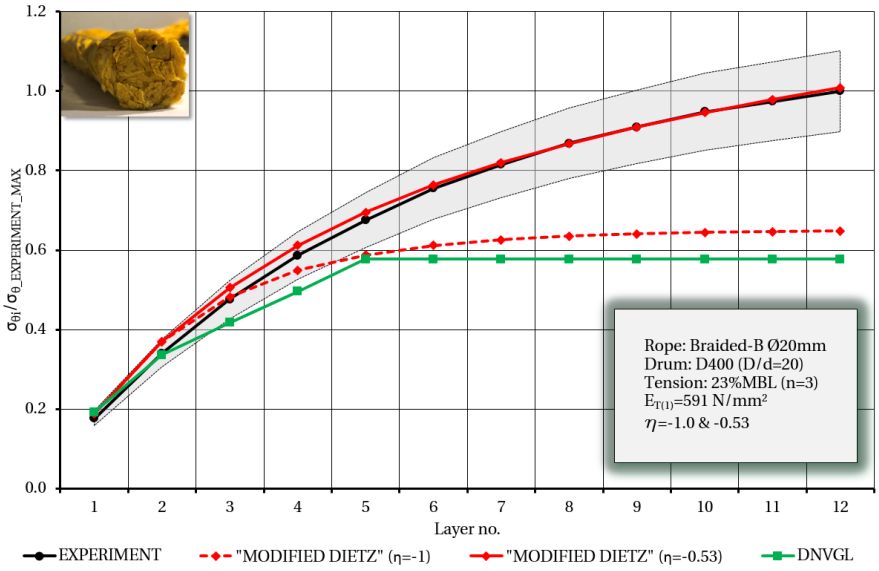

Figure G.22: Calculations vs. experiment, σ_θ - Ø20 mm Braided-B on D400, 23% MBL

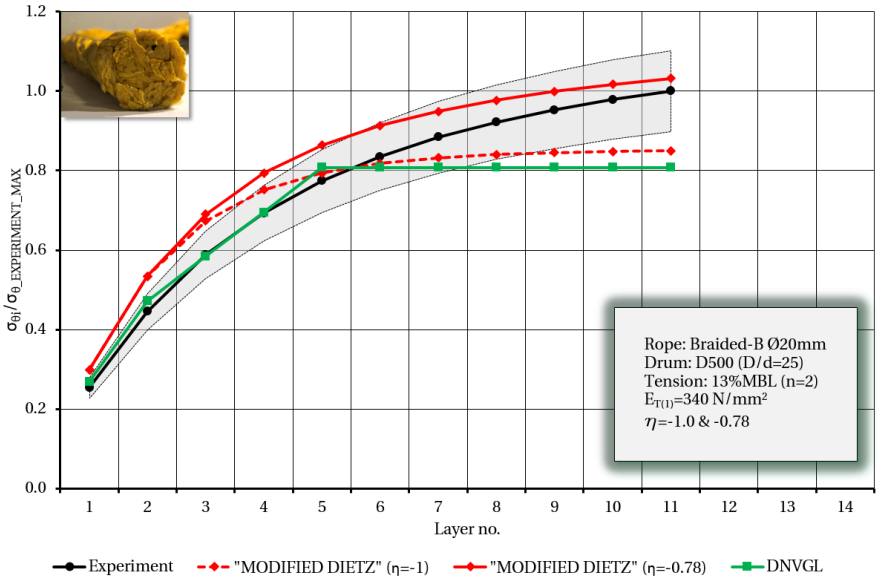

Figure G.23: Calculations vs. experiment, σ_θ - Ø20 mm Braided-B on D500, 13% MBL

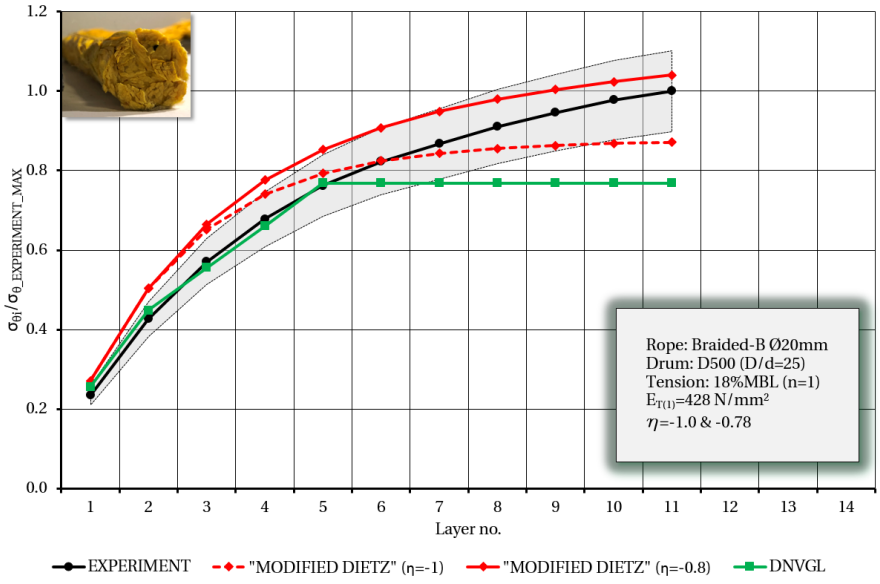

Figure G.24: Calculations vs. experiment, σ_θ - Ø20 mm Braided-B on D500, 18% MBL

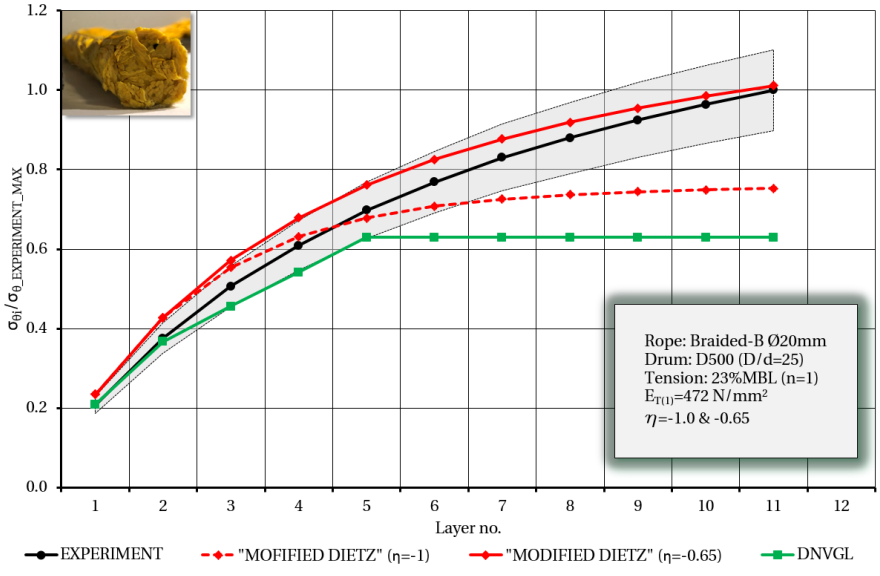

Figure G.25: Calculations vs. experiment, σ_θ - Ø20 mm Braided-B on D500, 23% MBL

G.7 Braided-C - Ø20 mm

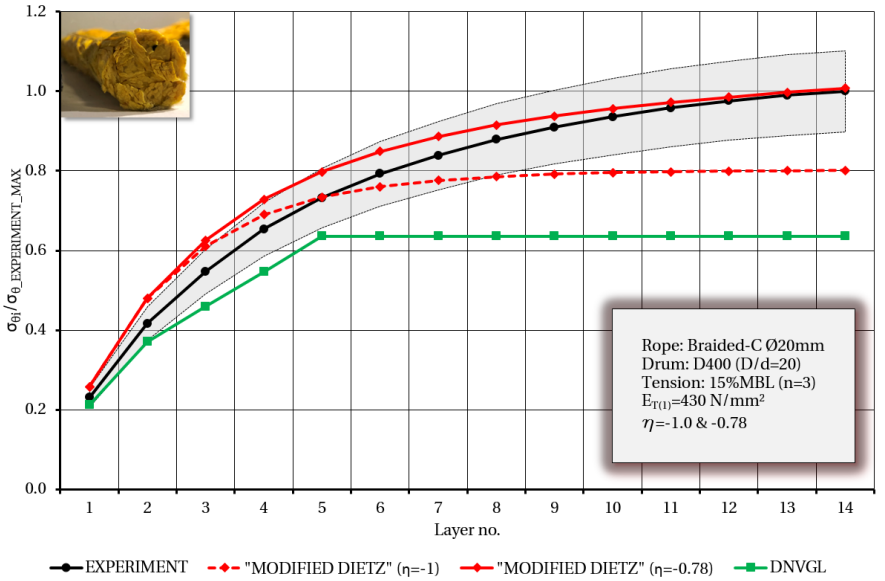

Figure G.26: Calculations vs. experiment, σ_θ - Ø20 mm Braided-C on D400, 15% MBL

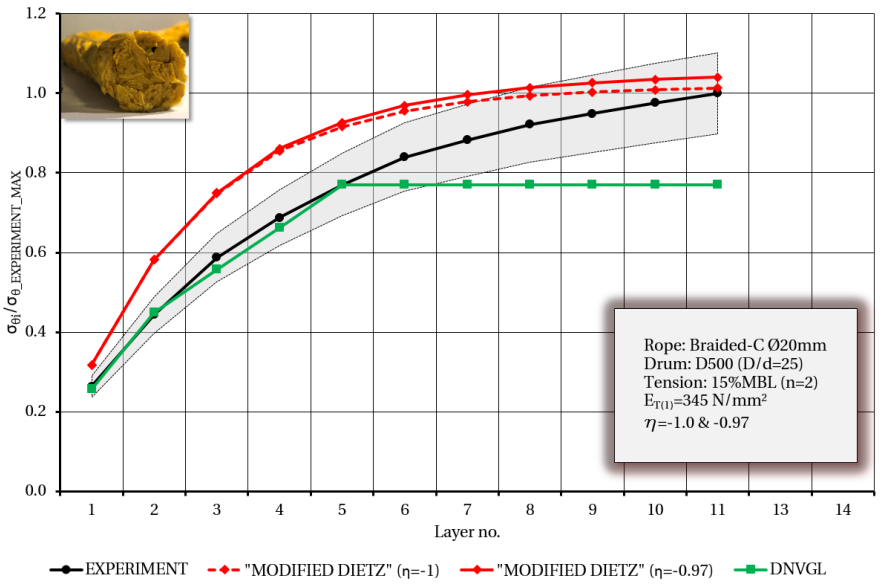

Figure G.27: Calculations vs. experiment, σ_θ - Ø20 mm Braided-C on D500, 15% MBL

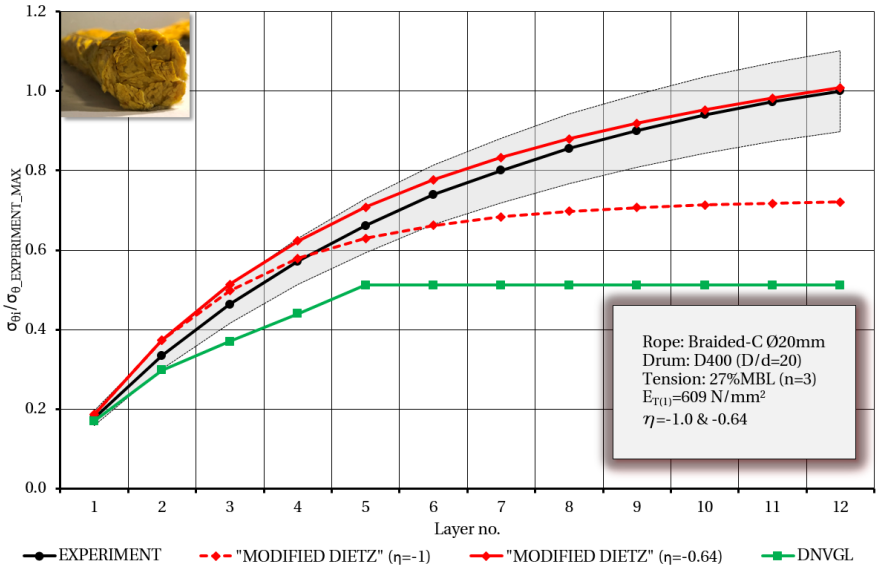

Figure G.28: Calculations vs. experiment, σ_θ - Ø20 mm Braided-C on D400, 27% MBL

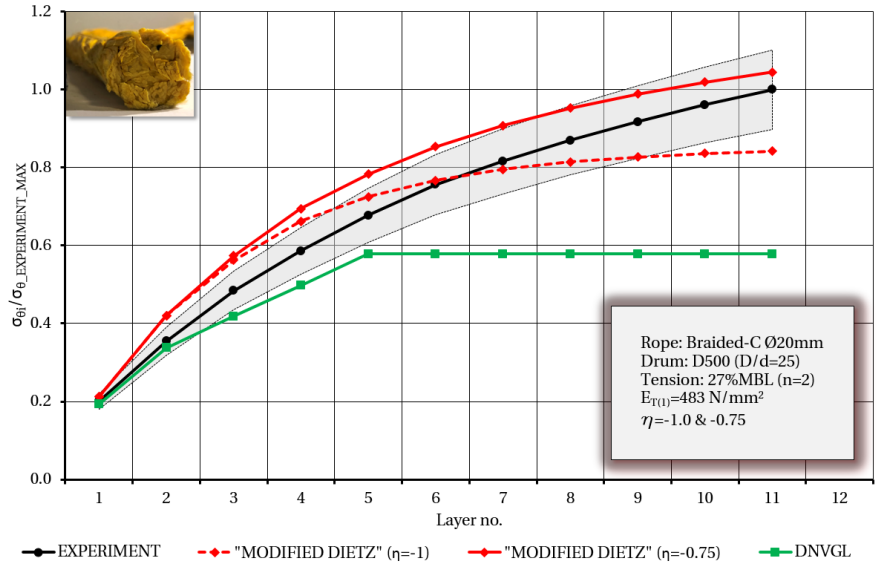

Figure G.29: Calculations vs. experiment, σ_θ - Ø20 mm Braided-C on D500, 27% MBL

G.8 Braided-C - Ø16 mm

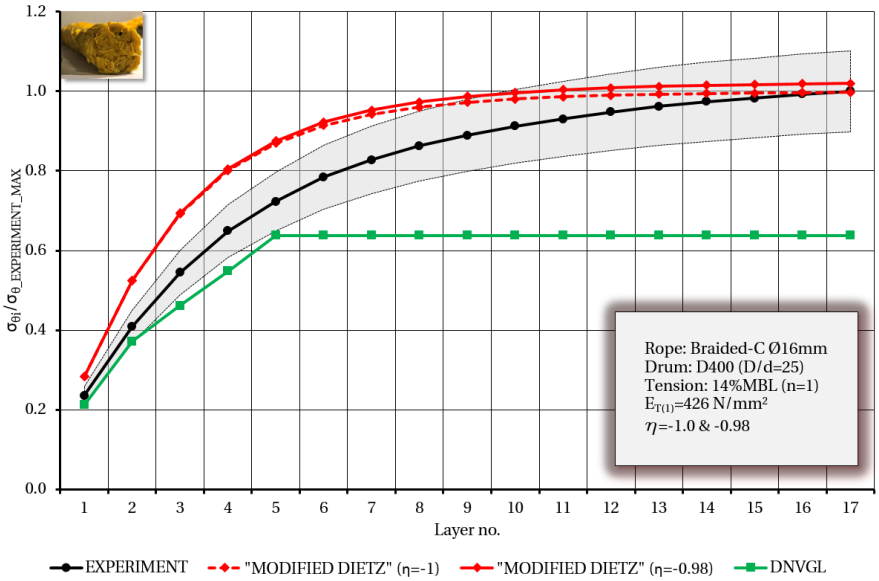

Figure G.30: Calculations vs. experiment, σ_θ - Ø16 mm Braided-C on D400, 14% MBL

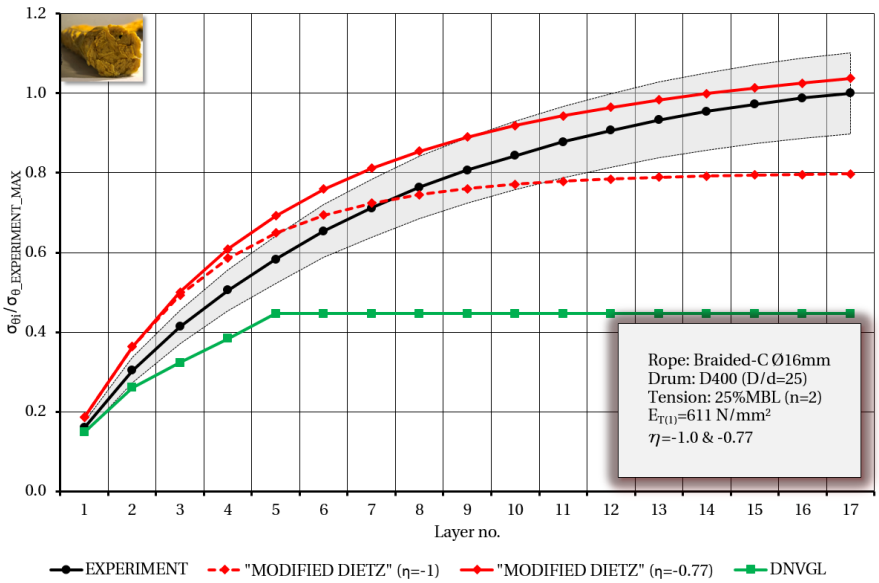

Figure G.31: Calculations vs. experiment, σ_θ - Ø16 mm Braided-C on D400, 25% MBL

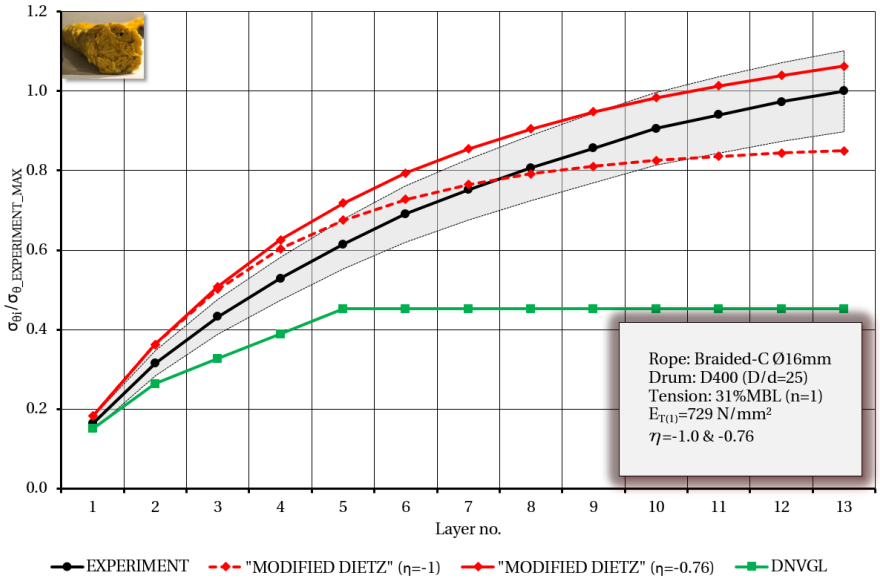

Figure G.32: Calculations vs. experiment, σ_θ - Ø16 mm Braided-C on D400, 31% MBL

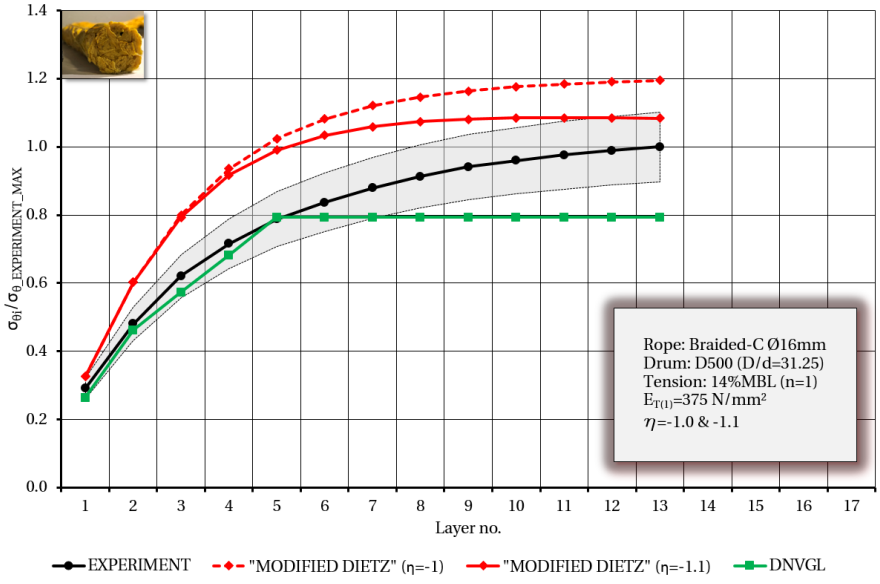

Figure G.33: Calculations vs. experiment, σ_θ - Ø16 mm Braided-C on D500, 14% MBL

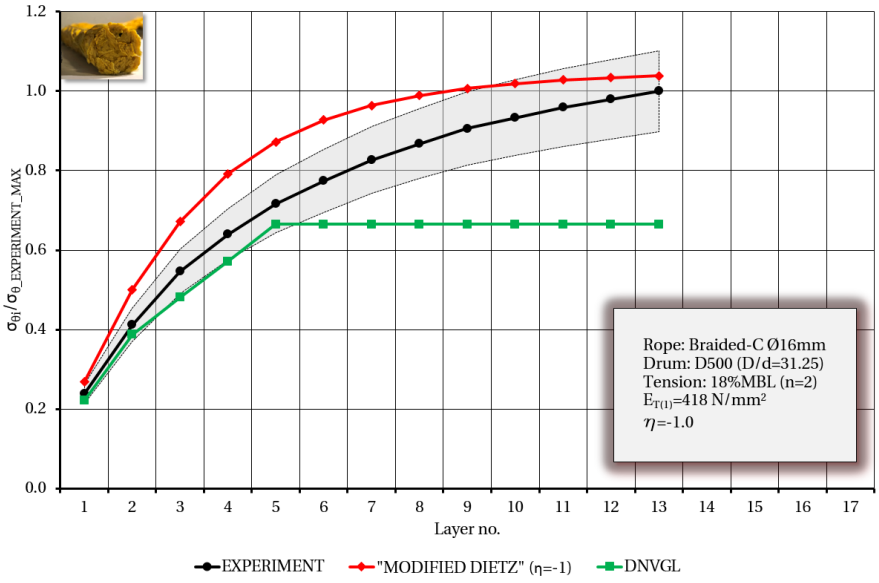

Figure G.34: Calculations vs. experiment, σ_θ - Ø16 mm Braided-C on D500, 18% MBL

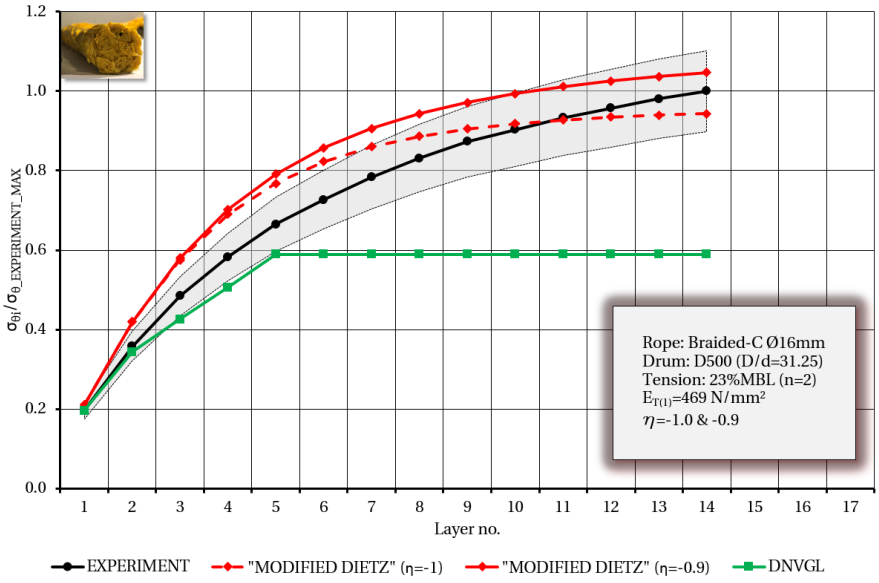

Figure G.35: Calculations vs. experiment, σ_θ - Ø16 mm Braided-C on D500, 23% MBL

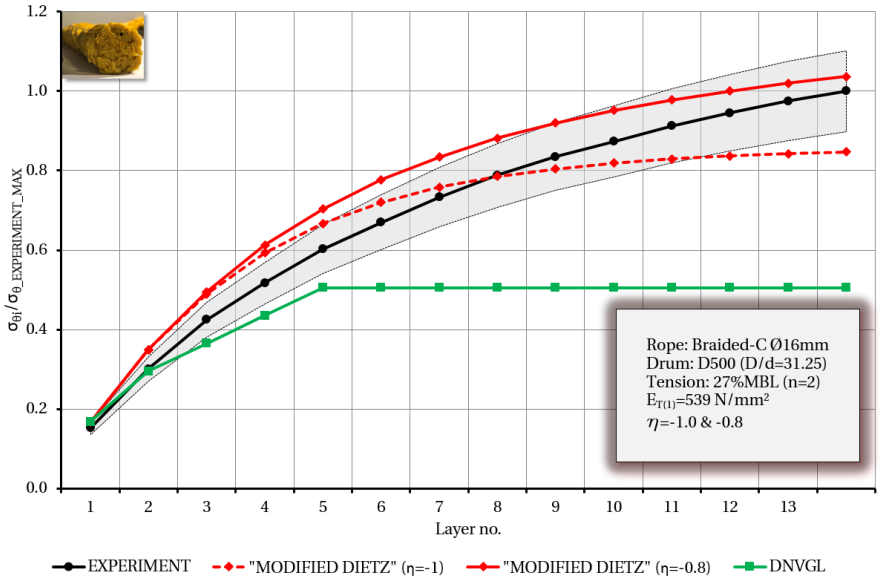

Figure G.36: Calculations vs. experiment, σ_θ - Ø16 mm Braided-C on D500, 27% MBL

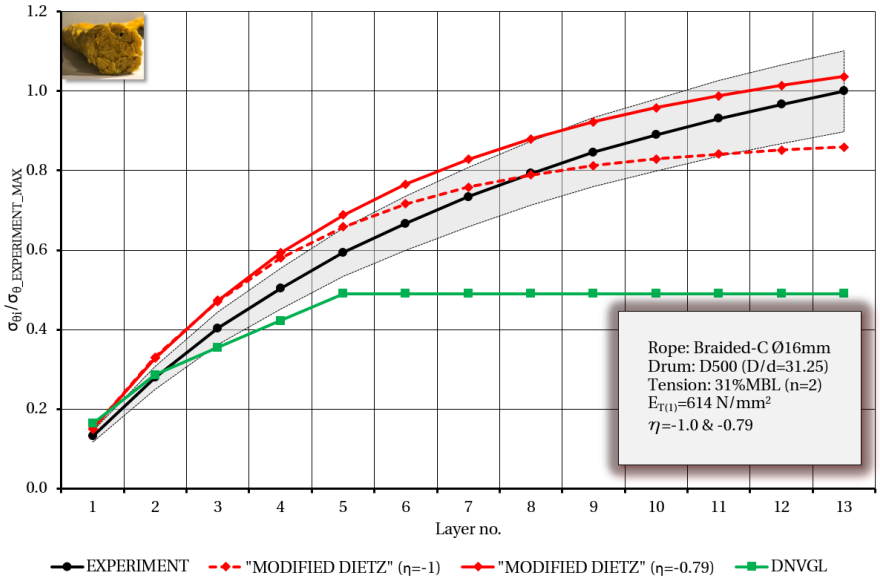

Figure G.37: Calculations vs. experiment, σ_θ - Ø16 mm Braided-C on D500, 31% MBL

G.9 Braided-C - Ø12 mm

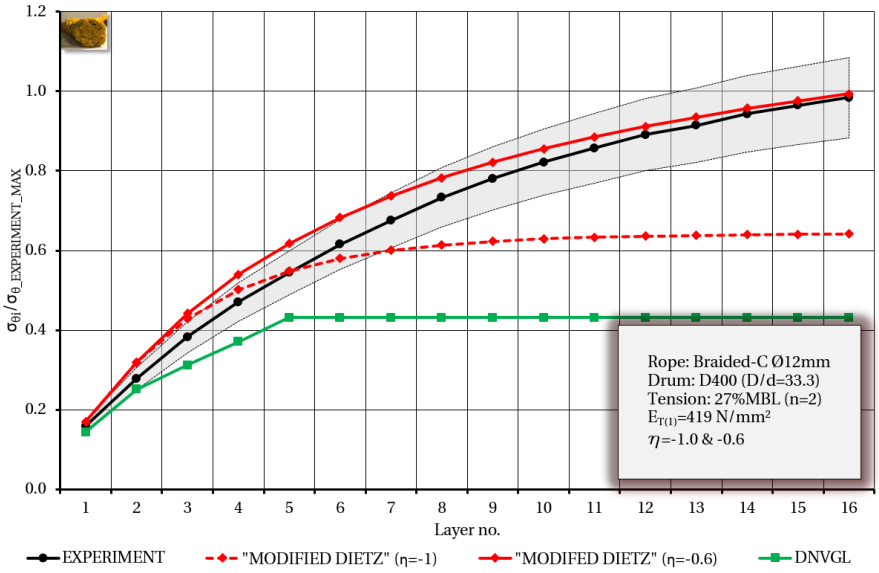

Figure G.38: Calculations vs. experiment, σ_θ - Ø12 mm Braided-C on D400, 27% MBL

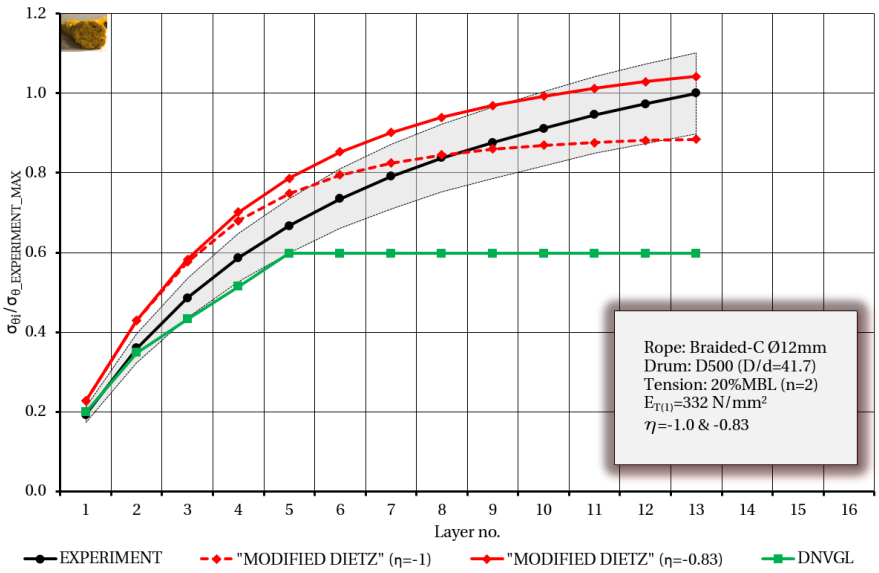

Figure G.39: Calculations vs. experiment, σ_θ - Ø12 mm Braided-C on D500, 20% MBL

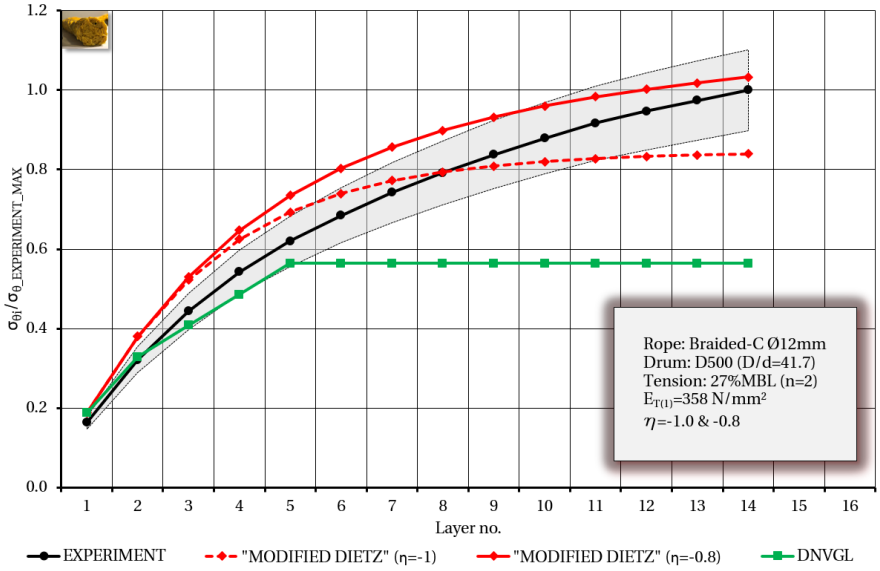

Figure G.40: Calculations vs. experiment, σ_θ - Ø12 mm Braided-C on D500, 27% MBL

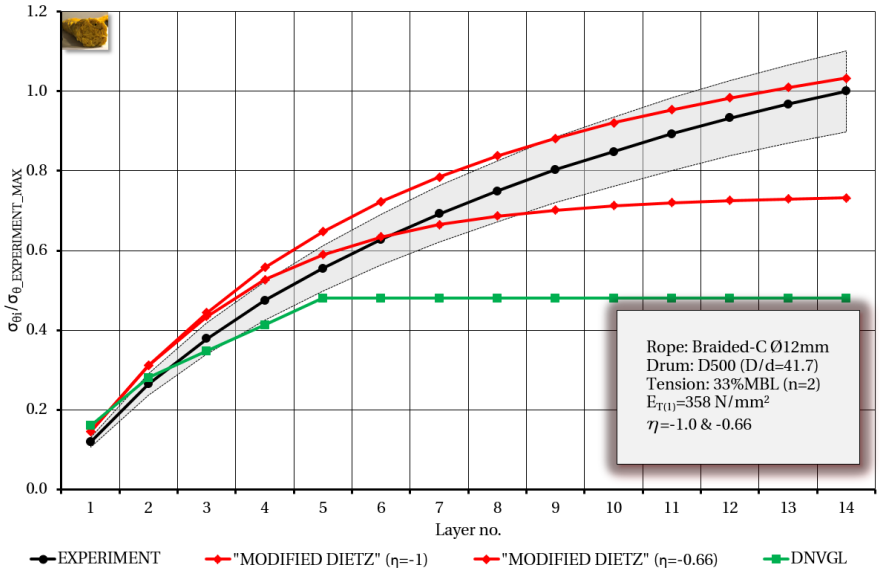

Figure G.41: Calculations vs. experiment, σ_θ - Ø12 mm Braided-C on D500, 33% MBL

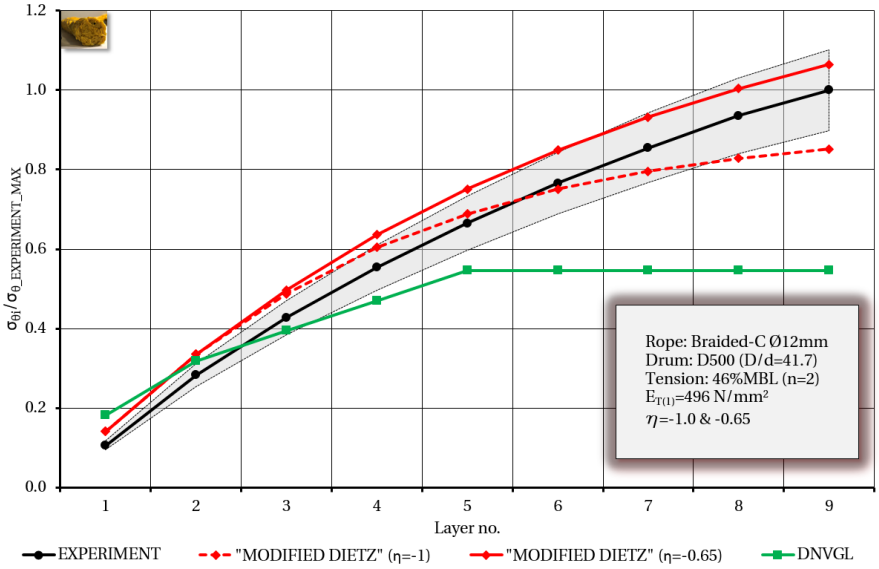

Figure G.42: Calculations vs. experiment, σ_θ - Ø12 mm Braided-C on D500, 46% MBL

G.10 Braided-D - Ø20 mm

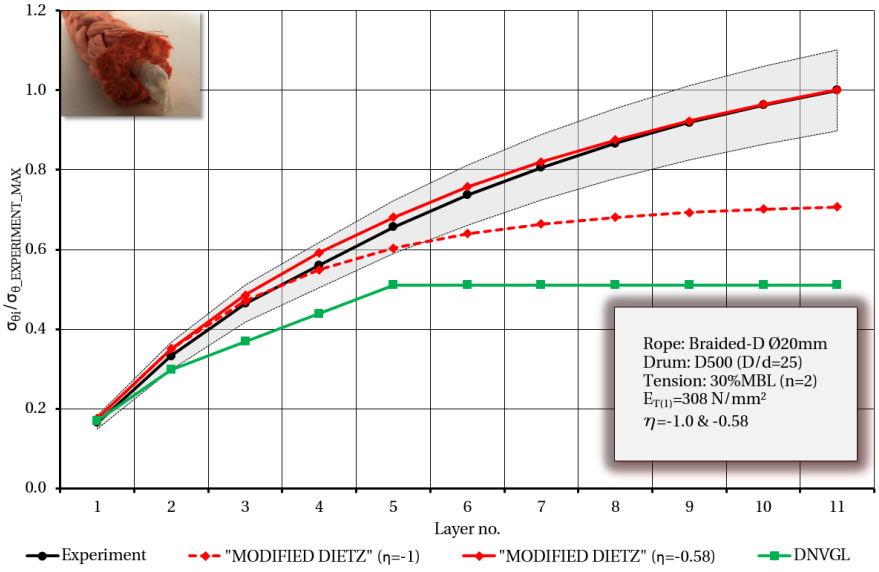

Figure G.43: Calculations vs. experiment, σ_θ - Ø20 mm Braided-D on D500, 30% MBL

Appendix H

Supplementary curves for evaluation of proposed calculation

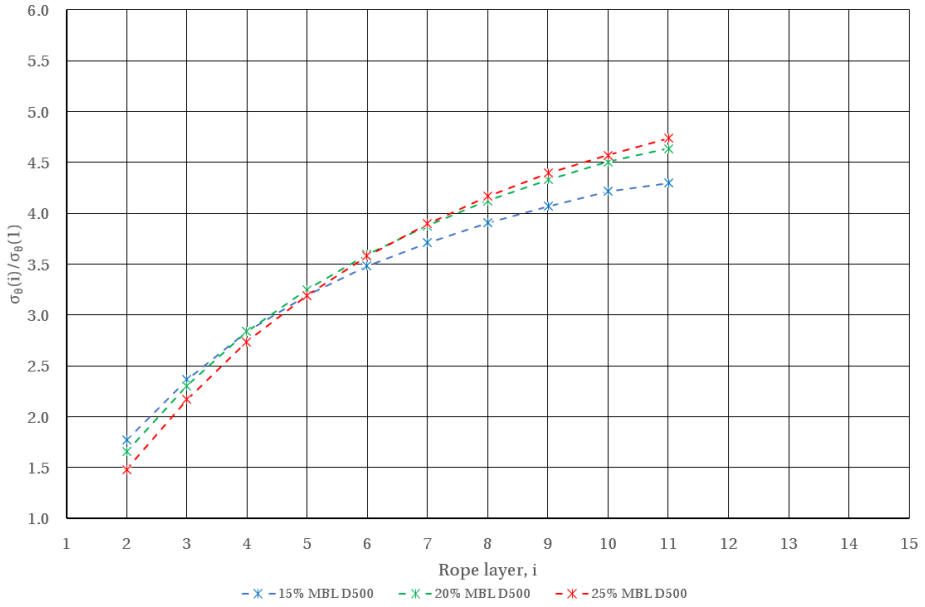

Figure H.1: Stress ratios - Braided-D (D500)

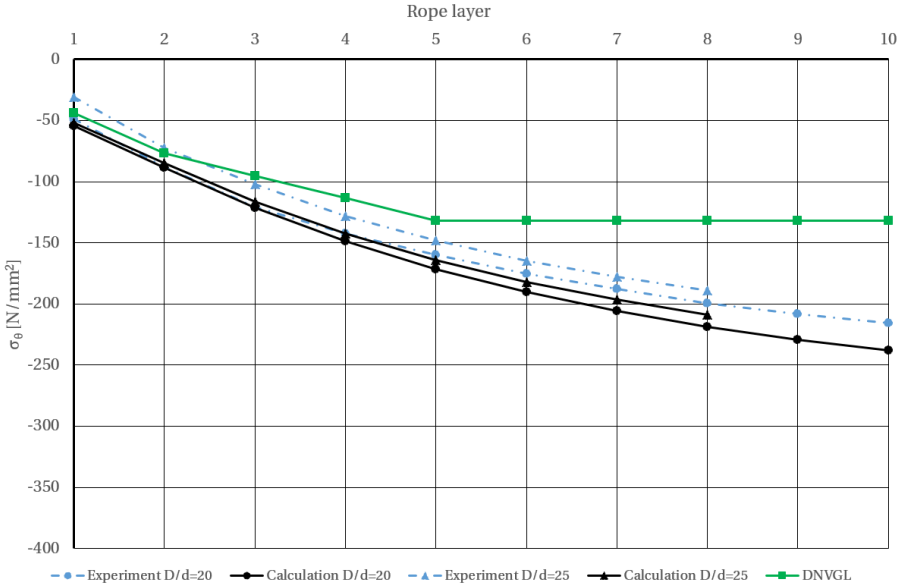

Figure H.2: Eqs. 8.2 and 8.3 vs. measured stresses - Ø20 mm Braided-A, 20% MBL

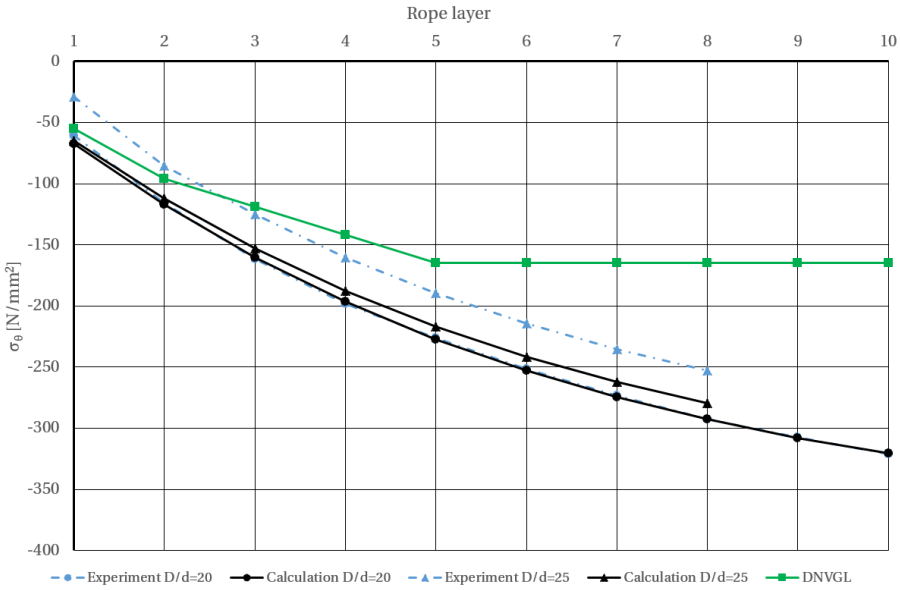

Figure H.3: Eqs. 8.2 and 8.3 vs. measured stresses - Ø20 mm Braided-A, 25% MBL

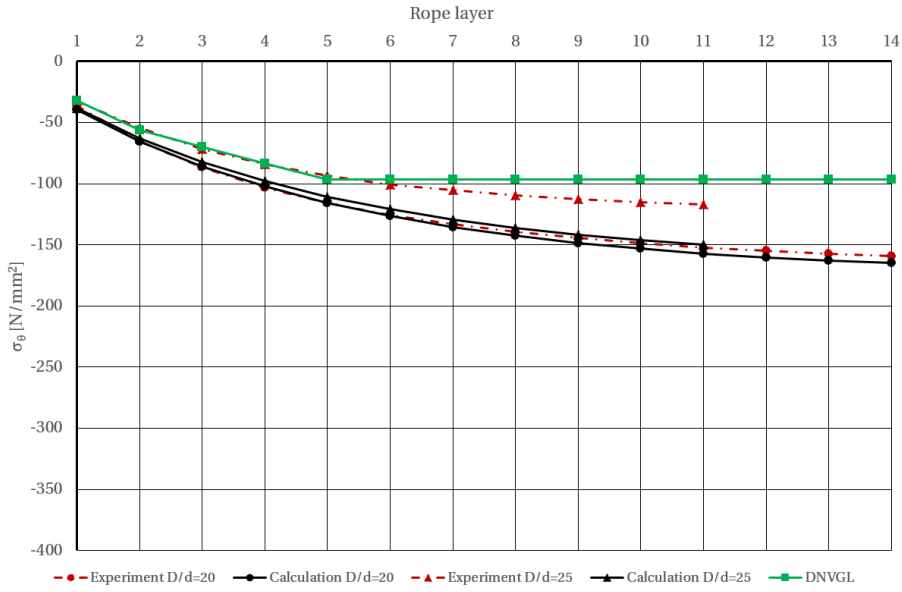

Figure H.4: Eqs. 8.2 and 8.3 vs. measured stresses - Ø20 mm Braided-C, 15% MBL

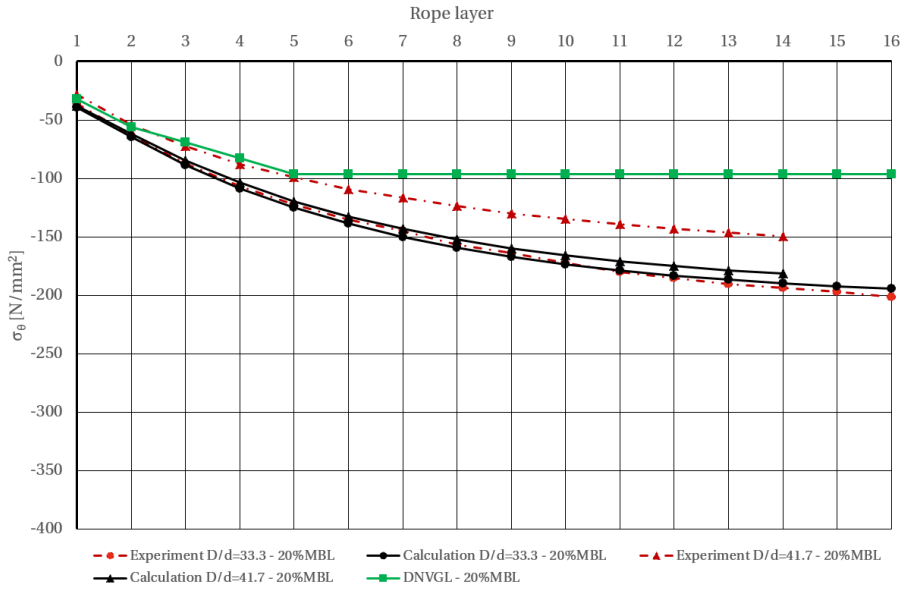

Figure H.5: Eqs. 8.2 and 8.3 vs. measured stresses - Ø12 mm Braided-C, 20% MBL

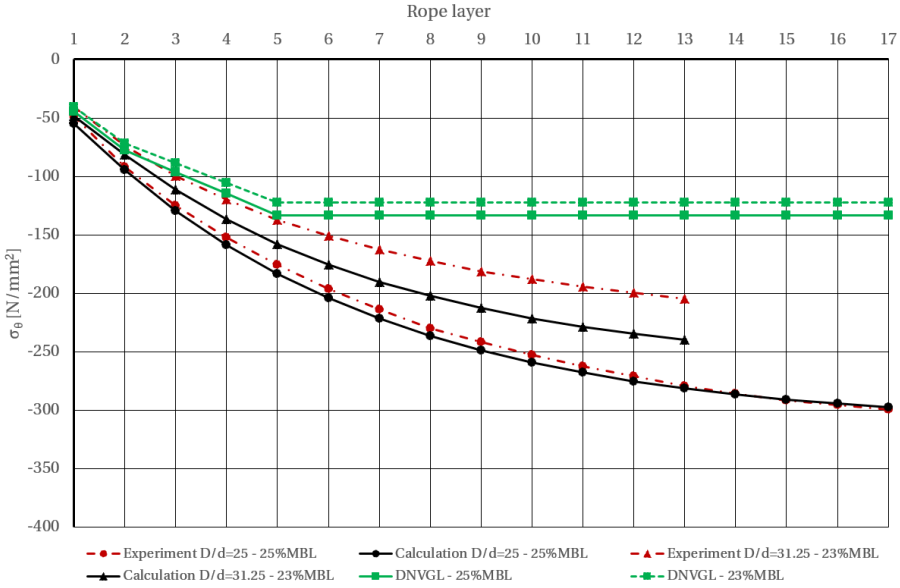

Figure H.6: Eqs. 8.2 and 8.3 vs. measured stresses - Ø16 mm Braided-C, 25% MBL

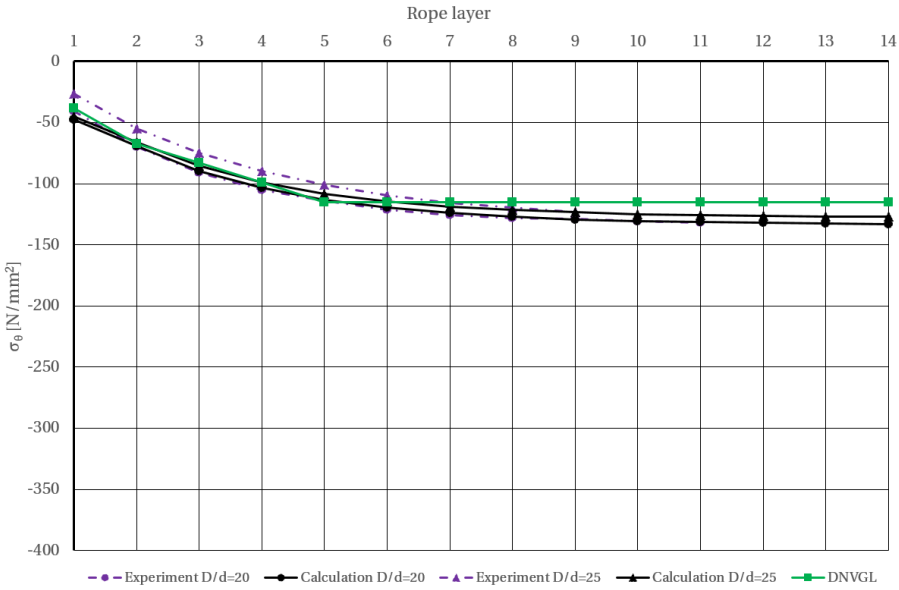

Figure H.7: Eqs. 8.2 and 8.3 vs. measured stresses - Ø20 mm DimStable, 17% MBL

Appendix I

Designing multilayer winches

A design procedure for improved load and stress assessments of multilayer winch drums is illustrated in Fig. I.1. This procedure is described in the following.

I.1 Multilayer winch design procedure

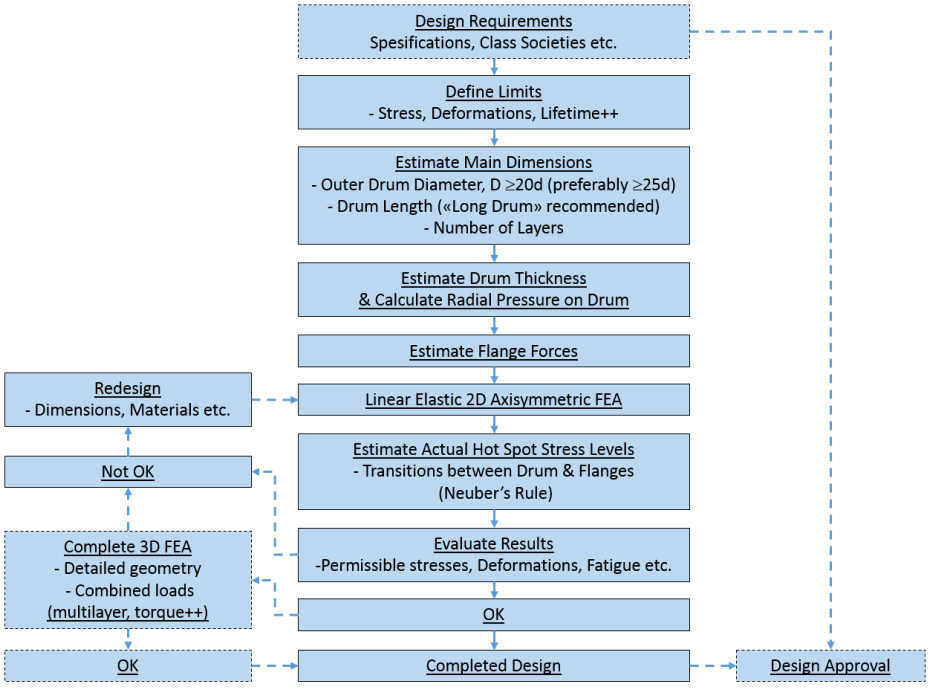

Figure I.1: Multilayer winch design procedure

Dependent on contracts, specifications and application of the winch, specific class rules or other requirements may apply. Therefore, an initial screening of specifications, requirements and rules is required at the start of the design process.

The next step is to estimate allowable stress limits, deformations and the required lifetime of the design. Main dimensions are defined based on the specified rope diameter and length. A D/d ratio of at least 25 is recommended, and a ratio less than 20 should be avoided. Preferably, the drum should fulfil the requirement of "long drums".

Further, a suitable drum thickness, radial pressure on drum and flange forces are estimated and applied in a linear-elastic axisymmetric FEA. The results are evaluated against allowable stresses and deformations. If required, fatigue calculations are carried out. Typically, stresses in transitions between flanges and drums exceed the material yield stress. Stress levels for the first load-cycle can be estimated from linear-elastic analysis by applying Neuber's rule.

The multilayer design process is completed if the values are OK. If not, modifications are carried out, and the FEA is rerun. In some cases, full 3D FEA with combined loading from multilayer spooling, brake torque, bending can be beneficial. If required, the design procedure is completed with design approval from class societies or other relevant authorities.

In case of spooling patterns causing distinct asymmetric loads, a full 3D solid FEA with loads according to Mupende [16] should be applied.

Further, Mupende's coupled method [16] can be applied for efficient initial parameter studies for both thin- and thick-walled winch drums [11].

I.1.1 Neuber's Rule

Local yielding is often unavoidable in drum flange transitions. This is usually no problem as long as the plastic zone is limited and the material is ductile. However, concerning fatigue calculations, relevant stress and strain levels need to be determined in these areas.

$$\sigma_{plastic}\epsilon_{plastic} = \sigma_{elastic}\epsilon_{elastic} \tag{I.1}$$

$$\sigma_{plastic} = \frac{\sigma_{max}^2}{E\epsilon_{plastic}} \tag{I.2}$$

Elastic-plastic analysis can be applied to determine more appropriate stress levels. However, such analyses are often complex and time-consuming. Alternatively,

Neuber's rule, Eq. I.1, can be applied with linear-elastic results to estimate the stress in notches for the first load cycle [41].

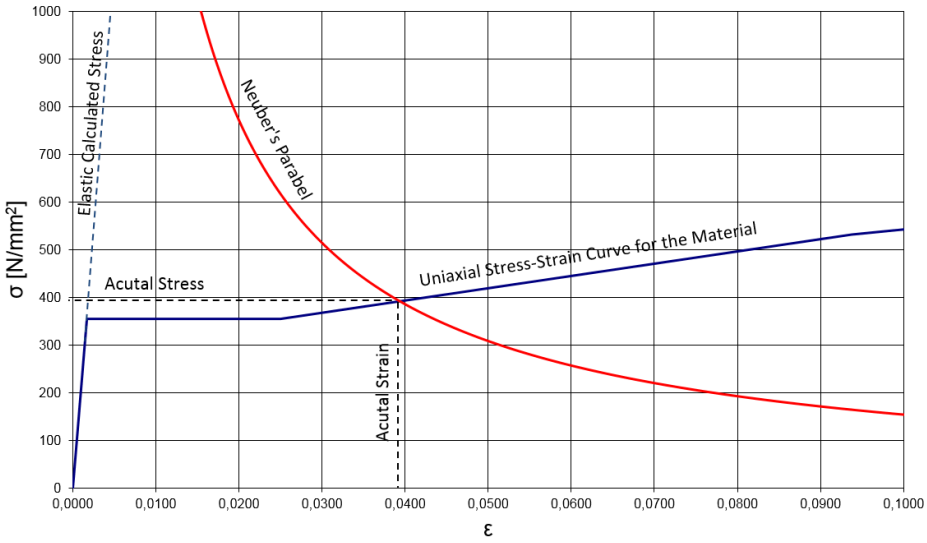

Figure I.2: Application of Neuber's rule

Figure I.2 shows an example of how this is applied. The stress and strain levels are determined from the intersection point between Neuber's parable and the uniaxial stress-strain curve of the material. The parable is calculated by Eq. I.2 where Hooke's law is combined with Eq. I.1. E is the elastic modulus of the material, and σ_{max} is the maximum stress in the flange-drum transition notch calculated by the linear-elastic analysis.

I.1.2 Practical equations

Equation I.3 calculates the minimum drum thickness for a multilayer winch drum with HPSFR. (σ_Y is the material yield stress, f_m is a factor less than one specifying the allowable yield stress capacity)

$$t \geq \frac{D}{2} - \frac{\sqrt{\sigma_Y f_m a D(\sigma_Y f_m a D - 4TS_F)}}{2\sigma_Y f_m a} \tag{I.3}$$

Dimensions of pure 12-strand braided ropes on multilayer winches can be approximated by Eq. I.4.

$$d_y \approx 0.7d, d_x \approx a \approx d_{nom} \tag{I.4}$$

ISBN 978-82-326-6714-7 (printed ver.)
ISBN 978-82-326-6048-3 (electronic ver.)
ISSN 1503-8181 (printed ver.)
ISSN 2703-8084 (online ver.)

NTNU

Norwegian University of
Science and Technology